ISTANBUL TECHNICAL UNIVERSITY ★ GRADUATE SCHOOL OF SCIENCE ENGINEERING AND TECHNOLOGY

CHARACTERIZATION INVESTIGATIONS OF W-xTi ALLOYS AND W-xTi/2 WT% LaB_6 COMPOSITES FABRICATED BY MECHANICAL ALLOYING AND SINTERED USING PRESSURELESS SINTERING OR SPARK PLASMA SINTERING TECHNIQUES

Ph.D. THESIS

Hadi Jahangiri

Metallurgy and Materials Engineering Department

Metallurgical and Materials Engineering Doctorate Programme

DECEMBER 2016

ISTANBUL TECHNICAL UNIVERSITY ★ GRADUATE SCHOOL OF SCIENCE ENGINEERING AND TECHNOLOGY

CHARACTERIZATION INVESTIGATIONS OF W-xTi ALLOYS AND W-xTi/2 WT% LaB_6 COMPOSITES FABRICATED BY MECHANICAL ALLOYING AND SINTERED USING PRESSURELESS SINTERING OR SPARK PLASMA SINTERING TECHNIQUES

Ph.D. THESIS
Hadi JAHANGIRI
(506112405)

Metallurgy and Materials Engineering Department

Metallurgical and Materials Engineering Doctorate Programme

Thesis Advisor Prof. Dr. M. Lütfi ÖVEÇOĞLU (ITU)

DECEMBER 2016

İSTANBUL TEKNİK ÜNİVERSİTESİ ★ FEN BİLİMLERİ ENSTİTÜSÜ

MEKANİK ALAŞIMLAMA VE BASINÇSIZ SİNTERLEME İLE SPARK PLAZMA SİNTERLEME YÖNTEMLERİYLE ÜRETİLEN W-xTi ALAŞIMLARIN VE W-xTi/AĞ. % 2 LaB_6 KOMPOZİTLERİNKARAKTERİZASYON ÇALIŞMALARI

DOKTORA TEZİ
Hadi JAHANGIRI
(506112405)

Metalurji ve Malzeme Mühendisliği Anabilim Dalı
Metalurji ve Malzeme Bilimi Mühendisliği Doktora Programı

Tez Danışmanı: Prof. Dr. M. Lütfi ÖVEÇOĞLU

ARALIK 2016

Hadi JAHANGIRI a Ph.D. student of İTU Graduate School of Science Engineering and Technology student ID 506112405, successfully defended the thesis/dissertation entitled "CHARACTERIZATION INVESTIGATIONS OF W-xTi ALLOYS AND W-xTi/2 WT% LaB_6 COMPOSITES FABRICATED BY MECHANICAL ALLOYING AND SINTERED USING PRESSURELESS SINTERING OR SPARK PLASMA SINTERING TECHNIQUES", which he prepared after fulfilling the requirements specified in the associated legislations, before the jury whose signatures are below.

Thesis Advisor :	**Prof. Dr. Mustafa Lutfi Öveçoğlu** ISTANBUL Technical University	.....
Jury Members :	**Prof. Dr. İsmail Duman** ISTANBUL Technical University	.....
	Prof. Dr. Burak Özkal ISTANBUL Technical University	.....
	Prof. Dr. Ayhan Mergen MARMARA University	.....
	Prof. Dr. Ayhan Mergen ISTANBUL University	.....

Date of Submission : 09 December 2016
Date of Defense : 28 December 2016

To: ***My dear Wife***

Father and Mother

FOREWORD

There are many people associated with this thesis deserving recognition. First of all, I would like to thank my supervisor Prof. Dr. M. Lütfi Öveçoğlu for his invaluable guidance, support and training during the course of my thesis and for being my mentor throughout my graduate studies. I would also like to thank to Prof. Dr. Ismail Duman for his guidance and also for keeping his door open and always having an answer. I am also thankful to Assoc. Prof. Dr. Burak Özkal for his advice, supportive actions and sharing his expertise with me.

I would like to express thanks to the members of Particulate Materials laboratories (PML). Hasan Gökçe, Duygu Ağaoğulları, Şeyma Duman, Merve Küçük, Aydın Şelte, Sultan Sönmez, Emre Tekoğlu, Didem Ovalı, Nazlı Akçamlı, Sıddıka Mertdinç, Hatice Turgut, Ceren Ergüneş, Meltem Bolluk, Nihan Özkan for their support and help.

I am extremely grateful to my dear wife and parents for their infinite support, help and motivation.

December, 2016 **Hadi JAHANGIRI**

TABLE OF CONTENTS

Page

LIST OF TABLES

Page

LIST OF FIGURES

Page

CHARACTERIZATION INVESTIGATIONS of W - xTi ALLOYS and W - xTi / 2 wt% LaB_6 COMPOSITES (x = 0.5, 1.0, 4.0 AND 10.0 wt%) FABRICATED by MECHANICAL ALLOYING and SINTERED USING PRESSURELESS SINTERING (PLS) and SPARK PLASMA SINTERING (SPS) TECHNIQUES

SUMMARY

Composites are materials composed of two phases: first phase is matrix and second phase is reinforcement. First phase is classified in itself into metal matrix, ceramic matrix, and polymer matrix. Metal matrix composites are categorized as high technology materials. These composites are generally used for high temperature applications. Various particulate reinforcements such as oxides, borides, and nitrides are used in this group of composites.

Particulate reinforcement powders (second phase) used in metal matrix composites (MMC) can be produced easily. Meantime, powder metallurgy has various advantages. Because of these advantages, MMCs reinforced by particulate material is usually categorized as a specific group. High elastic modulus, low density, high electrical and thermal conductivity, and etc. are some of main specifications of these composites. Particulate reinforced metal matrix composites (PRMMC's) have both metal and ceramic characteristics. Elements are homogeneously dispersed in PRMMC's. These composites have lower density and outstanding mechanical properties like higher wear resistance, hardness, or etc. compared to unreinforced matrixes. Generally, powders used in PRMMC's are produced by mechanical alloying (MA). By this technique, very fine sized (even nano sized) and brittle powders with homogeneous compositions can be fabricated. Based on MA, some solid solutions which are not possible to be produced thermodynamically in equilibrium condition can also be obtained.

Tungsten (W), being the densest (19.25 g/cm^3) and having one of the highest melting point (3422˚C) among other elements, is used as matrix material. W is a transition element located in VI group. W and its alloys have high melting temperature and high elastic modulus. These materials are used for developing matrix materials utilized at high temperatures due to their superior properties. Tungsten (W) and tungsten alloys have high melting temperatures, high thermal shock resistances, low thermal expansion coefficients which make them suitable for high temperature applications. However, production processes of W and its alloys are rather challenging, due to their high melting temperature and low ductility.

Production of W powders with high density by utilizing powder metallurgy (PM) and mechanical alloying (MA) needs high temperature conditions (1650˚C-1770˚C). Sintering temperature of these elements are decreased with addition of small amounts of transition metals such as Pd, Pt, Ni, Co, and Ti into matrix (1300˚C ~1500˚C).

Oxides, nitrides, borides and carbides like ZrC, TiN, Y_2O_3, LaB_6 powders are used in aid of developing high temperature characteristics of W powders. These reinforcements are located in grain boundaries therefore prevent grain growth and dislocation movements, ensuring material properties to increase at high temperatures.

W and its alloys are used in turbines, automobile production and electronic industry. Furthermore, these products are utilized in heavy materials, balance weigth, and some parts of motors as heavy alloys. Other applications of these products are electrode scrapers and electrodes of arc furnaces. The combination of W with various second phase particles of different ratios expands the appropriate function range of these composites.

According to the mentioned points, this PhD thesis is divided into two main parts. First part is based on MA, powder processing and powder characterization of W-Ti-LaB_6 powder composite, and second part consists of sintering produced composite powders. In powder processing part, MA is applied in room temperature via high energy milling. Based on this method, W nano composite powders are produced. In second part, sintering were achieved by two different methods: pressureless sintering (PLS) and spark plasma sintering (SPS). The main aim of this study is to fabricate W-xTi-2.0LaB_6 composite with the highest density, high hardness, high strength and high thermal shock resistance at lowest sintering temperature. Ti was used as activator and LaB_6 as reinforcement element.

This proposed research shows that mechanical alloyed tungsten (W) based matrix systems have nanostructure at room temperature by means of production via high-energy milling. The reason of using milling processes in general is to synthesize composite structures via mechanical alloying and to provide hybridization of ductile W-Ti matrixes in particular by reinforcing them with brittle and hard secondary particles (LaB_6). In spite of their superior properties such as high hardness, high thermal and wear resistance and good thermal values, there is no universal literature on the utilization of Ti as transition metal and LaB_6 as reinforcement in the W matrix. During powder characterization examinations, Ti solution in the W structure in non-equilibrium condition was measured by Vegard law, amount of Ti and effect of MA time on crystallite size and lattice internal strain were studied by W-H and Lorentzian methods. Tungsten based hybrid composites were manufactured by pressureless sintering (PLS) and spark plasma sintering (SPS) and characterized.

Final composite material consists of elements which are W as matrix, Ti as activator, and LaB_6 as reinforcement. Nano composite powders were produced by mechanical milling using different durations and a high-energy mill at room temperature which is one of the original approaches of this research. Investigations and resultant publications regarding the synthesis and characterization of W-Ti hybrid composites manufactured via these conditions will be the pioneering examples in the scientific literature. Furthermore, performing two different sintering methods (PLS and SPS) is the next priority of this thesis study. Microstructural and phase characterization investigations of the synthesized powders and sintered products were carried out by X-ray diffraction (XRD) and scanning electron microscopy (SEM) whereas thermal

characterization investigations were conducted by using differential thermal analysis (DTA) and differential scanning calorimetry (DSC). In the light of data obtained from microhardness measurements mechanical tests (wear resistance and microhardness) were also performed.

MEKANİK ALAŞIMLAMA ve BASINÇSIZ SİNTERLEME (PLS) İLE SPARK PLAZMA SİNTERLEME (SPS) YÖNTEMLERİYLE ÜRETİLEN W- xTi ALAŞIMLARIN ve W - xTi / ağ. % 2 LaB_6 KOMPOZİTLERİN (X = ağ. % 0.5, 1.0, 4.0 ve 10.0) KARAKTERİZASYON ÇALIŞMALARI

ÖZET

Geleneksel metal alaşımları ile seramik ve polimer malzemeler; günümüz modern teknolojisinin gereksinim duyduğu üstün fiziksel, kimyasal, mekanik ve termal özelliklere sahip değildirler. Geleneksel malzemelerin artan bu ihtiyacları karşılayamaması son 20 senedir ileri teknoloji seramik alaşımlar, kompozit malzemeler ve bu malzemelerin çeşitli kombinasonlarını içeren eşsiz özelliklere sahip yeni malzemelerin geliştirilmesine yönelik çalışmaların nedeni olmuştur.

Kompozitler, matriks malzemesi açısından sınıflandırdığımızda; metal, seramik ve polimer matriksli kompozit malzemeler olarak sınıflandırılmaktadır. Metal matriks kompozit malzemeler ileri teknoloji malzemeler grubunda yer alırlar. Bu kompozitler, genellikle yüksek sıcaklık uygulamalarında kullanılan malzeme grubuda yer almaktadılar. Bu tarz kompozitlerde tekviye malzemesi olarak genellikle çeşitli partikuler (oksit, borur, nitrür ve karbür) tercih edilmektedir.

Metal matriksli kompozit malzemeler sıfında yer alan partikül esaslı metal matriks kompozitler, üretimlerinde kullanılan malzemelerin kolay temini, ayrıca toz metalurjisi ve yönteminin avantajları, üretimlerinin kolaylığı göz önüne alındığında oldukça önemli bir malzeme grubunu oluştururlar. Bu malzemeler; yüksek elastik modül, yüksek sıcaklıklarda çalışabilme, düşük yoğunluk, düşük termal şok direnci, yüksek elektik ve termal iletkenlik gibi pekçok önemli özelliğe sahiptirler. Partikül takviyeli metal matriks kompozitler, metallerde ve aynı zamanda seramiklerde tek başlarına bulunmayan özelliklerin eşsiz bir bileşimini oluştururlar. Bu kompozitler, matriks dayanımını arttıran partiküllerin homojen dağılımları ile oluşurlar. Genel olarak, yüksek tokluk, sertlik ve takviyelendirilmemiş matriks malzeme ile kıyaslandığında daha düşük yoğunluklarda daha fazla dayanım göstermelerinin yanı sıra iyi aşınma dayanımı gösterirler. Metal matris kompozitler genel olarak, ana matris yapısı içine farklı özelliklere sahip ikincil fazların ilave edilmesi ile üretilmektedirler.

Partikül takviyeli metal veya seramik matrisli kompozitler tozlarının elde edilmesinde en çok kullanılan yöntemlerden birisi olarak mekanik alaşımlama tekniği söylenebilir. Bu yöntem ile oldukça küçük boyutlarda, hatta gevrek yapılı tozlarda nano boyutlu ve yapıya homojen olarak dağıtılmış tozlar üretilebilinmektedir. Mekanik alaşımlama, faz diyagramlarındaki sınırlamaları kaldırarak, termodinamik denge bakımından teorikte mümkün olmayan ya da diğer üretim yöntemleri kullanılarak oluşturulamayacak kompozisyondaki alaşımların üretilmesinin önünü açmaktadır.

Yapılan çalışmaların odak noktasında olan malzemeleren birisi olan ve en ağır metallerdenbirisi olan Volfram (W) 19.25 g/cm^3 yoğunluğuna sahiptir. Ergime noktası 3422˚C dir. W geçiş elementidir ve periyodik tabloda VI grubunda yer almaktadır. W ve W alaşımları yüksek ergime sıcaklığı, yüksek elastik modülüne sahiptirler. Bu malzemeler, direngenliklerinden dolayı yüksek sıcaklıklarda kullanılacak malzemelerin geliştirilmesinde matriks malzemesi olarak kulanılmaktadırlar. W ve W alaşımları; yüksek ergime sıcaklıkları, termal şoka karşı dayanımları, düşük termal genleşme katsayıları ve yüksek sıcaklıklarda gösterdikleri dayanımdan dolayı yüksek sıcaklıklarda kullanılacak malzemelerin geliştirilmesinde matriks malzemesi olarak öne çıkmaktadırlar. Genel olarak, yüksek ergime noktası ve düşük sünekliğinden dolayı volfram ürünlerinin üretimi zordur.

Toz metallurjisi ve mekanik alaşımlama yöntemleri kullanılsa bile yoğunluğu yüksek volfram üretimi için çok yüksek sinterleme sıcaklıklarına (1650 ˚C-1770 ˚C) ihtiyaç vardır. Bazı geçiş metallerinin (Pd, Pt, Ni, Co, ve Ti gibi) çok düşük miktarlardaki katkısı ile volframın sinterlenme sıcaklığı büyük oranda azaltılabilmektedir (1300 ˚C ~1500˚C).

Volfram ve alaşımlarının mekanik özelliklerinin geliştirilmesi amacıyla ZrC, TiN, Y_2O_3, LaB_6, gibi çeşitli refrakter karbürler, nitrürler, oksit ve borür fazları takviye elemanı olarak kullanılmaktadır. Bu takviye elemanları, volframın tane sınırlarına yerleşerek, tane büyümesi ve dislokasyon hareketini engellemekte ve malzemenin yüksek sıcaklık dayanımını artırmaktadır. Ayrıca, refrakter karakterli karbür ve nitrürlere ek olarak yüksek ergime sıcaklığı, yüksek sertlik değerleri ve iyi termal iletkenlikleri göz önünde bulundurularak geçiş metali borürleri de volfram alaşımlarında katkı malzemesi olarak kullanılmaya adaydır.

Volfram ve volfram alaşımlarının, türbin, otomobil uygulamalarından elektronik endüstrisine kadar birçok uygulaması mevcuttur. Ayrıca ağır alaşımlar olarak da bilinen bu alaşımlar yüksek yoğunluğa sahip malzemelerin gereksinim duyulduğu kinetik enerji penetratörleri, balans ağırlıkları ve motor aksamında kullanım alanı bulmaktadır. Genellikle oksijene kapalı sistemlerdeki yüksek sıcaklık uygulamalarında radyasyon kalkanı ve ısıtıcı elemanların geliştirilmesinde önem taşımaktadır. Bazı uygulamalarda da, kazıyıcı elektrot veya döner ark fırını elektrodu olarak kullanılmaktadır. Volfram ve çeşitli malzemelerin farklı oranlardaki katkısıyla geliştirilen volfram esaslı kompozitler, farklı malzeme özelliklerinin mükemmel bir kombinasyonunu sağladığından, uygulama alanları daha da genişlemektedir.

Bütün bu bilgilerin ışığında bu doktora çalışması iki farklı başlık altında yapılmıştır; birinci kısım, mekanik alaşımlama yöntemi ile partikül takviyeli W matriksli kompozit toz üretimi, ikinci kısım, üretilen kompozit tolarının sinterlenmesidir. Toz üretimi kısmında; oda sıcaklığında çalışan yüksek enerjili öğütücü kullanılarak mekanik alaşımlama (MA) yöntemi ile nano partikül boyutuna sahip volfram (W) matrisli nanokompozit tozları elde edilmiştir. İkinci bölümde, farklı kompozitlerin sinterlenmesi iki farkli metot ile (basıncsız sinterleme, Spark plasma sinterleme) yapılmıştır. Bu çalışmanın temel amacı yüksek sertlik, yüksek dayanım ve yüksek termal şok direncine sahip W matrisli hibrit kompozitlerin Ti ile aktive edilerek

düşük sıcaklıklarda ve yüksek yoğunluklarda üretilmesi ve üretilen nanokompozit tozların karakterizasyonudur.

Çalışma, mekanik öğütme/alaşımlama işleminin ardışık ve gerekirse tekrarlı olarak uygulanması ile genel olarak; mekanik alaşımlama ile kompozit yapıların sentezlenmesi konusunda, özel olarak ise; W-Ti gibi sünek matrislerin gevrek ve sert katkılarla (borür) hibritleştirilmesi yoluyla takviye edilmesi konusunda bir "ilk" olmuştur. Yüksek ısıl dirençleri, yüksek sertlik ve aşınma dirençleri ve iyi ısıl ve elektrik iletkenlikleri gibi üstün özelliklerine sahip W'in özelliklerini daha da geliştirmek amacıyla çeşitli geçiş metali diborürlerinin matris içerisinde takviye elemanı olarak kullanıldığı herhangi bir çalışmaya rastlanmamaktadır. Bu çalışmada, Ti ile aktive edilerek düşük sıcaklıklarda sinterlenebilecek W matrisli kompozitlerin LaB_6 fazı ile takviye edilmesiyle hibrit kompozit üretimi gerçekleştirilmiştir. Toz karakterizasiyonu kısmında Ti tozunun W matrisinde çözünürlüğünün artması çalışılmıştır. Bu artış Vegard kanunu ile ölçülüp değerlendirilmiştir. Ayrıca, Ti miktarının ve Mekanik alaşımlama suresinin tozların iç gerilmesine ve kristalit boyutuna olan etkileri W-H metodu ve Lorentzian metodu ile ölçülüp karşılaştırılmıştır.

Ayrıca bu çalışmada yaş ve kuru mekanik alaşmlamanın etkisi de son elde edilmiş ürünnlerde karşilaştırılmıştır. Elde edilen nano kompozit tozlarının morfoloji ve physiksel ozelikleri lçülmüştür. Buradan yola çıkarak mekanik alaşmlama için en uygun ortam seçilmiştir. Bu analizlerde kuru yontemin daha ince taneli toz yapısına sahip oldugu tespit edilmiş, ayrıca kuru ortamda üretilen nano kompozit tozlarının daha çok iç gerilime sahip oldukları yapılan hesaplamalar doğrultusunda tespit edilmiştir.

Tozlar kontrollü atmosferde basınçsız sinterleme yöntemi ve Spark plazma sinterleme (SPS) yöntemi kulanılarak sinterlendiler. Elde edilen numunelerin mekanik ve fiziksel özelikleri değişik analiz yöntemleri (SEM/EDS morfoloji analizi, Mikrovikers sertlik testi, Aşınma Testi, Arşimet, Piknometre yoğunluk testleri…..vb) kullanılarak belirlenmiştir . Optimum koşullar bulunduktan sonra ağ %2 LaB_6 kompozisiyona eklenerek sinterleme her iki yöntemde de uygulanmıştır. SPS ile elde edilen numunelerin en sert ve aşınmaya karşı en dirençli malzemeler oldukları tespit edilmiştir. Ayrica, ağ. %4 Ti ilavesi ile elde edilen kompozitlerini, üretilen kompozitler içerisinde en iyi mekanik özelliklere sahip olan kompozitler olduğu görülmüştür.

1. INTRODUCTION

Materials are important in the progress of civilization. The history of human civilization evolved from the Stone Age to the Bronze Age, the Iron Age, the Steel Age, and to the Space Age. Natural materials, like stone, clay, skins, and wood were used by people who lived in the Stone Age and those were in the origin of human life on Earth (Deborah D.L Chung, 2000).

By copper discovering, making it harder by alloying, the Bronze Age started about 3000 BC. The use of iron and steel as a stronger material that gave advantage in wars started at about 1200 BC. The third big step was the discovery of the iron extraction and steel production make steel around 1850. This development allowed the railroads and the building of the modern infrastructure of the industrial world (Song et al., 2003a; Tang et al., 2004).

The knowledge of materials specifications lets the designer to make the best material selection as a function of its application in a given product, meantime helps producers to overcome materials limits and constraints. Materials and transformation technologies become variables of the creation process. Modern technologies need materials with unique combinations of properties which cannot be accessed by metal alloys, ceramics, and polymeric materials. new materials like composites has been aroused to serve the request for new materials by unusual properties for notable plea when single materials could not prepare new requested requirements in the last decades (Song et al., 2003; Tang et al., 2004).

Composite materials are multiphase materials obtained by artificial combination of different materials to attain properties that the individual components cannot attain. In general, composites are classified according to their matrix materials. The main classes of composites are polymer-matrix, cement-matrix, metal-matrix, carbon-matrix, and ceramic-matrix (Deborah D.L Chung, 2000). Composites can also be classified based on the type of reinforcement used: fiber reinforced like as continuous or discontinuous, or particulate reinforced like as flakes, chopped fibers, shaped particles, and whiskers (Schwartz, 1984; Coskun, 2006).

Metal matrix composites (MMCs), like all composites; consist of at least two distinct phases, suitably distributed to provide properties not obtainable with either of the individual phases. Generally, there are two phases, e.g., a fibrous or particulate phase, distributed in a metallic matrix (Chawla and Chawla, 2006). The mechanical properties of the MMC's highly depend on the volume fraction and the type of the reinforcement as well as the type of the matrix (Stjernstoft, 2004).

For example one way to lower the coefficient thermal expansion (CTE) of a metal is to form a metal-matrix composite by using a low CTE filler. Ceramic particles such as AlN and SiC are used for this purpose because of their combination of high thermal conductivity and low CTE. As the filler usually has lower CTE and lower thermal conductivity than the metal matrix, the higher the filler volume fraction in the composite, the lower the CTE, and the lower the thermal conductivity (P.K. Rohatgi, 1993, Deborah D.L Chung, 2000).

Beside composites which offer broad ranges of requested mechanical and physical specifications during last decades in different industries, such as neuclear industry, aerospace sectors and etc, another groups of materials have found that namely nano structured materials or nano materials (Cahn, 2001) these groups of new detected materials have great and unique mechanical properties and special structure (Han et.al).

The production of ultrafine powders of different substances and nano structured materials for different areas of technology has been discussed in literature for many years now. In the last decade, the interest in nano powder has greatly increased because it was found that a decrease in the size of particles (grains, crystallites) below some threshold value may result in a large change of the properties (Gleiter H.,1992, Birringer R, et al. 1988). These effects appear when the average size of particles or grains does not exceed 100 nm, and are most evident when the particle or grain size is smaller than 10 nm. When examining the properties of superfine materials, it is necessary to take into account not only their structure and composition but also dispersion.

As dispersion strengtheners, refractory carbide, nitride and oxide phases, such as TiC, VC, ZrC, HfC, TiN, Y_2O_3, La_2O_3, Sm_2O_3, ThO_2, ZrO_2, etc. have been mainly used to improve the mechanical properties of tungsten and its alloys (Song et. al., 2002; Song et. al., 2003b; Lee et. al., 2004).

Keeping the above concepts in mind, the aim of this study has been to develop and characterize nanostructured LaB_6 particle-reinforced tungsten composite powders and their consolidated and sintered counterparts. Ti used as activation agent to investigate activated sintering of mechanically alloyed W-LaB_6.

2. LITERATURE REVIEW

2.1 Composites

Composite is combined in such a way enable the optimum use of their virtues while minimizing to some extent the effects of their deficiencies. This process of optimization can release a designer from the constraints associated with the selection and manufacture of conventional materials (Haris, B. 1999). Therefore, a composite material can be defined as a combination of two or more materials that results in better properties than those of the individual components used alone (Chung, D.L. 2000). In contrast to metallic alloys, each components of a composite material retains its separate chemical, physical, and mechanical properties. The two constituents are reinforcement and a matrix. The main advantages of composite materials are their high strength and stiffness, combined with low density, when compared with bulk materials, allowing for a weight reduction in the finished part (Campbel F. C., 2006; Mazumdar, S.K. 2002).

In general, according to their matrix materials, composites are classified. The main classes of composites are:

- Polymer-matrix,
- Cement matrix,
- Metal-matrix,
- Carbon-matrix,
- Ceramic-matrix,

Polymer-matrix and cement-matrix composites are the most common due to the low cost of fabrication. Polymer-matrix composites are used for lightweight structures (aircraft, sporting goods, wheelchairs, etc.) in addition to vibration damping, electronic enclosures, asphalt (composite with pitch, a polymer, as the matrix), and solder replacement. Cement-matrix composites in the form of concrete (with fine and coarse aggregates), steel-reinforced concrete, mortar (with fine aggregate, but no

coarse aggregate), or cement paste (without any aggregate) are used for civil structures, prefabricated housing, architectural precasts, masonry, landfill cover, thermal insulation, and sound absorption (Campbel, F. C. 2006). Carbon-matrix composites are important for lightweight structures (like the Space Shuttle) and components (such as aircraft brakes) that need to withstand high temperatures, but they are relatively expensive because of the high cost of fabrication (Chung, D.L. 2000; Mazumdar, S.K. 2002).

2.1.1 Metal matrix composite

As the name implies, for metal-matrix composites (MMCs), the matrix is a ductile metal. These materials may be utilized at higher service temperatures than their base metal counterparts. Furthermore, the reinforcement may improve specific stiffness, specific strength, abrasion resistance, creep resistance, thermal conductivity, and dimensional stability. Some of the advantages of these materials over the polymer matrix composites include higher operating temperatures, non-flammability, and greater resistance to degradation by organic fluids (Callister, W.D. 2001; Mazumdar, S.K. 2002). Metal-matrix composites are much more expensive than PMCs, and, therefore, their (MMC) use is somewhat restricted (Callister, W.D. 2001; Gay D. et. al. 2003).

Metal matrix composites (MMCs), like other composites, consist of at least two chemically and physically specific phases, suitably distributed to provide properties not obtainable with either of the individual phases. Generally, there are two phases, e.g., a fibrous or particulate phase, distributed in a metallic matrix (Chawla, C. 2006).

Metals are chosen as the matrix material in MMC structures mainly because of below mentioned specifications as compared with monolithic metals:

a) higher application temperature ranges,

b) higher transverse stiffnesses and strengths,

c) high toughness values,

d) high radiation resistances,

e) high electric and thermal conductivities,

f) higher strength-to-density,

g) stiffness-to-density ratios,

h) better fatigue resistances,

i) lower coefficients of thermal expansion (CTE),

j) better wear resistances,

k) they can be fabricated with conventional metal working equipment (Akovali and Uyanik, 2001).

Reinforcements can be divided into two major groups: (a) particulates or whiskers and (b) fibers. Fiber reinforcements can further be divided as continuous and discontinuous fibers. Fibers enhance strength in the direction of their orientation. Lower strength in the direction perpendicular to the fiber orientation is characteristic of continuous fiber reinforced MMCs. Discontinuously reinforced MMCs, on the other hand, display more isotropic characteristics (Chawla, 2006; Clyne, T.W. and Withers, P.J., 1993). Figuar 2-1 shows the schematic representations of these three major types of metal matrix composites

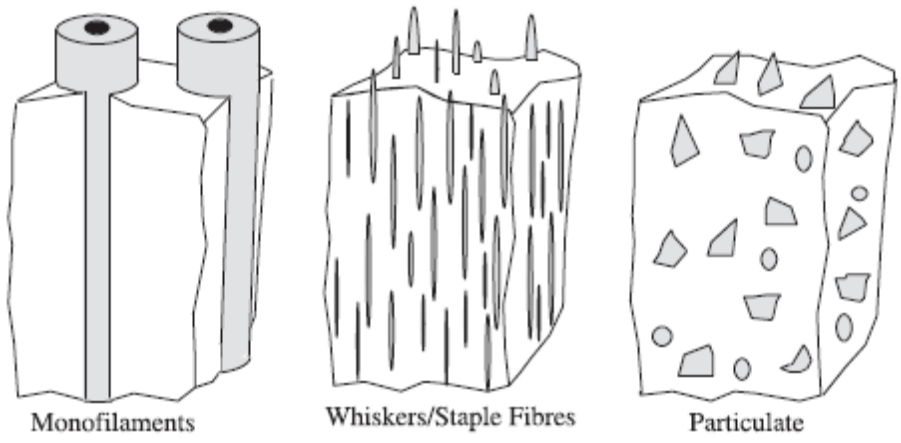

Figure 2.1 : Schematic representation of three shapes of metal matrix composite materials (J.I.Erausquin, 2011).

2.1.1.1 Particulate reinforced metal matrix composites (prmmc's)

The reinforcing phase in a composite can exist in a number of different configurations:, e.g. continuous filamament, short fiber, platelet, spheroid, particulate, sphere or irregular, and is classified by its shape, aspect ratio, geometric arrangement and concentration. Potentially, any material in particulate form can be used as the second phase in discontinuous composites (Smith, P.A. and Yeomans,

J.A. 2011). Particle size and the amount of reinforcement have pronounced effects on the mechanical properties of composites. Hardness and wear resistance of the composite is improved by proper addition of the reinforcement (Rahimian, M. 2012)

2.1.2 Particulate reinforced metal matrix composites (prmmc's)

Particulate reinforced metal matrix composites are comprised of the class of metals containing reinforcement phases exhibiting approximately equiaxed geometries, typically referred to as particles or particulates (Hunt, 2000). These differ from composites containing higher aspect ratio reinforcements such as fibers or whiskers in significant and important ways (Hunt, 2000). More recently, PRMMC's have received an increasing attention because of their relatively low costs, good formability and machinability as well as characteristic isotropic properties (Ibrahim et al., 1991; Sun et al., 2003).

Particulate reinforced composite systems can be considered in two sub-classes: 'large particle' and 'dispersion' strengthened composites, on the basis of the reinforcement or strengthening mechanisms.

2.1.2.1 Large particle composites

Particulate are the cheapest reinforcements. Many different ceramics are readily available in a wide range of sizes, but those of interest for MMCs are SiC and AI_2O_3 which are produced for grinding media. A tight particle size and control of purity are the main additional requirements for composites (Lloyd, d.J.1989).

The term 'large' is used to denote that particle-matrix interactions can not be treated on atomic or molecular level and 'continuum mechanics' is used. For composites reinforced by large particles, the reinforcing component is usually harder and stiffer than the matrix and they tend to restrain the movement of the matrix (Akovali and Uyanik, 2001). The matrix transfers some of the applied stress to the particles. The efficiency of reinforcement depends strongly on interaction at the particle-matrix interface (Akovali and Uyanik, 2001).

The choice of reinforcement is influenced by:

1) the application, which dictates the reinforcement form and cost level,

2) the compatibility between the reinforcement and the matrix,

3) the interfacial strength between the fibre and the matrix.

If the application requires the highest possible strength, continuous fibres or possibly whiskers are necessary, and this will involve considerable cost (Lloyd, d.J. 1989). If the part has to be secondary formed to shape, by processes such as extrusion, rolling, forging etc., whiskers and particulates are preferred because these undergo the least damage during any working process (Lloyd, d.J.1989). If the application is aimed for a low cost, mass market, particulates are the cheapest reinforcement (Lloyd, d.J. 1989).

Large particle composites are used widely as cutting tools for hardened steels. The hard carbide particles provide the cutting surface but they are not themselves capable of withstanding the cutting stresses because they are extremely brittle. Toughness is enhanced by their inclusion in the ductile metal matrix, which isolates the carbide particles from one another and prevents particle-to-particle crack propagation. Both matrix and particulate phases are quite refractory, to withstand the high temperatures generated by the cutting action on materials that are extremely hard (Askeland, 1984; Schwartz, 1984).

2.1.2.2 Dispersion-strengthened composites

In dispersion-strengthened composites, the fine dispersions of oxide, carbide, or boride particles impede the motion of dislocations so that the matrix is strengthened in proportion to the effectiveness of the dispersions as a barrier to the motion of dislocations (Asthana et al., 2006). For a dislocation to pass through a dispersion of fine particles, the applied stress must be sufficiently large to bend the dislocation line into a semicircular loop. Calculations show that interparticle separation for effective dispersion hardening should be between 0.01 and 0.3 μm (10 – 300 nm). To achieve this range of spacing between the dispersoid, the particle diameters should be less than 100 nm at volume fractions below 15% (Asthana et al., 2006). Of many dispersion-hardened alloy systems only a few have reached commercial significance, namely, aluminum, nickel, and tungsten; two others, copper and titanium, have proved succesful in laboratory and developmental stages (Schwartz, 1997). The development of oxide dispersion-strengthened (ODS) composites (e.g., W-ThO_2, Ni-$A1_2O_3$, Cu-SiO_2, Cu-$A1_2O_3$, NiCrA_1Ti-Y_2O_3, Ni-ThO_2, Ni-HfO_2, etc.) has led to considerable improvements in the elevated-temperature strength and creep-resistance

of the matrix alloys. The ODS composites contain small (<15%) amounts of fine second-phase particles, which resist recrystallization and grain coarsening, and act as a barrier to the motion of dislocations. Small quantities of fine oxide ceramics improve the strength without degrading the valuable matrix properties (Asthana et al., 2006).

2.2 Strengthening Mechanisms Of PRMMCs

The properties that are of particular interest in MMCs are:

- Elastic Modulus,
- Strength,
- High Temperature Strength,
- Coefficient of Thermal Expansion,
- Wear Resistance.

Properties which tend to be adversely affected by reinforcement are:

- Elongation,
- Toughness,
- Electrical Conductivity,
- Thermal Conductivity.

although a decrease in these properties can be used to advantage (Lloyd, d.J. 1989).

2.2.1 Rule of mixtures

There are lots of mathematical models which have been formulated for calculating the mechanical properties of PRMMC's (Liu, G.R., 1997, Ibrahim et al., 1991) . The simplest model is the rule-of-mixture model which is mainly used for particulate reinforced composites. In this model, the composite is assumed to be fully isotropic. So, the mechanical properties, such as strength, shear modulus and normal modulus of PRMMC can be estimated from the weighted average of the individual constituents (Ibrahim et al., 1991).

Continuously reinforced composites are expected to obey the rule of mixtures along the direction parallel to fiber axis both strength and elastic modulus:

$$E_c = E_f V_f + E_m V_m \qquad (2.1)$$

and

$$E_c = \sigma_f V_f + \sigma_m V_m \quad (2.2)$$

where E is the elastic modulus, σ is the strength, and V is the volume fraction, and the subscripts c, f and m refer to the composite, fibre and matrix respectively or the strength of a PRMMC the equation below can be written;

$$\sigma_{mmc} = f_c\sigma_c + (1-f_c)\sigma_m \quad (2.3)$$

where σ_{mmc} is the yield strength of the composite, σ_r is the yield strength of the reinforcement, σ_m is the yield strength of the matrix and f is the volume fraction of the reinforcement (Zhang, 2003, Lloyd, d.J. 1989).

The properties of composites are enhanced with increased volume fraction of fiber as expected from the rule of mixtures, but usually, even in continuously reinforced composites they fall below the theoretically expected values (Poquette**,** 2005).

The overall properties of particulates reinforced composites are somewhere between the dispersion strengthened and fiber reinforced composites even this place is strongly dependent on the size and shape of its reinforcement. In general, as the aspect ratio of the reinforcement increases the composite tends to exhibit increased amounts of fiber strengthening. On the other hand, as particle size decreases, the composite will tend to be primarily strengthened by dispersion methods (Poquette**,** 2005).

2.2.2 Shear lag theory

Compatibility between the matrix and the reinforcement is the most difficult condition to achieve. During the initial fabrication of the composite, compatibility is required so that the matrix can spread easily over the surface of the fibers and the fibers are well "wet". This will insure a void free composite. In general, ceramics are not easily wet by metals, and the wetting process is complicated. To achieve wetting, fibers or particulates are often surface treated prior to their incorporation into the matrix.

In perticular, it is difficult to achieve good compatibility with an Al matrix, because Al readily interacts to form intermetallics with most ceramics and it is also very difficult to achieve good wetting. SiC is essentially stable below the melting point of

Al, but reacts with most alloys at temperatures above the liquidus. (Warren and Andersson, 1984).

The reaction between Al and Sic can be expressed as:

$$Al + SiC = AlC + Si \quad (2.4)$$

This reaction produces aluminium carbide, which degrades the reinforcement and Si, which changes the composition of the matrix. However, if the Si content of the alloy is sufficiently high the reaction will tend to be reversed and will never happen, and the reinforcement will be stable (Lloyd, 1988).

Another important factor that is important is the achievement of high interfacial strength, since the strength of the composite is obtained by transferring matrix loading to fibre or particulates loading through the interface. To obtain maximum loading of the fibre, according to the shear lag theory the fibre has to be longer than a critical length, l_c, which is dependent on the interfacial strength (Lloyd, d.J. 1989)

$$l_c = \sigma_f d/2\tau \quad (2.5)$$

where σ_f is the fibre strength, τ is the level of the shear-sliding resistance and d is the fibre diameter. For particle reinforcement, the critical length is double that given by equation (Landis, C.M. and McMeeking, R.M. 1998, Lloyd, d.J. 1989)

Through this mechanism, the particle acts to bear some of the applied load. If the original model is modified considering that the particles are equiaxed, the yield strength of the composite can be calcuşlated using the equation below:

$$\sigma_{c=}\sigma_{rm+(1+(1/2).f)} \quad (2.6)$$

where σ_c is the yield strength of the composite, σ_{rm} is the yield strength of the unreinforced composite and f is the volume fraction of the reinforcement.

2.2.3 Orowan strengthening

Yielding in metals generally occurs through the process of dislocation motion. In composites containing small, incoherent particles (<1μm), inhibition of dislocation motion can arise as dislocations physically interact with small reinforcements (Callister, W.D. 2001). With small impenetrable particles, a passing dislocation will

bow between particles and finally pass by leaving behind an "Orowan" loop that is schematically shown in Figure 2-2.

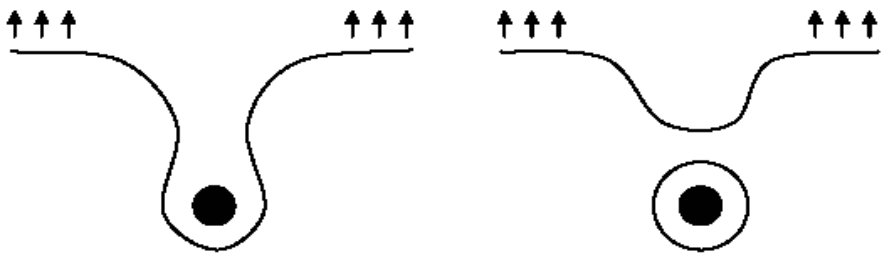

Figure 2.2 : The formation of an Orowan loop.

So, the strength of the materials is increased when the applied stress to bend the dislocation is increased. This Orowan stress is given below;

$$\tau = Gb/\lambda_{e-e} \tag{2.7}$$

Here, G is the shear modulus of the material, b is its atomic spacing, and λ_{e-e} is the edge to-edge spacing of the particles.

$$\lambda_{e-e} = \lambda_{c-c} - 2r \tag{2.8}$$

r is the average particle radius, and λ_{c-c} is the center-to-center particle spacing, which can be empirically expressed in Equation (2-9) as:

$$\lambda_{c-c} = 1.23r(2\pi/3f)^{1/2} \tag{2.9}$$

Here, *f* is the volume fraction reinforcement. From Equation (6) the strength of the composite is increased with decreasing particle size and increasing volume fraction of reinforcements. This is especially valid for particles in the submicron range. However, for particle sizes greater than 10 μm, strengthening mechanism is still predicted but not expected to be as effective as in the submicron-range (Mabuchi, 1997; Poquette**,** 2005).

2.2.4 Boundary strengthening

Ashby further developed Equation (2-7) by taking into account the inter-particle spacing and the effects of statistically distributed particles. The Ashby-Orowan relationship is given as Equation (2-10):

$$\Delta Б = 0{,}538((Gb\sqrt{f})/c).\ln(d/(2b)) \quad (2.10)$$

In Equation (2-10), ΔБ is the increase in yield strength, G is the shear modulus of the matrix, b is the magnitude of the Burgers vector, D is the real diameter of the particle, and f is the volume fraction of particles.

The Ashby-Orowan equation predicts negligible strengthening in composites having coarse or widely spaced reinforcements (Martin, J.W. 1980). This is due to the fact that composites of this type are influenced mainly by another mechanism, boundary strengthening. Again, yielding in metals in general occurs primarily through the creation and motion of dislocations, and this mechanism is based on crystallographic discontinuities or boundaries impeding this motion (Poquette, B. 2005). With the addition of reinforcement to a matrix, matrix/reinforcement boundaries are formed. When the material is stressed, dislocations tend to pile-up at these incoherent interfaces increasing the overall dislocation density and thus strength of the material as shown in Figure 2-3. This is similar to Hall-Petch strengthening in metals which is shown in Figure 2-4, which can simultaneously occur in the matrix due to grain refinement (Martin, J.W. 1980, Poquette, B.2005)

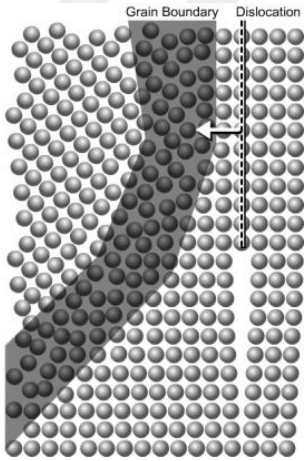

Figure 2.3 : The motion of a dislocation through a grain boundary (Chandrasekaran, D. and Nygårds, M.. 2003).

However, a dislocation cannot carry on moving forever. Eventually, it will run into a grain boundary, the jumbled mess of atoms at the edge of a grain. It will be stuck here unless it can jump the boundary into the next grain. Other dislocations piling up behind the first one can have the effect of increasing the surrounding stresses to the

point that the dislocation is forced through the boundary into the neighboring grain. This applies to all grains.

Grain size decreasing will duo to increment of grain boundary area in compared to the number dislocations in the grain. This decreases the number of dislocations that can pile up in order to force another dislocation across the grain boundary. This in turn increases the yield stress which in turn increases the hardness of the metal (Chandrasekaran, D. and Nygårds, M. 2003)

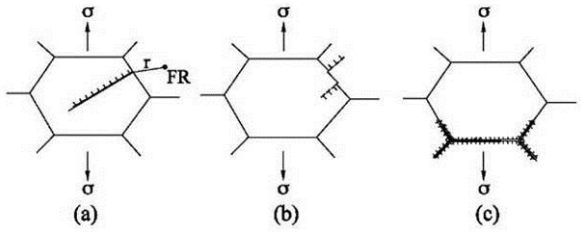

Figure 2.4 : Three models explaining the Hall-Petch behavior (Callister, 2000).

2.2.5 Solid solution strengthening

A single-phase metal can be strengthened by number of thermal and chemical methods, including solid solution formation and dispersion strengthening. Solute atoms introduced in the formation of solid solutions tend to segregate to dislocations because the total elastic strain energy associated with a dislocation and the solute atom is reduced (Mitchell, B.S. 2004). As a result, alloys are usually stronger than pure metals because impurity atoms that go into solid solution ordinarily impose lattice strains (either compressive or tensile, depending on the relative size of the impurity atom) on the surrounding atoms. In this way, lattice strain field interactions between dislocations and these impurity atoms restrict dislocation movement. These same lattice interactions exist during plastic deformation, too, so a greater stress is necessary to first initiate and then continue plastic deformation in solid-solution-strengthened alloys. Besides, relative size of the solute atoms, the effective elastic modulus of a solute atom also determines its effectiveness as a solid-solution strengthener (Mitchell, B.S. 2004). A solute atom disturbs the ideal lattice regularity. Thus, the movement of a dislocation can be hindered by the stress field around a misfitting solute atom: the dislocation can be attracted or repelled, depending on the local signs of the stress fields of the solute atom and the dislocation (Hull, D. and Bacon, D.J. , 2001).

A number of theories for solid solution strengthening have been developed through the years (Hull, D. and Bacon, D.J., 2001, Mittemeijer, 2010). The results display dependencies of the increase of strength (yield strength, critical shear stress and hardness) on the concentration of solute atoms, c, varying from $c^{1/2}$, to $c^{2/3}$ (see Equation (2-11) and Figure 2-5) and to c, where these proportionalities may pertain to certain ranges of the solute content). Experimental evidence for these relations has also been provided (Hull, D. and Bacon, D.J., 2001, Mittemeijer, 2010). The relation most often found and used for the increase of strength by solid solution strengthening may be:

$$\Delta(\text{strength}) = \text{constant} \times \sqrt{c} \tag{2.11}$$

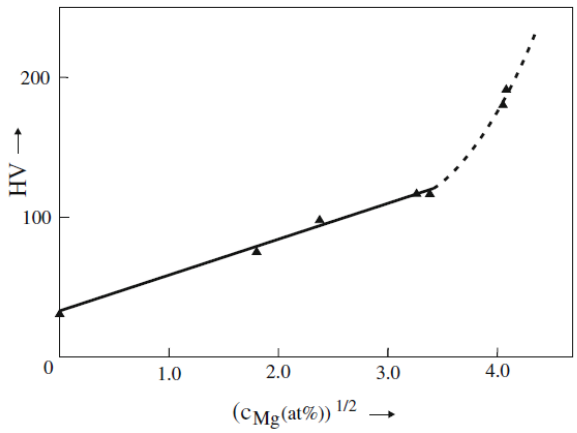

Figure 2.5 : Hardness as a function of Mg content for AlMg alloy specimens prepared by melt-spinning (Mittemeijer, 2010).

2.2.6 Strain hardening (work hardening)

The load necessary for further plastic deformation increases with continued straining. This is due to the effect of strain hardening also called work hardening. Upon plastic deformation, dislocation production can occur and, in general, the increase of the dislocation density makes dislocation propagation as a mechanism for glide more difficult, implying the application of larger loads to realize the same extension as at an earlier stage of plastic deformation (Mittemeijer, 2010). The plastic deformation that is not relieved immediately during the loading thus the plastic deformation that remains, is often called “cold work” (Mittemeijer, 2010). Primary dislocations produce loops by interaction with secondary dislocations, which give rise to local

dislocation tangles gradually developing into three-dimensional networks of sub-boundaries (Smallman and Bishop, 1999).

The average distance between the dislocations in a random distribution can be estimated as the reciprocal of the square root of the dislocation density ($1/\sqrt{\rho}$) (Mittemeijer, 2010). Thus, it follows that the increase of the strength (yield strength, shear stress, hardness) upon strain hardening due to dislocation generation can be given as below:

$$\Delta(\text{strength}) = \text{constant} \times \sqrt{\rho} \qquad (2.12)$$

This type of dependence of the increase of the yield strength on the produced dislocation density upon continued plastic deformation has been often observed (Mittemeijer, 2010) this relation can be shown in Figure 2-6.

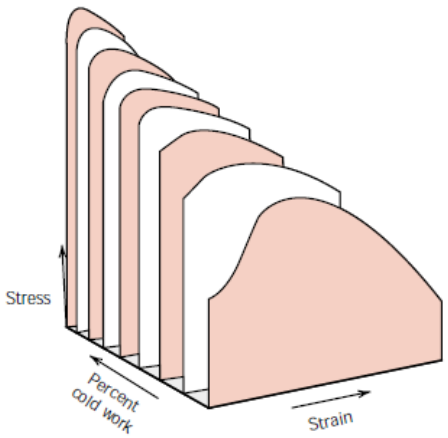

Figure 2.6 : The influence of cold work on the stress–strain behavior for low carbon steel (Callister, 2000).

2.3 Fabrication Of Particulate Reinforced Metal Matrix Composites (PRMMC)

There are various processing techniques used to fabricate PRMMC's. These fabrication methods can be grouped according to the temperature of the metal matrix during the process. So, there are liquid phase processes, solid state processes and two phase processes (Callister, W.D. 2001 and Ibrahim et al., 1991). Main liquid phase processes are molten metal mixing process, melt infiltration process and melt oxidation process. On the other hand, major solid state processes are powder metallurgy and high-energy and high-rate processes. Finally, two phase processes are

Osprey deposition, rheocasting and variable co-deposition of multi-phase materials (VCM) process (Ibrahim et al., 1991).

Industrial technology is growing at a very rapid rate and consequently there is an increasing demand and need for new materials. Particulate reinforced composites constitute a large portion of these new advanced materials. The choice of the processing method depends on the property requirements, cost factor consideration and future applications prospects (Callister, W.D. 2001).

Many different methods have been used to fabricate composites, and process details are often proprietary, but the different methods can be considered in terms of the two basic types of reinforcement: continuous and discontinuous (Lloyd, D.J. 1989).

Mechanical properties of a particle reinforced MMCs depend on factors such as reinforcement volume fraction, shape, contiguity, and spatial distribution within the matrix (Hamouda, A.M.S. et al., 2007). Although it is a very complex problem, various methods have been proposed to estimate the overall elastoplastic response as well as the bounds for effective elastic moduli of the composite (Hamouda, A.M.S. et al., 2007 , Casati, R. Vedani, M. 2014).

Some recently developed PRMMCs, using state-of-the-art high performance materials, such as tungsten, molybdenum, niobium and tantalum as the matrix material, are difficult to fabricate by using conventional liquid metallurgy process because these materials have incredibly high melting temperatures (Liu et al., 1994). In these cases, powder metallurgy seems attractive and has become the most important fabrication technique for this group of PRMMC's (Coskun, 2006).

2.4 Powder Metallurgy (PM)

The basic powder metallurgy (PM) technique to fabricate ceramic and metal parts involves the following steps:

- Making powders from metals or ceramics,
- Mixing or blending,
- Pressing or consolidation, and
- Sintering or firing.

In addition, a variety of secondary treatments such as coining (or sizing) and liquid infiltration are applied to sintered parts to create either fully dense parts, or special components such as oil-impregnated beatings (R.Asthana, et. al., 2006). The major advantages of PM are that difficult-to-melt refractory materials can be shaped into the final component without a need for melting of the raw materials, and parts with controlled porosity can be produced (e.g., filters, porous beatings, honeycomb structures, etc.) (R.Asthana, A.Kumar,N.B.Dahotre, 2006).

As early mentioned, the PM route is the most commonly used method for the preparation of PRMMCs (Liu et al., 1994; Huda et al., 1995). Blending of metallic powders with ceramic particles is a versatile technique for PRMMC production (Clyne, 2001). In the basic process, mixed or prealloyed powders are fed into a die, compacted into a desired shape and then are is sintered in a controlled atmosphere furnace to convert the mechanical bonds to the metallurgical bonds that link the powder particles (Newkirk and Kosher, 2004).

PM processes are usually very material efficient (high yield) with material utilization levels of nearly 95% or higher and allow mass production of complex parts such as gears. At present, nearly 70% of PM parts are used in the automotive industry (e.g., in bearing caps, connecting rods, etc.). The current world-wide PM market is roughly constituted by 25% ceramics, 60% metals, and 15% carbides (cutting tools, drill bits, etc.) (R.Asthana, A.Kumar,N.B.Dahotre, 2006). There are, however, some limitations of PM such as relatively high tooling cost, high cost of powders, porosity variation within a part, and limitations on part design (part must be ejectable from the die after compaction) (R.Asthana, A.Kumar,N.B.Dahotre, 2006). In spite of these limitations, powder metallurgy competes against fabrication processes such as machining and casting in terms of part precision and part complexity, and has an expanding niche market for specialized parts (d.j Lloyd, 1998, R.Asthana, A.Kumar,N.B.Dahotre, 2006).

2.4.1 Powder production

The starting raw materials for powder metallurgy are powders, typically in the size range of 0.1 to 200 μm. Melt atomization, electrodeposition, chemical synthesis and crushing and milling are commonly used methods to manufacture powders. A mechanical method of making powders from ceramic materials is milling. Milling

involves continuous collisions between hardened balls that impact the coarse powders entrapped between the balls via a process called microforging. This refines the powder size. Surface active agents are added to solid powder mixtures to prevent particle welding and agglomeration. The mechanical process of milling deforms, fractures and cold welds the particles through impact, abrasion, shear, and compression. Generally, metals do not respond well to milling because of their high ductility and tendency to cold weld. Also, because milling action generates heat, partial recrystallization could occur in metal powders (Suryanarayana, C. 2001). Milling is more useful to make fine powders from brittle ceramics than metals (Asthana, R. Kumar, A. Dahotre, N.B. 2006).

2.4.2 Powder mixing

Powder mixing is done to accomplish several objectives. Different size fractions of powders are blended to control the part porosity, aid sintering (e.g., with use of fine fractions), and facilitate powder compaction (e.g., with use of coarse fractions). New alloy compositions are obtained with greater ease by mixing different elemental powders than by mixing prealloyed powders. This is because prealloyed powders are often harder than elemental powders, have poorer compaction characteristics, and cause greater tool wear than elemental powders (Liu et al., 1994). Mixing also permits addition of binders to enhance the green strength of pressed part, and lubricants to assist pressure transmission during compaction and during part ejection after compaction. Stearate compounds (e.g., zinc stearate and calcium stearate) are commonly used lubricants for powders although other types of lubricants are also used (Suryanarayana, C. 2009). These compounds have low vaporization temperatures and are easily removed during the early stages of sintering. Mixing is done using rotating containers, screw mixers, and blade (impeller) mixers, which create different mixing pattems. Baffles are often added inside the mixing vessel to promote better mixing. Rotational speed and the amount of powders and other additives are important variables in mixing (Asthana, R. Kumar, A. Dahotre, N.B. 2006).

However, there are some problems, such as segregation and clustering, associated with the today's modern mixing or blending methods. The reasons of these problems include different flow characteristics between metal powder and reinforcement particles and the tendency of the agglomeration of particles to minimize their surface

energy (Liu et al., 1994). The segregation behavior of different sized particles is shown in Figure 2-7.

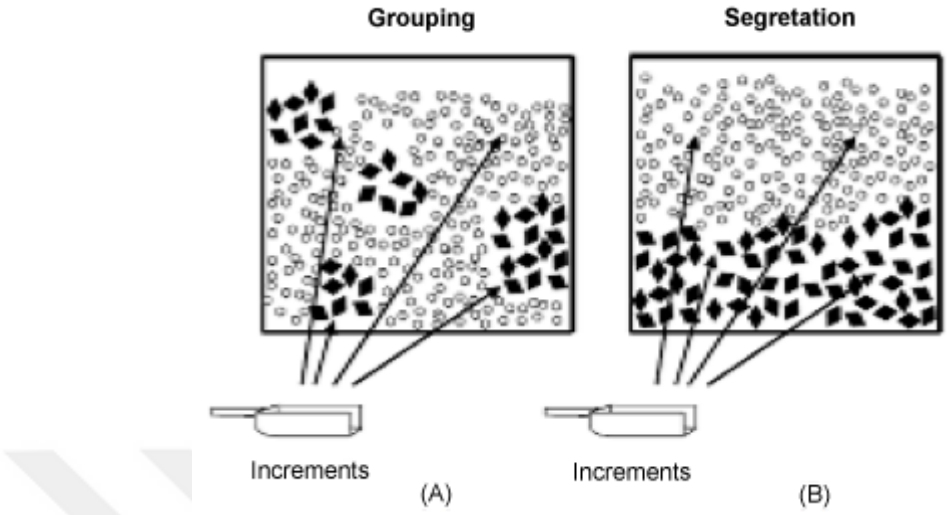

Figure 2.7 : Depiction of grouping (A) and segregation (B) of particles (USEPA. 2002e).

A seen in Figure 2-7, larger particles rise to top because they are moved upwards as smaller particles filled the voids beneath the larger particles. Furthermore, the effect of different densities between particles and metal powders of similar size is very important, too. The lighter particles tend to move upwards, while the heavier ones segregate at the bottom. However, these segregation and clustering problems can be overcome by a technique called "Mechanical Alloying (MA)" (Liu et al., 1994).

2.4.3 Mechanical alloying

Mechanical alloying (MA) is a powder processing technique that allows production of homogeneous materials starting from blended elemental powder mixtures. John Benjamin and his colleagues at the Paul D. Merica Research Laboratory of the International Nickel Company (INCO) developed the process around 1966. The technique was the result of a long search to produce a nickel-base superalloy, for gas turbine applications, that was expected to combine the high-temperature strength of oxide dispersion and the intermediate-temperature strength of gamma-prime precipitates. The required corrosion and oxidation resistance was also included in the alloy by suitable alloying additions (Suryanarayana, C 2001, Benjamin, J. S, 1992).

As a result, MA or non-equilibrium processing of materials has attracted the attention of a number of scientists and engineers due to the possibility of producing better and improved materials than it is possible by conventional methods (Suryanarayana et al., 2001).

In 1970, Benjamin introduced a pioneering development on ball milling technique for producing complex oxide dispersion-strengthened (ODS) alloys that were used for high temperature structural applications, such as jet engine parts. This unique method could be successfully used for preparing fine, uniform dispersions of oxide particles (Al_2O_3, Y_2O_3, ThO_2) in nickel-base superalloys. It is worth noting that these materials cannot be obtained by conventional powder metallurgy method (Eskandarany, M.S., et.al., 2000) .

However, the subsequent discovery of metastable phase formation by MA opened the door to important applications in Materials Science (Delogu et al., 2003). In addition to the metastable phases, equilibrium phases of commercially useful and scientifically interesting materials can be synthesized by MA, too (Suryanarayana et al., 2001).

2.4.3.1 Problems in mechanical alloying

Despite the advantages and simplicity of MA, the technique suffers from some problems. These can be discussed under three groups as: a) contamination, b) limited science content, and c) limited applications.

a. Contamination

The contamination of powders during MA is a major concern. The small size of the powder particles, availability of large surface area, and formation of new surfaces during milling all contribute to the contamination of the powder (Suryanarayana and et al.2001). In addition, the milling conditions (grinding medium, grinding vessel, time of milling, intensity of milling, etc.) and the atmosphere under which the powder is being milled also contribute to the contamination level. In many cases, especially when reactive metals like titanium and zirconium are being milled, the levels of contamination are high and unacceptable(Suryanarayana and et al.2001).

b. Limited science content

As mentioned, the scientific grounds for the MA process has been poor. Although it is known that the technique works and so is useful, one is not very clear how and why the technique works. This is because MA is a complex stochastic process and the number of variables involved is too many. Amongst others, these include the type of mill, size, shape, and weight of the grinding medium, velocity, angle and frequency of media impacts, ball-to-powder weight ratio, milling atmosphere, purity, size, shape, and hardness of the powder particles, milling time, milling temperature, and type and amount of the PCA. In spite of the complexities, some attempts have been made to model the process of MA and limited success has been achieved. For example, it has been possible to establish a relation between the experimentally observed phase formation and some of the process variables (Courtney, T.H. and Maurice, D., 1996., Suryanarayana and et al. 2001). But, it has not been possible to predict the final chemical constitution (type and description of phases) for a given set of milling conditions (Courtney,T.H. and et al. 1996).

c. Limited applications

The industrial applications of MA have been very few. The most significant applications seem to be about 350 t of ODS materials, 200 t of solder alloy, and 5 t of PVD target (Cr–V) alloys per year. Even though other potential applications have been suggested, many of them have not been industrial realities. The use of mechanochemical reactions in producing pure metals, alloys and compounds, dental filling alloys, catalyst materials, inorganic pigments, and fertilizers has been known for some time now but needs to be exploited further. Identification of some niche applications for the MA, products is likely to accelerate the rate of growth in this field (Suryanarayana and et al.2001).

2.4.3.2 MA processing parameters:

Different factors which influence MA and are known MA processing variables are as follows (Suryanarayana, 2001):

a. Type of mills (e.g., high-energy mills and low-energy mills),
b. The materials of milling tool (e.g., ceramics, stainless steel, and tungsten carbide),
c. Types of milling media (e.g., balls or rods),
d. Milling atmosphere (e.g., air, nitrogen, and an inert gas),
e. Milling environment (e.g., dry milling or wet milling),

f. Milling media-to-powder weight ratio,

g. Milling temperature,

h. Milling time,

i. Types of Mills.

a- Type of mills

Deferent types of high-energy milling equipment are utilized to produce mechanically alloyed powders. They differ in some parameteres as: capacity, efficiency of milling and additional arrangements for cooling, heating, etc (Suryanarayana, 2001).

Shaker mills such as SPEX mills which mill about 10-20 g of the powder at a time, are usually utulised in laboratory and for alloy screening purposes. These mills are manufactured by SPEX CertPrep, Metuchen, NJ, USA. The common variety of the mill has one vial, containing the sample and grinding balls, secured in the clamp and swung energetically back and forth several thousand times a minute. The back-and-forth shaking motion is combined with lateral movements of the ends of the vial that with each vial shaking, powders are mixed and milled simeltaniously, it is shown in Figure 2-8. Because of the about 5 cm amplitude and about 1200 rpm speed of the clamp motion, the ball move so fast (on the order of 5 m/s) and finally the force of the ball's impact is enormous. Therefore, these kind of mills can be classified as high-energy variety (Suryanarayana, 2001).

The usual type of these mills has one vial, containing the sample and grinding balls, secured in the clamp and shakes the milling container in three-mutually perpendicular directions at about 1200 rpm resulting in powder microstructural refinement with time (Suryanarayana, 2001; Goff, 2003). Ball-ball and ball-container collisions continually duo to powder refinment with time and finally lead to a homogeneous microstructure (Goff, 2003). Vial materials are variouse like: hardened steel, alumina, tungsten carbide, zirconia, stainless steel, silicon nitride, agate, plastic, and methacrylate (Suryanarayana, 2001).

Figure 2.8 : SPEX 8000 mixer/mill in the assembled condition and Tungsten carbide vial set consisting of the vial, lid, gasket, and balls (El-eskandarany M.S.,2000).

Planetary ball mill is another commen mill for performing MA experiments which a few hundred grams of the powder can be milled at a time. Because of vials planet-like movement, this kind of mills are called the planetary ball mill it is shown in Figure 2-9. The centrifugal force produced by the vials rotating around their own axes act on the vial contents, consisting of material to be ground and the grinding balls so trapped powder between balls and walls are refined. (El-Eskandarany M.S.,2000).

Figure 2.9 : Schematic view of planetary mills (El-eskandarany M.S.,2000).

Attritor milling is another conventional milling. An attritor composed of a vertical drum with a series of impellers inside it. Set progressively at right angles to each other, the impellers energize the ball charge, causing powder size reduction because of impact between balls, between balls and container wall, and between balls, agitator shaft, and impellers. Some size reduction appears to take place by interparticle collisions and by ball sliding. A powerful motor rotates the impellers, which in turn agitate the steel balls in the drum The operation of an attritor is simple.

The powder to be milled is placed in a stationary tank with the grinding media. This mixture is then agitated by a shaft with arms, rotating at a high speed of about 250 rpm to exert both shearing and impact forces on the material. The laboratory attritor works up to 10 times faster than conventional ball mills (Surryanarayana, 2001).

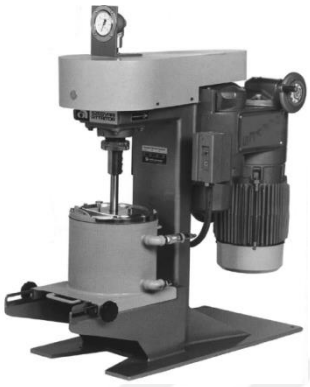

Figure 2.10 : Schematic view of attritor mills, (Surryanarayana, 2001).

Commercial mills for MA are much larger in size than attritor milling, SPEX milling or previouse mentioned ones and can process several hundred kilograms at a time. Mechanical alloying for commercial production is carried out in ball mills of up to about 1250 kg capacity, Figure 2-11 shows comertial industrial size ball mill. The milling time decreases with an increase in the energy of the mill. It has been reported that 20 min of milling in a SPEX mill is equivalent to 20 h of milling in a low-energy mill of the type Invicta BX 920/2 (.El-Eskandarany M.S., 2000). Table 2-2 shows capasity of different types of mills.

Table 2.1 : Different types of mills and their capasities (suryanarayana,C. 2001)

10	Sample weight
SPEX Mills	Up to 2x20 g
Planetary Mills	Up to 4x250 g
Attritors	0.5-100kg
Uni Ball mill	Up to 4x2000 g

As a rule of thumb, it can be estimated that a process that takes only a few minutes in the SPEX mill may take hours in an attritor and a few days in a commercial mill even though the details can be different depending on the efficiency of the different mills (.El-Eskandarany, M.S. 2000).

Figure 2.11 : Ball mills used in Iran copper concentration plant.

As described above, there are a number of different types of mills for conducting MA. These mills differ in their capacity, speed of operation, and their ability to control the operation by varying the temperature of milling and the extent of minimizing the contamination of the powders (Surryanarayana, 2001). Depending on the type of powder, the quantity of the powder, and the final constitution required, a suitable mill can be chosen. Most commonly, however, the SPEX shaker mills are used for alloy screening purposes (Surryanarayana, 2001). The Fritsch, the Pulverisette planetary ball mills or the attritors are used to produce large quantities of the milled powder. Specially designed mills are used for specific applications.

b- The materials of milling tool

Thematerial of grinding vessel, vial, jar, or bowl are some of the other terms container is important since due to impact of the grinding medium on the inner walls of the container, some material will be dislodged and get incorporated into the powder. Dislodged particles inter to the composition and contaminate the powder or alter the chemistry of the powder. Hardened steel, tool steel, hardened chromium steel, tempered steel, stainless steel, WC-Co, WC-lined steel, and bearing steel are the most common types of materials used for the grinding vessels (Surryanarayana, 2001). Some specific materials are used for specialized purposes; these include copper, titanium, sintered corundum, yttria-stabilized zirconia (YSZ), partially stabilized zirconia-yttria, sapphire, agate, hard porcelain, Si_3N_4, and Cu-Be (Surryanarayana, 2001).

c- Types of milling media

The size and material of the grinding medium also has an influence on the milling efficiency. Generally a large size of the grinding medium is useful since the larger weight of the balls will transfer more impact energy to the powder particles . It has also been reported that the final constitution of the powder is dependent upon the size of the grinding medium used.

d- Milling atmosphere

The major effect of the milling atmosphere is on the contamination of the powder. Therefore, the powders are milled in containers that have been either evacuated or filled with an inert gas such as argon or helium. (Nitrogen has been found to react with metal powders and consequently it cannot be used to prevent contamination during milling, unless one is interested in producing nitrides.) High-purity argon is the most common ambient to prevent oxidation and/or contamination of the powder. It has also been noted that oxidation can be generally prevented or minimized in the presence of nitrogen ambient (El-Eskandarany M.S.,2000).

Normally, the loading and unloading of the powders into the vial is carried out inside atmosphere-controlled glove boxes. These glove boxes are usually repeatedly evacuated and refilled with the argon gas. Investigators can be conducted the milling operation in mills that have been placed inside the evacuated glove boxes (Surryanarayana, 2001).

e- Milling environment

Metal powders are milled with a liquid medium and this is referred to as wet grinding; if no liquid is involved then it is referred to as dry grinding. It has been reported that wet grinding is a more suitable method than dry grinding to obtain finer-ground products because the solvent molecules are adsorbed on the newly formed surfaces of the particles and lower their surface energy. The less-agglomerated condition of the powder particles in the wet condition is also a useful factor. The rate of amorphization is faster during wet grinding than during dry grinding. A disadvantage of the wet grinding, however, is the increased

contamination of the powder. Thus, MA and mechanical milling (MM) usually performed dry (Surryanarayana and et. al., 2001).

f- Milling media-to-powder weight ratio

The ratio of the weight of the balls to the powder is sometimes referred to as charge ratio (CR), this ratio is an important variable in the milling process (El-Eskandarany M.S.,2000). This ratio can be varied from a value as low as 1:1 to as high as 220:1. Generally, a ratio of 10:1 is most commonly used while milling the powder in a small capacity mill such as a SPEX mill. But, when milling is performed in a large capacity mill, a higher ball-to-powder ratio (BPR) of up to 50:1 or even 100:1 is used. Besides, BPR values can influence milling period which by high values of BPR can led to shorter milling period (El-Eskandarany M.S.,2000).

Since alloying among the powder particles occurs due to the impact forces exerted on them, it is necessary that there is enough space for the balls and the powder particles to move around freely in the milling container. Thus, care has to be taken not to overfill the vial and generally about 50% of the vial space is left empty (Surryanarayana and et. al., 2001).

g- Milling temperature

Another important parameter in milling is The temperature. it is expected that the temperature of milling will have a significant effect in any alloy system. During powder processing in high temperature, strain values in powders is lower and crystallite size and grain size are large (Suryanarayana, 2001).

During the formation of nanocrystals, it was reported that the root mean square (rms) strain in the material was lower and the grain size was larger for materials milled at higher temperatures and solid solubility is completed faster (Suryanarayana, 2001).

h- Milling time

The time of milling is the most important parameter. Milling times have to be decided for type of mill used, the intensity of milling, the ball-to-powder ratio, and the temperature of milling. Normally, the time is so chosen as to achieve a steady state between the fracturing and cold welding of the powder particles. It should be

considered that long period of milling can causes to increasing of contamination. Figure 2-12 shows effect of milling time and BPR on particle size (Suryanarayana, 2001).

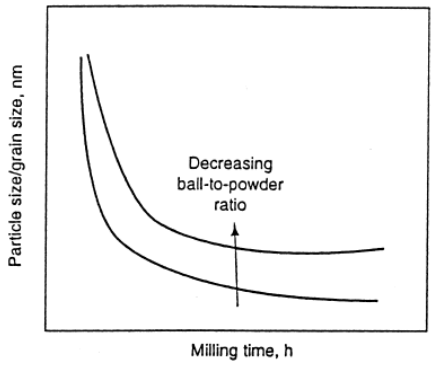

Figure 2.12 : Refinement of particle and grain sizes with milling time. Rate of refinement increases with higher milling energy, ball-to-powder weight ratio, lower temperature, etc. (Suryanarayana, 2001).

2.4.3.3 The technique and mechanism of mechanical alloying (MA)

MA is an advanced powder fabrication process that can produce ultra-fine and homogenous powders (Ryu et al., 2000). Even, nanocrystalline materials (with a grain size of few nanometers, usually<100 nm) are also produced by MA of powder mixtures. Additionally, it has been recognized that this technique can be used to induce chemical reactions in powder mixtures at room temperature or at much lower temperatures than normally required to synthesize pure metals (Suryanarayana et al., 2001).

In any mechanical alloying process, starting powder constituents are first mixed or blended according to the required stoichiometry for the given composite formulation. Then, they are put in the milling container with the appropriate ball charge and milled until a steady state of homogeneous dispersion is achieved (Goff, 2003). The central event of MA is the ball-powder collisions (Fecht H. L., 2002). Microstructural refinement during the MA process occurs due to repeated welding, fracturing, and rewelding of the dry powder constituents during their impact between ball-ball and/or ball-container collisions (Fecht H. L., 2002). Whenever two balls collide, typically around 1000 particles with an aggregate weight of about 0.2 mg are trapped during each collision. The force of the impact plastically deforms the powder

particles leading to work hardening and fracture (Suryanarayana, 2001; Fecht H. L., 2002). Figure 2-13 shows Schematic view of a ball-powder-ball collision.

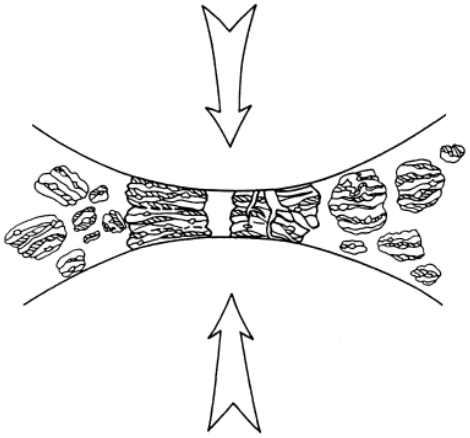

Figure 2.13 : Schematic view of a ball-powder-ball collision (Suryanarayana, 2001).

In addition, this severe working of powders produces a very fine grain size and substructural strengthening via high dislocation density and fine subgrain size. As a result, MA provides several strengthening mechanisms which are oxide dispersion strengthening, carbide dispersion strengthening, fine grain size strengthening, substructural strengthening and solid solution strengthening (Öveçoğlu, 1987).

In order to understand the physical phenomena that occur during MA processing better, it is useful to divide the typical process into three or four stages (Öveçoğlu, 1987; Goff, 2003). Figure 2-14 shows deformation characteristics of starting powders used in a typical MA process.

In the early stages of milling, the particles are soft (using either ductile-ductile or ductile-brittle material combination), so their tendency to weld together and form large particles is high (Suryanarayana, 2001). Variouse kind of particle sizes develops, with some as large as three times bigger than the starting particles which (Suryanarayana, 2001; Goff, 2003). The composite particles at this stage have a characteristic layered structure consisting of various combinations of the starting constituents (Öveçoğlu M.L., 1987).

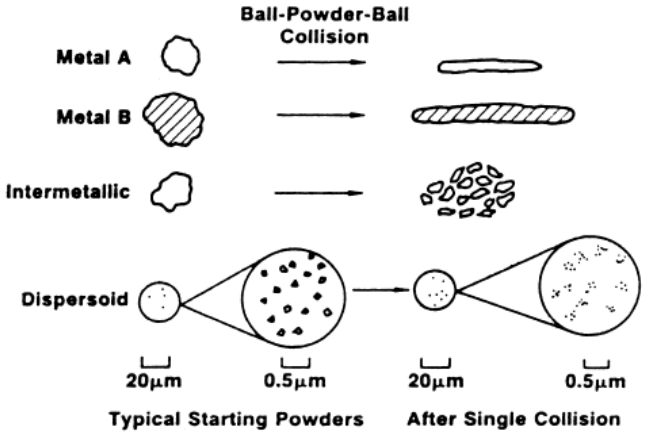

Figure 2.14 : Deformation characteristics of starting powders used in a typical MA process (Suryanarayana, 2001).

As the metallic phases are flattened and overlap during ball collisions, atomically clean surfaces are placed in contact with one another and subsequently cold weld together. At the same time, brittle constituents (intermetallics and dispersoids) are occluded by the ductile constituents thus becoming trapped along cold weld interfaces (Goff, 2003). Figure 2-15 show early stage of processing in which particles are layered composites of starting constituents.

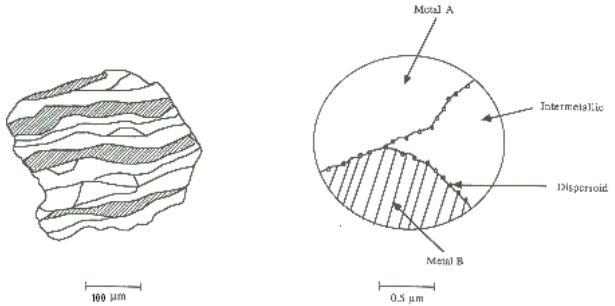

Figure 2.15 : Early stage of processing in which particles are layered composites of starting constituents (Öveçoğlu, 1987).

As depicted in Figure 2-16, in the intermediate stage the composite powder particles are further refined due to continual welding and fracturing of excessively work-hardened metallic phases and brittle intermetallics and/or dispersoids (Goff, 2003). At this stage, the tendency to fracture predominates over cold welding (Suryanarayana, 2001). The particles consist of convoluted lamellae. The reduction in particle size, increased microstructural mixing, and elevated temperature of the powder constituents due to the adsorbed kinetic energy of milling balls all help to

form areas of solute dissolution throughout the metallic powder matrix (Öveçoğlu, 1987). So, this potentially may lead to areas where new phases develop which is mainly due to an overall decrease in atomic diffusion distances between individual phases and decreased activation energies for diffusion due to the increase in temperature (Öveçoğlu, 1987; Goff, 2003). Consequently, the inter-layer spacing decreases and the number of layers in a particle increase (Suryanarayana, 2001).

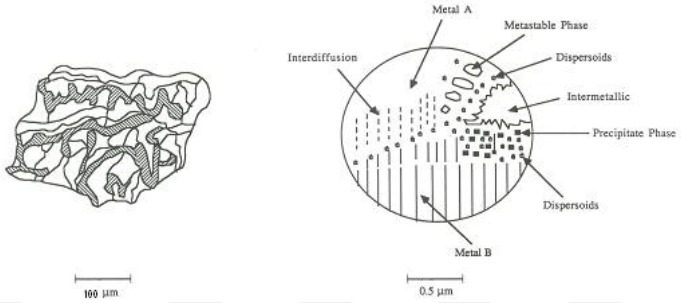

Figure 2.16 : Intermediate stage of processing showing reduced lamellae thickness, solute dissolution, and formation of new phases (Öveçoğlu, 1987).

In the final stage, steady-state equilibrium is attained when a balance is achieved between the rate of welding, which tends to increase the average particle size, and the rate of fracturing, which tends to decrease the average composite particle size which is shown in Figure 2-17. As a result smaller particles are able to withstand deformation without fracturing and tend to be welded into larger pieces, with an overall tendency to drive both very fine and very large particles towards an intermediate size (Suryanarayana, 2001).

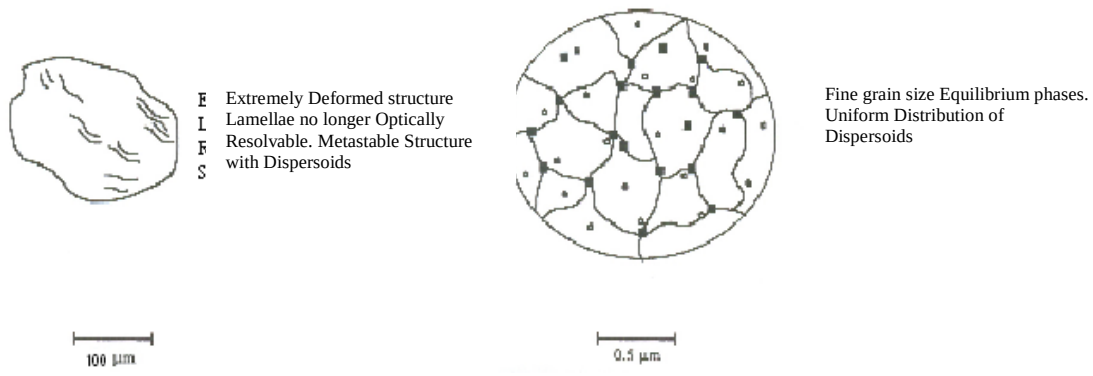

Figure 2.17 : The final stage of processing and consolidation (Öveçoğlu, 1987).

Furthermore, individual particle compositions are equal to the starting powder blend composition; the lamellae are no longer optically resolvable; and the dispersoid

spacing is equal to the distance between weld interfaces (Öveçoğlu, 1987). At this point, further processing would not improve the dispersoid distribution or serve to enhance the homogeneity of the composite microstructure (Öveçoğlu, 1987; Goff, 2003). The particle size distribution at this stage is narrow, because particles larger than average are reduced in size at the same rate that fragments smaller than average grow through agglomeration of smaller particles (Suryanarayana, 2001).

In order to complete the MA process and obtain a useable bulk composite form, the powders are heated to a temperature greater than half the melting temperature of the composite powder and consolidated. This serves to further homogenize the microstructure (Goff, 2003).

It is possible to conduct MA of three different combinations of metals and alloys:

- Ductile-ductile,
- Ductile-brittle,
- Brittle-brittle systems.

Therefore, it is convenient to discuss the mechanism of MA also under these categories (Fecht H. L., 2002).

Ductile-ductile combination is thought to be the ideal combination for the MA process. Alloying occurs due to the repeated action of cold welding and fracturing of powder particles therefore, cold welding cannot occur if the particles are not ductile so it is necessary to have at least 15% of a ductile component for achieving alloying.

In the early stages of MA, the ductile components get flattened to platelet/pancake shapes. A small quantity of the powder, usually one or two particle thickness, also gets welded onto the ball surfaces. This coating of the powder on the grinding medium is advantageous since it prevents excessive wear of the grinding medium; so, the contamination of the powder is prevented (Suryanarayana, 2001). In the next stage, these flattened particles get cold welded together and form a composite lamellar structure of the constituent metals (Öveçoğlu, 1987). An increase in particle size is also observed at this stage (Suryanarayana, 2001). For instance, it has been found that during MA of Fe-Cu powder mixture, agglomerates of multilayers are formed leading to microstructures very similar to those obtained by cold-rolling (Fecht H. L., 2002). With increasing MA time, the composite powder particles get work hardened, the hardness and consequently the brittleness increases, and the particles get fragmented resulting in particles with more equiaxed dimensions (Suryanarayana, 2001). With further milling, the elemental lamellae of the welded

layer and both the coarse and fine powders become convoluted rather than being linear Alloying begins to occur at this stage due to the combination of decreased diffusion distances, increased lattice defect density, and any heating that may have occurred during the milling operation (Öveçoğlu, 1987). The hardness and particle size tend to reach a saturation value at this stage, called the steady-state processing stage. With further milling, true alloying occurs at the atomic level resulting in the formation of solid solutions, intermetallics, or even amorphous phases. The layer spacing becomes so fine or disappears at this stage that it is no longer visible under an optical microscope (Öveçoğlu M. L., 1987; Suryanarayana C., 2001).

Considering ductile-brittle combinations, in the initial stages of milling, the ductile metal powder particles get again flattened by the ball-powder-ball collisions, while the brittle oxide or intermetallic particles get fragmented. These fragmented brittle particles tend to become occluded by the ductile constituents and trapped in the ductile particles. The brittle constituent is closely spaced along the interlamellar spacings (Öveçoğlu M. L., 1987). With further milling, the ductile powder particles get work hardened, the lamellae get twisted, and refined. With continued milling, the lamellae get further refined, the interlamellar spacing decreases, and the brittle particles get uniformly dispersed, if they are insoluble, in the ductile matrix (Öveçoğlu M. L., 1987; Suryanarayana C., 2001). Figure 2-18 shows Schematics of microstructural evolution during milling of a ductile-brittle combination of powders.

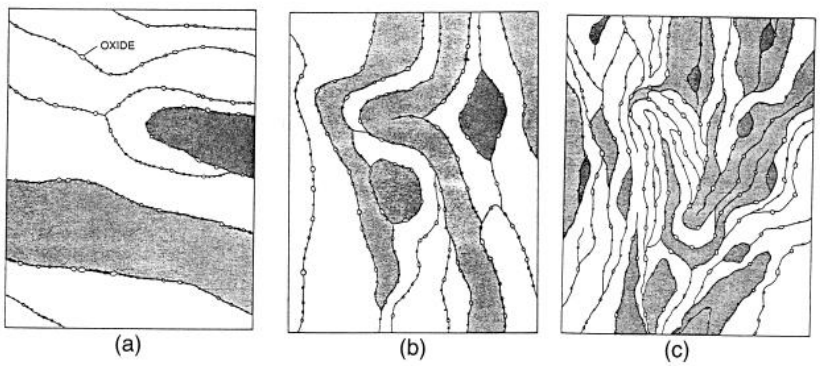

Figure 2.18 : Schematics of microstructural evolution during milling of a ductile-brittle combination of powders. This is typical of an oxide dispersion strengthened case (Suryanarayana C., 2001).

2.4.4 Compaction and consolidation

The next step after blending or mixing operation, is the consolidation and pressing of the powder mixture to form the green compacts (Liu et al., 1994). This step is the one

of the most critical steps in the PM process, because it sets the density of the powder and the uniformity of the density throughout the product. Because final properties strongly depend on density, uniform properties require uniform density (Newkirk and Kosher, 2004). The compaction process has the following major functions:

- To consolidate the powders into the desired shape,
- To impart, as much as possible, the desired final dimensions considering any dimensional changes resulting from sintering,
- To give the desired level of porosity,
- To provide sufficient strength for subsequent handling (Upadhyaya, 2000**).**

Compaction comprises specific stages that involve sliding and rearrangement of particles, elastic compression at particle contact points, plastic yielding for metals or fragmentation for brittle materials (C. Suryanarayana, 1999). Similar steps are seen in nano powder compaction. The principal differences in nanoparticles arise from the specifics of small particle sliding and friction, as well as from the changes in dislocation assisted deformation behavior. Sliding and rearrangement in nano powders are severely restricted owing to large frictional forces among powder particles (Groza J.R., 1999, Suryanarayana C., 1999)

Powder compaction allows the basic part shape to be created through partial densification of powders under an external pressure. Two common compaction configurations are single-action compaction and double-action compaction which shown in Figure 2-8. Single-action compaction is used for relatively simple shapes and involves uniaxial pressing of powders in a suitable die with the help of a single punch. More uniform densification is achieved with the use of double-action compaction in which two movable punches press powders from opposite directions. Depending upon the complexity of the part, additional punches may be used to achieve a uniform density (Suryanarayana C., 1999).

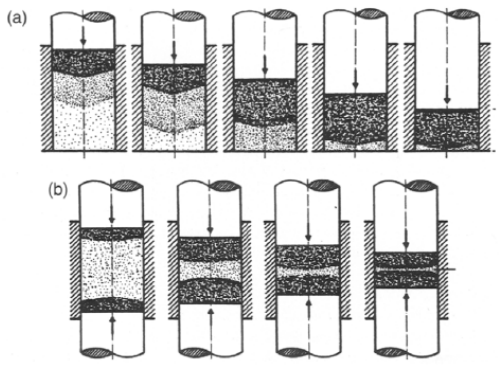

Figure 2.19 : Powder compaction with a-single punch b-double punch(R.Asthana, A.Kumar,N.B.Dahotre, 2006).

In double-action compaction, minimum pressure and minimum densification occur at the midplane or neutral axis in the powder bed and maximum pressure and densification at the ends(Asthana R., et.al , 2006). However, even in double-action compaction the compact might develop an uneven density along the pressure axis because of inter particle friction and friction at the die wall (Asthana R., et.al., 2006). Because the porous central portion of the pressed part shrinks more than the end regions during sintering, the part may become uneven. Such variations can be reduced by use of advanced net-shape powder-forming processes such as powder injection-molding, gel-casting, hot-pressing, and shock consolidation (Asthana R., et.al., 2006).

2.4.5 Sintering

Although casting and melting methods are very popular for many manufactured materials, the melting points of many ceramic and some metallic materials are too high for processing by melting and casting. These relatively refractory materials are manufactured into useful shapes by a process that requires the consolidation of small particles of a powder into a solid mass (German R.M. 1996, Askland, 2011). In Table 2-2 variable afecting parameters on sintering is offered.

Table 2.2 : Variables affecting sinterability and microstructure (Kang, 2005).

Variables related to raw materials (material variables)	Powder Shape Size Size distribution Agglomeration Chemistry Composition Impurity Homogeneity
Variables related to sintering conditions (process variables)	Temperature Time Pressure Atmosphere Heating Cooling rate

Sintering acts to bond particles together into strong, useful shapes. It is used to fire ceramic pots and in the fabrication of complex, high-performance shapes, such as medical implants. Sintering is irreversible since the particles give up surface energy associated with small particles to build bonds between those particles (German R.M. 1996, Fang Z.Z., 2010, Ring T.A. 1996; Boch, P. and Leriche, A., 2001). Prior to sintering, the particles flow easily while after sintering the particles are bonded into a solid body. From a thermodynamic standpoint, sinter bonding is driven by the surface energy reduction. Small particles have more surface energy and sinter faster than large particles. Since atomic motion increases with temperature, sintering is accelerated by high temperatures (Boch, P. and Leriche, A., 2001). The driving force for sintering comes from the high surface energy and curved surface inherent to powder particles (Fang Z.Z., 2010, Kang, 2005). The initial stage of sintering corresponds to neck growth between contacting particles where curvature gradients normally dictate the sintering behavior. The intermediate stage corresponds to pore rounding and the onset of grain growth. During the intermediate stage the pores remain interconnected, so the component is not hermetic (Kang, 2005, Callister, W.D. 2005, Ring T.A. 1996). Final stage sintering occurs when the pores collapse into closed spheres, giving a reduced impediment to grain growth (German R.M.,1996, Fang Z.Z., 2010) Microstructural changes that occur during sintering are shown in Figure 2-9 schematically. Usually the final stage of sintering starts when the component is more than 92% dense. During all three stages, atoms move by several transport mechanisms to create the microstructure changes, including surface diffusion and grain boundary diffusion (Fang Z.Z., 2010, Callister W.D., 2005)

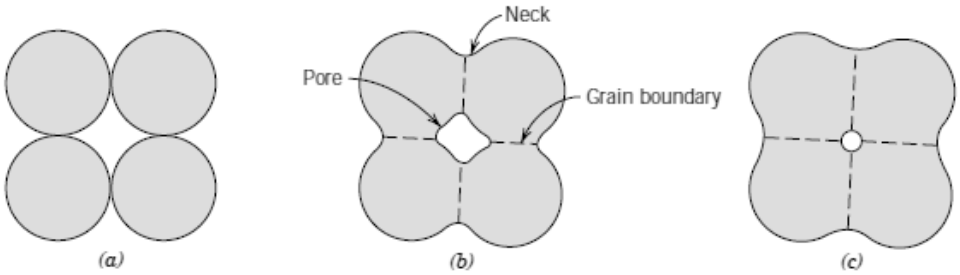

Figure 2.20 : Microstructural changes that occur during sintering, (W.D.Callister, 2005).

Basically, sintering process can be divided into the two types as :1) Solid-state sintering and 2) Liquid phase sintering. Solid-state sintering occurs when the powder compact is densified fully in a solid state at the sintering temperature, while liquid phase sintering occurs when a liquid phase is present in the powder compact during sintering (Kang, 2005).

2.4.5.1 Solid state sintering

Traditionally, refractory metals have been solid-state sintered either by direct current sintering or furnace sintering for purification and densification prior to deformation processing into fully dense mill product shapes (Coble, 1961).

Densification of refractory metals occurs through solid-state sintering and can be broken down into three stages as: initial, intermediate and final stage (Coble, 1961, Beere, 1976). In the initial stage, particles in contact with each other undergo neck growth and densification occurs as the centers of the particles approach each other. The driving force for densification is the decrease in surface energy that accompanies dissipation of the curvature of the neck region. After approximately 3% shrinkage, the curvature of the neck region decreases sufficiently that initial stage sintering equations are no longer valid. The microstructure of the intermediate stage is characterized by smooth, interconnected pores at the grain boundaries (Coble, 1961, Beere, 1976, Ring T.A. 1996). Finally, as densification proceeds, the pores begin to close, and the microstructure is better represented by spherical pores at the grain boundaries. Sintering enters the final state at a porosity level of about 8% when all of the pores are closed. Grain growth proceeds during both the intermediate and final stages.

Several sintering mechanisms can be concurrently active during the three sintering stages. In the initial stage, surface diffusion can be significant, but results in neck growth without densification. The dominant low-temperature densification mechanism of W and other refractory metals is grain boundary diffusion (German and Munir, 1976a).

Solid-state sintering occurs when the powder compact is densified fully in a solid state at the sintering temperature, while liquid phase sintering occurs when a liquid phase is present in the powder compact during sintering (Kang, 2005).

In general, the solid-state sintering processes are carried out in protective atmospheres in a furnace at temperatures below the melting point of the base metal. The process leads to a decrease in the surface area, an increase in compact strength and mostly shrinkage in the compact. Longer sintering duration at high temperatures decreases the number of pores and makes the pore shape become smooth. Also, grain growth can be expected (Upadhyaya, 2000).

2.4.6 Activated sintering

Activated sintering involves a small addition to the powder mix or, more rarely, to the sintering atmosphere in order to promote sintering kinetics. The action of the activator may be to remove the surface oxide from the powder particles or to facilitate more rapid diffusion of the metal's atoms (Upadhyaya, 2000; Gupta V.K. et.al. 2007). A high-melting-temperature material requires a high sintering temperature to induce significant diffusion. However, a lower-melting-temperature phase will have inherently faster diffusion rates.

Activated solid-state sintering occurs when there is rapid mass transport through a high-diffusivity second phase, which provides a short circuit diffusion path (German, 1996). The most effective second phases have a high solubility for the base metal, but low solubility in the base, so that it will remain segregated at the grain boundaries (Zovas et al., 1983; German and Rabin, 1985). They also have a low liquidus temperature, indicating a low activation energy and high diffusivity. Systems that form intermediate compounds with high melting points are unfavorable. Most research investagations on activated sintering have involved the refractory metals of molybdenum, tungsten, chromium, rhenium, and tantalum (German, 1996; Gupta V.K. et.al. 2007).

Generally, it is very difficult to fabricate tungsten because of its high melting point, and low ductility. Even when powder metallurgy techniques are used, processing of tungsten requires very high sintering temperatures up to 2400˚C – 2800˚C to achieve near fully dense structures (Li and German, 1983). The addition of small quantities of some transition metals such as Pd, Pt, Ni, Co, and Fe provides a major reduction in the sintering temperature of W (Li and German, 1983; German and Munir, 1976; Vacek, 1959; Hayden and Brophy, 1963, Genç, A. and Öveçoğlu, M.L., 2010, Genç, A. et.al., 2012, Ağaoğulları, D., et.al. ,2013) Figure 2-21 shows effect of Co, Fe, Ni, and Pd as activator on sintered density of W powder. This reduction of the sintering temperature is due the decrement of the activation energy between W particles. Activation energy for volume self-diffusion of tungsten, which is 135 kcal/mol becomes 68 kcal/mol in the case of Ni activated W (Hayden and Brophy, 1963; Gupta V.K. et.al. 2007).

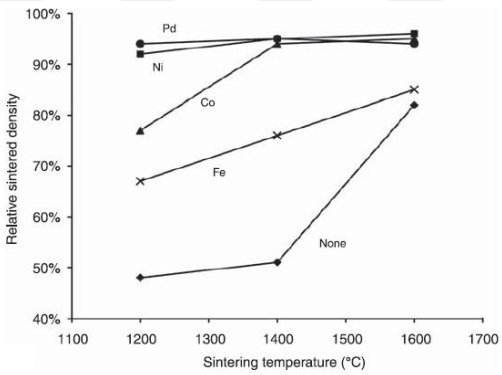

Figure 2.21 : Effect of Co, Fe, Ni, and Pd on sintered density of a 0.7 μm W powder (Li and German, 1983).

Hayden and Brophy interpreted the mechanism of the activated sintering in terms of three main stage in their study (Hayden and Brophy, 1963). After the appearance on the tungsten particle surface of a “supporting phase” formed by activating agent, the dissolution of tungsten at the points of contact between particles takes place and the diffusion of tungsten atoms along the interface between the “supporting phase” and the particle provides densification. On this basis, the distance between the centers of adjacent particles decreases and consequently fuller shrinkage is completed. Figure 2-22 shows sintering mechanism of nickel-coated tungsten powder schematicly (Hayden and Brophy, 1963; Samsonov and Yakovlev, 1967; Gupta V.K. et.al. 2007).

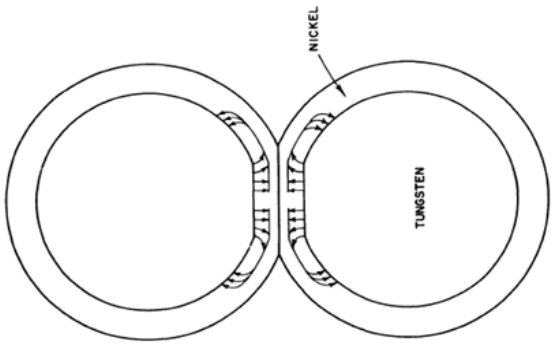

Figure 2.22 : Schematic representation of sintering nickel-coated tungsten powder (Brophy et. al., 1963).

In another elucidation of the activated sintering mechanism, the dissolution of tungsten at the activator-tungsten interface was followed by volume diffusion outwards through the activator layer and subsequent surface diffusion like what is shown in Figure 2-23 (Toth and Lockington, 1967). Diffusion through the activator layer to the contact point between adjacent particles results in the formation of sintering "necks" (Toth and Lockington, 1967, Corti, 1986).

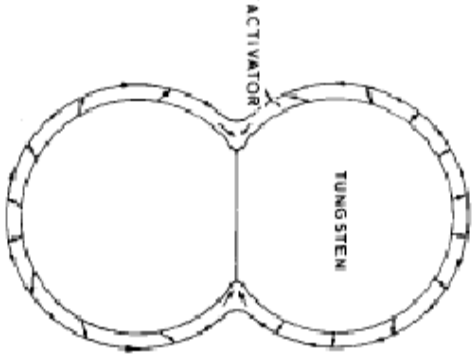

Figure 2.23 : Schematic representation of activated sintering of tungsten (Toth andLockington, 1967).

Samsonov and Yakovlev stated activated sintering in terms of the electron structure of the activators and tungsten; an increase of the stable d-bonds in the system lowers the free energy, activating the sintering process in which diffusion is accelerated by the activators for which tungsten acts as an electron donor and this ease of electron transfer gives rise to the high solubility in the activating element (Samsonov and Yakovlev, 1969).

German and Munir reported that the activator has a role in providing enhanced grain boundary diffusion with the activator layer wetting the interparticle grain boundary (German and Munir, 1982) Figure 2-24 show activator mechanism based on their description. The relative solubility criterion is a prerequisite for enhanced diffusion of the refractory metal. Enhanced mass transport, and hence densification, results from the lowering of the activation energy for the refractory metal in the activator (German and Munir, 1982, Corti, 1986).

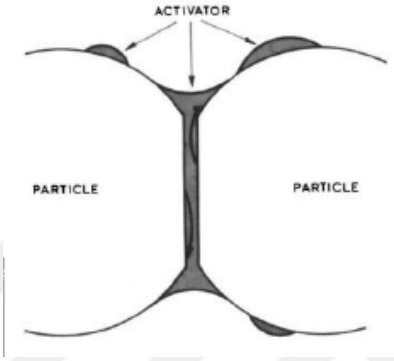

Figure 2.24 : Schematic representation of the activated sintering (German and Munir,1982).

2.5 Nanostructured Materials

The production of ultrafine powders of different substances and nanostructured materials for different areas of technology has been discussed in literature for many years now. In the last decade, the interest in this subject has greatly increased because it has been found that a decrease in the size of particles (grains, crystallites) below some threshold value may result in a large change of the properties (Kurlov A. S. and Gusev A. I., 2013, El-Eskandarany et al., 2000). These effects appear when the average size of particles or grains does not exceed 100 nm, and are most evident when the particle or grain size is smaller than 10 nm. When examining the properties of superfine materials, it is necessary to take into account not only their structure and composition but also dispersion (Kurlov A. S. and Gusev A. I., 2013).

Mechanical alloying (MA) which is a well known process for preparing several amorphous, metal nitrides, metal carbides and alloys, has also been considered as a powerful technique for synthesizing numerous nanostructured materials(El-Eskandarany et al., 2000). Nanostructured materials that are defined as materials

with grain sizes less than 100 nm. They have received much attention as advanced engineering materials with improved physical and mechanical properties (El-Eskandarany et al., 2000). Because of the extremely small size of the grains, a large fraction of the atoms in these materials is located in the grain boundaries and as a result the material exhibits enhanced combinations of physical, mechanical, and magnetic properties (compared to material with a more conventional grain size, i.e., >1 μm) (Fecht H. L., 2002, Suryanarayana C., 2001). Nanostructured materials show increased strength, high hardness, extremely high diffusion rates, and consequently reduced sintering times for powder compaction (Suryanarayana C., 2001).

Recently, MA process has become a popular method to fabricate nanocrystalline materials due to its simplicity and relatively inexpensive equipment (El-Eskandarany et al., 2000) The advantage of using MA for the synthesis of nanocrystalline materials lies in its ability to produce bulk quantities of material in the solid state using simple equipment and at room temperature (Suryanarayana C., 2001). In this process, lattice defects are produced by pumping energy into powder particles of typically 50 μm particle diameter. This internal refining process with a reduction of the average grain size by a factor of 103-104 results from the creation and self organization of small-angle and high-angle grain boundaries within the powder particles during the mechanical deformation process (Fecht H. L., 2002). Grain sizes with nanometer dimensions have been observed in almost all mechanically alloyed pure metals, intermetallics, and alloys (Suryanarayana C., 2001). The elemental processes leading to formation of nanostructures include three basic stages. Firstly, the deformation is localized in shear bands which contain a high dislocation density (Fecht H. L., 2002). Their typical width is approximately 0,5-1 μm (Suryanarayana C., 2001). At a certain level of strain within the high strained regions, these dislocations annihilate and recombine to small-angle grain boundaries separating the individual grains (Fecht H. L., 2002). This results in a decrease of the lattice strain. With the continuing process, deformation occurs in shear bands located in previously unstrained parts of the material. The grain size decreases steadily and the shear bands unite. The small angle boundaries are replaced by higher angle grain boundaries and, consequently, dislocation-free nanostructured grains are formed (Suryanarayana C., 2001).

MA'd powders can be compacted to obtain a useable bulk composite form. In principle, the compaction of nanopowders is similar to that of the conventional powders. However, some differences in nanoparticles appear from the specifics of small particle sliding and friction (Suryanarayana C., 2001; Groza J. R., 2003). Sliding and rearrangement in nanopowders are severely limited because of the large frictional forces. These forces are a result of mechanical, electrostatic, Van der Waals phenomena that become more important with decreasing particle size. Mechanical friction resistance is high due to the numerous interparticle contact points. Furthermore, irregular boundaries favor agglomerate formation. As a result, particle rearrangement is limited and lower green densities are achieved compared to the conventional powders (Groza J. R., 2003). The key to the consolidation of nanopowders is to achieve densification with minimal microstructural coarsening and undesirable microstructural transformations (Suryanarayana, 2001, Groza J. R., 1999).

Ingeneral, the sintering mechanism of the MA'd powders is the same as the sintering mechanism of conventional powders. However, the tendency of the grains to grow is very strong due to the very little diffusion distance and extreme curvature of nanoparticles. The coarsening kinetics may be slowed down by limiting the grain boundary mobility using a solute drag or particle pinning effect (Groza J. R., 1999). Small particles stabilize a fine grain size at high temperatures. On the other hand, the solute drag effect is based on the decrease of grain boundary mobility and the free energy when solute atoms segregate at grain boundaries. The simplest way to control grain coarsening is to take advantage of the pinning effect of open pores and limit the density to ~90%, if it is acceptable for the final product. However, grain growth will be accelerated as soon as the pores are closed (Groza J. R., 1999). Sintering of nanoparticles was found to start at temperatures of 0,2-0,4 T_m compared to 0,5-0,8 T_m for conventional powders due to the increasing driving forces. These lower temperatures may minimize or even eliminate the use of grain growth inhibitors or sintering additives (Groza J. R., 1999.). Additionally, a two-step sintering process has recently been employed to solve this grain growth problem, that allows full density while grain growth is arrested during the second stage (Chen and Wang, 2000; Chen, 2000).

The synthesis of small particles, clusters, and nanocrystals has gained increased interest after the discovery of the fact that a decrease in crystallite size below some threshold value results in both a significant alteration of crystal structure and the manifestation of quantum properties. When the particle size is less than 10 nm, quantum effects are the most pronounced (Gusev AI, Rempel AA., 2000)

During the last twenty or twenty five years, nanocrystalline materials have been extensively investigated and found wide applications. In this respect, there arises a need for their characterization according to the particle size. The size of small particles can be determined using electron microscopy, sedimentation, photon correlation spectroscopy, gas adsorption, magnetic measurements, and other methods. One of the most accessible and universally employed methods for determining the particle size and microstrains in bulk and powdered nanocrystalline substances consists in analyzing the broadening of X-ray diffraction reflections, i.e., X-ray diffraction (XRD) method (Kurlov A. S. and Gusev A. I., 2013).

2.5.1 X-ray diffraction method of determination of the small particle size and microstrains

Cristalline defects cause displacements of atoms from the lattice sites. This results in a change in the intensity and/or the shape of diffraction reflections in the diffraction experiment. Krivoglaz obtained the known relationship for the intensity of Bragg reflections from defect crystals, which makes it possible to conventionally separate all defects into two groups (Krivoglaz M.A. 1969, Krivoglaz M.A. 2012). Defects of the first group only decrease the intensity of diffraction reflections, whereas defects of the second group are responsible for the broadening of reflections (Krivoglaz M.A. 1969, Krivoglaz M.A. 2012). The defects of the second group are associated primarily with the small size D of grains (crystallites, particles) and microstrains ε of the crystal lattice. The broadening β_s due to the small size D of particles (grains, crystallites) and stacking faults is proportional to sec θ, where θ is the glancing angle in the diffraction experiment. The broadening β_d caused by the lattice microstrains ε and randomly distributed dislocations is proportional to tan θ. One more type of defects of the second group, such as an inhomogeneity, is less known. Inhomogeneity causes a variation of the compound composition (i.e., the non-uniform composition of a compound) over the volume of the specimen. The

broadening of diffraction reflections due to the inhomogeneity can be observed for compounds and materials with atom or atom–vacancy substitution.

The X-ray diffraction reflection width can be described by the Gaussian function. The Gaussian function is possibly the best-known peak function in the universal literature since many physical and chemical processes are governed by Gaussian statistics. The Gaussian function can be expressed in terms of powder diffraction terms as:

$$I(2\theta) = I_{max} \exp\left[-\pi(2\theta - 2\theta_0)^2/\beta^2\right] \quad (2.13)$$

Where I (2θ) is the peak intensity at 2θ and I_{max} is the maximum peak intensity, $2\theta_0$ is the 2θ position of the peak maximum, and the integral breadth, β is related to the Full width half maximum (FWHM) peak width.

I (2θ) can also be expressed using the Lorentz function (this function is named the Cauchy distribution in mathematics) as

$$I(2\theta) = \beta^2 / \beta^2 + (2\theta - 2\theta_0)^2 \quad (2.14)$$

Combination of different functions is an attempt to get the "best of both worlds" as far as peak shape is concerned. The combination can be by convolution (e.g. the Voigt function) or by simple addition (e.g. pseudo-Voigt which is a close approximation to the Voigt function) .(A. S. Kurlov and A. I. Gusev, 2013). However, the diffraction reflection profile can be most accurately described with a linear superposition of these functions, which is known as the pseudo-Voigt function:

$$I(2\theta) = I_{hkl}[\eta\, L\,(2\theta - 2\theta_0) + (1-\eta) G(2\theta - 2\theta_0)] \quad (2.15)$$

where $L(2\theta - 2\theta_0)$ and $G(2\theta - 2\theta_0)$ represent suitably normalized Lorentz and Gaussian functions respectively, and η (the "Lorentz fraction") and (1−η) represent the fractions of each used. The main features of combination functions are:

a. Their precise form of combination can be tailored to a specific peak shape,

b. The Voigt and pseudo-Voigt are popular functions for modeling peak shapes and,

c. Their calculation tends to be more labor-intensive though as stated before this is not significant in computing terms.

The Gaussian function g(θ) at the maximum is equal to "A". The Gaussian function takes the value equal to half the maximum value, i.e.,g(θ)=A/2, at $\theta(1)=\theta_0+\theta_G\sqrt{(2.\ln 2)}$ and $\theta(2)=\theta_0-\theta_G\sqrt{(2.\ln 2)}$. Correspondingly, $FWHM_G=\theta(1)-\theta(2)=2\theta_G\sqrt{(2\ln 2)}\approx 2.355\theta G$ for the Gauss function.

The full width at half-maximum (FWHM) for the Lorentz function L(θ) is determined in the same manner as for the Gauss function. The maximum value of the Lorentz function L(θ) is equal A. Let the Lorentz function L(θ) be equal to half the maximum value, i.e., L(θ)=A/2. In this case from relationship, therefore $\theta(1)=\theta+\theta_L$ and $\theta(2)=\theta-\theta_L$. Since the full width at half-maximum is equal to $\theta(1)-\theta(2)=2\theta_L$, so $FWHML = 2\theta_L$ for the Lorentz function. The Gaussian function and the Lorentz function are shown in Figure 2-25.

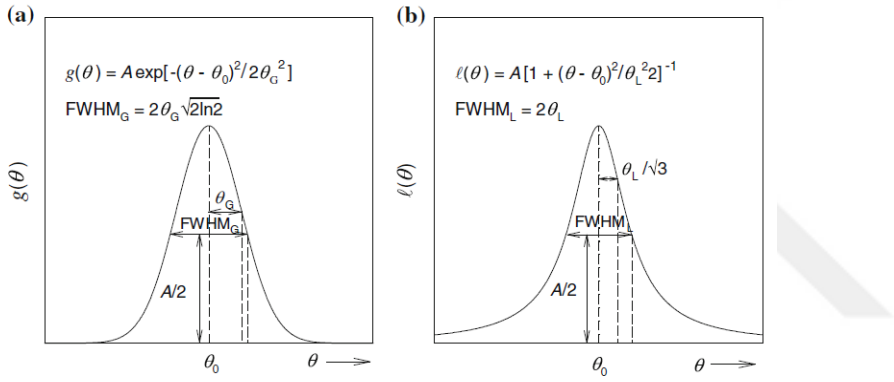

Figure 2.25 : a)Gaussian g(θ) and b)Lorentzian (Cauchy).

Gaussian g(θ) and Lorentzian (Cauchy) L(θ) are used distributions, used for model description of the shape of the diffraction lines. In the Figure 2-25 a shows relationship between the parameter θ_G of the Gauss function and the full width of the function g(θ) at half of its maximum, $FWHM_G$; and Figure 2-25 b shows for the Lorentz function parameter $\theta_L=FWHM_L/2$, and the second momentum of the Lorentz L(θ) function is equal to $\theta_L/\sqrt{3}$.

Combining both the Gaussian and Lorentzian functions, the FWHM of pseudo-Voigt function will be equal to:

$$FWHM_V = cFWHM_L+(1-c)FWHM_G=2c\theta_L+2\sqrt{(2.\ln 2)}(1-c)\theta_G\approx 2c\theta_L+2.355(1-c)\theta_G. \quad (2.16)$$

2.5.2 The diffractometer resolution function

The instrumental function of the angular resolution of the diffractometer is determined in a special experiment by measuring the full widths at half-maximum FWHM of diffraction reflections over a wide range of 2θ angles for a compound containing no defects that can lead to an additional broadening. In other words, a well annealed and completely homogeneous substance with particles (grains) more than 1 μm in size should be used as a reference compound. In this case, only the instrumental broadening of diffraction reflections will be observed. Lanthanum hexaboride (LaB_6) (NIST Standard Reference Powder 660a) with the cubic lattice constant a = 0,41569 ± 0.097 nm can be used for determining the diffractometer resolution function.

Each reflection was described by the pseudo-Voigt function, and the full width at half-maximum $FWHM_R$ was obtained from pseudo-Voigt equation (2-16). Then, the angular dependence of the full width at half-maximum $FWHM_R(2\theta)$ was constructed

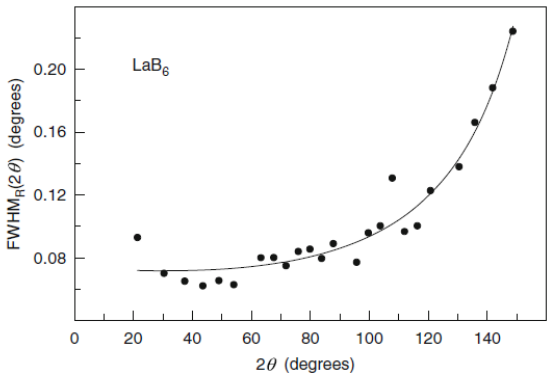

Figure 2.26 : Instrumental function of the angular resolution obtained for lanthanum hexaboride LaB6.

The instrumental function of angular resolution was described analytically by (2.17).

$$FWHM_R(2\theta)=(u\tan^2\theta+v\tan\theta+ w,)^{1/2} \qquad (2\text{-}17)$$

Equation 2-13 which was proposed by Cagliotti et al. (Cagliotti G, Paoletti A, Ricci FP, 1958) and was introduced into a wide scientific use by Rietveld (Rietveld HM, 1969). The approximation of the experimental dependences $FWHM_R(2\theta)$ by this relationship allowed finding the parameters *u*, *v*, and *w* of the instrumental functions of the angular resolution for different diffractometers.

2.5.3 Determination of the reflection broadening, average particle size, and microstrains

In order to determine the broadening of diffraction reflections, the X-ray diffraction pattern of the compound under investigation is measured, each reflection is described by the pseudo-Voigt function, and the full width at half-maximum $FWHM_{exp}$ is determined from diffrent formulae.

For the first time, the idea of determination of the size of small particles by an X-ray method was stated by P. Scherrer. In 1918, he proposed the formula connecting the width of diffraction reflection on half of its height with the size of a particle of investigated substance (Scherrer P.,1918):

$$\tau = (K\lambda)/(\beta\cos\theta) \tag{2.18}$$

τ is the size of the crystallite K is a Constant factor, with a value close to unity λ is the X-ray wave length β is the line broadening at half the maximum FWHM. Later in 1925, the article (Kurlov, A.S. and Gusev, A.I., 2013) appeared in which the similar relationship between the reflection width and the size of a particle was derived by soviet scientist N.Y. Selyakov. Therefore in Russian literature this formula sometimes is named as Selyakov-Scherrer formula. Nevertheless the priority belongs to P. Scherrer undoubtedly.

In a general case, when the particles of the substance have an arbitrary shape, the average particle size can be determined by the Debye-Scherrer formula (Gusev AI, Rempel AA, 2004)

$$<D> \approx V^{1/3} \tag{2.19}$$

V is volume of the particle.

$$<D>=(K_{hkl}.\lambda)/(\cos\theta.FWHM_{exp}(2\theta)) \equiv (K_{hkl}.\lambda)/(2\cos\theta.FWHM_{exp}(\theta)) \tag{2.20}$$

where λ is the radiation wavelength, and $K_{hkl} \approx 1$ is the Scherrer's constant whose value depends on the shape of the particle (crystallite, domain) and on diffraction reflection indices (hkl).

In a real experiment, the reflection is broadened as a result of a finite resolution of a diffractometer and cannot be less than the instrumental reflection width. In other

words, in above formula one should use the reflection broadening β with respect to the instrumental width $FWHM_R$, rather than the experimental width FWHMexp(2θ) of reflection.

$$(\beta(2\theta))^2=(FWHM_{exp})^2-(FWHM_R)^2\text{Equation} \quad (2.21)$$

Formula 2-21 should be used, if physical broadening β and the instrumental width $FWHM_R$ are described by the Gauss or the pseudo-Voight functions with large contribution of the Gauss functions. In practice just such description of the experimental broadening and the instrumental resolution function of a diffractometer is the most widespread. If physical broadening and the instrumental width are described by the Lorentz (Cauchy) functions, then the physical broadening is equal to a difference of full width of experimental reflection and the instrumental width of this reflection, i.e. $\beta = FWHM_{exp} - FWHM_R$.

The broadening of diffraction reflections due to the small size of particles (size broadening) is represented in the form

$$\beta s(2\theta)=(k_{hkl}.\lambda)/< D > cos\theta \approx \lambda/< D > cos\theta \text{ [rad]} \quad (2.22)$$

and the broadening caused by the strain-induced distortions of the crystal lattice (strain broadening) can be written in the following form:

$$\beta_d(2\theta)=4\varepsilon \tan\theta \text{ [rad]} \quad (2.23)$$

With allowance for relationship, the average particle size D in the diffraction experiment is determined using the Warren method (Warren BE, Averbach BL, Roberts BW, 1951)

$$< D >=(k_{hkl}.\lambda)/ < D > \beta s(2\theta) \equiv (k_{hkl}.\lambda)/2\cos \beta s(2\theta) \quad (2.24)$$

Note that $\beta(2\theta) \equiv 2\,\beta(\theta)$

For nanostructured materials, the broadening as a rule is caused by both the small size of particles and the microstrains. In order to separate these contributions to the experimental reflection broadening, the extrapolation Williamson-Hall method (Williamson GK, Hall WH, 1953) is used. It is based on the construction of the dependence of the reduced broadening

$\beta^*(2\theta)=[\beta(2\theta)\cos\theta]/\lambda$ of the (hkl) diffraction reflection on the scattering vector $s=(2\sin\theta)/\lambda$. The foundation of the Williamson-Hall method is the assumption that size and strain broadenings are described by the Lorentz (Cauchy) functions.

As a result, total reflection broadening is a sum of size and strain broadenings:

$$\beta(2\theta)=\beta_s(2\theta)+\beta_d(2\theta) =(4/(< D > cos\theta)) + 4\varepsilon \tan\theta \quad (2.25)$$

The average particle size <D> is determined by extrapolating the dependence of the reduced broadening $\beta^*(2\theta) = 1/<D>+2\varepsilon s$ on the scattering vector s to the value s = 0; that is:

$$<D>=1/(\beta.(2\theta)) \quad \text{when } (s=0) \quad (2.26)$$

The average value of the microstrains ε is obtained with the use of the expression

$$\varepsilon =[(\tan\varphi)/2].100\% \quad (2.27)$$

from the slope angle φ of the straight line, which approximates the dependence $\beta^*(s)$. In the physical meaning, the quantity $\varepsilon=\Delta d/d_0$ is the microdeformation of the lattice and it characterizes the uniform strain averaged over the crystal volume, i.e., the relative variation in the interplanar spacing in comparison with the perfect crystal. Note that d_0 and Δd are the interplanar spacing in a perfect crystal and the mean variation in the distance between the (hkl) planes in the volume V of the crystal, respectively. It is clear that theWilliamson-Hall method should be used if reflection broadening β is described by the Lorentz function or the pseudo-Voight function with large contribution c of the Lorentz function (at $c \geq 0.7$).

2.6 Material Selection:

A composite material can be defined as a combination of two or more materials that results in better properties than those of the individual components used alone. In contrast to metallic alloys, each constituent in composite materials retains its separate chemical, physical, and mechanical properties. The two constituents are a reinforcement and a matrix. The main advantages of composite materials are their high strength and stiffness, combined with low density, when compared with bulk materials, allowing for a weight reduction in the finished part (Campbell F.C., 2006).

Selection of an appropriate combination of matrix and reinforcement has been the main aim of design and production of PRMMC's. Since, the great advantage of MMC materials is a superior combination of different properties of metallic matrix and hard reinforcement. However, these properties can only be obtained with proper selection of matrix material and reinforcement (Lindroos et al., 2004).

The matrix of the composites has to be mainly designed for two major tasks, which is firstly to bind and support the reinforcing phase and, secondly, to satisfy special properties based on the requirements in service. Binding strength between the matrix, whose main function is to transfer and distribute the load to the reinforcement, and the reinforcement depends on the type of matrix and reinforcement (Huda et al., 1995; Lindroos et al., 2004). The interface formed between the matrix and the reinforcement is interesting because the characteristics of this region determine load transfer and crack resistance of the composite during deformation. It is now widely known that in order to maximize interfacial bond strength, it is necessary to promote wetting (when a liquid phase process is present), control chemical interactions and minimize oxide formation (Ibrahim et al., 1991). On the other hand, the hardness of the matrix is the key factor in supporting the reinforcing phase. Furthermore, other considerations such as, cost, weight, fabricability and availability of the matrix materials should be made (Lindroos et al., 2004). Generally, Al, Ti, Mg, Ni, Cu, Pb, Fe, Ag, Zn, Sn and Si are used as the matrix materials (Huda et al., 1995). In addition to these, tungsten (W) has lately received some attention as a matrix material (Song et al., 2002; Song et al., 2003).

Thr reinforcement phase in composite materials are mainly used to increase the strength, stiffness, temperature resistance capacity and to lower the density. Generally, ceramics are used as the reinforcement phase, which are typically oxides, carbide and nitrides (Huda et al., 1995). Selection criteria for these ceramic reinforcements include elastic modulus, tensile strength, density, melting temperature, thermal stability, coefficient of thermal expansion, size and shape, compatibility with matrix material and cost (Ibrahim et al., 1991). Common reinforcement compounds are SiC, Al_2O_3, SiO_2, TiC, B_4C and Si_3N_4 (Huda et al., 1995).

All these things considered, in this study tungsten has been chosen as the matrix material.

2.6.1 Tungsten (W)

Tungsten (wolfram, W), is a transition metal in the third long period and group 6 of the periodic table. Its electron configuration is [Xe] $6s^2$ $4f^{14}$ $5d^4$ but can also be interpreted as [Xe] $6s^1$ $4f^{14}$ $5d^5$. The naturally occurring isotopes have relative atomic mass 180 (0.14%), 182 (26.42%), 183 (14.40%), 184 (30.64%), and 186 (28.41 %). There are also 17 known artificial isotopes and isomers from 137W to 189W, with half-lives between 14 μs and 140 d. In nature, tungsten occurs only in a chemically combined state (mainly as tungstate). The metal, which has a silvery white luster, has a very high density (19.3 g/cm3 at 20˚C), and the highest melting point (3410˚C) of all the metallic elements(F.Habashi, 1997) some of W physical properties are offered in Table 2-3.

Tungsten has high melting point (3422˚C) and it also has one of the highest densities. When combined with carbon, it transforms into one of the hardest man-made materials. While the tungsten filaments for light bulbs are widely used, its most common and most valuable use is in metal cutting, mining, and oil drilling tools. Although tungsten can be used at high temperatures, an oxide film forms which is volatile above temperature of approximately 540˚C. So, for use at extremely high temperatures, tungsten parts must be coated, used in a vacuum, or be surrounded by a protective atmosphere. Typical uses involving protective atmospheres or vacuum include incandescent lamp filaments, electron tube electrodes, and various types of heating elements. Silicide coating and noble metal cladding are effective oxidation resisting coatings, for example, cladding the tungsten with a platinum gold alloys. Tungsten is resistant to many severe environments which readily attack other metals. It resists nitric, sulfuric, and hydrofluoric acids at room temperatures. It is only subject to slight attack by hot alkaline solutions such as potassium, sodium, and ammonium hydroxides. Tungsten also has good resistance to sevaral liquid metals including sodium, mercury, gallium, and magnesium; to oxide ceramics such as alumina, magnesia, zirconia and thoria. It is often used for crucibles to melt these materials in an inert atmosphere (Habashi F., 1997)

A large number of tungsten alloys and composites were investigated in the past. However, only some of them achieved technical importance. The aim of alloying tungsten is to improve its chemical, physical and mechanical properties at both ambient conditions and at elevated temperatures. However, alloying of tungsten (W)

has been relatively less studied than of some of the other refractory metals. Most of the tungsten used until now in aerospace applications has been in the unalloyed form, which is much easier and less expensive to produce and fabricate (Lassner and Schubert, 1999, F.Habashi, 1997). Also, it has been found that, particularly at temperatures above 2200°C, the strengthening effects of many alloying agents decrease disproportionately (Lassner and Schubert, 1999).

Table 2.3 : Physical Properties of Tungsten (Lassner and Schubert, 1999).

Period	6
Atomic Number	74
Atomic Mass	183.85
Electronegativity	1.7
Space Group	Im3m
Lattice Parameter	3.16524 A^o
Density	19.25 g/cm^3
Melting Point	3422 C^o
Boiling Point	5663 C^o
Specific Heat	0.0317 cal/gK
CTE	$4.32\text{-}4.68x10^{-6}$ K^{-1} (25 ^oC)
Tensile Strength	172.4 MPa
Young's Modulus	390-410 GPa
Shear Modulus	156-177 GPa
Bulk Modulus	305-310 GPa
Poisson' Ratio	0.28-0.30
Hardness	350-450 kg/mm^2

Tungsten is mainly consumed in three forms a) Tungsten carbide b) Alloying additions c) Pure tungsten.

Tungsten carbide accounts for about 65% of tungsten consumption (Lassner and Schubert, 1999). It is combined with cobalt as a binder to form the so-called cemented carbides, which are used in cutting tool and wear applications because of their high hardness, good wear resistance, good fracture resistance and high temperature strength (Zhang et al., 2003) Cemented carbides such as WC-Co and WC-Co-TiC are the most widely used materials for metalworking. As a consequence, a considerable amount of research effort has been spent to develop alternative cemented carbide systems in order to improve the microstructure and mechanical properties of these materials (Acchar et al., 2004).

Three tungsten alloys are produced commercially: tungsten-titanium (W-Ti), tungsten-tantalum (W-Ta), and tungsten-rhenium (W-Re) (Lassner and Schubert, 1999).

Re is the most important alloying element for tungsten. Re additions increase the ductility at low temperatures and also improve the high temperature strength and plasticity. Moreover, Re additions stabilize the grain structure, increase the recrystallization temperature and improve the weldability. It also improves the corrosion resistance of tungsten (Lassner and Schubert, 1999). On the other hand, W-Ta alloys combine the good corrosion resistance and high elasticity of Ta with the better high temperature strength of W and W-Ta alloy is used as a sputtering target in the manufacture of microelectronics devices (Lassner and Schubert, 1999).

Another type of W alloys are the W heavy-metal alloys (WHA's). These are a category of tungsten-base materials that typically contain 90 to 98 wt% W in combination with some mix of nickel (Ni), iron (Fe), copper (Cu), and/or cobalt (Co) (Ryu and Hong, 2003.). The bulk of WHA production falls into the 90 to 95% W range. As a consequence, WHA's gain their basic properties from those of the tungsten phase, which provides both high density and high elastic stiffness. These are the two properties that give rise to most applications for this family of materials (Lassner and Schubert, 1999).

2.6.2 Tungsten composites

In order to improve properties of tungsten, dispersion-strengthened and precipitation hardened composites were developed. Its first application can be considered as non-sag tungsten (tungsten doped with potassium) which is used as filaments in lamps is one kind of dispersion-strengthened composites, which have excellent creep resistance. The term non-sag refers to the resistance of the material against deformation (sagging) under its own weight at incandescent temperatures (Lassner and Schubert, 1999).

Moreover, oxide-dispersion-strengthened tungsten composites were mainly used in literature. The addition of small amounts of finely dispersed oxides increases the mechanical properties of tungsten. The most common one is the W-ThO2 alloy which contains a dispersed second phase of 1 to 2% thorium (Lassner and Schubert, 1999). The thorium dispersion enhances thermionic electron emission, which in turn improves the starting characteristics of gas tungsten arc welding electrodes (Lassner and Schubert, 1999). It also increases the efficiency of electron discharge tubes and imparts creep strength to wire at temperatures above one-half the absolute melting

point of tungsten (Lassner and Schubert, 1999; Chen et al., 2000). However, it is desirable to replace ThO_2 with non-radioactive activators because of the radioactive pollution of thorium during fabrication, service or handling. In the last decade, considerable efforts have been directed to develop new materials, especially to explore new activators. It has been found that tungsten electrodes activated with rare-earth metal oxides (such as La_2O_3, Y_2O_3, CeO_2, etc.) exhibit superior arc characteristics compared to pure W and W-ThO_2 electrodes (Chen et al., 2000). Particularly, W- La_2O_3 composites exhibit good mechanical properties and have no radioactive potential (Lassner and Schubert, 1999). Furthermore, there are studies about strengthening the WHA's by adding Y_2O_3. As a result, the strength of WHA's are improved with decreasing particle size which is proportional to the Y_2O_3 content (Ryu and Hong, 2003.).

There are also different refractory carbides, such as HfC, TiC, ZrC, TaC, and NbC used as dispersoids which some of physical properties of some carbides are offered in Table 2-4 and 2-5 (Lassner and Schubert, 1999, Shackelford, 2001). Recently, mechanical and thermophysical and ablation properties of TiC/W and ZrC/W at elevated temperatures are studied. As a result, it is proved that both of them possess excellent high temperature strength and good thermophysical properties, which make them good candidates for high temperature applications (Song et al, 2002; Song et al, 2003a; Song et al, 2003b). Tables 2-4, and 2-5 list respectively the youngs moduls, the tensiale strengths and hardness values of some carbides for comparsion

Table 2.4 : Young's modulu of some carbides (Shackelford, 2001).

Ceramic	**Young's Modulus (GPa)**	***Temperature***	**Tensile Strength (MPa)**	***Temperature***
Boron Carbide (B_4C)	290-450	Room temp.	155	980 ^oC
Silicon Carbide (SiC) (pressureless sintered) (hot pressed)	 303 440	 Room temp. Room temp.	34-138 200 40-150	25 ^oC 20 ^oC 1400 ^oC
Tantalum Monocarbide (TaC)	285-629	Room temp.	14-290	1000 ^oC
Titanium Monocarbide (TiC)	439 310-379	Room temp. 1000 ^oC	119	1000 ^oC
Tungsten Monocarbide	669-714	Room temp.	345	1000 ^oC
Zirconium Monocarbide (ZrC)	195-480	Room temp.	110 81-99 89-109	Room temp. 980 ^oC 1250 ^oC

Table 2.5 : Hardness values of some carbides (Shackelford, 2001).

Ceramic	Hardness
Boron Carbide (B_4C)	Knoop 100g: 2800 kg/mm^2 Knoop 1000g: 2230 kg/mm^2 Vickers : 2400 kg/mm^2
Silicon Carbide (SiC)	Vickers 25g : 3000-3500 kg/mm^2 Knoop 100g : 2500-2550 kg/mm^2
Tantalum Monocarbide (TaC)	Knoop 50g: 1800-1952 kg/mm^2 Knoop 100g: 825 kg/mm^2 Vickers 50g: kg/mm^2
Titanium Monocarbide (TiC)	Knoop 100g: 2470 kg/mm^2 Knoop 1000g: 1905 kg/mm^2 Vickers 50g: 2900-3200 kg/mm^2 Vickers 100g: 2850-3390 kg/mm^2
Tungsten Monocarbide (WC)	Knoop 100g: 1870-1880 kg/mm^2 Vickers 50g: 2400 kg/mm^2 Vickers 100g: 1730 kg/mm^2
Zirconium Monocarbide (ZrC)	Knoop : 2138 kg/mm^2 Vickers 50g : 2600 kg/mm^2 Vickers 100g : 2836-3840 kg/mm^2
Hafnium Monocarbide (HfC)	Knoop : 1790-1870 kg/mm^2 Vickers 50g : 2533-3202 kg/mm^2

2.6.3 Titanium

Titanium is a member of group 4 of the periodic table. It has two 4s and two 3d valence electrons and is a transition element. The electronic configuration is $1s^2\ 2s^2p^6\ 3s^2p^6d^2\ 4s^2$.Natural titanium is a mixture of five stable isotopes (F.Habashi, 1997).

Pure titanium is a silvery white, ductile metal, melting point of Titanium is 1668˚C. The atomic radius is 0.145 nm for coordination number six in the crystal lattice. Ti has hexagonal structure of the Mg type, almost close-packed and somewhat compressed along the c-axis (F.Habashi, 1997). The lattice constants of Ti at room temperature are c=0.4679 nm, a=0.2951 nm, c/a=1.585. At 882.5 ^oC titanium transforms into the body-centered cubic p-phase, the heat of transformation being 3.685 kJ/mol. Extrapolation of the lattice constants of titanium alloys whose β-phase can be quenched to room temperature, gives a lattice constant a = 0.3269 nm at room temperature and 0.328 nm above 620 ^oC (Habashi F., 1997).

2.6.4 Ti as activator

High sintering temperatures are generally needed to process refractory metals due to their high melting temperatures, but specific conditions depend on the particular alloy, particle size and impurities. The tendency of refractory metals to oxidize requires reducing atmospheres or vacuum for sintering. W, Mo and Re are often sintered in 100% hydrogen (Fang Z.Z., 2010).

Tungsten (W) is relatively common and its melting temperature of 3410˚C is the highest of any metal. It also has the lowest vapor pressure of any metal. Its main disadvantages are relatively poor oxidation resistance and a ductile-to-brittle transition between 200˚C and 500˚C (Fang Z.Z., 2010). Since W and its alloys are the most commonly sintered refractory metals, they serve as good examples for discussion of specific sintering conditions. Most W products are produced by pressing and sintering W billets, which then undergo a complex sequence of hot and cold forming processes to eliminate porosity and produce intermediate shapes, such as sheets, rods and tubes. The billets are usually pressed from W powders with particle sizes of 3 to 6 μm. Green densities of 55–65% of theoretical can be achieved with compaction pressures of 200 to 400 MPa. For direct sintering, the green billets are presintered at 1100˚C to 1300˚C in hydrogen to provide sufficient strength for clamping. Tungsten billets are sintered either directly or indirectly at temperatures ranging from 2000˚C to 3050˚C in a flowing dry H_2 atmosphere to achieve a density of 92–98% with typical grain sizes of 10 to 30 μm (Lassner and Schubert, 1999). Hydrogen improves sintering by removing the oxide layer from the W particles, while high temperatures help volatilize other impurities, such as alkali, earth-alkali or transition metals, that can significantly reduce the ductility of W (Fang Z.Z., 2010). Heating rates must be slow enough to prevent rapid densification and pore closure before the impurities have been evaporated. Heating rates for furnace sintering depend on the part size, but are generally on the order of 1 to 4˚C/minute. Heating rates as fast as 100˚C/minute can be used with direct sintering since the billet heats up from the inside, which promotes diffusion and evaporation of impurities (Fang Z.Z., 2010).

Activated solid-state sintering occurs when there is rapid mass transport through a high-diffusivity second phase, which provides a short circuit diffusion path. The most effective second phases have a high solubility for the base metal, but low solubility in the base, so that it will remain segregated at the grain boundaries (Zovas et al., 1983; German and Rabin, 1985). They also have a low liquidus temperature, indicating a low activation energy and high diffusivity. Systems that form intermediate compounds with high melting points are unfavorable. Most research on activated sintering has involved W.

The most effective sintering activators for W are transition elements such as Co, Fe, Ni, Pd and Pt which meet the solubility requirements and have relatively low liquidus temperatures which W-Ti phase diagram is offered in Figure 2-27 (Li and German, 1983; German and Munir, 1976a; Panichkina V.V. 1967; Munir and German, 1977, Ağaoğulları, D. et.al. 2013, Coşkun, S. and Öveçoğlu, M.L., 2011, Demirkan, Ö.U.et. al. 2012, Genç, A., et.al. 2010, Genç, A., et.al. 2012). Small amounts of these elements greatly reduce the sintering temperature of W and promote grain growth. The optimal amount of additive corresponds to an activated layer one to four monolayers thick (Li and German, 1983; German and Munir, 1976a; Munir and German, 1977; Massalski T.B. 1990). Palladium and Ni are the most effective activators of W (German and Munir, 1976b; German and Ham, 1976; Li and German, 1983; Munir and German; 1977), Cobalt and Fe additions result in the formation of the intermetallic phases W_6Co_7 and W_6Fe_7 respectively (Fang Z.Z., 2010; Panichkina V.V. 1967; Massalski T.B. 1990)

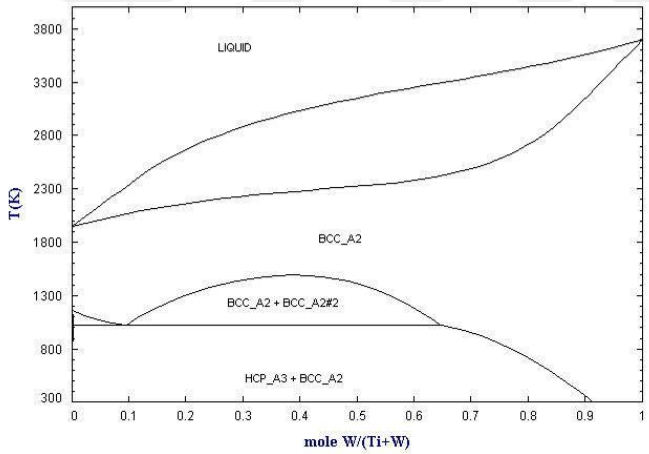

Figure 2.27 : Binary W-Ti phase diagram (Url-1).

These intermetallics have relatively high melting temperatures indicating lower diffusivities. Consequently, mass transport is improved, but is less rapid than with other activators (Li and German, 1984). Unfortunately, all of the sintering activators embrittle W. Transition metal additions also enhance densification of other refractory metals. Pt and Pd are the most effective activators for Re (German and Munir, 1977; Panichkina V.V. 1967; Massalski T.B. 1990).

Despite all these information and literature reviews regarding W matrix composites and activated sintering of W, there exist no detailed studies about the sintering

behaviour and microstructural properties of dispersion strengthened W-based composites sintered with the presence of Ti as transition metal constituent. This study aims to fulfill this gap with investigations of sintering behaviour and mechanical properties of mechanically alloyed and Ti activated sintered W-LaB_6 composites. The specific aim of the present study is to report on the microstuctural characterization and physical properties of mechanically alloyed and sintered W-2wt% LaB_6-(0.5-1.0-4.0-10.0)wt% Ti composites.

3. EXPERIMENTAL PROCEDURE

The experimental procedure of this study consist of the identification of raw materials, the milling-assisted of the powders and mechanical alloying, the consolidation of the raw and mechanical alloyed powders via pressureless sintering and spark plasma sintering techniques and characterization investigations carried out on the powders and sintered products.

3.1. Raw Materials

The use of low-cost starting materials is one of the major purposes of this study in order to suggest economically-efficient techniques for obtaining high- tech products. In this study, tungsten (W) powders (99.95% purity, 44 μm average particle size) as the matrix of the composite and titanium (Ti) powders (99.95% purity, 44 μm average particle size) as activating agent are used in this study and Lanthanum Hexaboride (*LaB_6*) powder (99.95% purity, 44 μm average particle size) as reinforcement particle.

Table 3.1 shows the characteristics of the raw materials used in the experiments. Pure W, Ti and LaB6 were used as raw materials for the formations of W based composite. Ti powders were used as activator in the mechanical synthesis experiments. LaB_6 was used in the process as the reinforcing agent. Figure 3-1 shows the stereomicroscope (SM) images of the raw materials. The images of all raw materials were captured by using a Zeiss™ Discovery.V12 Stereomicroscope (SM) coupled with a Zeiss™ Axiocam ERc5s high resolution digital camera which shown in Figure 3-2.

Table 3.1 : Raw materials used in the experiments.

Raw material	Provided from	Purity (%)	Average Particle Size (μm)
W	Alfa Aesar™	99.95	(-325 mesh) 44
Ti	Alfa Aesar™	99.95	(-325 mesh) 44
LaB_6	Alfa Aesar™	99.95	(-325 mesh) 44


a
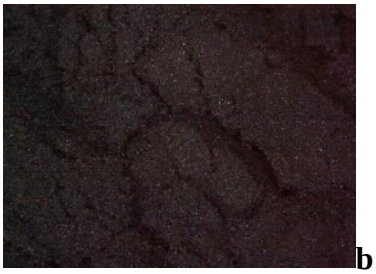
b

c

Figure 3.1 : stereomicroscope (SM) images of the raw materials: (a) W, (b) Ti, (c) LaB6.

Figure 3.2 : Zeiss™ Discovery.V12 Stereomicroscope.

The phases of all raw materials were identified using a Bruker™ D8 Advanced Series X-ray diffractometer (XRD) with CuKα (1.54060 ˚A) radiation in the 2θ range of 10-90 with 0.02 steps at a rate of 2˚/min which is offered in Figure 3-4. International Centre for Diffraction Data (ICDD) powder diffraction files were utilized for the crystalline phase identification of the raw materials. The XRD patterns of the raw materials are illustrated in Figure 3-3(a) through Figure 3-3(c). Figure 3.3(a), (b), and (c) respectively present the crystalline peaks of W (ICDD Card No:01-070-8747, Bravais lattice: primitive orthorhombic, a=1.150 nm, b=0.355 nm, c= 0.435 nm), Ti (ICDD Card No: 01-071-0336, Bravais lattice: primitive orthorhombic, LaB_6 (ICDD Card No: 034–0427, Bravais lattice: primitive cubic, a=b=c= 0.416 nm) respectively.

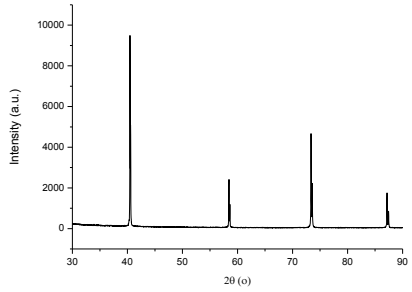

a

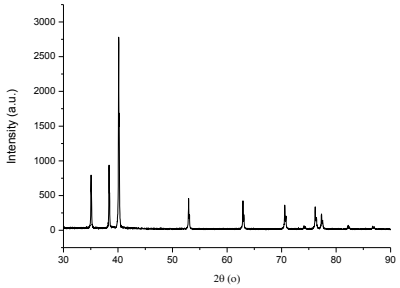

b

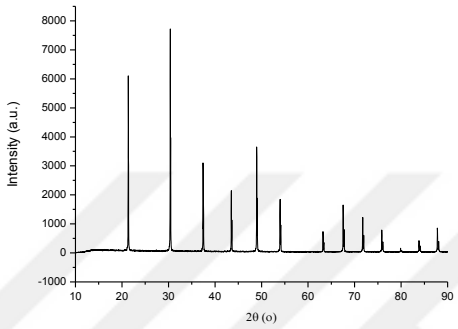

c

Figure 3.3 : XRD patterns of the raw materials: (a) W, (b) Ti, (c) $LaB_{6.}$

Figure 3.4 : Bruker^{TM} D8 Advanced Series.

Milling and mechanical alloying (MA) were done in a tungsten carbide (WC) vial with WC balls having a diameter of 6.35 mm (¼ inches). Figure 3-5 shows the milling vials the milling SPEX^{TM} Duo mixer/mill 8000D, and WC balls. These vials are shielded by WC which are used for milling hard materials.

Figure 3.5 : WC vial and WC Balls and Spex™ Duo Mixer/Mill 8000D.

Ti is categorizes as an active material that should be protected. High-purity argon was chosen as the milling atmosphere to prevent oxidation and contamination of powder since the presence of air in the vial causes to produce oxides and nitrides in the powder, especially if the powders are reactive in nature. Thus, loading and unloading of the powders into the vial was carried out inside a "Pluslabs™" atmosphere-controlled glove box in Ar atmosphere which presented in Figure 3-6.

Figure 3.6 : Pluslabs™ Glow box.

Primarily, mechanical alloying (MA) experiments were carried out using a Spex™ Duo Mixer/Mill 8000D with a speed of 1200 rpm for 1 h, 2 h, 4 h, 10 h and 20 h in a tungsten carbide (WC) vial with WC balls having a diameter of 6.35 mm (¼ inches). The ball-to-powder (BPR) weight ratio was 10:1. W-(0.5, 1.0, 4.0, 10.0 wt%)Ti (hereafter referred as W0.5Ti, W1.0Ti, W4.0Ti, W10.0Ti) were mixed and MA'd for 1 hr, 2 hr, 4 hr, 10 hr, and 20 hr in first part of experiments where both effects of MA

and activated sintering were investigated as concurrent experimental, W powder were pre-milled. Pre-milling was carried out for 1hr, 2hr, 4hr, 6hr, 8hr, 10hr and 20hr inorder to achieve the small W particles. . Pre-milling was done by Spex™ Duo Mixer/Mill 8000D with a speed of 1200 rpm for 1 hr, 2 hr, 4 hr, 10 hr and 20 hr in a tungsten carbide (WC) vial with WC balls having a diameter of 6.35 mm (¼ inches). The ball-to-powder (BPR) weight ratio was 10:1.

Powder particle size measurements were carried out in a Malvern™ Mastersizer Laser particle size analyzer (Figure 3-7a). Microstructural characterization investigations of MA'd powders were conducted using a JCM-6000PLUS Neo Scope Benchtop (SEM) (Figure 3-7b) (XRD) using CuK_{α} radiation at 45 kV and 40 mA. Specific surface area measurements of MA'd powders were made using Quantachrome™ by the Brunauer, Emmett and Teller (BET) method of adsorption of nitrogen gas which shown in Figure 3-7c.

Figure 3.7 : a- Malvern™ Mastersizer Laser particle size analyzer b- Jeol™-6000PLUS Neo Scope Benchtop (SEM) c- Quantachrome™ by the Brunauer, Emmett and Teller (BET).

3.2. Milling And Mechanical Alloying Of The Powder Blends

One of the major aims of this dissertation is to find an effective technique for preparing W based composites which could overcome the limitations of conventional production techniques and represent the advantages of time and energy savings, simplicity and high-purity products. Milling-assisted and mechanical alloying methods were utilized in this dissertation. To enable W sintering at lower temperatures, Ti was used as an activator to reduce the sintering temperature. During this process, W powders were pre-milled and used as raw material along with the unmilled W powders. Following pre-milled and mechanical alloying, powder

consolidation was carried out by different sintering techniques such as cold pressing/pressureless sintering (without or with Co addition) and spark plasma sintering (SPS).

3.3. Consolidation Of The Prepared Powders Via Different Sintering Techniques

The mechanically alloyed powders were consolidated by two methods:

a) by cold pressing in a tool-steel die at a pressure of 400 MPa into cylinder shaped green compacts with a diameter of ≈6.36 mm for 1 minute by using a 10 ton capacity "MSE" one-action hydraulic pressthat is offered in Figure 3-8. Then Sintering was performed for 1 hour in a Linn™ 1800 M Vac Graphite furnace. The furnace works under gas sintering conditions using vacuum and H_2, Ar and N_2 gases as sintering media. The Linn™ 1800 M Vac Graphite furnace and the sintering regime is shown in Figure 3-9 a and b.

Cylindrical samples were sintered in a Linn^{TM} high temperature hydrogen furnace at 1400°C and 1500°C under inert Ar (introduced between 20°C-650°C and 1100°C-(1400°C-1500°C) and reducing H_2 (introduced between 650°C and 1100°C) gas flowing condition for 1h. Two cylindrical samples of each composition shaped and consolidated. Finally, samples were sintered based on offered regime in Figure 3-9b.

Figure 3.8 : MSE one-action hydraulic press.

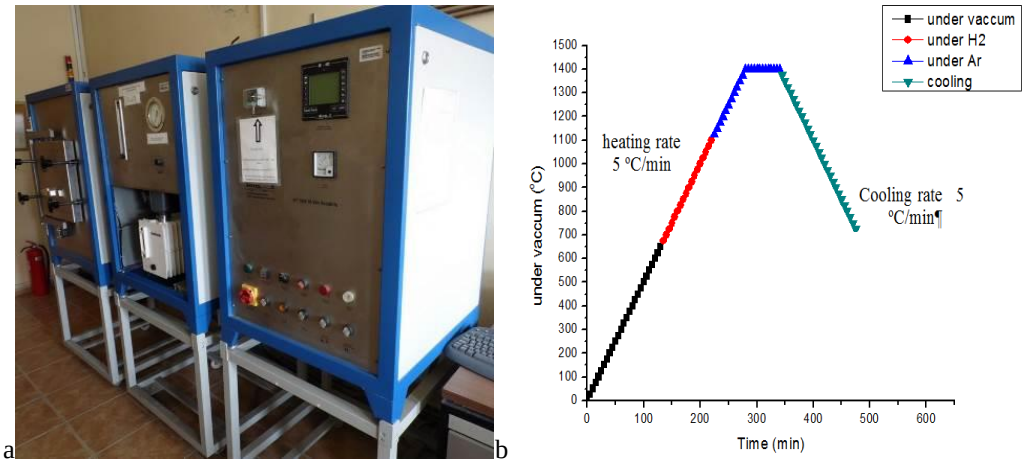

Figure 3.9 : a- Linn™ 1800 M Vac Graphite furnace b-sintering regime.

b) Spark plasma sintering (SPS) experiments were performed by FCT Systeme™ HP D 25 SPS equipment which shown in Figure 3-10. Powders were loaded in a graphite die with an inner diameter of 20 mm and sintered at 1400˚C for 5 min with heating and cooling rates of 100˚C /min under an applied holding pressure of 50 MPa. Composition W^{p}-x wt%Ti-2.0 wt% LaB_6 (x=0,5, 1,0 4,0and 10,0) also spark plasma sintered at the same conditions but at 1400˚C and 1500˚C in order to investigate the effect of sintering temperature.

Figure 3.10 : FCT Systeme™ HP D 25 SPS.

Bulk products were hereafter referred as the sample names given in Table 3.2.

Table 3.2 : Sintering conditions of the optimized samples selected for the consolidation experiments.

Pressure less Sintering			**Spark Plasma Sintering**	
W-0.5 wt%Ti	W^p-0.5 wt%Ti	W^p-0.5 wt%Ti-2.0 wt% LaB_6	W^p-0.5 wt%Ti	W^p-0.5 wt%Ti-2.0 wt% LaB_6
W-1.0 wt%Ti	W^p-1.0 wt%Ti	W^p-1.0 wt%Ti-2.0 wt% LaB_6	W^p-1.0 wt%Ti	W^p-1.0 wt%Ti-2.0 wt% LaB_6
W-4.0 wt%Ti	W^p-4.0 wt%Ti	W^p-4.0 wt%Ti-2.0 wt% LaB_6	W^p-4.0 wt%Ti	W^p-4.0 wt%Ti-2.0 wt% LaB_6
W-10.0 wt%Ti	W^p-10.0 wt%Ti	W^p-10.0 wt%Ti-2.0 wt% LaB_6	W^p-10.0 wt%Ti	W^p-10.0 wt%Ti-2.0 wt% LaB_6

Whole of compositions were mechanically alloyed for 1, 2, 4, 10 and 20 h.

3.4. Characterization Investigations Of The Powders And Sintered Products

Characterization investigations conducted on the powders in this dissertation comprise the detailed microstructural analyses, the determination of phases, thermal properties and particle sizes of both the milled and final powders. Moreover, purity and density values of the final powders are identified by various methods. Phase and microstructural properties and densities of the sintered products are also determined comprehensively. Furthermore, mechanical properties of the selected samples are reported in terms of microhardness, wear resistance.

3.4.1. Characterization investigations of the powders

X-ray diffraction (XRD) investigations of the as-blended, milled, and mechanically alloyed powders and the sintered samples were performed in a Bruker^{TM} D8 Advanced Series powder diffractometer with CuK_α (λ=0.154 nm) radiation in the 2θ range of 10-90 incremented at a step size of 0.02°at a rate of 2°/min. The International Center for Diffraction Data (ICDD) powder diffraction files were utilized for the identification of crystalline phases. Average crystallite sizes and lattice strains of the mechanically alloyed powders were determined utilizing Bruker-AXS^{TM}TOPAS V5.0 software based on the modified Scherrer's formula (Suryanarayana and Norton, 1998). The most intense diffraction peaks of the phases were fitted according to the Lorentzian profile by applying fundamental parameters approach. Particle size measurements were conducted on the milled and mechanically alloyed powders using a Microtrac^{TM} Nano-flex particle size analyzer (PSA). smaller powders were measred by Zeta potential-nano sizer microtrac ^{TM} which shown in Figure 3-11 a. In

order to prevent agglomeration of the particles, powders were homogenized in a Bandelin Sonopuls^{TM} ultrasonic homogenizer for 2 min using distilled water as aqueous media prior to particle size measurements which are offered in Figure 3-11b.

Figure 3.11 : a- Microtrac Stabino ^{TM} Zeta potential-nano sizer b- Sonopuls^{TM} ultrasonic homogenizer.

The thermal properties of the as-blended, milled and final powders were examined using a TA^{TM} Instruments SDT Q600 Differential Scanning Calorimeter (DSC)/Thermogravimetric Analyzer (TGA). DSC/TGA experiments were conducted in an alumina crucible up to a heating temperature of 1400°C with a heating rate of 10°C/min under an Ar atmosphere that is shown ing Figure 3-12.

Figure 3.12 : TA™ Instruments SDT Q600 Differential Scanning Calorimeter (DSC) Thermogravimetric Analyzer (TGA).

Microstructural characterizations of the powders were carried out using Jeol ™ Scanning Electron Microscope (SEM) coupled with an energy- dispersive X-ray spectrometer (EDX) - energy dispersive spectrometer (EDS).

The densities of the final powders were measured using a Micromeritics™ AccuPyc II 1340 gas pycnometer in 1 cm^3 sample chamber at room temperature using He gas (Linde™, in purity of 99.996%) as the displacement medium. Density result of each powder product includes the arithmetic mean of ten successive measurements and standard deviations which are shown in Figure 3-13a and 3-13b respectively.

a  b 

Figure 3.13 : a-Micromeritics™ AccuPyc II 1340 b- arithmetic density.

The specific surface areas of some powders were measured using the Brunauer–Emmet–Teller (BET) method by a Quantachrome Autosorb-1 MP device, at 150°C by degassing under N_2 gas for 5 hr and by absorbing with N_2 (for analysis) and He (for reference) gases.

3.4.2. Characterization investigations of the sintered products

Microstructural characterizations of the sintered products were carried out using the XRD technique at the same conditions as those of powders, the Jeol ™ scanning electron microscope (SEM) operating at 15 kV and the optical microscope (OM, Nikon, Eclipse). The densities of the sintered samples were measured in ethanol using the Archimedes method and the results were reported as the arithmetic means of three different measurements taken from the same sample. In order to obtain scratch-free mirror finish for the SEM analyses, Vickers microhardness measurements and reciprocating sliding wear tests, all sintered samples were subjected to a typical metallographic preparation procedure. Sintered samples were hot-mounted in a Struers™ LaboPress-1 (Figure3-14 a), ground and polished in a Struers™ Tegrapol-15 instrument (Figure 3-14 b).

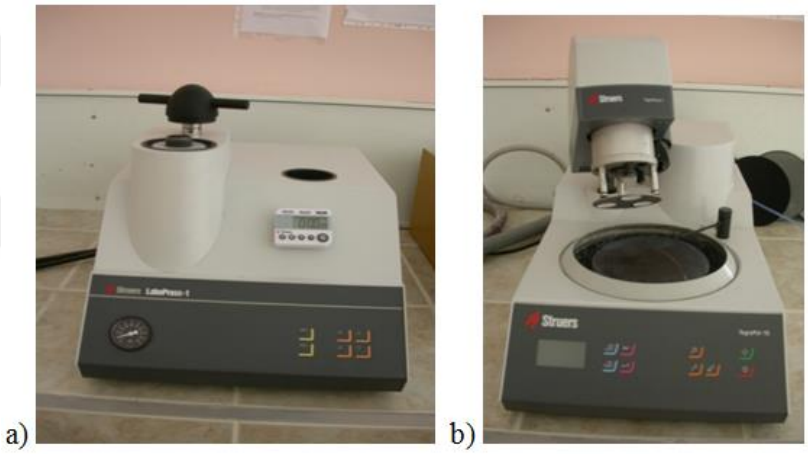

Figure 3.14 : a- hot-mounted in a Struers™ LaboPress-1 b- Struers™ Tegrapol-15 instrument.

Vickers microhardness measurements of the sintered samples were conducted using a Shimadzu™ HMV Microhardness Tester under a load of 200 g for 15 s. Microhardness test result for each sample includes the arithmetic mean of twenty successive indentations and standard deviations which Shimadzu™ HMV Microhardness Tester is shown in Figure 3-15 a. Some of the sintered samples were subjected to reciprocating sliding wear tests at ambient condition (room temperature and laboratory atmosphere) in a Tribotech™ Oscillating Tribotester using a 6 mm alumina ball under an applied force of 4 N, with a sliding speed of 6 mm/s and a stroke length of 2 mm for a total sliding distance of 20 m. Wear tracks of all the sintered samples were examined by a Veeco™ Dektak 6M Stylus Profilometer. Wear

test results in terms of wear volume loss (WVL = (1/4) x width x depth x length) values are the arithmetic mean of three different measurements for each sample. Relative wear resistance values were calculated as the ratio of highest wear volume loss to the wear volume of each sample that Tribotech™ Oscillating is shown in Figure 3-15 b.

a  b 

Figure 3.15 : a- Shimadzu™ HMV Microhardness Tester b- Tribotech™ Oscillating Reciprocating machine.

4. RESULTS AND DISCUSSION

The experimental procedure section of this thesis provides functional data which can be categorized in three parts regarding Tungsten (W) – based composites sintered by using of Titanium (Ti) as activator.

The first part consists of pre-milling of W and mechanical alloying of W-Ti composite powders followed by sintering using conventional sintering. Thanks to Ti activator, W-Ti composites were sintered at the lowest temperature under controlled atmosphere.

Second part is belonging to the sintering of W under pressure by using of Spark Plasma Sintering (SPS) method. The optimized condition in the first part tried by SPS and pertaining characterization investigations were detailed.

Thirdly, LaB_6 powders as second phase and improving part of physical and mechanical properties were added and tried to sinter in pressure less (PLS) and under pressure (SPS).

4.1. Powder Processing

Tungsten (W) powders (99.9% purity, 14 μm average particle size) as the matrix of the composite and titanium (Ti) powders (99.9% purity, 14 μm average particle size) as activating agent were used in this study.

Milling and mechanical alloying (MA) were carried in (WC) vials with WC balls having a diameter of 6.35 mm (¼ inches). Figure 3-5 shows WC vial and WC balls and Specx^{TM} Duo Mixer/Mill 8000D.

Ti powders have a high affinity to oxygen and small milled particles with large surfaces are more vulnerable to oxidation than the unmilled ones. Therefore, exposure to oxygen must always be avoided during storage, processing and sinteringof the milled powders. In other words, vacum and protective atmosphere should be provided in closed container, i.e. glove box. Powders were filled in vials in Plaslabs^{TM} glow box which protected and filled by pure Ar 99.99%. Vials were

filled in glove box under Ar atmosphere and the taps were closed and sealed there. After that, sealed vials were placed in a Spex™ Duo Mixer/Mill 8000D for milling.

Mechanical alloying (MA) experiments were carried out using a Spex™ Duo Mixer/Mill 8000D with a speed of 1200 rpm for 1 h, 2 h, 4 h, 10 h and 20 h in a tungsten carbide (WC) vial with WC balls having a diameter of 6.35 mm (¼ inches). The ball-to-powder (BPR) weight ratio was 10:1. W-(0.5, 1.0, 4.0, 10.0 wt%)Ti (hereafter referred as W-0.5Ti, W-1.0Ti, W-4.0Ti, W-10.0Ti) were blended and MA'd for 1, 2, 4, 10, and 20h in the first part of experiments where both effects of MA and activated sintering were investigated. In addition, the to investigaate the effects of pre-milling, W powders were milled for 1, 4, 6, 8, 10 and 20 h to achive the smallest W particle sizez. Pre milling was carried in a Spex™ Duo Mixer/Mill 8000D with a speed of 1200 rpm for 1, 2, 4, 10 and 20 h using a tungsten carbide (WC) vial with WC balls having a diameter of 6.35 mm (¼ inches). The ball-to-powder (BPR) weight ratio was 10:1. As a result of pre-milling experiments, 10 h of pre-milling time was selected as the best which yielded the lowest particle size and highest internal strain. Powder particle size measurements were carried out in a Malvern^{TM} Mastersizer Laser particle size analyzer. For measuring of smaller powders Zeta potential-nano sizer microtrac ^{TM} were carried out. It showed that by 10 h pre-milling particle size reached 154 nm which shown in Figure 4-1.

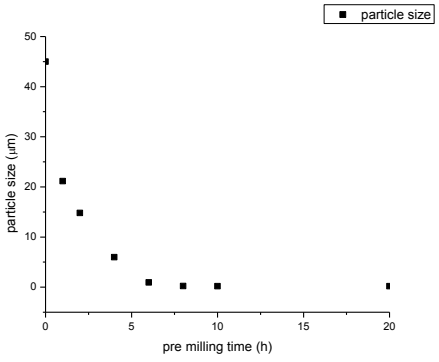

Figure 4.1 : W particle size distribution during Pre-milling.

Figure 4-2 a and 4-2 b clear show W particle sizes shifting to lower sizes with increaseing milling times.

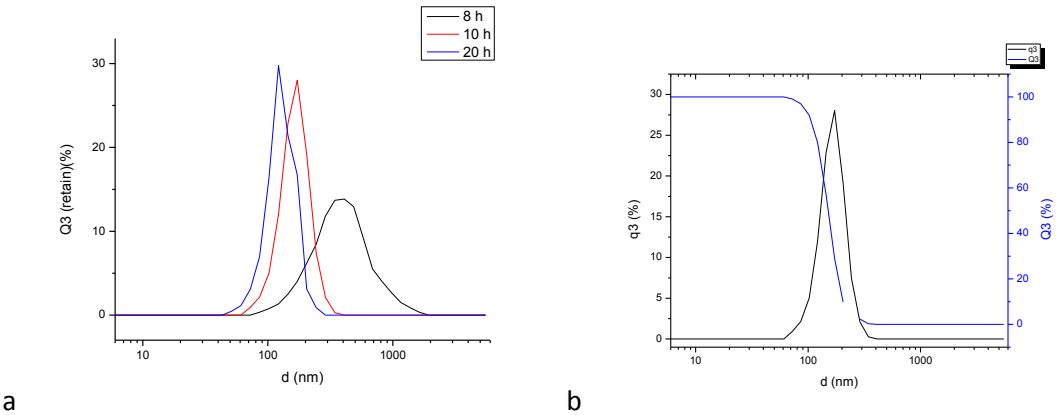

a b

Figure 4.2 : a- W Pre-milled particle size distribution comparison after 8, 10 and 20 h b-W particle size distributions after 10 hours.

Pre-milling after 10 h resulted in an avrage particle size of 154 nm which did not charge after 20 h. between 1 and 4 h, fracturing and welding of particles took place and at milling times exceeding 4 h, fracturing become dominant. There is hardly any special difference between 10 h and 20 h pre-milling times so 10 h pre-milling were selected as elementary W. It means that there is equilibrium between welding and fracturing after 10 h therefore W particle size were in the same size approximately. It can be predicted that XRD of Pre-milled W peaks pre-milled W powders get broader and amorphized portion of W increases in milling. XRD patterns of pre-milled W powders were ploted in the Figure 4-3.

a b

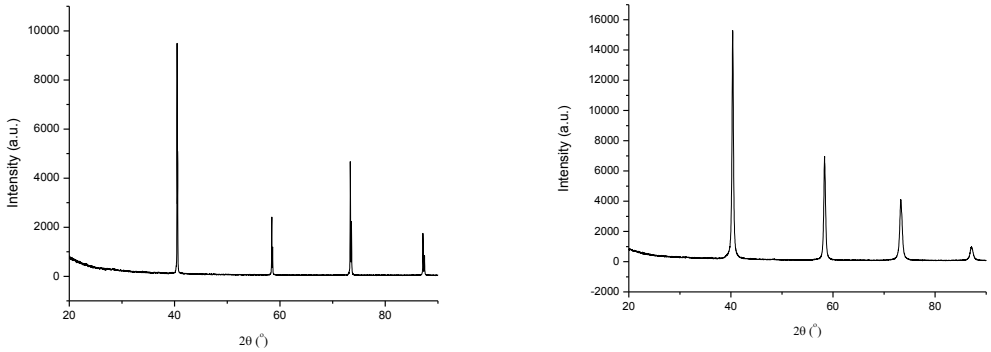

Figure 4.3 : XRD pattern of pre-milled W Pre-milling after a-0h, b-1h, c-2h, d-4h, e-6h, f-8h, g-10h and h-20h.

c

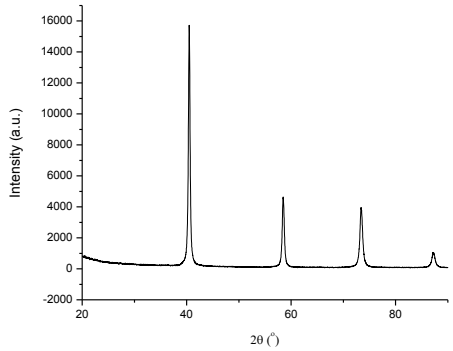

d

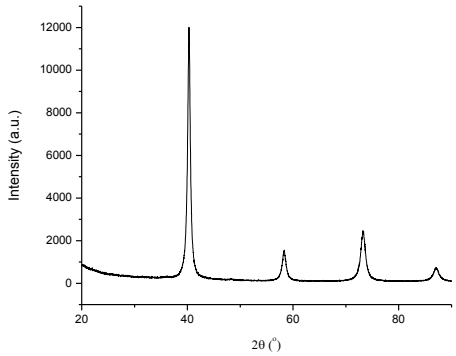

e

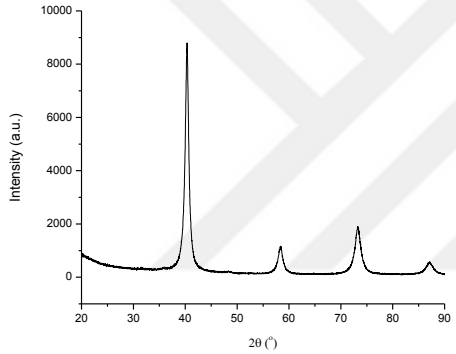

f

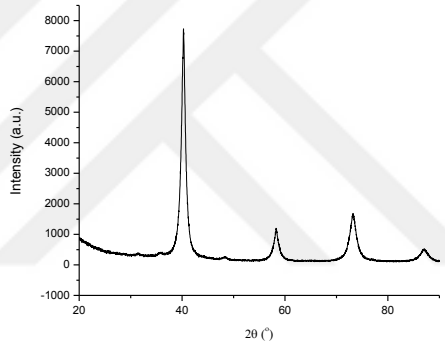

g

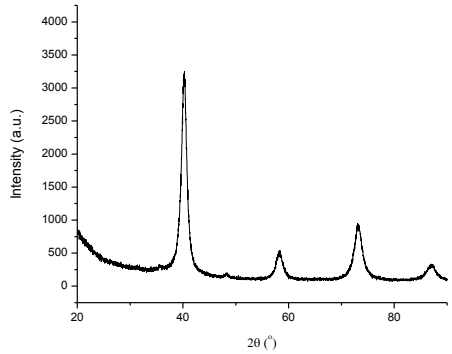

h

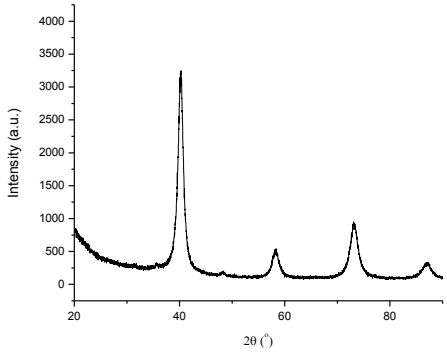

Figure 4.3 (continoued) : XRD pattern of pre-milled W Pre-milling after a-0h, b-1h, c-2h, d-4h, e-6h, f-8h, g-10h and h-20h.

Long time of milling time can cause patterns to get broader and decrease intensity. Comparing of patterns which is offered in Figure 4-4 completely approved it. It is

clear that, XRD patterns belonging to 10 h and 20 h milling are very similar to each other. This being the case, 10 h was prefered to 20 h in order to awoid contaminations arissing from the milling media at long milling durations.thus an optimum pre-milling time of 10 h was selected.

to the 10 h and 20 h are so similar to each other and there is so little differences between them that it approved that 10 h pre-milling is the optimum time for W milling.

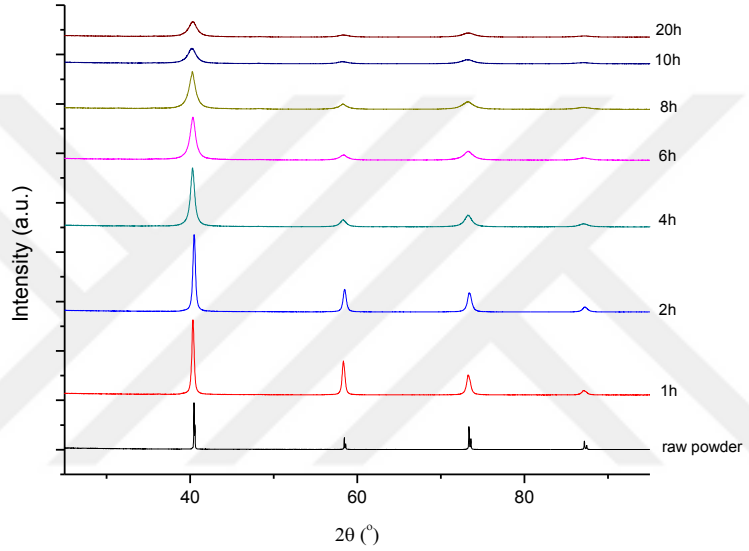

Figure 4.4 : XRD pattern comparison of different pre-milled W powder.

As seen in Figure 4-4 by increasing of milling time some W peaks got broader and hidden too. Figure 4-5 shows the crystallite size of pre-milled W with milling time. By increasing of Pre-milling time of W particle size, crystallite size of W got smaller. As seen in Figure 4-5 the smallest crystallite size is reached after milling for 10 h. Increasing the milling duration had not any specific effect so, like particle size distribution which offered in Figure 4-2, crystallite size were decreased at first steps after 10h smallest crystallite size were caught and more milling had not suitable effect.

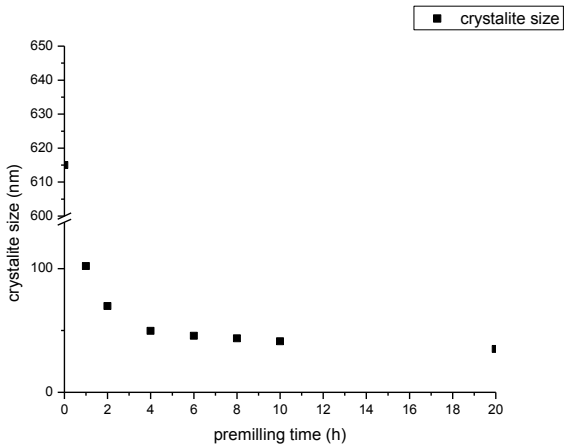

Figure 4.5 : Crystallite size variation of pre-milled W powders.

Based on Figure 4-6 it can see that, long period of milling can reach to increase of internal strain too. Stain increasing rate that can find as the slop of Figure 4-6 decreased after 10h. This curve had smallest slop at 10 h. It means that after 10 h, W couldn't be deformed more therefore, W had the maximum internal strain and highest amounts of dislocation density.

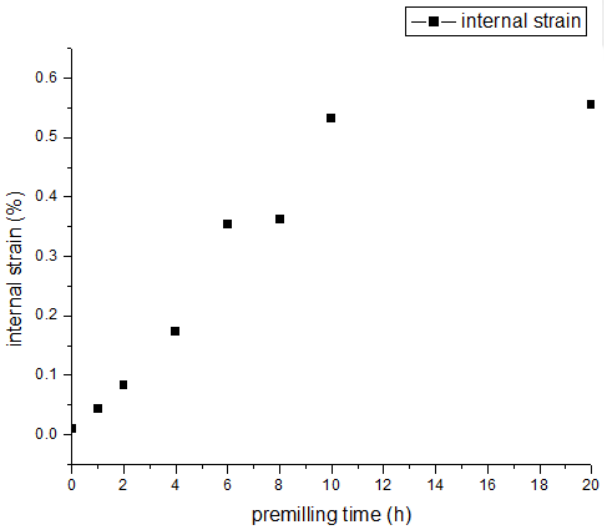

Figure 4.6 : Internal strain variation of pre-milled W powder.

W powders Crystallite sizes, strain vlues and amorphized percentages variations were shown in Table 4-1. After 10 h milling, amorphization got stable and it is another endorsement of 10 h milling is the optimum time. Based on above mentioned items, 10 h pre-milled W (hereafter referred as W^P) used as elementary materials like which was mentioned at first. Therefore, W^P (0.5, 1.0, 4.0, 10.0 wt%) Ti (hereafter

referred as W^P-0.5Ti, W^P-1.0Ti, W^P-4.0Ti, W^P-10.0Ti) were mixed and MA'd for 1, 2, 4, 10, and 20h in first part of experiments, effects of MA and activated sintering were investigated too.

Table 4.1 : Crystallite size, Stain and amorphized degree of pre-milled powders.

Milling time (h)	Crystallite size (nm)	Stain (%)	Amorphized degree (%)
0	615.0	0.0106	0
1	102.0	0.04369	0
2	69.7	0.0832	1.40
4	49.7	0.1730	5.47
6	45.7	0.3530	9.27
8	43.6	0.4103	11.03
10	41.2	0.5327	14.10
20	38.3	0.5439	14.51

4.1.1. Mechanical alloying of elementary powders

This part started with using of two kind of W. first were done by raw W by 45 μm and second groups were mechanically alloyed by 10 h pre-milled W by 150 nm. Other differences of these two kind of W are Listed in Table 4-2.

Table 4.2 : Physical properties of raw materials.

	Particle size	Crystallite size	strain	Crystallized degree
Raw W	45 μm	615 nm	0.0106 %	100 %
10 hr pre milled	150 nm	44 nm	0.5327 %	85.90 %
Raw Ti	45 μm	500 nm	0.00321 %	100 %

Each vial was filled with 20 g W, 200 g balls, and relative Ti amounts in the glove box under argon atmosphere and closed and sealed there. Four compositions of composites were loaded in SPEX^{TM} and milled for 1, 2, 4, 10, and 20 h.

4.1.2. Dry and wet milling analyzing

The MA'd powders characterization involves the determination of size, particle Characterization investigations were carried out on MA'd W-0,5wt%Ti powders using Malvern^{TM} Mastersizer, Micromeritics^{TM} AccuPyc II 1340 gas pycnometer, Jeol^{TM}-6000PLUS Neo Scope Benchtop (SEM) and Bruker^{TM} D8 Advanced Series X-ray diffractometer (XRD). Milling times were increased from 10 h up to 20 h to

observe the effect of milling time on the size and shape of W-0.5wt.%Ti and the results are shown in Figure 4-7. The W-0.5wt.%Ti powders looks differently when milling medias were changed.

The evolution of morphology of the dry milled powders is shown by the SEM micrographs in Figure 4-7 a and d. We can see that the powders MA'd by dry milling method for 10h and 20 h have spherical and particle size is under 400 nm. Because of high surface energy of dry milled, powders were aggregated. Between 10 h and 20 h MA'd powders was not dramatically changed with regard to particle size and form. On the other hand, as shown in Figure 4-7 b, c, e and f in wet milling, layered morphology formed after 10 h MA process. Then, as MA continued, particles shatter into smaller fragments, and the particle size reduce. As seen in Figure 4-7 b, c, e and f, particles which MA'd in IPA has smaller than which milled in ethanol. EDS analysis shows that small particles of WC in the wet milled powders. Meanwhile, this analysis shows that Ti homogeneously distributed in to the W matrix.

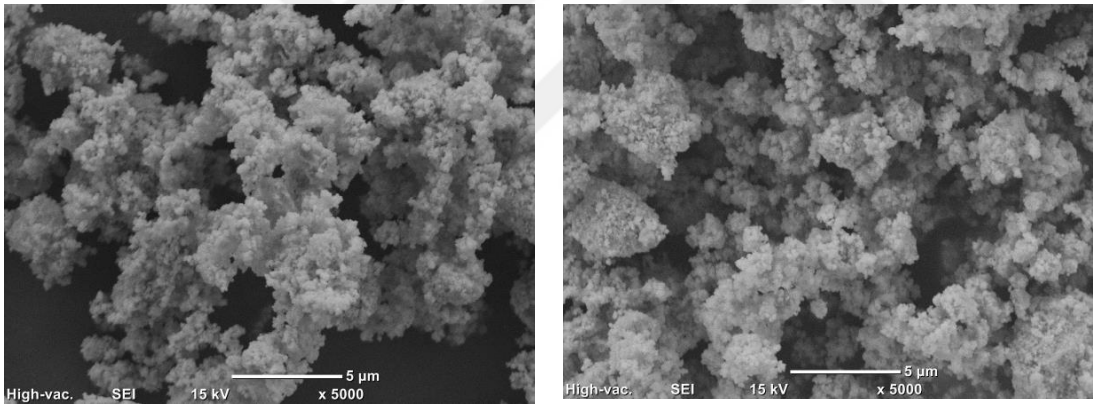

(a) 10h Ar (d) 20h Ar

Figure 4.7 : SEM micrograph of MA'd W-0.5wt.%Ti powders in different milling media after 10h and 20h MA.

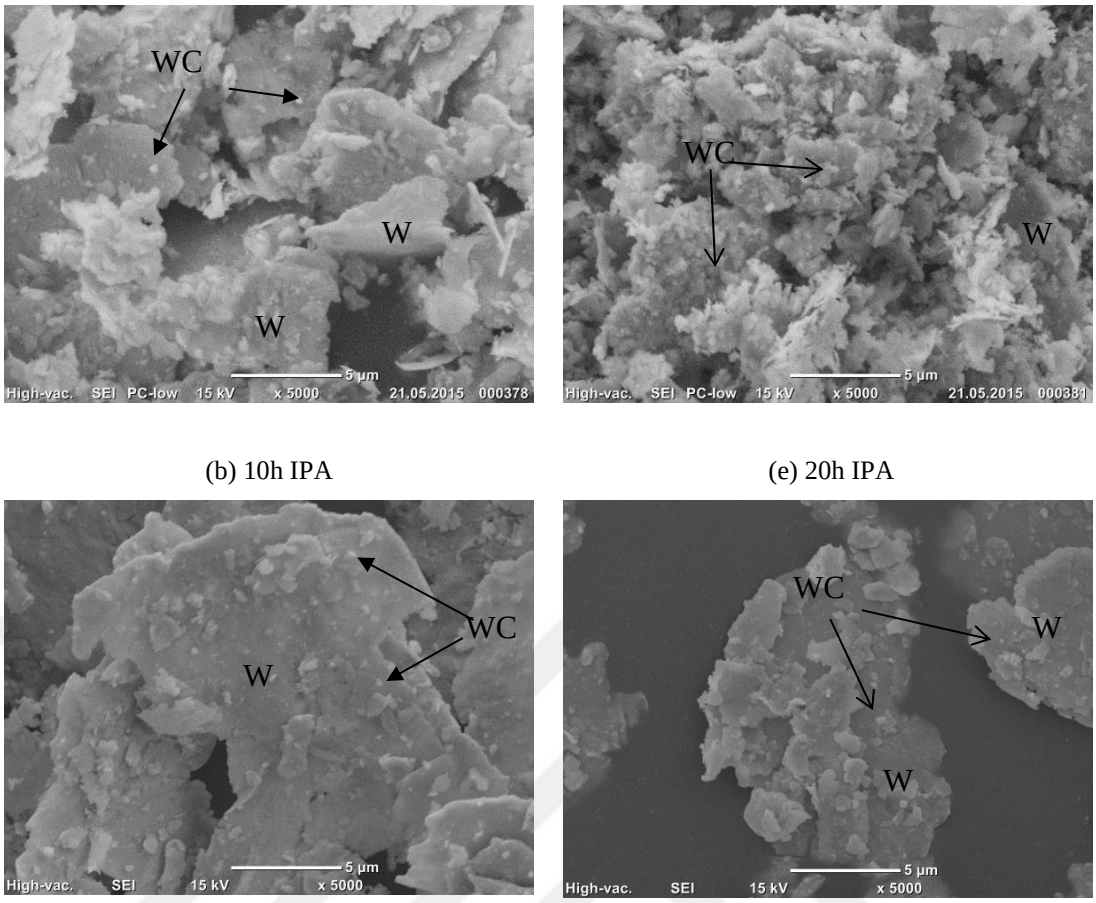

(b) 10h IPA (e) 20h IPA

(c) 10h Ethanol (f) 20h Ethanol

Figure 4.7 (continoued) : SEM micrograph of MA'd W-0.5wt.%Ti powders in different milling media after 10h and 20h MA.

XRD patterns of MA'd W-0.5wt.%Ti powders are illustrated in Figure 4-8. The XRD patterns included Ti_x-$W_{(1-x)}$ and WC peaks of the W-0.5wt.%Ti powders reveals the presence of the characteristic peaks of $Ti_xW_{(1-x)}$ phase (Bravais lattice: b.c.c.; S.G.: Im-3m (229); a=0.316 nm; ICDD#49-1440) and the WC phase (Bravais lattice: h.c.p.; S.G.: P-6m2 (187); a = 0.290 nm, c = 0.283 nm ; ICDD #57-0939). Due to small amounts of Ti (0.5wt.%) and its solution in W matrix, its peaks were not appeared.

Mechanical alloying decreased the peak intensities of W and increased peak line broadening. MA'd powders underwent deformation and cold welding caused by continuous collision and splitting between balls and powders. As can be seen in Figure 4-8, the intensity of the diffraction peaks decreased with increasing milling time and became wider. As the milling time increased, drastically reduction in peak

height and broadening of the peak were observed. This may be ascribed to a severe lattice distortion and grain size refinement.

As seen in Figure 4-8, due to the effects of MA, intensive WC contamination was appeared after MA. Presumably, these peaks arose from the milling media (vial and balls) owing to the excessive impact energy accumulated during the long-time mechanical alloying. Comparing wet and dry MA, shows that WC peaks are more intense in wet milling, particularly in IPA. In Ar atmosphere, powders covered whole surface of WC balls and during balls colliding get smaller however, in wet milling, the surface of the WC balls were clean and during colliding these balls were eroded and interred to composition. Duo to this phenomena, it can be predicted that milled and alloyed powders in dry atmosphere have small crystallite size and high lattice strain. As shown in Figure 4-7, small particles of WC are seen in wet MA'd powders and the EDS results supported the WC contamination in the long-time milling, as presented in Figure 4-8 b,c,e and f., while these particles was not found in SEM micrograph of dried MA'd Powders.

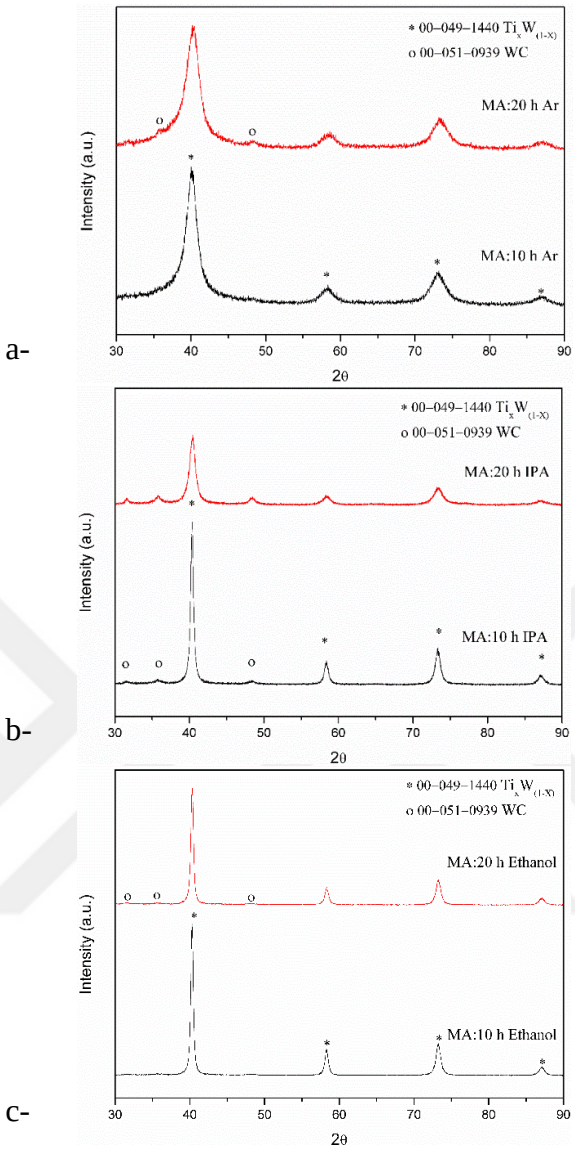

Figure 4.8 : XRD Pattrens of MA'd W-0.5wt.%Ti powders in different milling media after 10h and 20h MA a)Ar, b)IPA, c) Ethanol.

Crystallite size and lattice internal strain determination is one of the most important applications in powder X-rays diffractometry for materials characterization. Table 4-3 shows the variation of the crystallite size with milling time (10 and 20 h) in three different milling media which calculated by Lorentzian and Gaussian methods.

In, very high speed ball milling powders caused a decrease in peak intensity as well as a broadening in full width at half maximum (FWHM) owing to a reduction in the crystallite size and an accumulation of the lattice strain. These changes were very drastic with the milling time and milling media was reduced. There was a rapid decrease in crystallite size of W-0.5wt.%Ti powders occurs from 0 to 10 h of MA,

but after 10 h of MA only a slight further decrease in crystallite size occurs measured by Lorentzian and Gaussian methods as supported by Zuhailawati and Mahani. The results indicate that selected MA medias were highly effective in reducing crystallite size by increasing milling time. As shown in Table 4-3, the smallest crystallite size is belonged to the dried milled powders meanwhile, powders MA'd in ethanol has greatest crystallite sizes. This can be also confirmed with peak broadening shown in Figure 4-8. The calculated crystallite sizes by Gaussian method are slightly smaller than measured by Lorentzian methods however; the strain amounts calculated by Gaussian method are slightly higher than measured by Lorentzian method.

Table 4.3 : Crystallite size, lattice strain wet and dry MA`d particles.

Milling Media	Pure W	Ethanol		IPA		Ar	
MA time (h)	0	10	20	10	20	10	20
Crystallite Size L (nm)	510.47	61.00	57.07	41.30	17.27	6.53	4.93
Crystallite Size G (nm)	436.90	31.17	30.13	20.67	13.30	5.73	5.57
Strain L	0.0029	0.0357	0.3409	0.3402	1.4823	2.1784	3.4140
Strain G	0.0024	0.0436	0.6308	0.4636	1.8015	2.5255	3.5669

Figure 4-9 shows that "a" values increased from 0h to 10h with MA than decreased. It means that, maximum lattice parameter was calculated as 3.175, 3.163 and 3.158 nm for Ar, ethanol and IPA after 10 h MA respectively, furthermore minimum 2Ɵ values measured as 40.14, 40.295 and 40.35 degree for Ar, ethanol and IPA after 10 h MA respectively. As shown in Figure 4-9 with up to 20 h MA, crystallite rate linearly decreased with increment of MA time. The maximum and minimum crystallite rate measured as 65% and 91% after 20 h MA in Ar and ethanol medium, respectively.

a-

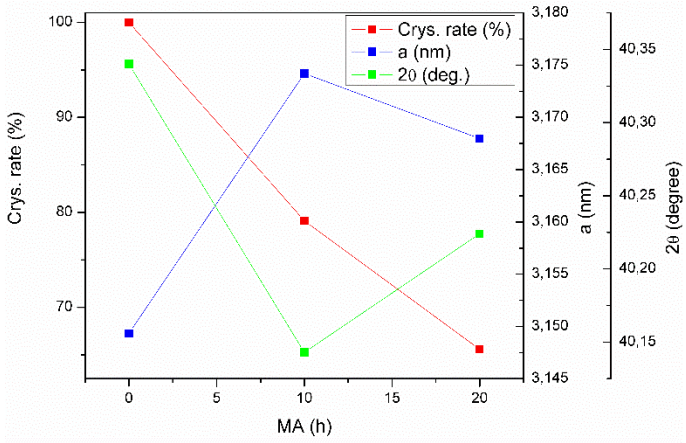

b-

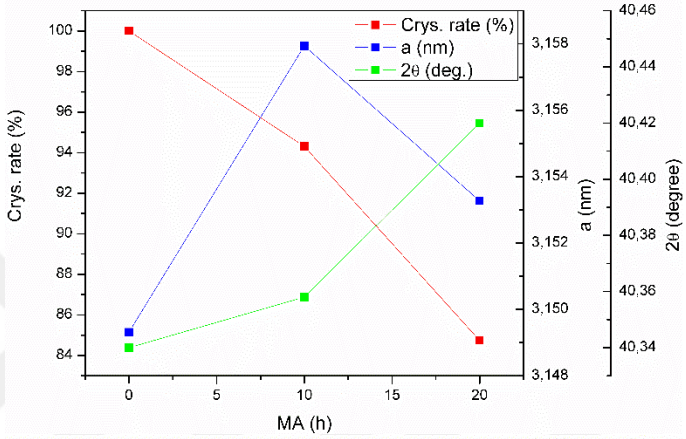

c-

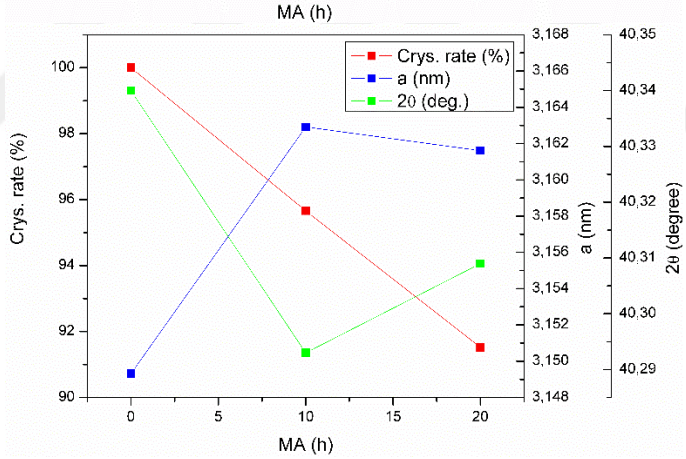

Figure 4.9 : Crystalite rates, lattice parameters and 2Θ(110) degrees of MA'd W-0.5wt.%Ti powders in different milling media after 10h and 20h MA a)Ar, b)IPA, c) Ethanol.

As shown, powder densities of MA'd W-0.5wt.%Ti powders offered in Table 4-4. The MA'd W-0.5wt.%Ti powders milled in ethanol have highest densities this phenomena supported with sharp XRD peaks shown in Figure 4-8 c, however, the powders MA'd in IPA have lowest densities. Due to collision between vial and balls, WC impurities increased more and more with MA time, particularly in IPA media, this fact supported with Figure 4-8, that shows, MA'd powders in IPA have more intense WC peaks than the others. Probably, increment of the WC particles might

have caused density decrement of the MA'd W-0.5wt.%Ti powders. Based on these results, dry milling was preferred.

Table 4.4 : Powder densities of MA'd W-0.5wt.%Ti powders.

Milling Media	*Milling Time*	
	10 h	**20 h**
Ethanol	18.23±0.02	18.15±0.03
Argon	15.38±0.02	14.86±0.02
IPA	12.88±0.02	12.24±0.02

4.1.3. X-ray diffraction analyzing of prepared powders

- W-0.5Ti

Applying long period of MA were related to the decrease of peaks intensity which after 10 h MA some peaks were disappeared besides peaks got broader it shows that internal strain and dislocation density increased by enforcing of long period of MA. Peaks of Ti were not appeared, it can because of low amounts of added Ti. All diffraction peaks seen in Figure 4-10 can be assigned to the body center cubic phase with Im-3m space group, JCODS card NO. 00-049-1440 and unit cell parameter a=b=c=0.316489 nm. It can be inferred that, with increased MA duration, the intensity of appeared peaks decreased and values of the full width at the half maximum (FWHM) increased and the position of peaks shifted lower values of 2θ.

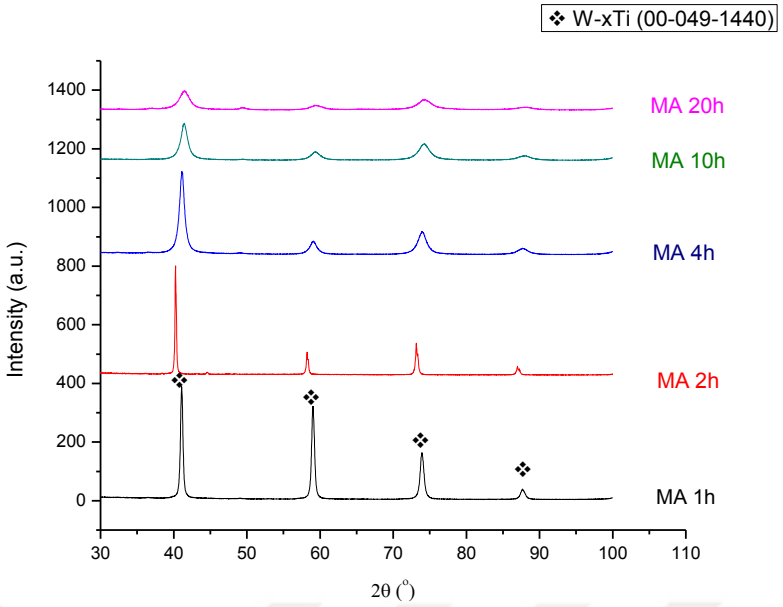

Figure 4.10 : XRD pattern of W -0.5Ti MA`d for 1, 2, 4, 10, and 20 h.

The significance broadening of peaks reveals grain refinement along with the large strain, associated with the powder. Peak broadening has 3 reasons that offered in given Equation 2-21 and is related to the Instrument, Crystallite size and lattice strain.

$$(\beta_{hkl})^2 = (\beta_{hkl})^2_{measured} - (\beta_{hkl})^2_{Instrument} \quad (3.1)$$

β_{hkl} here referred to the FWHM which composed of 2 factors as β_S and β_C, lattice strain broadening and crystallite size broadening parameters, respectively. To remove these aberrations, it is needed to assemble a diffraction pattern from the line broadening of a standard material to determine instrumental broadening. By applying long period of milling powders crystallite size, internal strain, and powder crystallite rate were changed.

Table 4.5 : Physical properties of Wp-0.5Ti after MA.

MA Duration	Crystallite size (nm) (100)	Strain (%)	Amorphized degree (%)	Powder density (g/cm^3)
1h	44.2	0.06909	100	16.90
2h	58.5	0.04052	100	16.90
4h	19.5	0.07054	98	16.82
10h	14.2	0.34346	93	16.71
20h	10.6	0.67239.	88	16.65

As shown in Table 4-5, some crystal specifications of milled Powders. As shown in Figure 4-11 by applying long period of MA crystallite size were decreased and lowest crystallite size is belong to the 20 h MA. Internal strains were increased and it can because of internal defects increasing. MA applied huge force to the crystal of powders this enforcement cause to appearance of defects and dislocations. Besides, increasing of defects were related to the decreasing of powder density. Crystals deformed to reduce the effect of this imported energy and it can turn up as decreasing of crystallite size. Meantime, by applying MA crystallized degree of powders decreased and amorphized degree were increased which are show in Table 4.5 and Figure 4-11.

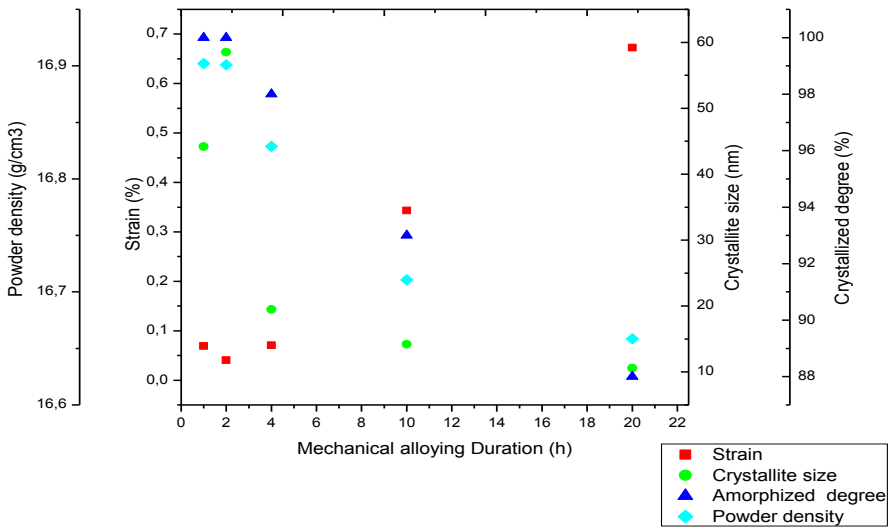

Figure 4.11 : Physical properties of W-0.5Ti after MA.

As shown in Figure 4.11 applying long period of MA will caused to crystallite size decreasing this declining happened by increasing of internal dislocations. Increasing

of dislocation density caused to increase of lattice internal stain. Furthermore, defects density declined powder density even crystallite powder deformed and amorphized gradually. This amorphized degree increased by MA.

- W-1.0Ti

MA time effects on the peaks intensity which by applying long MA time, some peaks were disappeared besides, peak`s FWHM got broader it is shows by enforcing of long period of MA internal lattice strain and dislocation density increased in Figure 4-12. It can be inferred that, with increasing MA duration, the intensity of appeared peaks decreased and values of the FWHM was increased and the position of peaks shifted lower values of 2θ. Peaks of Ti were not appeared here too, it can because of low amounts of added Ti. All diffraction peaks seen in Figure 4-12 can be assigned to the body center cubic phase card NO. 00-049-1440.

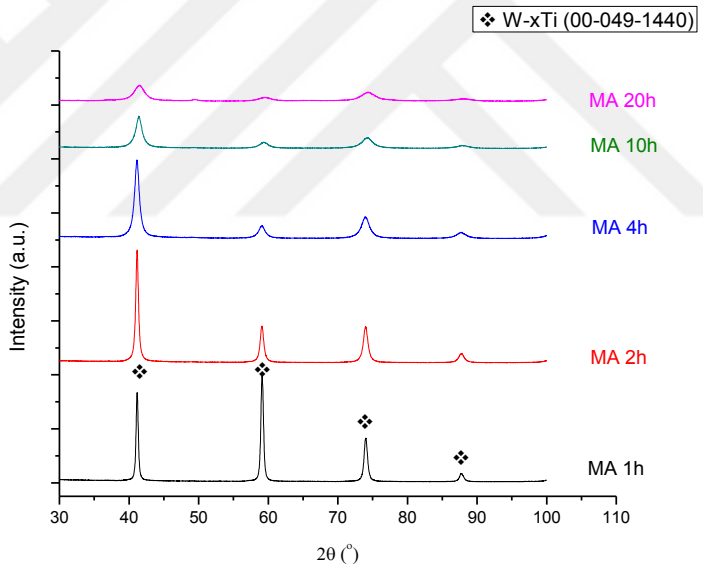

Figure 4.12 : XRD pattern of W -1.0Ti MA`d for 1h, 2h, 4h, 10h,and 20h.

Table 4-6 shows that by applying long period of MA crystallite size were decreased and lowest crystallite size is belong to the 20 h MA too which calculated by TOPAS 3 via Lorentzian method. Strain values were increased. This increament is because of dislocation increasing. Milling forces to the crystal of powders. This enforcement cause to appearance of defects and dislocations. Furthermore, powders densities and crystallite size and powder crystallized degree were decreased which can be shown in Table 4-6 and Figure 4-13.

Table 4.6 : Crystallite size, Strain value, Amorphized degree and powder density of W-1.0Ti after MA.

MA Duration	Crystallite size (nm) (100)	Strain (%)	Amorphized degree (%)	Powder density (g/cm^3)
1h	49.7	0.07109	100	16.90
2h	41.1	0.07852	100	16.90
4h	19.7	0.08054	95	16.85
10h	14.1	0.39346	92	16.71
20h	10.2	0.75902	85	16.65

Figure 4-18 shows that powder density, Crystallite size and amorphized degree had same relation by appling long period of MA. MA related to decrease of powder density, Crystallite size and amorphized degree. Unlike them internal strain grew up.

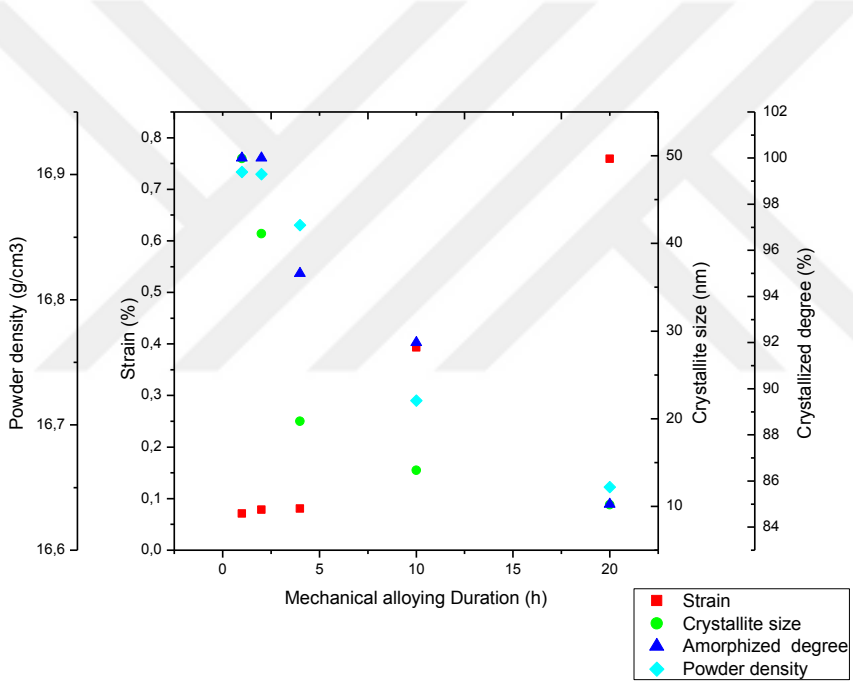

Figure 4.13 : Crystallite size, Strain value, Amorphized degree and powder density of W-1.0Ti after MA.

- W-4.0Ti

By applying long period of MA, some peaks were disappeared besides, peak`s FWHM got broader. Enforcing of long period of MA causes internal lattice strain. With increasing MA duration, the intensity of appeared peaks decreased and values of the FWHM increased and peaks (200), (220) and (310) got hidden completely after 10 h milling process meantime, the position of peaks shifted lower values of 2θ. Based on Figure 4-14, Ti Peaks were seen after 1 h MA but by applying further MA

Ti Peaks disappeared besides, Ti peaks disappearance other peaks intensities decreased and peaks got broader.

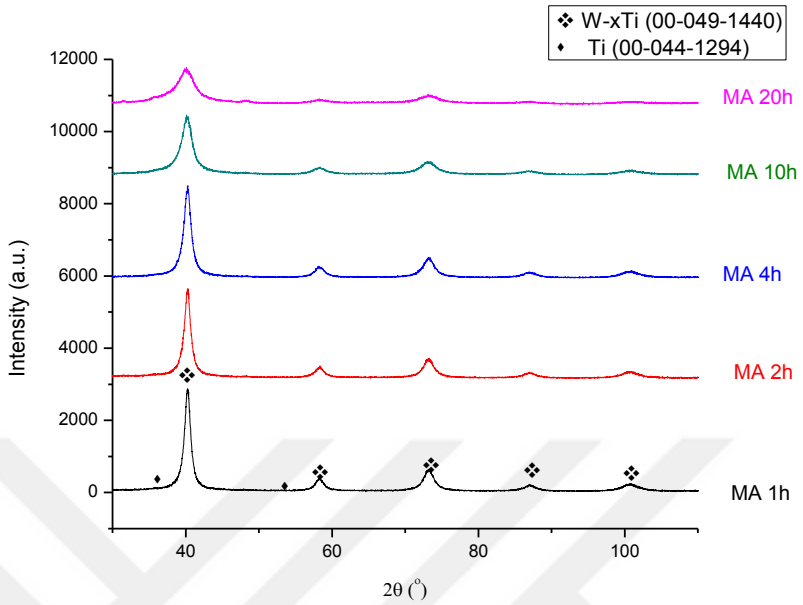

Figure 4.14 : XRD pattern of W -4.0Ti MA`d for 1h, 2h, 4h, 10h, and 20 h.

According to Table 4-7, crystallite size were decreased and lowest crystallite size is 9.9 nm after 20 h MA. Crystallite size and internal strain were calculated by TOPAS 3 via Lorentzian method. Internal lattice strain values were increased it can because of dislocation density increasing. By high energy milling, external power applied to the crystal of powders, this enforcement causes to appearance of defects and dislocations. Furthermore, powders densities and crystallite size and powder crystallized degree were decreased which can be shown in Table 4-7 and Figure 4-15.

Table 4.7 : Crystallite size, Strain value, Amorphized degree and powder density of W-4.0Ti after MA.

MA Duration	Crystallite size (nm) (100)	Strain (%)	Amorphized degree (%)	Powder density (g/cm^3)
1h	52.7	0.07119	100	15.87
2h	44.7	0.07877	100	15.78
4h	23.0	0.08423	96	15.73
10h	19.3	0.42001	93	15.64
20h	9.9	0.78221	83	14.99

Figure 4-15 shows the Table 4-7 graphically as shown, powder density, Crystallite size and amorphized degree had same relation vs. MA time. MA time related to decrease of powder density, Crystallite size and Crystallized degree. Unlike them internal strain values grew up.

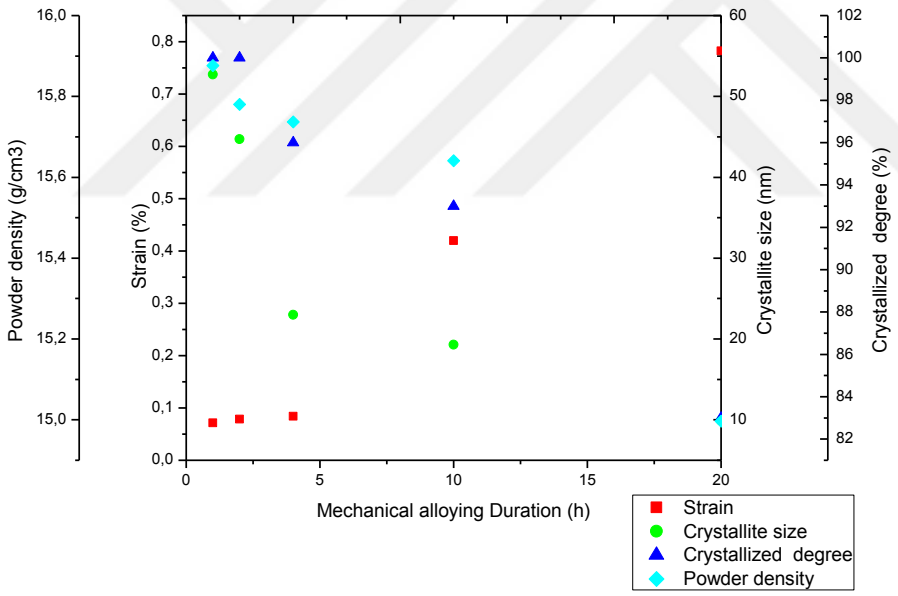

Figure 4.15 : Crystallite size, Strain value, Amorphized degree and powder density of W -4.0Ti after MA.

- W-10.0Ti

W-10.0 Ti were MA'd for 1 h, 2 h, 4 h, 10 h and 20 h. Long period of MA duration were led to peaks got broader and (200), (220) and (310) were faded. With increasing MA duration, the intensity of appeared peaks decreased and values of the FWHM increased and peaks (200), (220) and (310) intensity got decreased and finally got

hidden completely after 20 h. Meantime, the position of peaks shifted lower values of 2θ. Based on Figure 4-21, Ti peaks were seen but by applying MA, Ti related peaks disappeared besides, Ti peaks intensities decreased and peaks got broader.

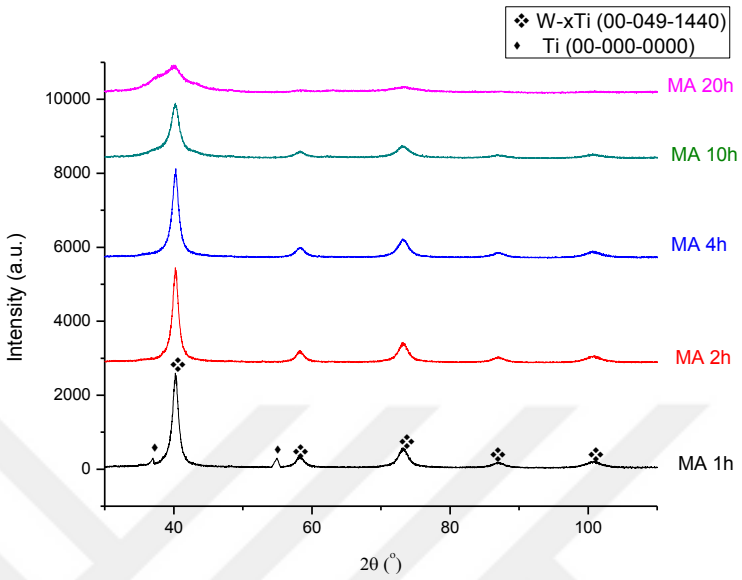

Figure 4.16 : XRD pattern of W -10.0Ti MA`d for 1h, 2h, 4h, 10h, and 20h.

As shown in Figure 4-16, Ti peaks are seen at lowest milling duration and at long period, these peaks were disappeared. As seen in Figures 4-10 4-12, 4-14 and 4-16 Peaks intensity declining and width broadening can be shown too. As mentioned previously, W have low intensity and wide peaks specially, peaks (200), (220) and (310) got hidden completely too. Based on Figures 4-10 4-12, 4-14 and 4-16, Ti peaks were seen firstly but by applying MA it disappeared besides, Ti peaks disappearance other peaks intensities decreased and peaks got broader.

Table 4-8 shows crystallite size, strain value, amorphized degree and powder densities for W-10.0wt%Ti. It is important to notify that compositions with higher Ti amounts, have the higher strain values after 20 h MA. The strain values of W-4.0wt%Ti after 20 h MA is 0.78221% which is so near to W-10.0wt%Ti strain values 0.79001. W-4wt%Ti powder has the least Crystallite size and crystallized degree than other compositions.

Table 4.8 : Crystallite size, Strain value, Amorphized degree and powder density of W-10.0Ti after MA.

MA Duration	Crystallite size (nm)	Strain (%)	Crystallized degree (%)	Powder density (g/cm^3)
1h	54.9	0.07122	100	13.59
2h	43.6	0.07862	99	13.38
4h	24.0	0.08322	95	13.33
10h	20.7	0.44302	94	12.98
20h	10.1	0.79001	92	12.69

Figure 4-17 shows that powder density, crystallite size and amorphized degree data which mentioned in Table 4-8 garaphically. MA increasing led to decrease of powder density, crystallite size and crystallized degree. Unlike them internal strain grew up.

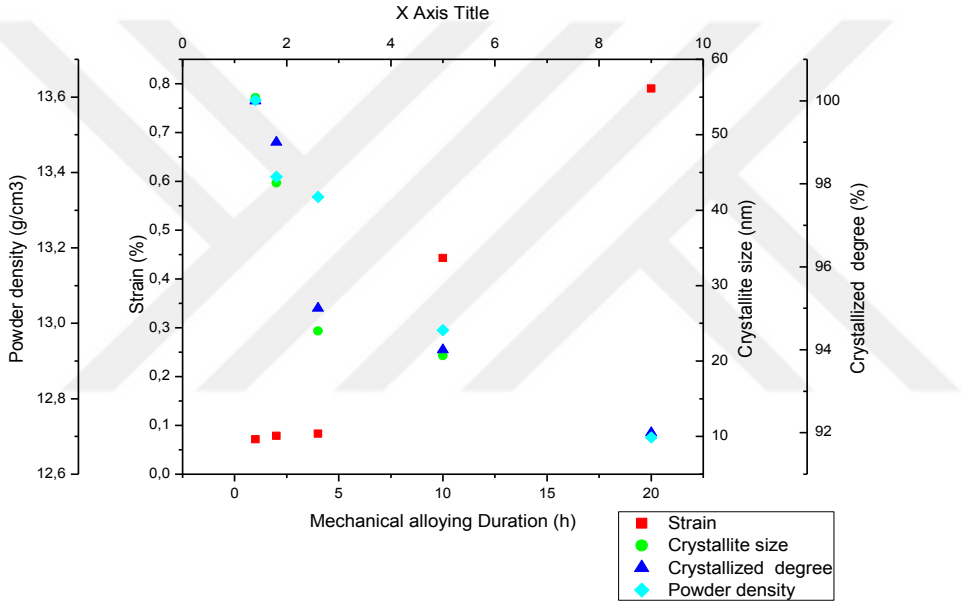

Figure 4.17 : Crystallite size, strain value, amorphized degree and powder density of W-10.0Ti after MA.

- W^P-0.5Ti

Figure 4-18 shows XRD patterns of W^p-0.5Ti after variouse MA times. Different period of MA (1 h, 2 h 4 h, 10 h and 20 h) which carried out on pre-milled W and Ti as raw materials. (200), (220) and (310) peaks of the Pdf 00-049-1440 were faded. Pre-milled powders have peaks with low intensity and broader width. The peaks which are shown in Figure 4-18 are so broader than peaks are offered in Figure 4-10 (XRD pattern of W-0.5Ti MA`d for 1h, 2h, 4h, 10h,and 20h) meantime, XRD peaks of W-xTi are more intese and sharper that W^P-xTi.

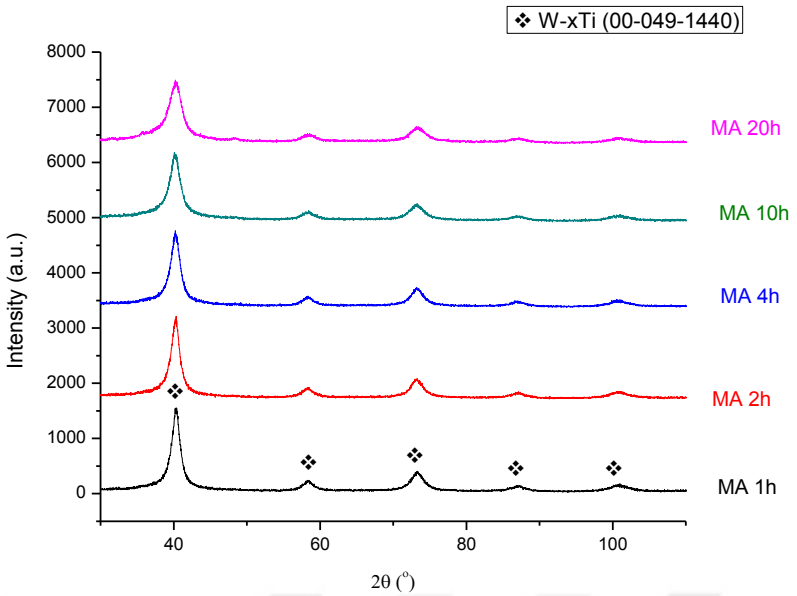

Figure 4.18 : XRD pattern of W^p -0.5Ti MA`d for 1h, 2h, 4h, 10h, and 20h.

Analyzing results which are offered in Table 4.9 indicated that powder densities, strains, crystallite size and crystallized degree decreased too but calculated amounts here are so smaller than the compositions which used unmilled W.

Table 4.9 : Crystallite size, strain value, amorphized degree and powder density of W^p-0.5Ti after MA.

MA Duration	Crystallite size (nm) (100)	Strain (%)	Crystallized degree (%)	Powder density (g/cm^3)
1h	20.4	0.6769	74	16.62
2h	17.8	0.6276	71	16.62
4h	15.5	1.2445	69	16.58
10h	11.6	1.2550	64	16.13
20h	6.6	1.4640	62	16.02

As shown in Figure 4-19, MA caused to reduction of crystallite size. This declination happened by increasing of internal dislocations. Dislocation density was caused to increase of internal lattice stain. Furthermore, powder deformed and amorphized gradually so, amorphized degree increased by MA time too.

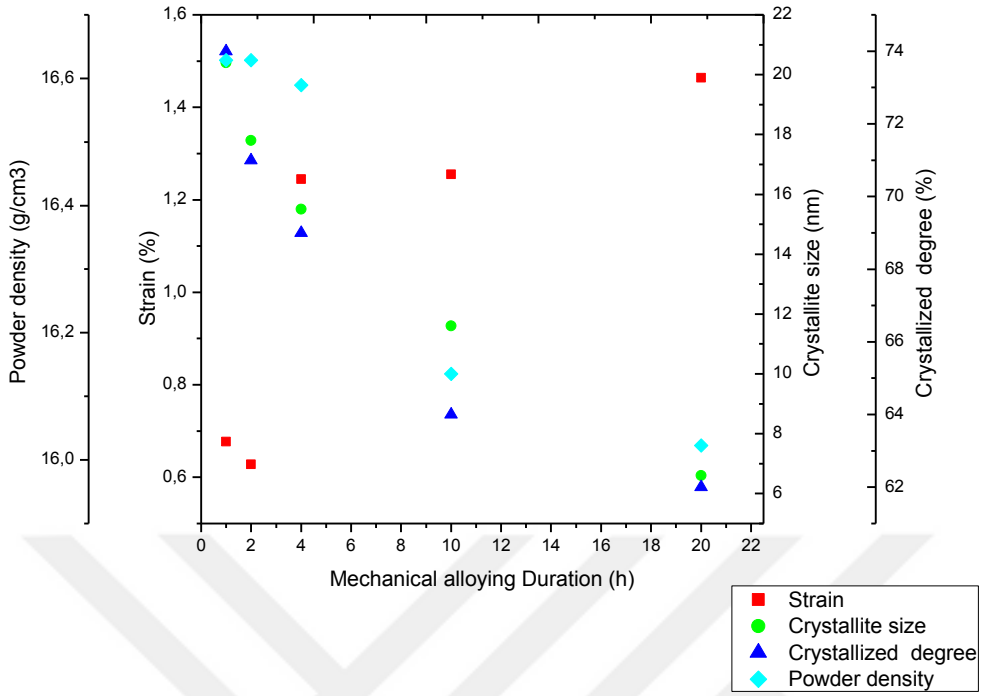

Figure 4.19 : Crystallite size, strain value, amorphized degree and powder density of W^p-0.5Ti after MA.

- W^p-1.0Ti

Figure 4-20 shows XRD pattern of W^p -1.0Ti after different period of MA time. Like Figure 4-18 some peaks of related to the Pdf 00-049-1440 were faded from beginning. As seen in Figure 4-20 applying long period of milling caused to peaks broadening. By comparing Figure 4-12 (XRD pattern of W-1.0Ti MA`d for 1h, 2h, 4h, 10h,and 20h), it can be understood that powders which used pre-milled have peaks with low intensity and broader width. Moreover, analyzing calculated results which are offered in Table 4-10 indicate that powder densities, crystallite size and crystallized degree decreased too.

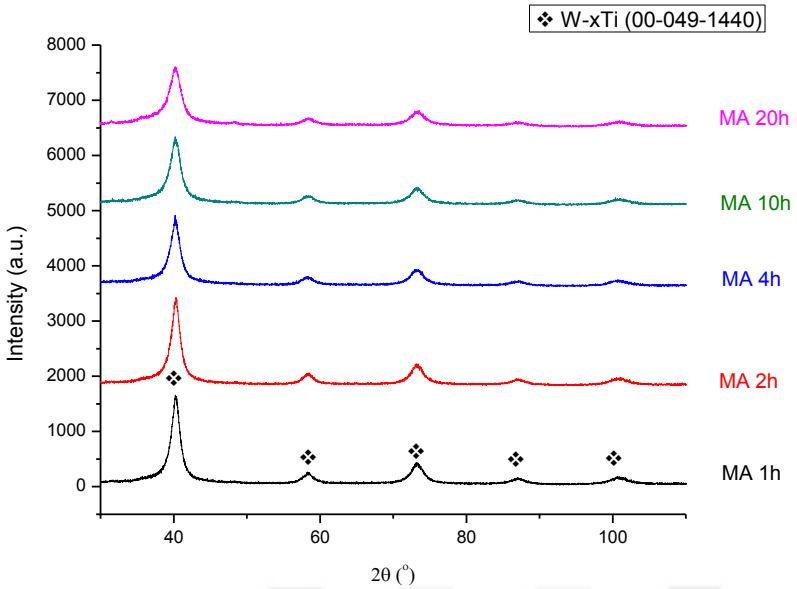

Figure 4.20 : XRD pattern of W^p -1.0Ti MA`d for 1h, 2h, 4h, 10h,and 20h.

Calculated amounts belong to the pre-milled ones are so smaller than powders used unmilled W. Table 4-10 values are shown in Figure 4-21 graphically.

Table 4.10: Crystallite size, strain value, amorphized degree and powder density of W^p-1.0Ti after MA.

MA Duration	Crystallite size (nm) (100)	Strain (%)	Crystallized degree (%)	Powder density (g/cm^3)
1h	28.36	0.7727	72	16.60
2h	16.66	0.9833	70	16.60
4h	10.06	1.1304	69	16.56
10h	5.23	2.2250	65	16.08
20h	3.73	2.8311	62	16.01

As shown in Figure 4-21 MA caused to reduction of crystallite size. This declination happened by increasing of internal dislocations. Dislocation density was caused to increase of lattice internal stain. Furthermore, defects of crystals declined powder density even, powders were deformed and amorphized gradually so, amorphized degree increased by MA.

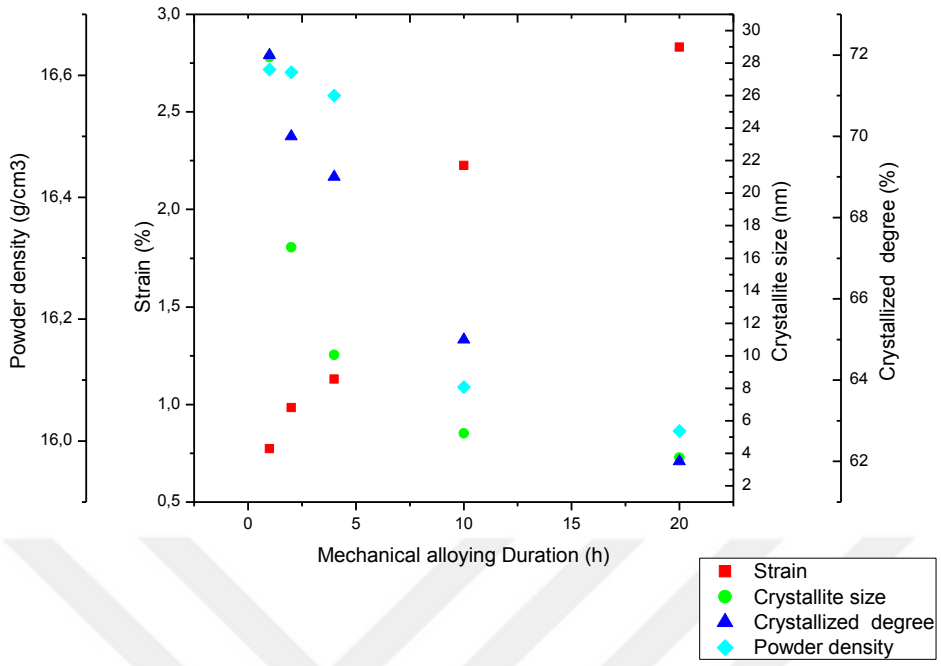

Figure 4.21 : Crystallite size, strain value, amorphized degree and powder density of W^{p}-1.0Ti after MA.

- W^{p}-4.0Ti

Peaks intensity declining and width broadening can be shown in Figure 4.22 clearly. As mentioned previously, produced powders by pre-milled W have low intensity and wide peaks especially, peaks (200), (220) and (310) got hidden completely after long milling process. Based on Figure 4-22 Ti Peaks were seen but by applying MA it disappeared besides Ti peaks disappearance other peaks intensities decreased and peaks got broader. Figure 4-22 shows different period of MA which carried out on 10 h pre-milled W and Ti as elementary materials. Like other compositions that used pre-milled W, peaks are so broader and XRD peaks have low intensity. Strain increasing and crystallite size decreasing are predictable which is approved by data mentioned in Table 4-11.

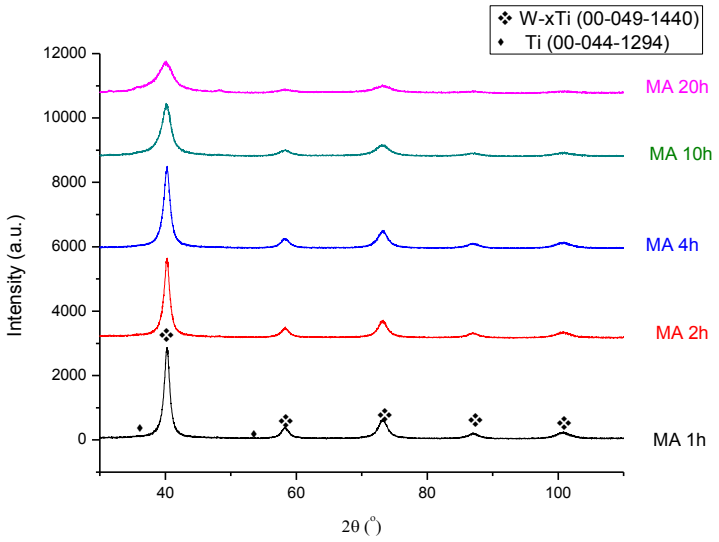

Figure 4.22 : XRD pattern of W^p -4.0Ti MA`d for 1h, 2h, 4h, 10h, and 20h.

Tables 4-7 and Table 4-11 indicate that compositions with WP, powder densities, crystallite size and crystallized degree of Wp-4.0Ti is smaller than W-4.0Ti. Table 4-11 is graphically illusterated in Figure 4-23.

Table 4.11 : Crystallite size, strain value, amorphized degree and powder density of W^P-4.0Ti after MA.

MA Duration	Crystallite size (nm) (100)	Strain (%)	Crystallized degree (%)	Powder density (g/cm^3)
1h	21.50	0.9311	74	15.79
2h	15.76	1.2017	71	15.78
4h	8.53	1.8650	68	15.73
10h	5.93	3.0402	60	15.63
20h	2.10	3.9715	57	14.01

Figure 4-28 shows strain increament by MA time linearly meantime, cristallized degree decreased by MA time linearly too. powder densities, crystallite size, strain and crystallized degree are obeying MA. At different compositions, crystallite size, and powder density decreased though amorphized degree and crystal lattice strain grew up.

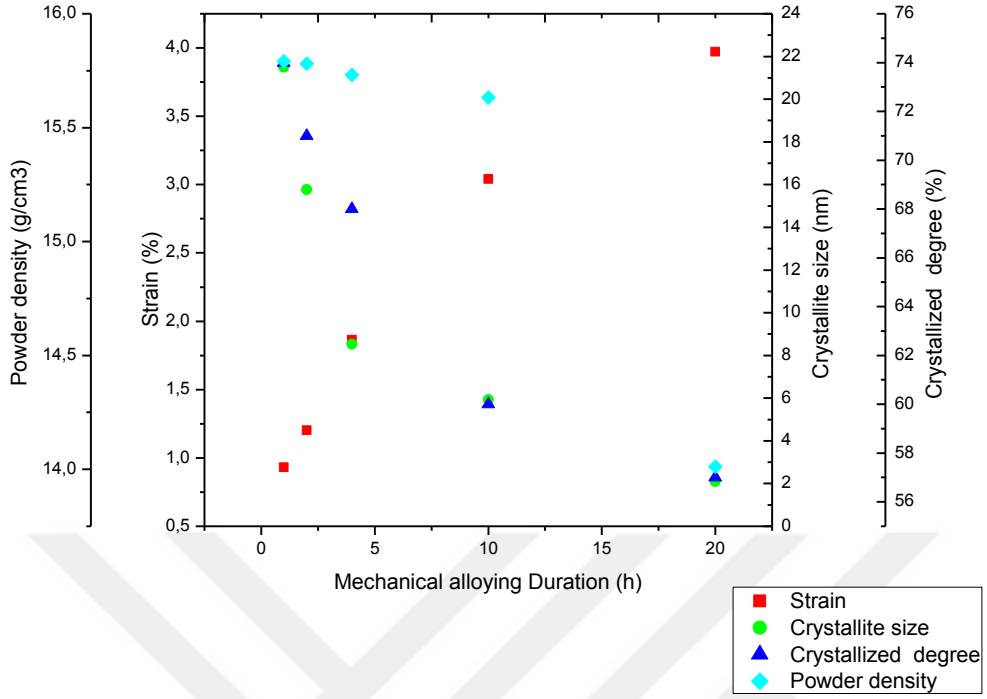

Figure 4.23 : Crystallite size, strain value, amorphized degree and powder density of W^P-4.0Ti after MA.

- W^P-10.0Ti

Figure 4-24 shows XRD Pattern WP-10.0Ti. Ti peaks are seen at low milling duration and after 2 h MA these peaks were disappeared. Peaks intensity declining and FWHM broadening can be shown clearly. Based on Figure 4-29 Ti peaks were seen but by applying MA Ti peaks disappeared besides, other peaks intensities decreased and peaks got broader. Figure 4-24 shows different period of MA which performed on WP-4.0Ti powders. Like other compositions that used WP, peaks are so broader and have lower intensities. After 10 h, peaks (220) and (310) where completely disappeared. Based on these signs, strain increasing and crystallite size decreasing can be predictable which is approved by data mentioned in Table 4-12.

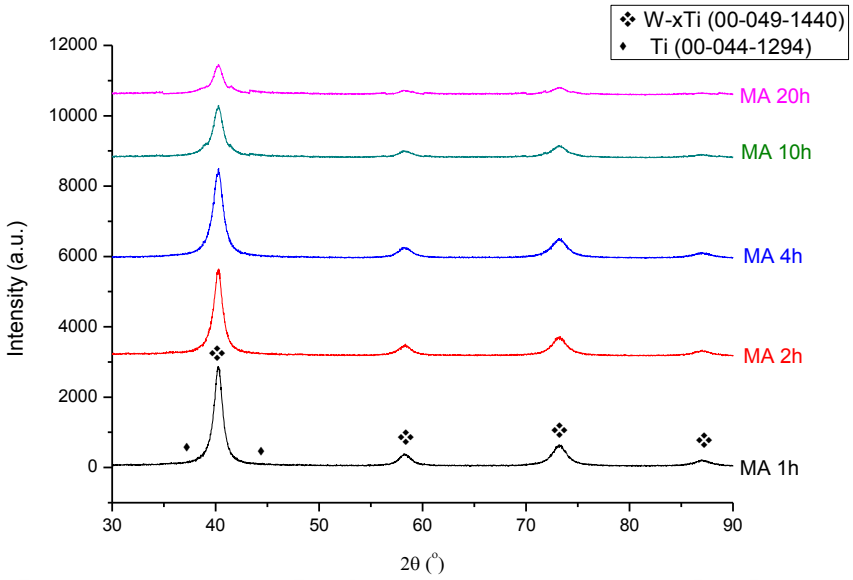

Figure 4.24 : XRD pattern of W^P -10.0Ti MA`d for 1h ,2h, 4h, 10h, and 20h.

Analyzing calculated results which are offered in Table 4-12 indicate that powder densities, strains, crystallite size and crystallized degree varied by MA. The lowest density is belong to WP-10.0Ti after 20h which is 12.9981 g/cn3 meantime, the smallest crystallite size is 5.78 nm after 20 h MA.

Table 4.12: Crystallite size, strain value, amorphized degree and powder density of W^P-10.0Ti after MA.

MA Duration	Crystallite size (nm) (100)	Strain (%)	Crystallized degree (%)	Powder density (g/cm^3)
1h	26.60	0.8054	72	13.59
2h	12.67	1.1329	70	13.49
4h	10.47	1.9520	68	13.49
10h	5.96	3.1509	63	13.00
20h	5.78	4.0117	60	12.99

As shown in Figure 4-25, MA caused to reduction of crystallite size this declination is because of internal dislocations increasing. Dislocation density was caused to increase of lattice internal stain.

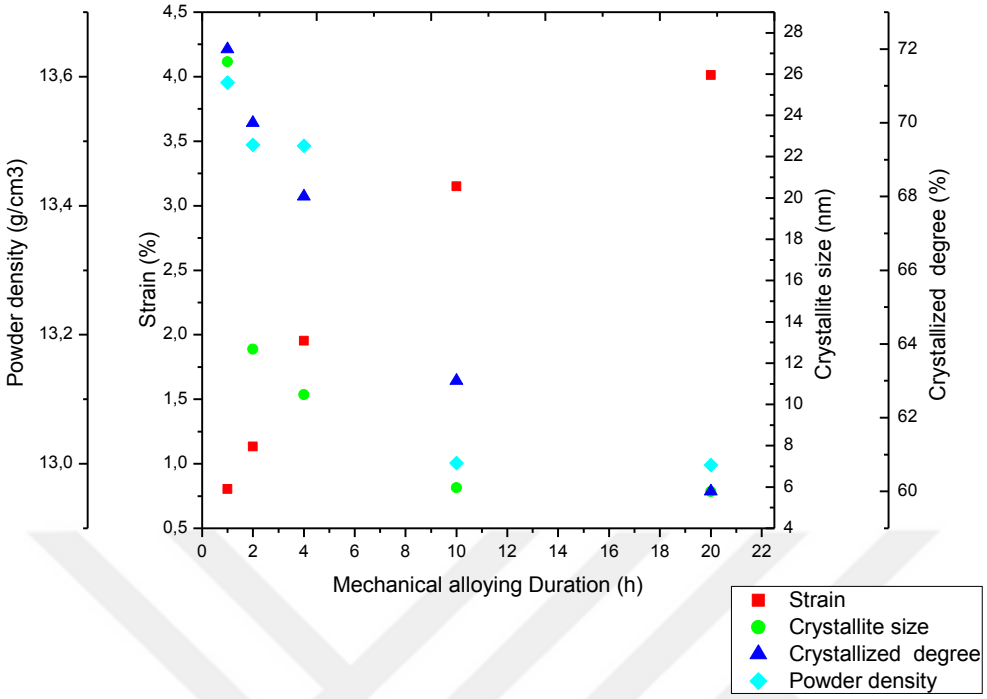

Figure 4.25 : Crystallite size, strain value, amorphized degree and powder density of W^P-10.0Ti after MA.

4.1.4. Determination of crystallite size, strain and solubility in mechanically alloyed W–xTi (x = 0.5, 1.0, 4.0 and 10.0 wt %) powder alloys,

The XRD patterns of the W^P-0.5wt%Ti, W^P-1.0wt%Ti, W^P-4.0wt%Ti and W^P-10.0wt%Ti powder mixtures milled at different times are shown in Figure 4-18, 4-20, 4-22 and 4-24 respectively. Diffraction peaks seen in Figure 4-18, 4-20, 4-22 and 4-24 can be assigned to a body centered cubic (b.c.c.) W–xTi or β(W,Ti) solid solution phase (Lattice parameters: a=0.3165 nm, S.G. : Im-3m, ICDD Card# : 00-049-1440) and to hexagonal close packed (h.c.p.) Ti phase (Lattice parameters: a=2.9505 nm and c=4.6826 nm S.G.: P63/mmc, ICDD Card#: 00-044-1294). It can be inferred that, with increasing MA duration and Ti content, the peak intensities of the solid solution phase decrease and their full width half maximum (FWHM) values increase and the positions of peaks shift to lower 2θ values. In addition, peaks shifts for the milled powders containing higher Ti amounts (4.0 wt% and 10.0 wt%) are larger than those having low Ti amounts (0.5wt% and 1.0wt%). It is also evident from Fig.1 that except for the W-4wt%Ti and W-10wt% Ti powders MA'd for 1 h, Ti peaks completely disappear after MA for 10 hours for all compositions. On the basis of this, three possible scenarios about Ti at high Ti contents and longer MA durations

can be stated: a) Ti is completely dissolved in β(W,Ti) solid solution, or b) Ti is completely amorphized or c) partial dissolution of Ti in the β(W,Ti) solid solution takes place and the remaining Ti is amorphized during MA.

The significance of peak broadening reveals grain refinement along with the large strain, associated with the powders. Peak broadening is contributed by the instrument, crystallite size and lattice strain. By acquiring a diffraction pattern from the line broadening of a standard material, it is possible to remove the instrumental broadening contribution as given in Figure 4-26.

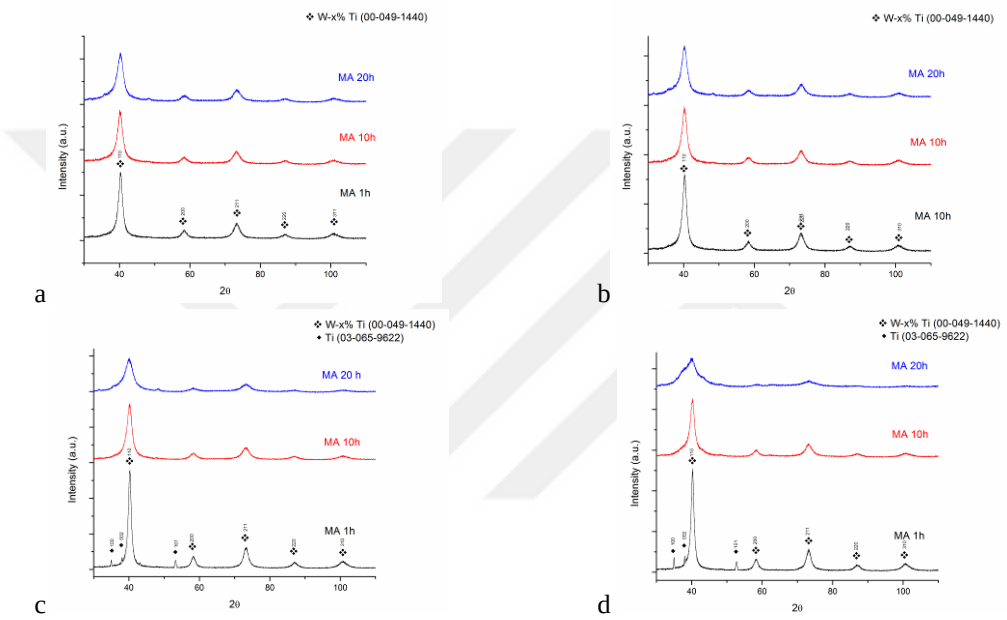

Figure 4.26 : XRD patterns of pre-milled W powders containing different amounts of Ti (W^p-x%wtTi) mechanically alloyed at different durations a- **W^p-0.5 wt% Ti MA`d 1, 10,20 h** b- **$W^p$-1.0 wt% Ti MA`d 1, 10,20 h** c- **W^p-4.0 wt% Ti MA`d 1, 10,20 h** d- **$W^p$-10.0 wt% Ti MA`d 1, 10,20 h.**

As presented in Equation (3.1) β_{hkl} is the full width half maximum (FWHM) composed of crystallite size broadening, β_c and lattice strain broadening, β_s.

$$\beta_{hkl}=\beta_c+\beta_s=(k\lambda/D\cos\theta)+4\varepsilon\tan\theta_{hkl} \quad (4.1)$$

where D is crystallite size, k is shape factor (≈0.9), and λ is wavelength of the CuK_α radiation and ε is the lattice strain. Rearranging Equation (4.1) :

$$\beta_{hkl}\cos\theta_{hkl}=(k\lambda/D)+ 4\varepsilon\sin\theta_{hkl} \quad (4.2)$$

The equations (4.1) and (4.2) are the Williamson-Hall (W-H) equations (Williamson G.K., Hall W.H. 1953, Lubarda, V.A. 2003) On the basis of the equation 4-3, linear

plots of $\beta_{hkl}\cos\theta_{hkl}$ as a function of $4\sin\theta_{hkl}$ (Figure 4-27) can be generated at each MA duration (1 h, 10 h, and 20 h) for all compositions having different Ti amounts. As seen in Figsure 4-27, average lattice strain (ε) values are the slopes and the crystallite sizes, D are determined from the y-increments (kλ/D) of the plots.

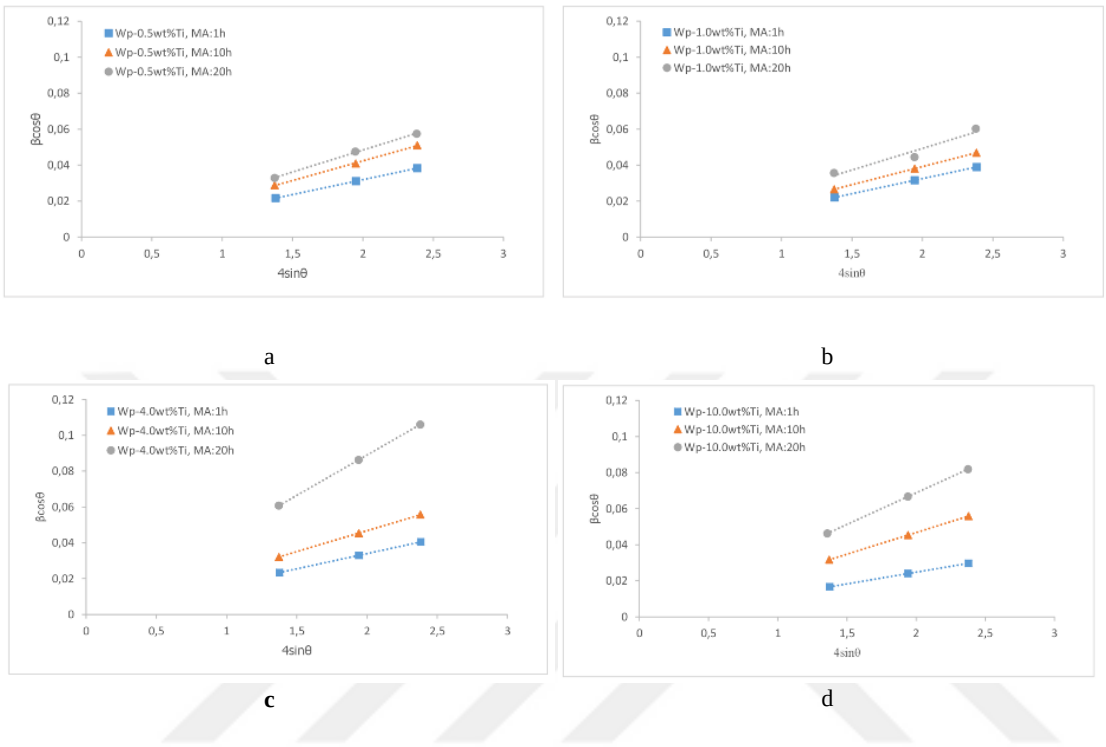

Figure 4.27 : Plots based on the W-H equation (Eq.2a) of the W^p-xTi (βW,Ti) solid solution phases MA'd for 1,10 and 20 h :a) W-0.5 wt%Ti, b)W-1.0 wt%Ti, c) W-4.0 wt%Ti, d)W-10.0 wt%Ti.

As shown in Figure 4-27, increasing MA duration leads to increasing slopes resulting from increases in lattice internal strains. Thus, for all plots the lowest strain value and highest strain values belong to 1 hr of MA and 20 hr of MA, respectively. Besides, positive slopes for all cases indicate the presence of tensile strain due to combined effects of Ti content and MA durations. Average lattice strain, □ (as% strain) and crystallite sizes, D determined from W-H plots (Figures 4-27(a)- 4-27 (d)) along with those obtained by Lorentzian method using TOPAS 5 from XRD graphs in Figure 4-26 are listed in Table 4-13.

Table 4.13 : Crystallite size and average lattice strain values of mechanically alloyed W^p- x Ti alloy (x = 0.5 wt%, 1.0 wt%, 4.0 wt% and 10.0 wt%) powders predicted by using the W-H and Lorentzian methods.

	ε (%Strain)		**D (crystallite size, nm)**	
	Williamson-Hall	TOPAS (Lorentzian)	Williamson-Hall	TOPAS (Lorentzian)
W^p-0.5%wt Ti MA:1h	0.93	0.78	14.55	18.34
W^p-0.5%wt Ti MA:10h	2.12	2.40	4.80	10.80
W^p-0.5%wt Ti MA:20h	2.46	3.65	3.81	4.02
W^p-1.0%wt Ti MA:1h	1.04	0.88	14.65	18.22
W^p-1.0%wt Ti MA:10h	2.07	2.01	5.02	10.41
W^p-1.0%wt Ti MA:20h	2.42	3.63	2.24	7.16
W^p-4.0%wt Ti MA:1h	1.26	0.95	14.32	17.85
W^p-4.0%wt Ti MA:10h	2.38	2.34	4.31	9.81
W^p-4.0%wt Ti MA:20h	4.57	4.57	2.21	3.96
W^p-10.0%wt Ti MA:1h	1.23	0.98	14.01	16.91
W^p-10.0%wt Ti MA:10h	2.42	2.24	4.20	6.47
W^p-10.0%wt Ti MA:20h	3.52	3.52	2.91	2.19

Both ε and D values predicted by using the W-H and TOPAS methods are of the same order of magnitude. As expected, among all W-xTi powder alloys, maximum crystallite sizes and minimum lattice strain values belong to those MA'd for 1 h. The lowest crystallite size of 2.21 nm is predicted for the W^p - 4.0 wt% Ti powder alloy MA'd for 20 h. Similarly, the same powder alloy MA'd for the same duration (20 h) comprises the maximum lattice strain of about 4.57%. The solid solubility of Ti in W during MA can be estimated using the Vegard's law, as described in Equation (4.3).

$$a_{eff}=(1-x)a_W+xa_{Ti} \quad (4.3)$$

where a_W, a_{Ti} are the lattice parameters for pure W and Ti as solvent and solute in the same crystal structure and x is the mole fraction of the solute (Ti). a_{Ti} should be calculated in equivalent body centered cubic (BCC) crystal structure and a_{eff} is the effective lattice constant of the W^p-xTi (β(W,Ti))solid solution. Using Vegard's law, W and Ti structures are both assumed to be body centered cubic (BCC) with coordination number of 8. For the bcc Bravais lattice, the relationship between lattice parameter a and interplanar spacing d_{110} is given by $d_{110}=(\sqrt{2}/2)a=(4/\sqrt{6})r$ and lattice parameter a can be obtained from the measured d_{110} values in XRD graphs (Figure 4-26). Since Ti has a hexagonal closed packed (HCP) structure, its crystal lattice should be converted to the bcc structure and the d_{110} of bcc equivalent Ti is calculated to be 0.2397 nm.

It is evident from Fıgure 4-28 that effective lattice parameter values (a_{eff}) predicted both by TOPAS 5 software and Vegard's law increase linearly with Ti contents. It should be mentioned that Vegard's law is independent of MA. As seen in Figure 4-28, a_{eff} values predicted by TOPAS are in good agreement with those predicted by Vegard's law at low Ti contents (0.5wt% and 1.0wt%Ti), but they display negative deviations from the Vegard's law for the powder alloys having higher Ti contents (4.0 and 10.0 wt% Ti). As expected, adding larger Ti solute atoms (r_{Ti}=0.147 nm) to W (r_W=0.139 nm) increase the effective lattice parameter (a_{eff}) of the W-xTi (β(W,Ti)) solid solution. Ti solubility in 10 h MA'd W-xTi ((β(W,Ti)) solid solutions having high Ti contents can be determined by analyzing and comparing the a_{eff} values predicted by TOPAS (empirical) with those predicted by Vegard's law (theoretical). Thus, from Figure 4-28, the Ti solubility of the 10 h MA'd W–4wt% Ti alloy predicted by Vegard's law is 1.78wt% (6.5at%) and that for the 10 h MA'd W-10wt% Ti powder alloy is 3.12 wt% (11.0at%) (Kasper, E et.al. 1995, Vegard, L 1921) . The maximum equilibrium solubility of Ti in b.c.c. β(W,Ti) solid solution is about 2.51wt% (9at%), indicating that a Ti solubility extension of about 0.6wt% (≈2at%) occurs for the W-10 wt% Ti powder alloy MA'd for 10 h. Therefore, it is likely that Ti which does not go into the (β(W,Ti) solid solution remains as amorphous Ti for the W-10wt% Ti powder alloy MA'd for 10 h.

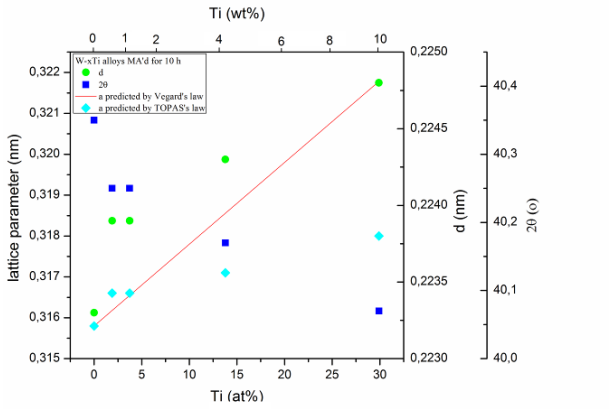

Figure 4.28 : Interplanar distance d_{110}, $2\theta_{110}$ and lattice parameter variations for the W^p – xTi (x = 0.5, 1.0, 4.0 and 10.0 wt%) powder alloys MA'd 10 h.

4.1.5. Powders surface area measurements by Bet:

MA and MM were led to increase of dislocation density which it is equal to decrease of powder density. These phenomena were related to increase of particles surface.

The specific surface area of a powder is estimated from the amount of nitrogen adsorbed in relationship with its pressure, at the boiling temperature of liquid nitrogen under normal atmospheric pressure. The observations are interpreted following the model of Brunauer, Emmett and Teller (BET Method). Surface area and porosity are important physical properties that impact the quality and utility of solid phase chemicals. Differences in the surface area and porosity of particles within the material, which can influence its performance characteristics. Surface area and porosity play major roles in the processing, blending of chemical products.

Based on Table 4-14 it can be understood that the highest surface area is belong to the W^p-4.0Ti and W^p-10.0Ti which are 1.89 and 1.99 m^2/g respectively, it means that, LaB_6 resisted in front of milling it can be approved by particle size and powders density. Powders with LaB_6 had lower powder density and coarser particle sizes. Meantime, comparing of as blended powders by MA`d powders shows that by applying MA powders surface area were increased tremendously.

Table 4.14 : Surface area of powders measured by BET.

	MA period (h)	*Surface area (m^2/g)*
W^P-0.5Ti	10	1.62
W^P-1.0Ti	10	1.62
W^P-4.0Ti	10	1.89
W^P-10.0Ti	10	1.99
W^P-4.0Ti	0	0.23
W^P-0.5Ti-2.0LaB_6	10	0.94
W^P-1.0Ti-2.0LaB_6	10	0.92
W^P-4.0Ti-2.0LaB_6	10	1.23
W^P-10.0Ti-2.0LaB_6	10	1.16
W^P-4.0Ti-2.0LaB_6	0	0.17

As shown in Figure 4-29, powders without LaB_6 have higher surface area it can help us to predict that powders with lanthanum hexaboride need higher sintering temperature. Based on these data, it can be reached that increasing of Ti helps to the increasing of surface area. By Ti solving in W powders, lattice parameters were enlarged which approved by data. This growth of lattice parameters cause to enforced W lattice, therefore, particles can be broken easily.

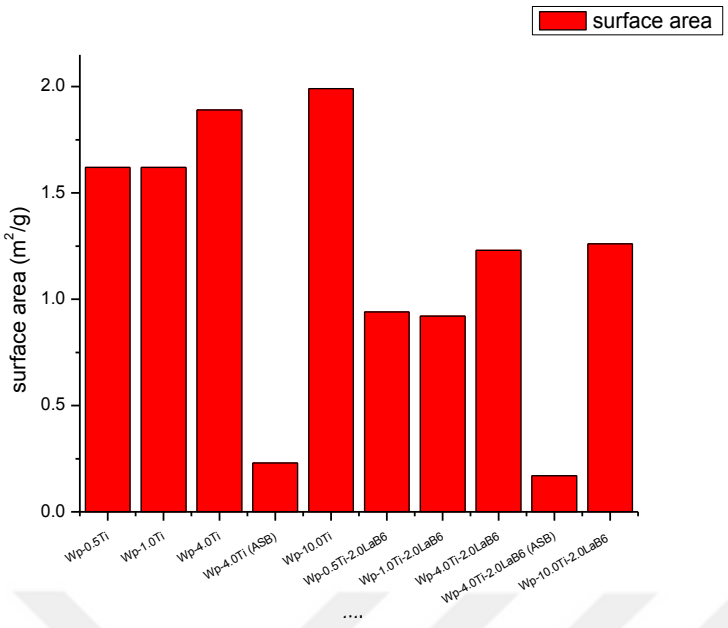

Figure 4.29 : Surface area of MA`d Powders.

4.1.6. SEM micrographs of MM'd and MA'd powders

Different SEM Micrographs are offered in Figure 4-30. a and b show pure W powder. Pure powders are in 10-40 µm with smooth faces meantime 4-30 c and d show W-4.0Ti as mixed powder. Ti powders are a little coarser and their faces are not smooth which can distinguish from W. Figure 4-30 g and h show pure W after 10 h pre-milling. As shown, particles get smaller they are in 0.5-2 µm rang. Some agglomerated particles are seen too. W^p and Ti are mixed together which are shown in Figure 4-30 i, j. Ti particles are surrounded by sub-micron size W powder particles. Pre-milled W has huge surface area therefore they have huge surface energy that prefer to stick each other as agglomerated or stick Ti powders faces to reduce their energy. MA'd powders are shown in 4-30 at e, f and k,l. W-4Ti after 10 h MA is shown in Figure 4-30 e and f and W^P-4Ti after 10 h MA is shown in Figure 4-30 k an l. some agglomerated powder particles are seen in e, f and k, l. Ti powders at e and f are coarser than k and l. Powders at k and l have homogeneous distribution

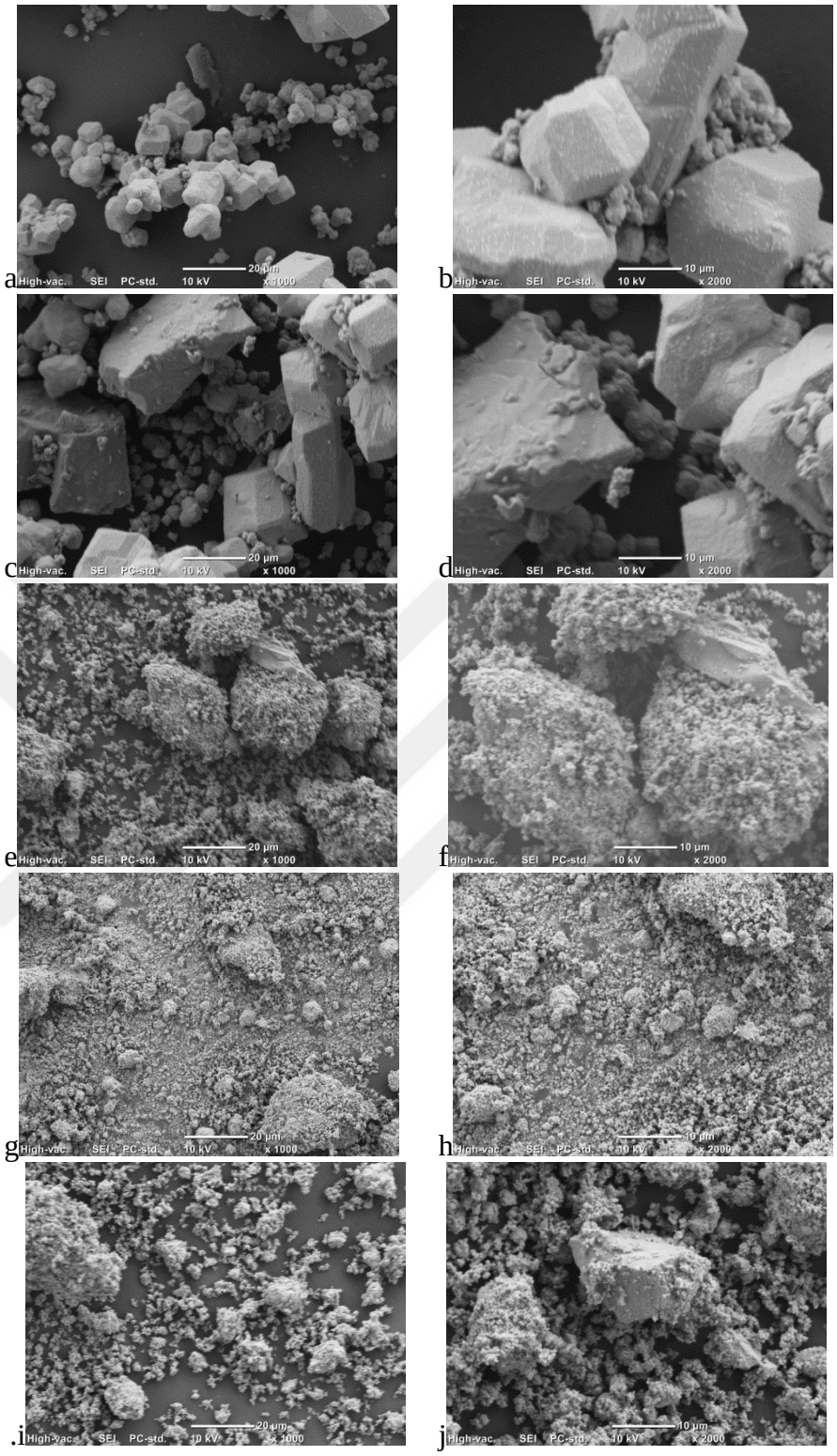

Figure 4.30 : Powder SEM Micrographs x1000: a- Pure W c- W-4%Ti MA0h e- W-4%Ti MA10h g- Pure W after 10 Pre-Milling (W^P) i- W^p-4%Ti MA0h k- W^P-4%Ti MA10h. x2000: b-Pure W d- W-4%Ti MA0h f- W-4%Ti MA10h h- Pure W after 10 Pre Milling (W^P) j- W^p-4%Ti MA0h l- W^P-4%Ti MA10h.

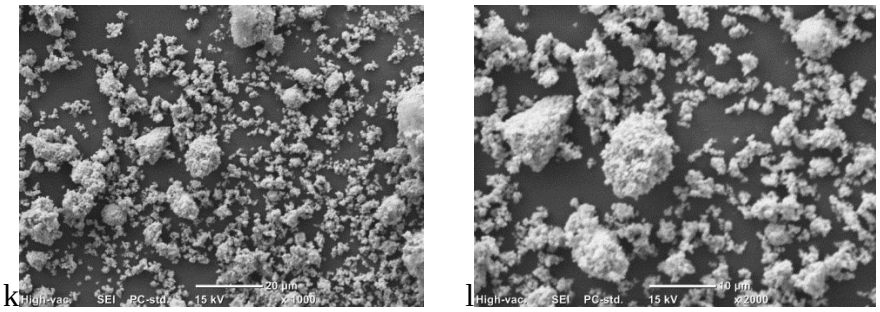

k l

Figure 4.30 (continoued) : Powder SEM Micrographs x1000: a- Pure W c- W-4%Ti MA0h e- W-4%Ti MA10h g- Pure W after 10 Pre-Milling (W^P) i- W^P-4%Ti MA0h k- W^P-4%Ti MA10h. x2000: b-Pure W d- W-4%Ti MA0h f- W-4%Ti MA10h h- Pure W after 10 Pre Milling (W^P) j- W^P-4%Ti MA0h l- W^P-4%Ti MA10h.

4.1.7. Powder analyzing by DTA-DSC

As shown in Figure 4-31, weight was not changed and was stable approximately. But in whole of composition there were wide endothermic peaks. It can predicted that it belong to the required energy during solid state sintering. Based on these figures 4.31 by increasing of Ti diffusion distance were decreased therefore peaks were smaller.

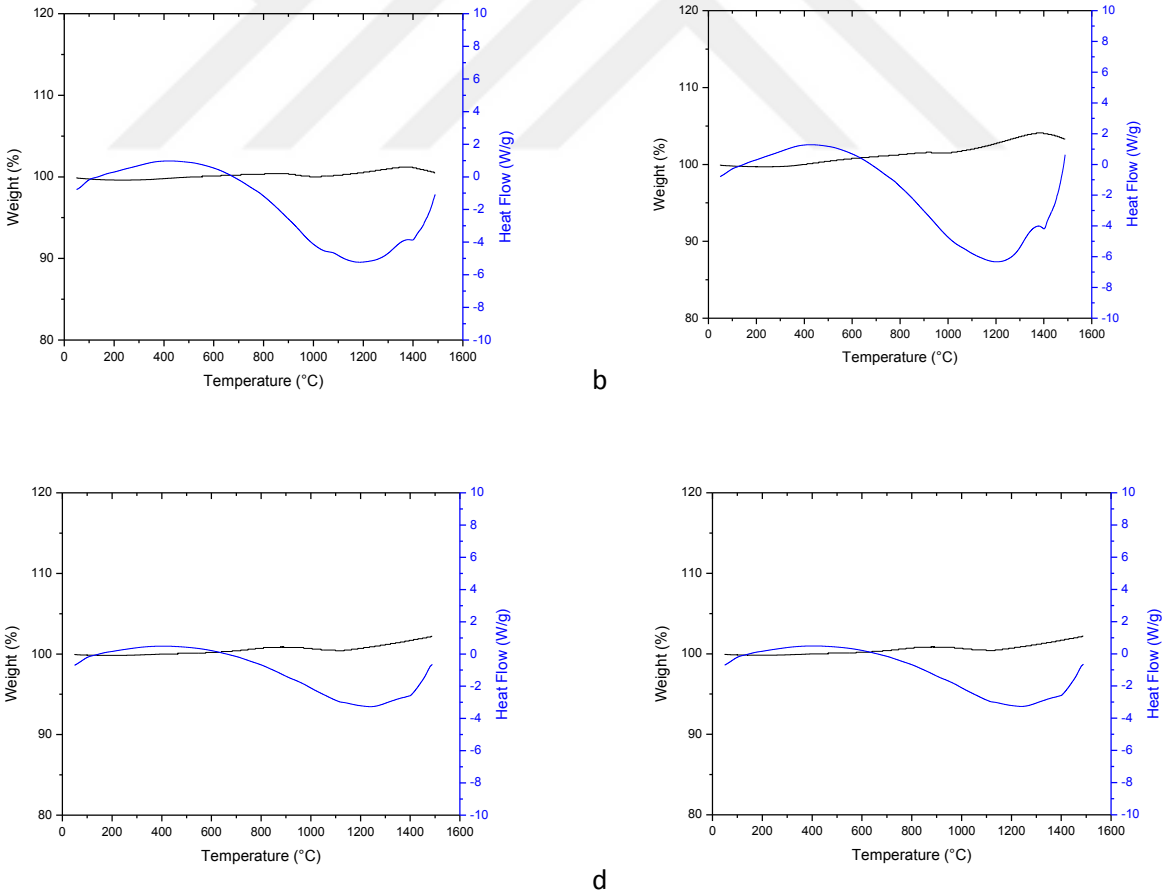

a b c d

Figure 4.31 : DTA-DSC diagrams of MA`d Powders a-W^P-0.5Ti, b- W^P-1.0Ti, c-W^P-4.0Ti, W^P-10.0Ti.

Based on these graphs 1400˚C -1500˚C can be suitable sintering temperature.

4.2. Powder Consolidation:

The mechanically alloyed powders were consolidated by two methods:

a) by cold pressing in a tool-steel die at a pressure of 400 MPa into cylinder shaped green compacts with a diameter of ≈6.36 mm for 1 minute by using a 3 ton. Then Sintering was performed for 1 hour in a Linn™ 1800 M Vac Graphite furnace under gas sintering conditions using vacuum and H_2, Ar and N_2 gases as sintering media. Finally, samples were sintered based on offered regime in Figure 3-9b.

b) Spark plasma sintering (SPS) experiments were performed by FCT Systeme™ HP D 25 SPS equipment. Powders were sintered at 1400˚C for 5 min with heating and cooling rates of 100˚C /min under an applied holding pressure of 50 MPa.

4.3. Sintering (Pressure less sintering (PLS) and Spark plasma sintering (SPS))

4.3.1. Pressure less sintering (PLS)

- W-0.5Ti MA`d conventional sintering

Figure 4-32 shows XRD patterns of W-0.5Ti MA`d after 1 h, 2 h, 4 h, 10 h and 20 h. After sintering of unmilled W with the lowest contents of Ti (0.5wt%) XRD pattern were not changed dramatically. Peaks width and their intensity were changed. After sintering, peaks got finer and their intensities increased. By increasing of MA time, the intensity of whole peaks got increased. 1400˚C and 1500˚C were examined for them but after sintering in both temperatures there were not appeared any new phase. In some patterns, WC phases were seen which can be estimated that they were removed via vials and balls.

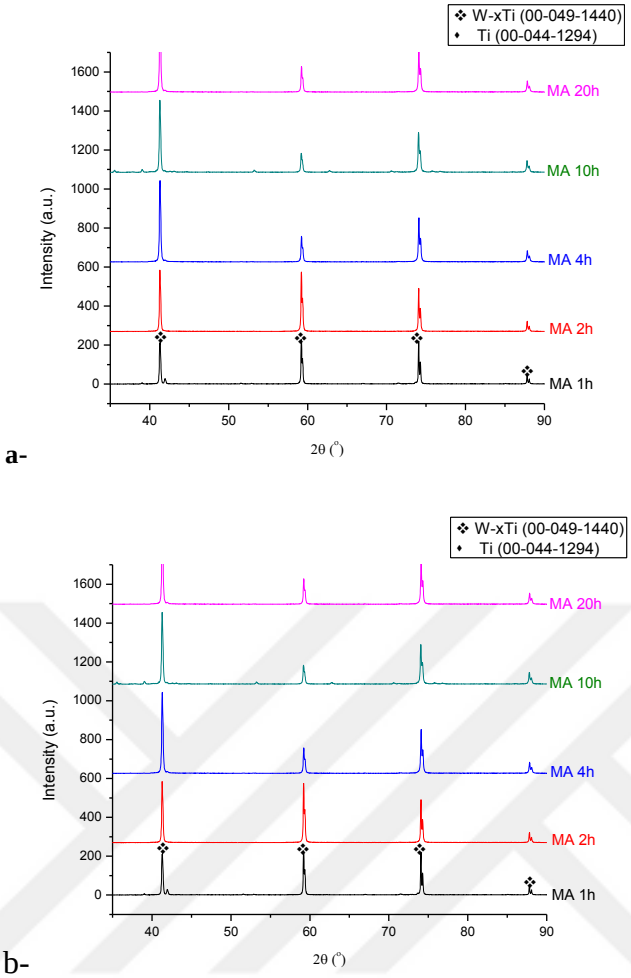

Figure 4.32 : XRD pattern of W-0.5Ti MA`d for 1, 2, 4, 10 and 20 h sintered by PLS at: a-1400°C b-1500°C.

In Table 4-15, values show that sintering were not completed however, by increasing of MA samples got denser besides, the densest samples were seen after sintering at 1500°C it means that increasing of temperature helped to the sintering phenomena however it is not enough for this composition.

Table 4.15 : sintered density of W -0.5Ti MA`d for 1, 2, 4, 10, and 20 h by PL sintering.

	Samples Name	Density (g/cm^3)	Relative Density (%)
1400˚C	W-0.5%Ti MA1h	15.21	80.12
	W-0.5%Ti MA2h	15.21	80.11
	W-0.5%Ti MA4h	15.43	81.28
	W-0.5%Ti MA10h	16.18	85.21
	W-0.5%Ti MA20h	16.19	85.24
1500˚C	W-0.5%Ti MA1h	15.24	80.29
	W-0.5%Ti MA2h	15.25	80.32
	W-0.5%Ti MA4h	15.53	81.78
	W-0.5%Ti MA10h	16.41	86.41
	W-0.5%Ti MA20h	16.37	86.23

As seen in Figure 4-33 after 20 h MA at 1500˚C samples were not sintered and they are green yet. The lighter regions are sintered positions and darker places remain green and sintering was not completed.

a b c

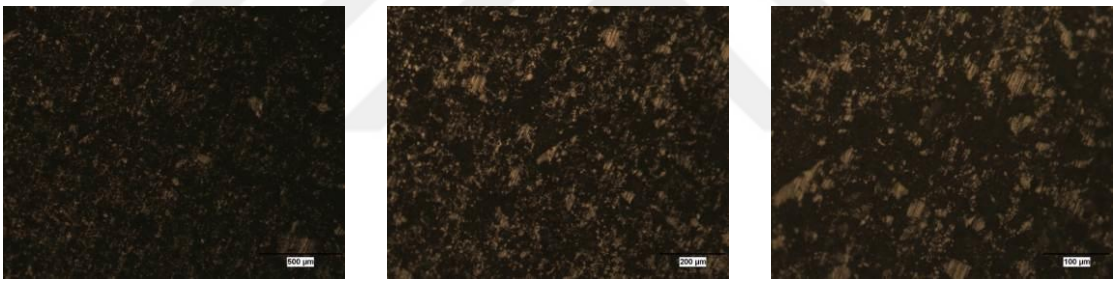

Figure 4.33 : Optical microscopy image of W-0.5%Ti MA 20h sintered at 1500°C by PL sintering. a- x50 b- x100 c- x200.

- W-1.0Ti MA`d conventional sintering

XRD pattern of PL sintered W-1.0Ti MA`d after 1, 2, 4, 10, and 20 h at 1400˚C 1500˚C are offered in Figure 4-34. After sintering of unmilled W with 1.0 wt% Ti XRD pattern were not changed too. Like 0.5 wt% Ti composition, peaks width got narrower and their intensity were increased after sintering. By increasing of MA duration samples behaved like primmer. By increasing of MA time, the intensity of whole peaks got increased. 1400˚C and 1500˚C were examined for this composition too however, after sintering in both temperatures, there were not appeared any new phase.

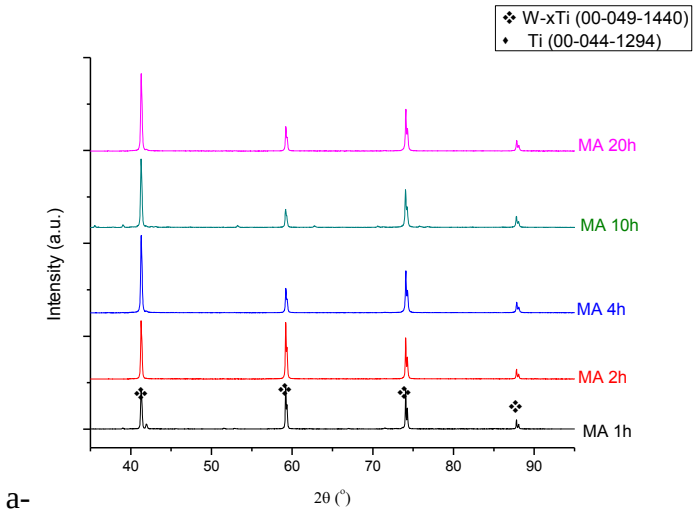

a-

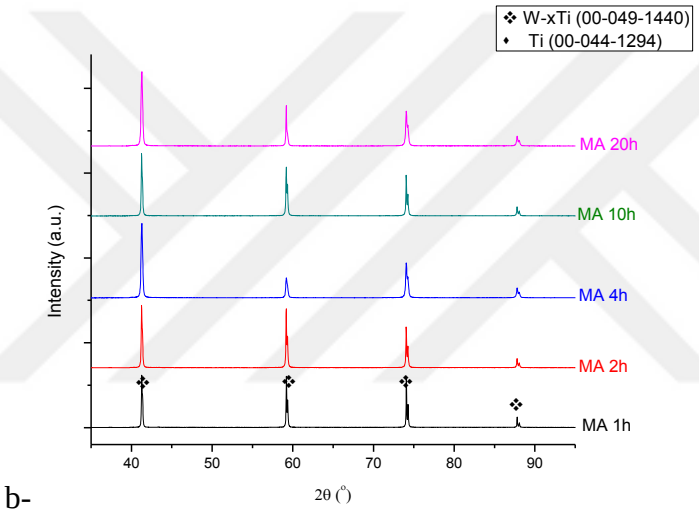

b-

Figure 4.34 : XRD pattern of W -1.0Ti MA`d for 1, 2, 4, 10, and 20 h sintered by PLS at: a-1400°C b-1500°C.

Sintering was not completed that was shown in Table 4-16. However, by increasing of MA time, samples got denser. Besides, the denser samples were seen after sintering at 1500°C. It means that increasing of temperature helped to the sintering phenomena however, it is not enough for this composition too. Comparing W-0.5Ti and W-1.0Ti showed that increasing of Ti amount helped sintering and samples with more Ti were denser as in the same sintering regime.

Table 4.16 : sintered density of W -1.0Ti MA`d for 1, 2, 4, 10, and 20 h by PL sintering.

	Samples Name	Density (g/cm^3)	Relative Density (%)
1400˚C	W-1.0%Ti MA1h	14.98	80.14
	W-1.0%Ti MA2h	14.98	80.16
	W-1.0%Ti MA4h	15.14	81.04
	W-1.0%Ti MA10h	15.90	85.1
	W-1.0%Ti MA20h	16.00	85.65
1500˚C	W-1.0%Ti MA1h	15.18	81.26
	W-1.0%Ti MA2h	15.18	81.23
	W-1.0%Ti MA4h	15.39	82.34
	W-1.0%Ti MA10h	16.01	85.67
	W-1.0%Ti MA20h	16.05	85.89

As seen in Figure 4-35 after 20 h MA at 1500°C samples were not sintered and they are green yet. Some positions are lighter which are sintered and the dark regions are green. The lighter position rate is increased by increasing of Ti amounts.

a b c

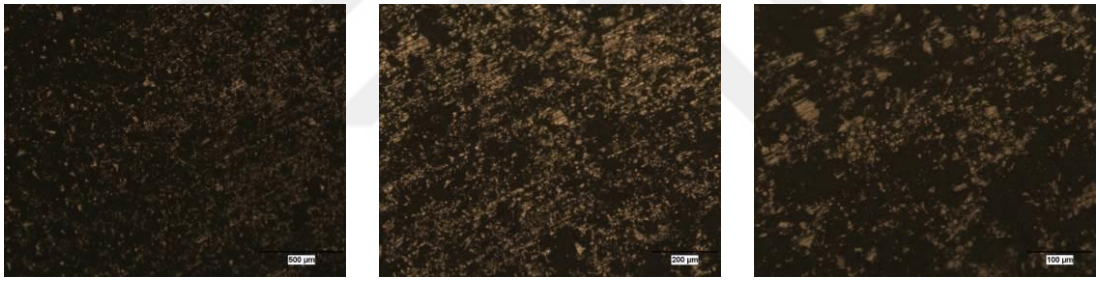

Figure 4.35 : Optical microscopy image of W-1.0 %Ti MA 20h sintered at 1500°C by PL sintering. a- x50 b- x100 c- x200.

- W-4.0Ti MA`d conventional sintering

At Figure 4-36, XRD pattern of PL sintered W -4.0Ti MA`d after 1, 2, 4, 10, and 20 h at 1400˚C and 1500˚C are shown. After sintering of unmilled W with 4.0 wt% Ti, XRD patterns were not changed too. By sintering, like 0.5 and 1.0 wt% Ti composition, peaks width got narrower and their intensity were increased. Although, Ti amounts were increased but Ti peaks were not appeared yet. Only W peaks were seen and some of WC peaks were released. It can be estimated that Ti were solved in W lattice. By increasing of MA duration samples behaved like compositions with lower Ti amounts. By increasing of MA time, the intensity of whole peaks got increased. 1400˚C and 1500˚C sintering temperature were performed on this

composition too however, after sintering in both temperatures, there were not appeared any new phase.

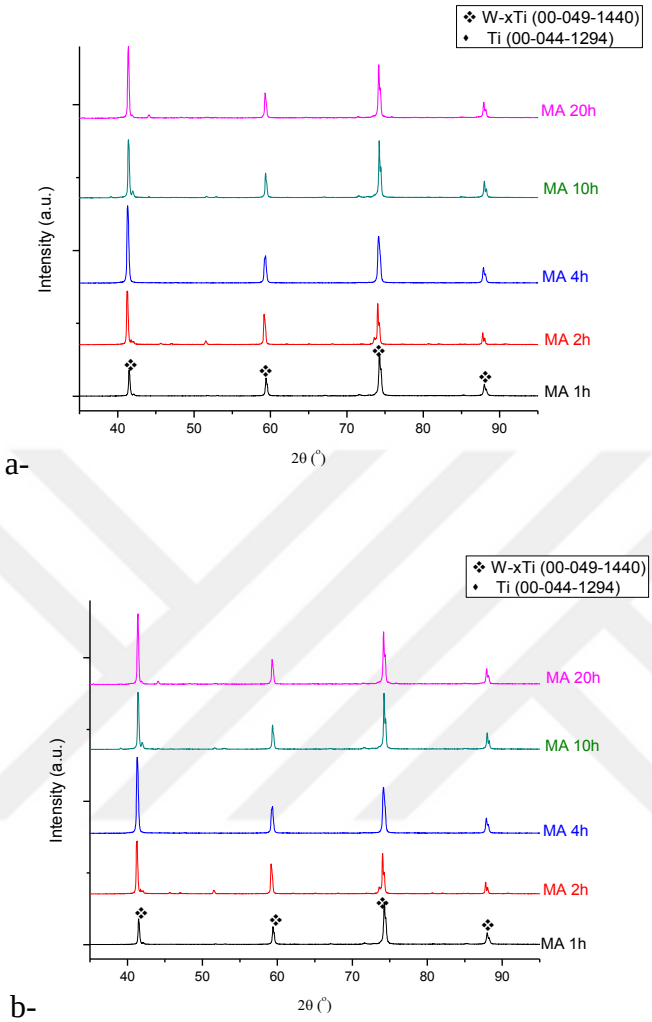

Figure 4.36 : XRD pattern of W -4.0Ti MA`d for 1, 2, 4, 10, and 20 h sintered by PLS at: a-1400°C b-1500°C.

As shown in Table 4-17, samples were not sintered however, increasing of Ti aids sintering. Maximum density was caught at 1500°C too. Besides, the denser samples were seen after sintering at 1500˚C. It means that increasing of temperature helped to the sintering phenomena however it is not enough for this composition yet. Comparing with composition with lower Ti amounts, shows that increasing of Ti amount helped sintering and samples with more Ti were denser in the same sintering temperature.

Table 4.17 : Sintered density of W -4.0Ti MA`d for 1,2,4,10,and 20 h by PL sintering.

	Samples Name	Density (g/cm^3)	Relative Density (%)
1400˚C	W-4.0%Ti MA1h	14.36	84.2
	W-4.0%Ti MA2h	14.44	84.67
	W-4.0%Ti MA4h	14.57	85.39
	W-4.0%Ti MA10h	15.03	88.1
	W-4.0%Ti MA20h	15.03	88.12
1500˚C	W-4.0%Ti MA1h	14.58	85.44
	W-4.0%Ti MA2h	14.66	85.93
	W-4.0%Ti MA4h	14.71	86.22
	W-4.0%Ti MA10h	15.20	89.1
	W-4.0%Ti MA20h	15.37	90.12

As seen in Figure 4-37 after 20 h MA at 1500˚C samples were sintered partially too. Some parts with lighter zones are sintered positions. Black zones were decreased and sintering area was increased.

a b c

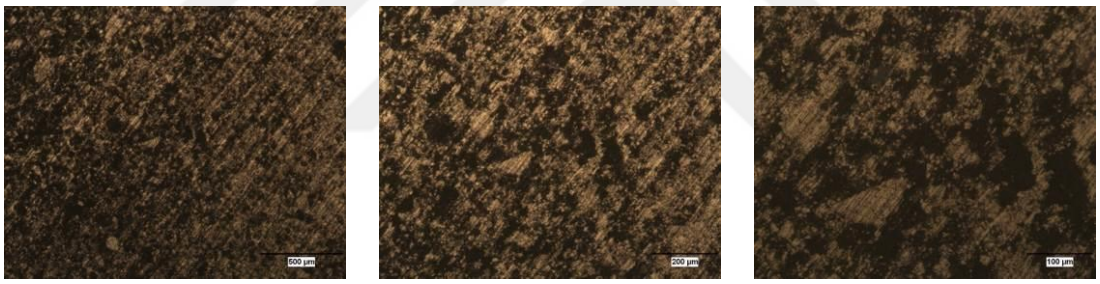

Figure 4.37 : optical microscopy image of W-4.0 %Ti MA 20h sintered at 1500°C by sintering a- x50 b- x100 c- x200.

- W-10.0Ti MA`d conventional sintering

Figure 4-38 shows XRD pattern of W-10Ti MA'd after 1, 2, 4, 10 and 20h and sintered conventionally at 1400˚C and 1500˚C. Unmilled W with 10.0 wt% Ti XRD pattern was not changed too. Like 0.5, 1.0 and 4.0 wt% Ti composition peaks width got narrower and their intensity were increased. Although, Ti amounts were increased too but Ti peaks were not appeared yet. Only W peaks were seen and some of WC peaks were released. It can be estimated that Ti were solved in W lattice and lattice parameters were increased it can be detected via peaks movements. By increasing of MA duration samples behaved like primmer. By increasing of MA time, the intensity of whole peaks got increased. 1400˚C and 1500˚C were examined

for this composition too however, after sintering in both temperatures, there were not appeared any new phase.

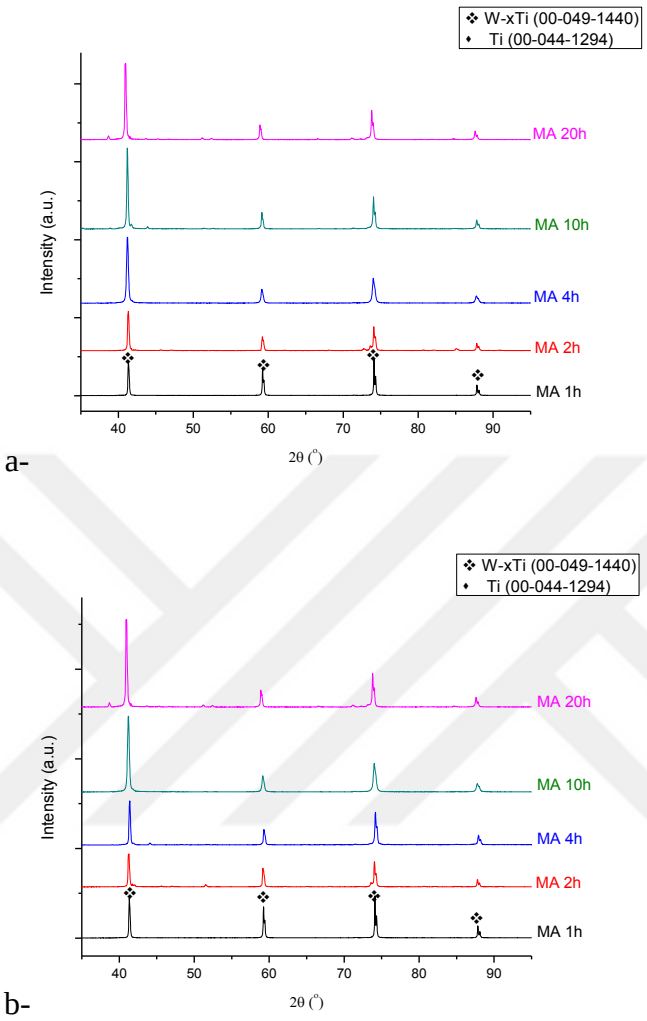

Figure 4.38 : XRD pattern of W -10.0Ti MA`d for 1, 2, 4, 10, and 20 h sintered by PLS at: a-1400°C b-1500°C.

As shown in Table 4-18 10.0% samples were not sintered completely however, increasing of Ti aids sintering. Besides, the denser samples were seen after sintering at 1500°C. It means that increasing of temperature helped to the sintering phenomena however it is not enough for this composition too. Comparing with lower amounts of added activators,shows that increasing of Ti amounts helped sintering and samples with more Ti were denser.

Table 4.18 : Sintered density of W-10.0Ti MA`d for 1, 2, 4, 10, and 20 h by PL sintering.

	Samples Name	Density (g/cm^3)	Relative Density (%)
1400˚C	W-10.0%Ti MA1h	12.28	84.52
	W-10.0%Ti MA2h	12.36	85.09
	W-10.0%Ti MA4h	12.37	85.11
	W-10.0%Ti MA10h	12.78	87.98
	W-10.0%Ti MA20h	12.82	88.23
1500˚C	W-10.0%Ti MA1h	12.44	85.6
	W-10.0%Ti MA2h	12.46	85.73
	W-10.0%Ti MA4h	12.67	87.19
	W-10.0%Ti MA10h	13.10	90.14
	W-10.0%Ti MA20h	13.14	90.45

As shown in Figure 4-39 after 20 h MA at 1500°C samples were sintered partially too. Some parts with lighter zones are sintered positions. Darker zones were decreased and sintering area was increased. By applying polishing, darker regions as original powders were taken apart and porous matrix was gotten.

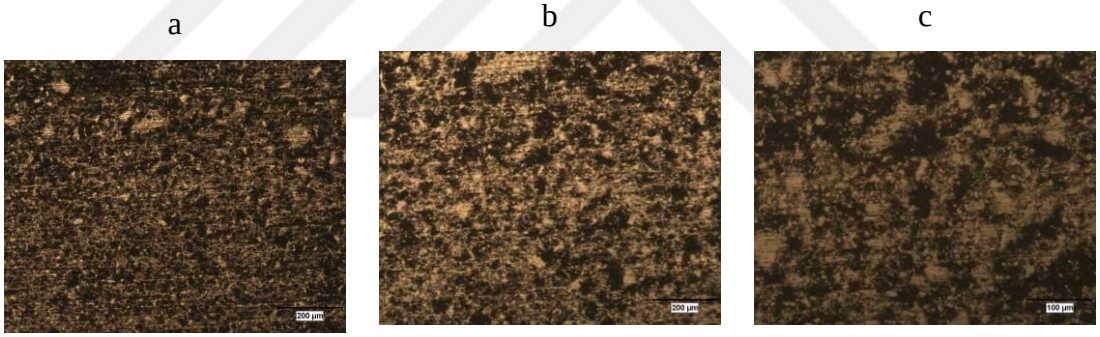

Figure 4.39 : Optical microscopy image of W-10.0 %Ti MA 20h sintered at 1500°C by PL sintering.a- x50 b- x100 c- x200.

- W^p-0.5Ti MA`d conventional sintering

Figure 4-40 shows XRD pattern of Wp -0.5Ti MA'd for 1, 2, 4, 10, and 20 h sintered conventionally at 1400˚C and 1500˚C. 10 h pre-milled W with 0.5 wt% Ti XRD pattern was sharper and narrower. Because of low amounts of Ti, its peaks were not appeared. Only W peaks were seen and some of WC peaks were released. It can be estimated that Ti were solved in W lattice and lattice parameters were increased it can be detected via peaks movement to the low values of 2θ. By increasing of MA time, the intensity of peaks got increased. 1400°C and 1500°C were examined for

this composition too however, after sintering in both temperatures, there were not appeared any new phase.

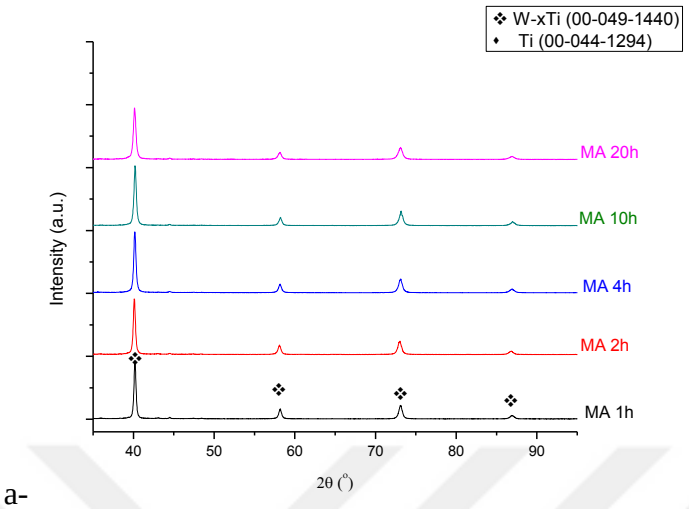

a-

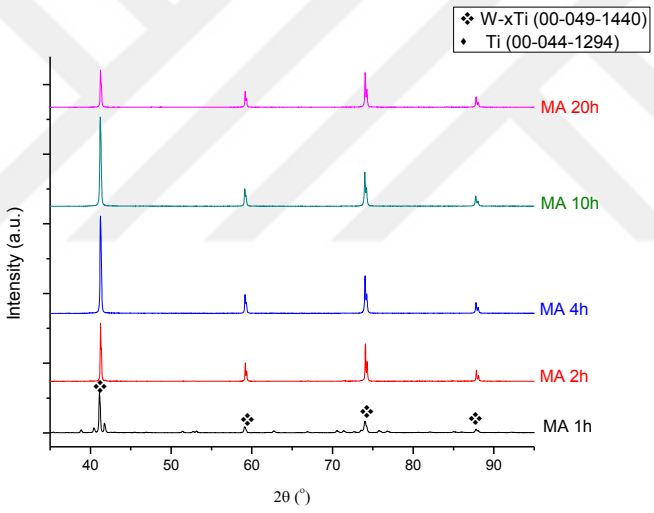

b-

Figure 4.40 : XRD pattern of W^p -0.5Ti MA`d for 1, 2, 4, 10, and 20 h sintered by PLS at: a-1400°C b-1500°C.

Densities of samples were increased by mechanical alloying and increasing of sintering temperature these data are offered in Table 4-19. Wp-0.5%Ti after 10 h MA has the most density values meantime, as shown in Table 4-19 increasing temperature led to increment of density too. Archimedes densities were smaller than pycnometric density. Archimedes density was measured in water medium and pycnometric density was measured in He atmosphere. Density values of samples MA'd after 20 h is smaller than samples MA'd 10 h.

Table 4.19 : Sintered density of W^p-0.5 Ti MA`d for 1, 2, 4, 10, and 20 h sintered by PLS.

	Samples Name	Archimedes density (g/cm^3)	Pycnometeric Density (g/cm^3)	Relative Density (%)
1400˚C	W^p-0.5%Ti MA 1h	17.84	17.86	94.04
	W^p-0.5%Ti MA 2h	17.87	17.90	94.22
	W^p-0.5%Ti MA 4h	17.92	17.95	94.54
	W^p-0.5%Ti MA 10h	18.59	18.63	98.1
	W^p-0.5%Ti MA 20h	18.44	18.48	97.31
1500˚C	W^p-0.5%Ti MA 1h	17.85	17.87	94.11
	W^p-0.5%Ti MA 2h	17.88	17.91	94.32
	W^p-0.5%Ti MA 4h	17.91	17.96	94.61
	W^p-0.5%Ti MA 10h	18.61	18.65	98.21
	W^p-0.5%Ti MA 20h	18.45	18.49	97.36

By increasing MA duration, hardness was increased like density and hardness was declined after 10 h MA. Gain growth in samples with longer MA duration starts sooner so hardness has decreased drastically. As shown in Figure 4-41 during hardness test, 30 places of samples were analyzed. Increasing sintering temperature increased hardness standard deviation but hardness values were approximately the same.

a- b-

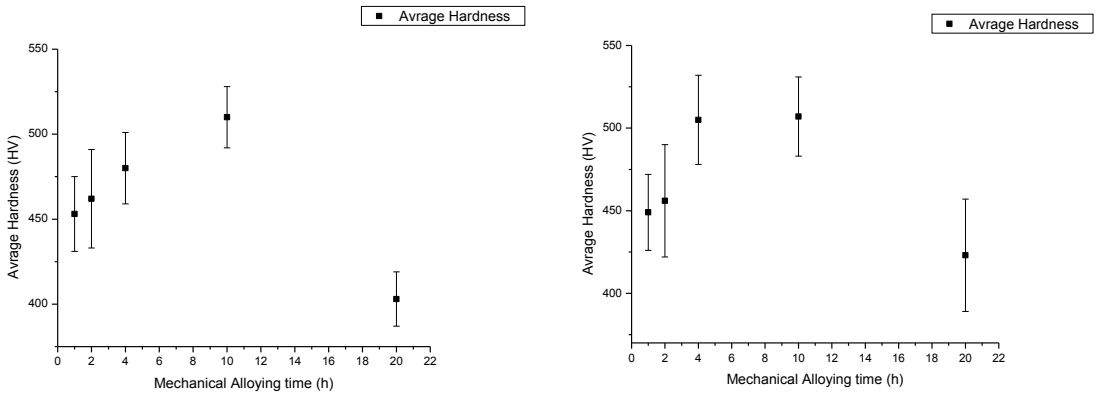

Figure 4.41 : Micro Vickers hardness of W^p -0.5 Ti MA`d for 1, 2, 4, 10, and 20 h sintered by PLS. at: a-1400°C b-1500°C.

- W^p-1.0Ti MA`d conventional sintering

As shown in Figure 4-42, 10 h pre-milled W with 1.0 wt% Ti XRD pattern was sharper and narrower like when W^p-0.5Ti in same condition. Because of low amounts of Ti, Ti peaks were not appeared too. Only W peaks were seen and some of

WC peaks which were added during MA were released. It can be estimated that Ti were solved in W lattice and lattice parameters were enlarged it can be detected via peaks movement to the lower values of 2θ. By increasing of MA time, the intensity of peaks got increased. Samples were sintered at1400°C and 1500°C, after sintering in both temperatures, there were not appeared any new phase yet.

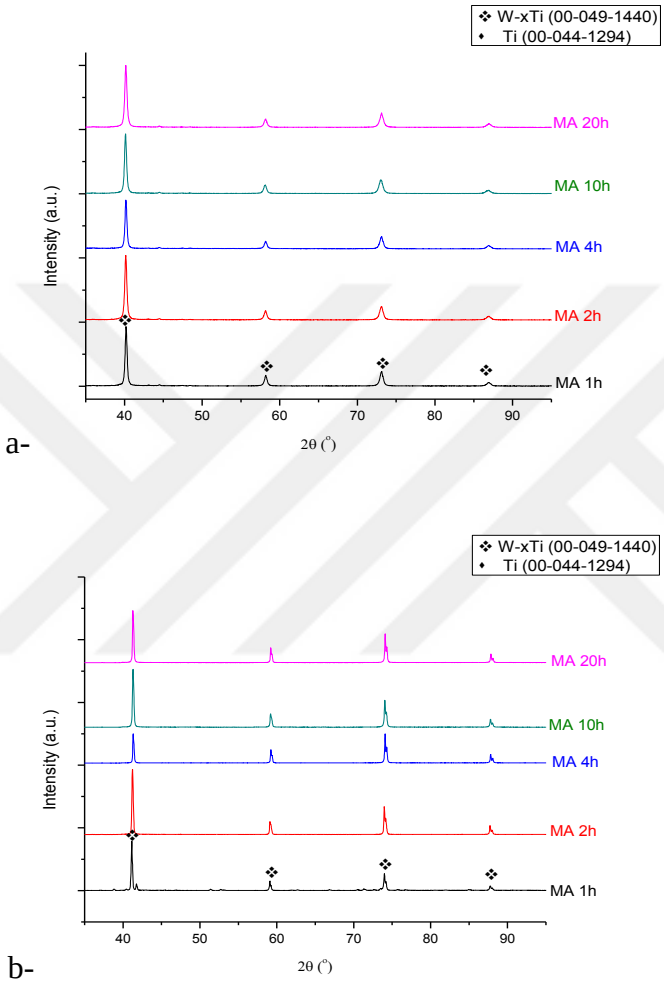

Figure 4.42 : XRD pattern of W^p -1.0Ti MA`d for 1, 2, 4, 10, and 20 h sintered by PLS.at: a-1400°C b-1500°C

Same as W^P-0.5Ti composition, densities of W^p-1.0%Ti samples were increased by mechanical alloying and increasing of sintering temperature. W^P-1.0Ti after 20 h MA had the most density values meantime, as shown in Table 4-20, increasing temperature led to increment of density too.

Table 4.20 : Sintered density of W^p -1.0 Ti MA`d for 1, 2, 4, 10, and 20 h sintered by PLS.

	Samples Name	Archimedes density (g/cm^3)	Pycnometeric Density (g/cm^3)	Relative Density (%)
1400˚C	W^p-1.0%Ti MA 1h	17.50	17.55	93.9
	W^p-1.0%Ti MA 2h	17.59	17.62	94.3
	W^p-1.0%Ti MA 4h	17.67	17.73	94.86
	W^p-1.0%Ti MA 10h	18.19	18.23	97.54
	W^p-1.0%Ti MA 20h	18.25	18.30	97.91
1500˚C	W^p-1.0%Ti MA 1h	17.55	17.60	94.2
	W^p-1.0%Ti MA 2h	17.63	17.65	94.43
	W^p-1.0%Ti MA 4h	17.62	17.63	94.37
	W^p-1.0%Ti MA 10h	18.23	18.25	97.68
	W^p-1.0%Ti MA 20h	18.23	18.31	98.01

As increasing MA duration, hardness was increased like density and hardness was declined after 10 h MA too. Gain growth in samples with longer MA duration starts sooner so hardness has decreased drastically it was shown in Figure 4-43. During hardness test, 30 places of samples were analyzed. By increasing sintering temperature, hardness standard deviation increased too but hardness values were approximately the same too.

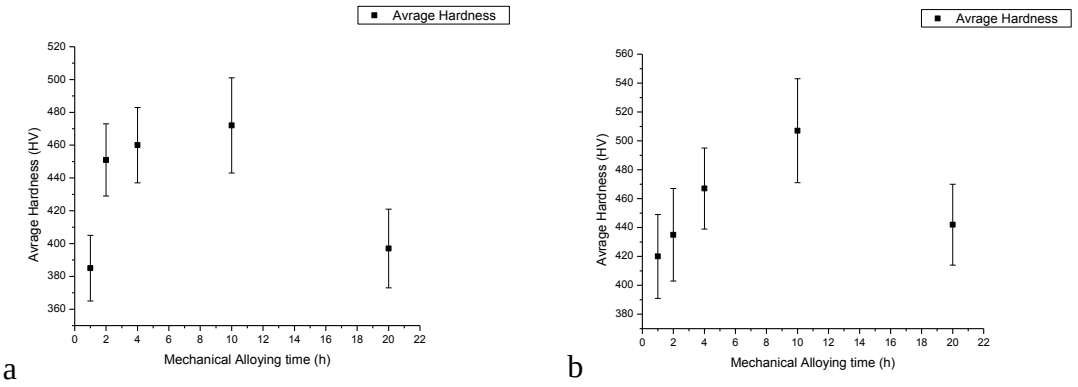

a b

Figure 4.43 : Micro Vickers hardness of W^p-1.0 Ti MA`d for 1, 2, 4, 10, and 20 h sintered by PLS. at: a-1400°C b-1500°C

- W^p-4.0Ti MA`d conventional sintering

As shown in Figure 4-44 XRD peaks after sintering at 1400°C and 1500°C were completely belong to the W and any peaks of Ti were not seen. Peaks were shifted to the lower degrees. Ti atomic radios is larger than W so when Ti placed in W structure, lattice parameters were enlarged which it related to the XRD peaks

movement to the lower positions. Positions of peaks based on sintering temperature were approximately the same.

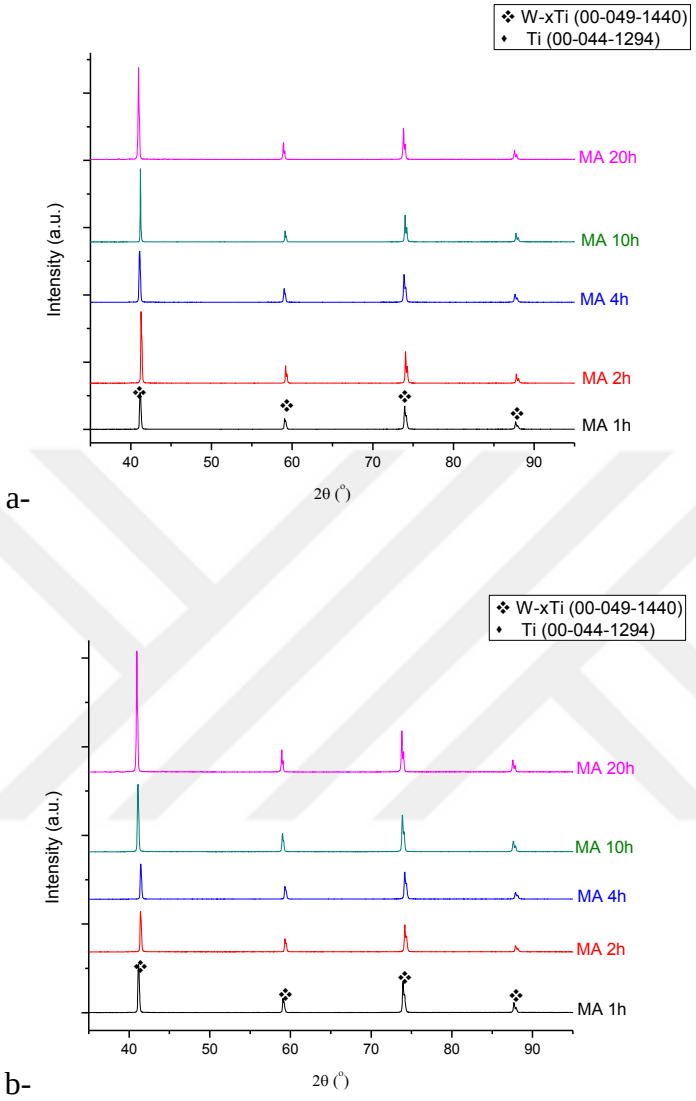

Figure 4.44 : XRD pattern of W^p-4.0Ti MA`d for 1, 2, 4, 10, and 20 h sintered by PLS: a-1400°C b-1500°C

By increasing of Ti amounts density of samples were decreased but relative density were increased meantime, densities of samples were increased by MA time and sintering temperature increasing. The denser samples were gotten by W^p-4.0%Ti after 10 h MA furthemore, as shown in Table 4-21, relative density values show that W^p-4.0Ti after 10 h MA was the densest.

Table 4.21 : Sintered density of W^P -4.0 Ti MA`d for 1, 2, 4, 10, and 20 h by PL sintering.

	Samples Name	Archimedes density (g/cm^3)	Pycnometeric Density (g/cm^3)	Relative Density (%)
1400˚C	W^P-4.0%Ti MA1h	15.58	16.07	94.21
	W^P-4.0%Ti MA2h	15.58	16.08	94.27
	W^P-4.0%Ti MA4h	16.25	16.36	95.87
	W^P-4.0%Ti MA10h	16.74	16.78	98.35
	W^P-4.0%Ti MA20h	16.55	16.58	97.19
1500˚C	W^P-4.0%Ti MA1h	15.58	16.09	94.31
	W^P-4.0%Ti MA2h	15.59	16.15	94.67
	W^P-4.0%Ti MA4h	16.33	16.38	96.02
	W^P-4.0%Ti MA10h	16.76	16.78	98.37
	W^P-4.0%Ti MA20h	16.54	16.58	97.18

Like density values by increasing MA duration, hardness was increased and hardness was declined after 10 h MA too. Grain growth in samples with longer MA duration starts sooner so hardness has decreased drastically. During hardness test, 30 places of samples were analyzed. Increasing sintering temperature increased hardness standard deviation but hardness values were approximately the same too. Ti has positive effects on the hardness of samples. As shown in Figure 4-45 samples after 4 h MA hardness is near to the samples with 10 h MA.

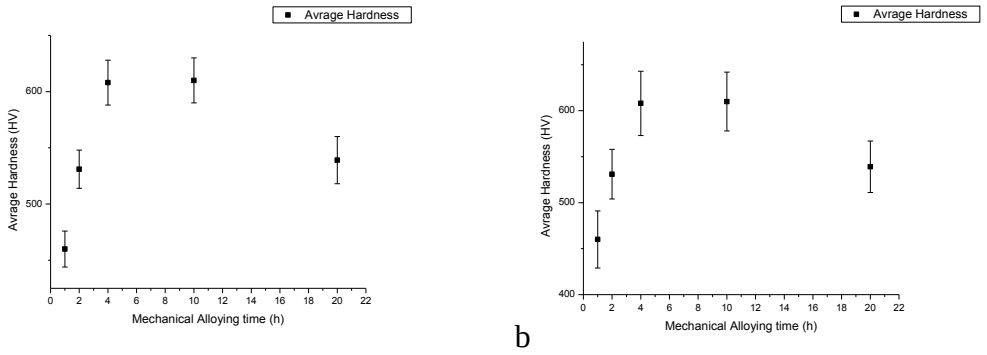

a b

Figure 4.45 : Micro Vickers hardness of W^p -4.0 Ti MA`d for 1, 2, 4, 10, and 20 h sintered by PLS at: a-1400°C b-1500°C.

- W^P-10.0Ti MA`d conventional sintering

As shown in Figure 4-46, whole of XRD peaks of sintered samples at 1400°C and 1500°C temperature are belong to the W and Ti XRD peaks were not seen. Whole of Peaks were shifted to the lower degrees. As before mentioned Ti has larger radios than W so when Ti atoms were located in W structure, lattice crystal structure were

enlarged. Based on crystal structure enlargement, the XRD peaks shifted to the lower positions. Sintering temperature has not effects of peaks positions.

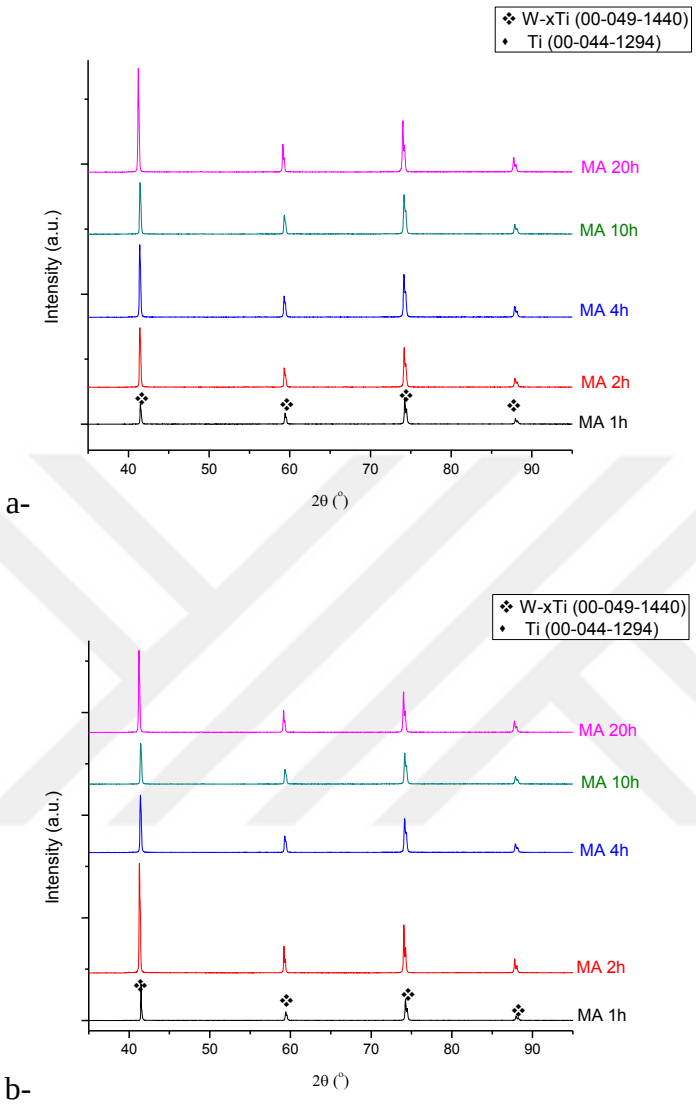

Figure 4.46 : XRD pattern of Wp -10.0Ti MA`d for 1, 2, 4, 10, and 20 h sintered by PLS at: a-1400°C b-1500°C.

By increasing of Ti amounts Archimedes density values and Pycnometeric density values of samples were decreased because of lower density of Ti. In samples with the same compositions, density where increased by MA duration as shown Pycnometric density increased from 13.7334(g/cm3) and 13.7508(g/cm3) after 1 h MA and sintering at 1400˚C and 1500˚C to 14.0806(g/cm3) and 14.1199(g/cm3) after 10 h MA and sintering at 1400°C and 1500°C respectively. Based on MA time, it can be known that relative densities of samples were increased by MA and increasing of sintering temperature. The samples with higher density were gotten by Wp-10.0%Ti

after 10 h MA meantime, as shown in Table 4-22, increasing temperature led to increment of density. Relative density comparing shows that W^p-10.0%Ti after 10 h MA is the densest.

Table 4.22 : Sintered density of W^p -10.0 Ti MA`d for 1, 2, 4, 10, and 20 h by PL sintering.

	Samples Name	Archimedes density (g/cm^3)	Pycnometeric Density (g/cm^3)	Relative Density (%)
1400˚C	W^p-10.0%Ti MA1h	13.72	13.73	94.52
	W^p-10.0%Ti MA2h	13.76	13.8002	94.98
	W^p-10.0%Ti MA4h	13.80	13.85	95.32
	W^p-10.0%Ti MA10h	13.97	14.08	96.91
	W^p-10.0%Ti MA20h	13.97	14.03	96.58
1500˚C	W^p-10.0%Ti MA1h	13.74	13.75	94.64
	W^p-10.0%Ti MA2h	13.77	13.83	95.16
	W^p-10.0%Ti MA4h	13.83	13.87	95.45
	W^p-10.0%Ti MA10h	14.04	14.12	97.18
	W^p-10.0%Ti MA20h	13.99	14.07	96.85

By MA time increasing in Figure 4-47, hardness was increased till 10h like density and hardness was declined after 10 h MA too. Grain growth in samples with longer MA duration starts sooner so hardness has decreased drastically. Increasing sintering temperature increased hardness standard deviation but hardness values were decreased. Ti amount increment led to highest hardness of samples shifted to the lower MA duration.

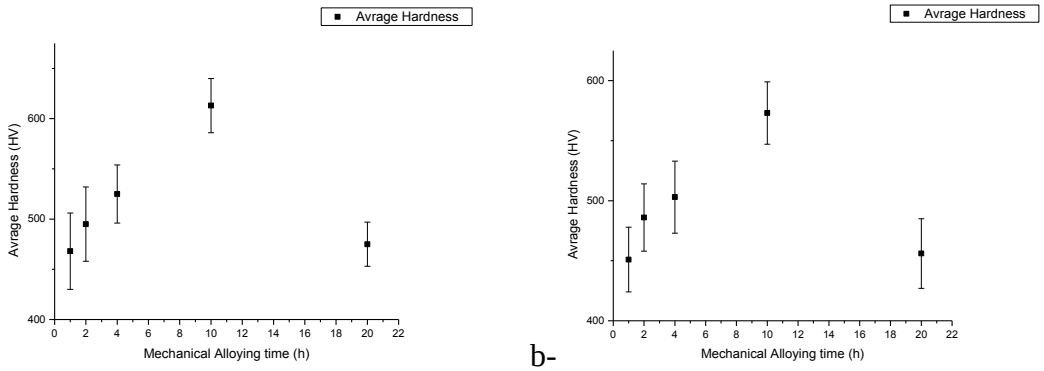

a- b-

Figure 4.47 : Micro Vickers hardness of W^p -10.0 Ti MA`d for 1, 2, 4, 10, and 20 h sintered by PLS at: a-1400°C b-1500°C.

- W^P-0.5Ti-2.0LaB_6 MA`d conventional sintering

XRD patterns of samples sintered at two different temperatures shows that there are not any new phases after sintering. The WC XRD peaks seem increased it can be cause of LaB_6 which used as second phase. During MA, WC particles may be abraded and LaB_6 powders help WC balls to be abraded more. It was detected during MA process. WC balls weighted before MA and after MA are weighted. Ball weight were lost 0.12 percent after 20h when in compositions without LaB_6 but when LaB_6 were added weight lost rate was more and equal 0.22 percent after 20h. Ti amounts did not any special effects on balls abrasion. Figure 4-48 shows XRD pattern of W^P-0.5Ti-2.0LaB_6 and sintered at 1400˚C and 1500˚C. as shown in Figure 4-48 Ti and Lab_6 peaks were not seen only WC Peaks were appeared which added because of balls erosion, abrasion and friction.

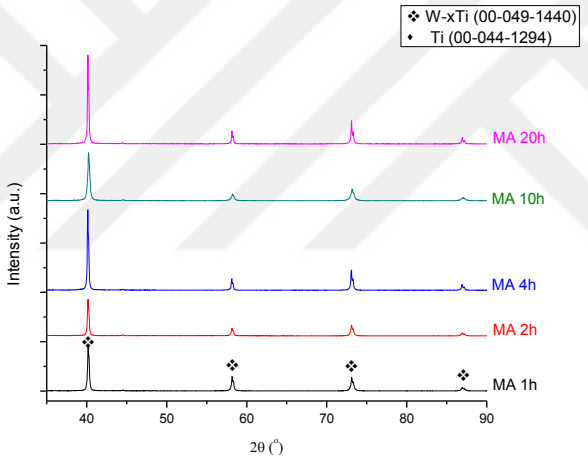

a

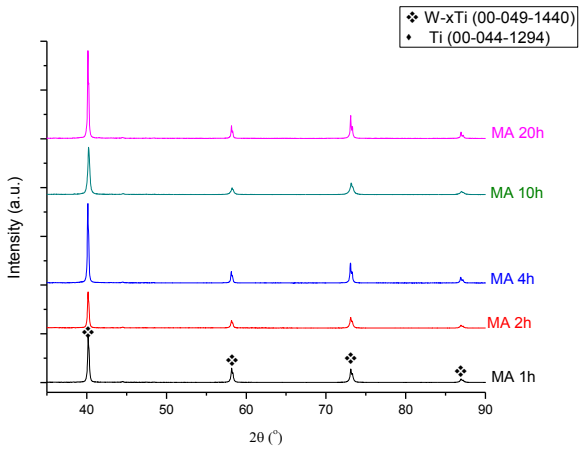

b

Figure 4.48 : XRD pattern of W^p -0.5Ti -2,0LaB_6 MA`d for 1, 2, 4, 10, and 20 h sintered by PLS at: a-1400°C b-1500°C.

Table 4-23 shows density results of sintered samples at 1400˚C and 1500˚C. LaB_6 addition, was led to density declining because of lower density of LaB_6 meantime, relative density of sintered samples were decreased too. LaB_6 particles restricted solidification and particle diffusions. MA time increment causes to increasing of density values. The densest samples were produced after 10 h MA. Furthermore, samples with LaB_6 have lower density and relative density than same samples without LaB_6 in the same conditions. Besides, calculated Archimedes density in water was smaller than Pycnometric density. He gas because of small volume can penetrate into the open porous easily so measured Pycnometric densities were larger than Archimedes density.

Table 4.23 : Sintered density of W^p -0.5Ti -2,0LaB_6 MA`d for 1, 2, 4, 10, and 20 h by PL sintering.

	Samples Name	Archimedes density (g/cm^3)	Pycnometeric Density (g/cm^3)	Relative Density (%)
1400˚C	Wp-0.5Ti-2.0LaB6 MA1h	15.57	15.61	86.78
	Wp-0.5Ti-2.0LaB6 MA2h	16.67	16.80	93.4
	Wp-0.5Ti-2.0LaB6 MA4h	16.88	17.05	94.81
	Wp-0.5Ti-2.0LaB6 MA10h	17.50	17.53	97.45
	Wp-0.5Ti-2.0LaB6 MA20h	16.72	16.74	93.09
1500˚C	Wp-0.5Ti-2.0LaB6 MA1h	15.60	15.62	86.88
	Wp-0.5Ti-2.0LaB6 MA2h	16.60	16.63	92.45
	Wp-0.5Ti-2.0LaB6 MA4h	16.94	17.07	94.9
	Wp-0.5Ti-2.0LaB6 MA10h	17.51	17.54	97.51
	Wp-0.5Ti-2.0LaB6 MA20h	16.74	16.78	93.33

Figure 4-49 shows the micro vickers hardness values of PL sintered samples. Microhardness values are increased during 10 h MA and decreased after 10 h. By increasing sintering temperature, microhardness of samples was decreased. The maximum micro Vickers hardness were measured after 10h MA 548±51 and 512±43 at 1400°C and 1500°C sintering temperatures respectively. LaB_6 addition was led to increment of hardness values. As increasing MA duration, hardness was increased like density and hardness was declined after 10 h MA too. Grain growth of samples with longer MA duration (after 10h) initiates sooner so hardness decreases drastically. Increasing sintering temperature decreased hardness because of grain growth.

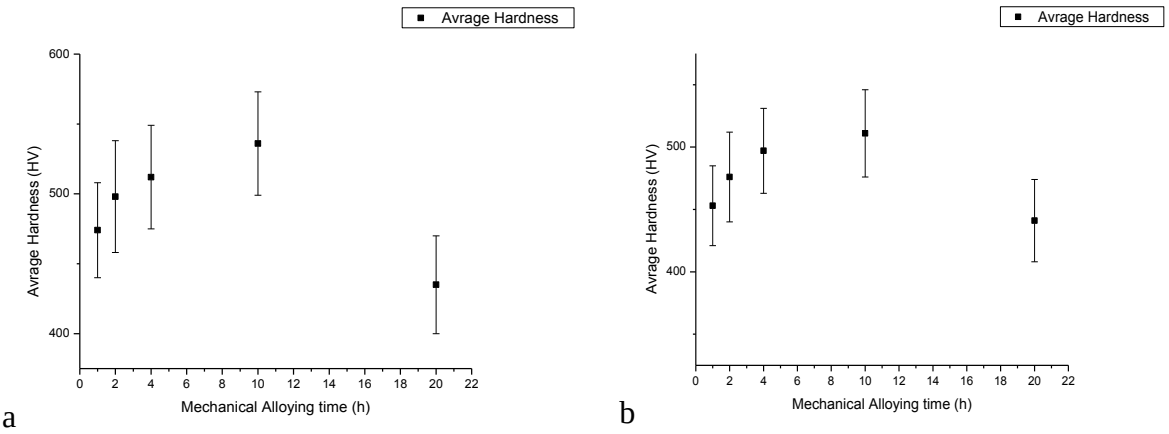

Figure 4.49 : Micro Vickers hardness of W^p -0.5 Ti -2,0 LaB_6 MA`d for 1, 2, 4, 10, and 20 h sintered by PLS. at: a-1400°C b-1500°C.

- W^P-1.0Ti-2.0LaB_6 MA`d conventional sintering

Figure 4-50 shows XRD patterns of W^P-1.0Ti-2.0LaB_6 and sintered at 1400˚C and 1500˚C. Studying of samples XRD patterns shows that like compositions without LaB_6, there are not any new phases. After sintering, WC XRD peaks seems increased it can because of LaB_6 which used as second phase. During MA, WC particles was abraded and LaB_6 powders helped WC balls to be abraded more. It was detected during MA process. WC ball weighted before MA and after it. Ball weight were lost 0.12 percent after 20h when in compositions without LaB_6 but when LaB6 were added weight lost rate was more and equal 0.23 percent after same time. Ti amounts did not any special effects on balls abrasion.

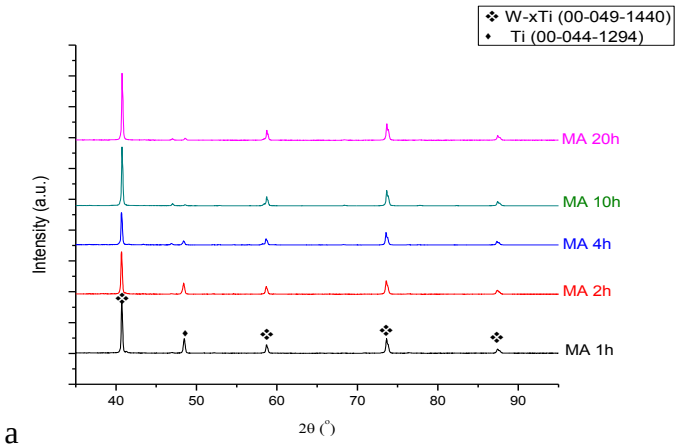

a

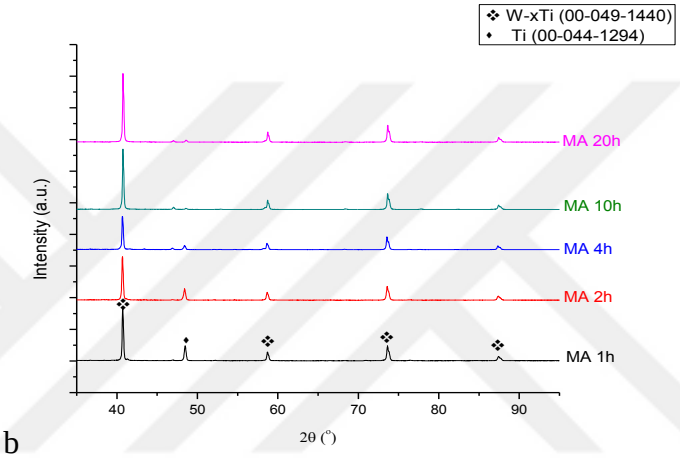

b

Figure 4.50 : XRD pattern of W^P -1.0Ti -2,0LaB_6 MA`d for 1, 2, 4, 10, and 20 h sintered by PLS.at:a-1400°C b-1500°C.

Archimedes density, Pycnometeric density and relative density of W^P-1.0Ti -2.0LaB_6 MA`d after 1, 2, 4, 10, and 20 h are shown in Table 4-24. Due to lower density of LaB_6, its addition was led to density values decreaseing meantime; LaB_6 particles restrict diffusions so relative density of sintered samples was decreased too it can be released from lower relative density of samples with LaB_6 than same samples without LaB_6 in the same conditions. MA duration increased density and the densest samples were fabricated after 10 h MA. Furthermore, Calculated Archimedes density in water was smaller than Pycnometric density.

Table 4.24 : Sintered density of W^p -1.0Ti -2,0LaB_6 MA`d for 1, 2, 4, 10, and 20 h by PL sintering.

	Samples Name	Archimedes density (g/cm^3)	Pycnometeric Density (g/cm^3)	Relative Density (%)
1400˚C	W^P-1.0Ti-2.0LaB6 MA1h	15.65	15.71	88.68
	W^P-1.0Ti-2.0LaB6 MA2h	16.02	16.16	91.24
	W^P-1.0Ti-2.0LaB6 MA4h	16.13	16.21	91.5
	W^P-1.0Ti-2.0LaB6 MA10h	16.70	16.77	94.66
	W^P-1.0Ti-2.0LaB6 MA20h	16.48	16.55	93.43
1500˚C	W^P-1.0Ti-2.0LaB6 MA1h	15.66	15.77	89.04
	W^P-1.0Ti-2.0LaB6 MA2h	16.10	16.26	91.78
	W^P-1.0Ti-2.0LaB6 MA4h	16.14	16.24	91.67
	W^P-1.0Ti-2.0LaB6 MA10h	16.78	16.85	95.1
	W^P-1.0Ti-2.0LaB6 MA20h	16.65	16.71	94.34

LaB_6 increased hardness values this phenomenon is shown Figure 4-51. by increasing MA time, hardness was increased like density and hardness was declined after 10 h MA too. Increasing sintering temperature decreased hardness because of grain growth. Comparing microhardness of W^P -1.0Ti -2,0LaB_6 with W^P -1.0Ti shows that microhardness values increased by addition of 2,0LaB_6. The maximum microhardness of samples which sintered at 1400˚C, increased from 475±23 for powder composition Wp -1.0Ti to 513±42 Wp -1.0Ti -2,0LaB_6.

a

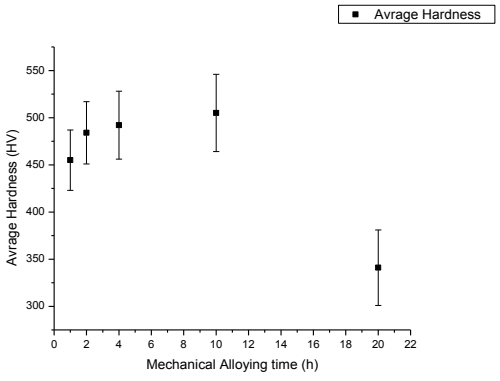

b

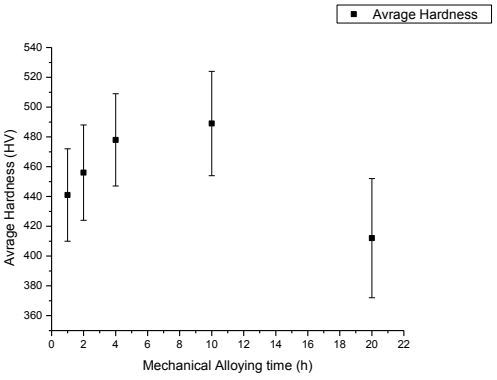

Figure 4.51 : Micro Vickers hardness of W^P -1.0Ti -2,0 LaB_6 MA`d for 1, 2, 4, 10, and 20 h sintered by PLS at: a-1400°C b-1500°C.

- W^P-4.0Ti-2.0LaB_6 MA`d conventional sintering

Studying of XRD W^P-4.0Ti-2.0LaB_6 patterns of samples in Figure 4-52, which were sintered at two different temperatures (1400ºC and 1500ºC), shows that, like W^P-4.0Ti composition, there are not any new phases after sintering. It is important to

notify that, the WC XRD peaks seems increased it can because of LaB_6 which used as second phase. During MA WC balls were abraded and LaB_6 helps WC Balls to be abraded more. WC inter to the composition from WC vial and WC balls. It was detected during MA process. WC ball weighted before MA and after it. 0.21% of balls weight was lost after 20 h MA it can be estimated that similar rate of vial were entered to the composition. Balls lost weight during MA of W^p -4.0Ti was 0.18%.

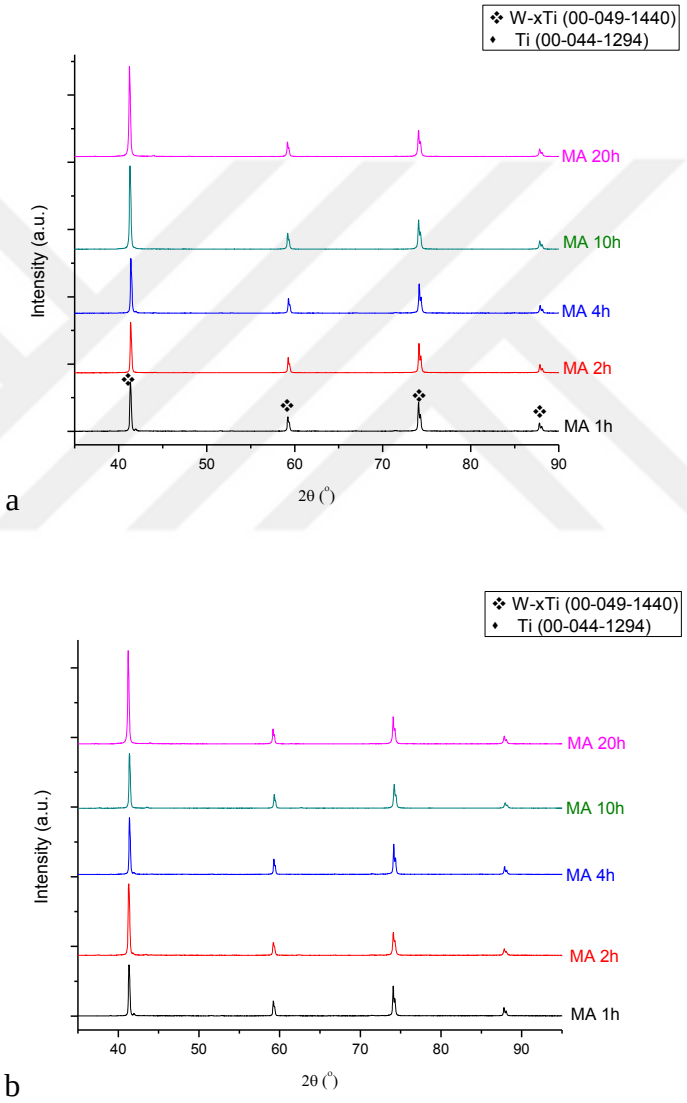

Figure 4.52 : XRD pattern of Wp -4.0Ti -2,0LaB6 MA`d for 1, 2, 4, 10, and 20 h sintered by PLS at: a-1400°C b-1500°C.

Table 4-25 shows density values of consolidated samples after sintering at 1400˚C and 1500˚C. Densities of samples were increased by MA till 10 h and after 10 h densities were decreased. Increasing of sintering temperature led to increasing of

density. As shown in Table 4-25 maximum measured relative densities are 97.44% and 97.57% after 10 h MA sintered at 1400°C and 1500°C respectively.

Table 4.25 : Sintered density of W^p -4.0Ti -2,0LaB_6 MA`d for 1, 2, 4, 10, and 20 h by PL sintering.

	Samples Name	Archimedes density (g/cm^3)	Pycnometeric Density (g/cm^3)	Relative Density (%)
1400˚C	Wp-4.0Ti-2.0LaB6 MA1h	15.70	15.75	96.96
	Wp-4.0Ti-2.0LaB6 MA2h	15.64	15.66	96.43
	Wp-4.0Ti-2.0LaB6 MA4h	15.68	15.72	96.78
	Wp-4.0Ti-2.0LaB6 MA10h	15.89	15.99	97.44
	Wp-4.0Ti-2.0LaB6 MA20h	15.76	15.78	97.13
1500˚C	Wp-4.0Ti-2.0LaB6 MA1h	15.71	15.74	96.87
	Wp-4.0Ti-2.0LaB6 MA2h	15.65	15.69	96.56
	Wp-4.0Ti-2.0LaB6 MA4h	15.71	15.74	96.89
	Wp-4.0Ti-2.0LaB6 MA10h	15.94	16.01	97.57
	Wp-4.0Ti-2.0LaB6 MA20h	15.75	15.79	97.22

Figure 4-53 shows the microhardness values of PL sintered samples. Microhardness amounts are increased to 10 MA and decreased after that. By increasing sintering temperature, microhardness of samples were decreased. The maximum microhardness values were 628±28 at 1400°C and 587±27 at 1500°C after 10 h MA.

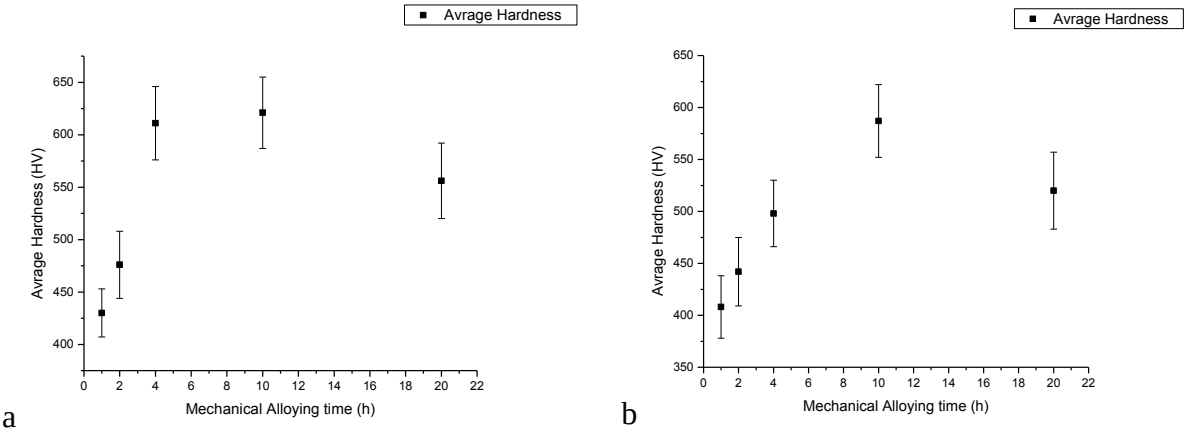

Figure 4.53 : micro Vickers hardness of W^p -4.0Ti -2,0LaB_6 MA`d for 1, 2, 4, 10, and 20 h by sintered by PLS at: a-1400°C b-1500°C.

- W^P-10.0Ti-2.0LaB_6 MA`d conventional sintering

As shown in Figure 4-54, sintering was performed at two different temperatures. Like previous compositions, there is not appear any new phases and only W-xTi are seen. It should be notified that, the WC XRD peaks seem increased by MA time.

During MA, WC particles abraded and LaB_6 causes to WC Balls to be abraded more. It was detected during MA process. WC ball weighted before and after MA. 0.22% of balls weight (200g) was lost after 20 h MA, similar rate of vial composition were entered to the composition. Balls lost weight after 20 h MA of W^p -10Ti was 0.15%.

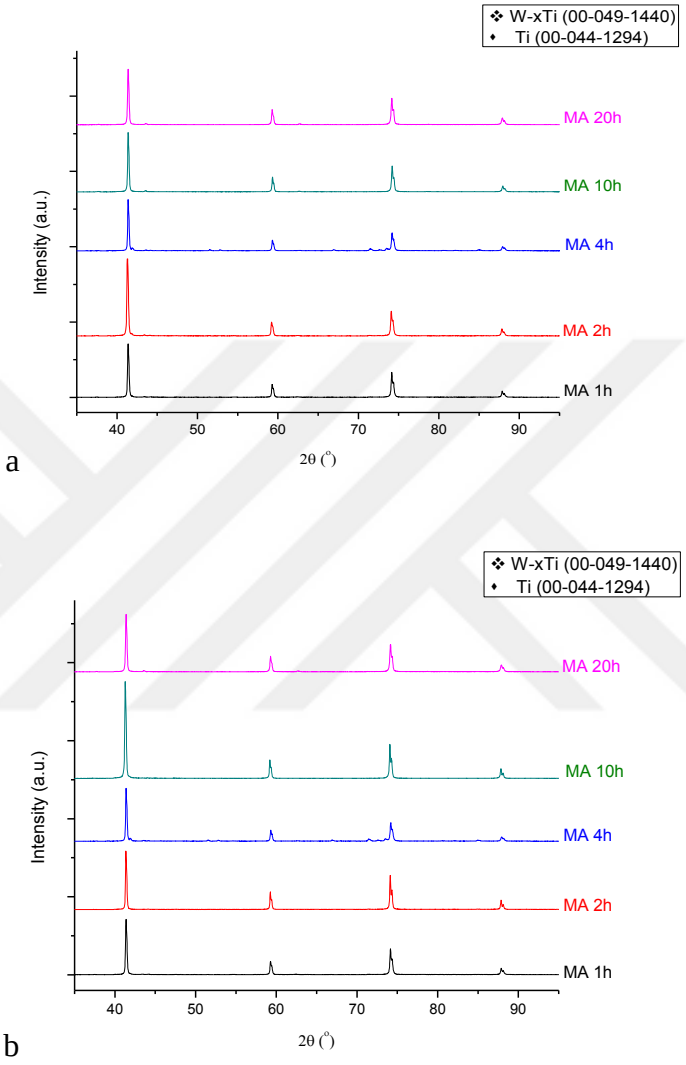

Figure 4.54 : XRD pattern of W^p -10.0Ti -2,0LaB_6 MA`d for 1, 2, 4, 10, and 20 h sintered by PLS at: a-1400°C b-1500°C.

samples density was increased by MA till 10 h and after 10 h density values were decreased. Increasing of sintering temperature led to increasing of density. As shown in Table 4-26 maximum relative density values are 97.43% and 97.49% after 10 h MA and sintering at 1400°C and 1500°C respectively. These measured densities are so near densities values of W^P-0.5Ti-2.0LaB_6 but is less than W^P-10.0Ti.

Table 4.26 : Sintered density of W^p -10.0Ti -2,0 LaB_6 MA`d for 1, 2, 4, 10, and 20 h by PL sintering.

	Samples Name	Archimedes density (g/cm^3)	Pycnometeric Density (g/cm^3)	Relative Density (%)
1400˚C	Wp-10.0Ti-2.0LaB6 MA1h	13.12	13.18	94.57
	Wp-10.0Ti-2.0LaB6 MA2h	13.34	13.43	96.41
	Wp-10.0Ti-2.0LaB6 MA4h	13.37	13.44	96.47
	W-10.0Ti-2.0LaB6 MA10h	13.56	13.61	97.43
	Wp-10.0Ti-2.0LaB6 MA20h	13.55	13.61	97.40
1500˚C	Wp-10.0Ti-2.0LaB6 MA1h	13.15	13.19	94.67
	Wp-10.0Ti-2.0LaB6 MA2h	13.39	13.45	96.55
	Wp-10.0Ti-2.0LaB6 MA4h	13.44	13.47	96.67
	W-10.0Ti-2.0LaB6 MA10h	13.61	13.64	97.49
	Wp-10.0Ti-2.0LaB6 MA20h	13.57	13.61	97.37

The microhardness amounts of PL sintered samples are offered in Figure 4-55. Microhardness amounts are increased to 10 MA and decreased after that. By increasing sintering temperature, microhardness values were decreased. The maximum microhardness values were measured after 10h MA . Those were 562±41 and 545±42 at 1400˚C and 1500˚C sintering temperatures respectively.

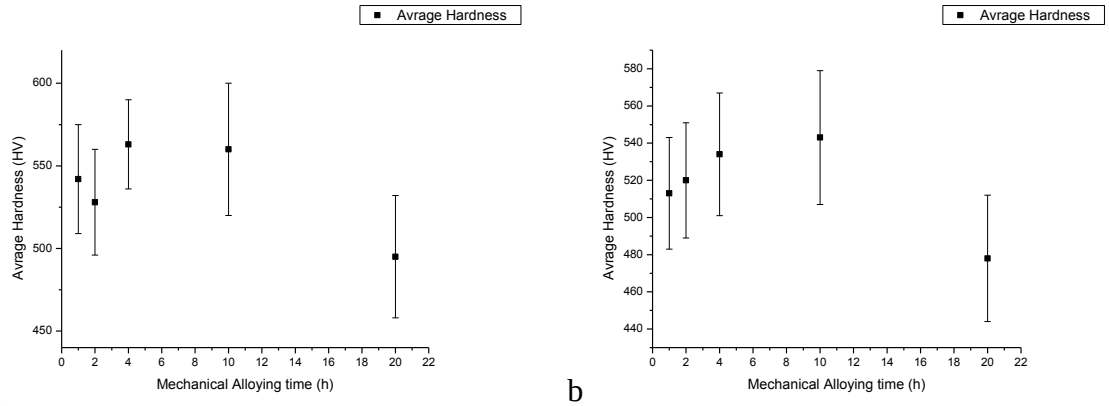

a b

Figure 4.55 : Micro Vickers hardness of W^p -10.0Ti -2,0LaB_6 MA`d for 1, 2, 4, 10, and 20 h sintered by PLSat: a-1400°C b-1500°C.

4.3.2. Spark plasma sintering (sps)

- W^P-xTi x=(0.5, 1.0, 4.0, 10.0) MA`d SPS sintering

Samples with pre-milled W were sintered by Spark Plasma Sintering (SPS) at 1400˚C under vacuumed condition. During sintering, samples were under 50 MPa

pressure. Heating rate was 100˚C/min and at 1400˚C samples held for 5 min. this processes were applied to all compositions. Studying of XRD patterns of samples after 10 h Ma in Figure 4-56 , shows that only beta phase of W-xTi are seen. By increasing of Ti peaks shifted to the left side and low 2θ positions. As conventional sintering there are not any other phases.

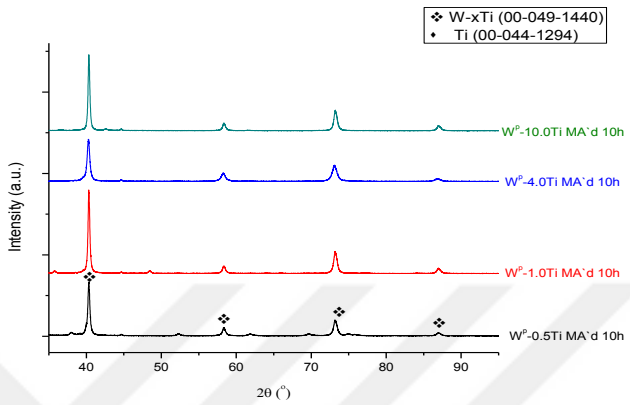

Figure 4.56 : XRD pattern of W^P – (0.5, 1.0, 4.0 and10.0) Ti MA`d for 10 h and sintered by SPS at 1400°C.

Sintered samples density values are offered in Table 4-27. Density values increased by Ti addition till 4.0wt%. W^p-4.0Ti is the densest and its relative density is 98.41 percent. After 4.0wt% Ti density values were decreased. Like PL sintering, maximum relative density was gotten by W-4.0wt% Ti compositions after 10 h MA. Samples sintered in PL sintering method have higher densities values than samples sintered in SPS method except W-0.5wt% Ti. Archimedes density of samples is smaller than measured Pycnometeric density. It is because of the He diffusibillity in the micro porous.

Table 4.27 : Density values of W^P–(0.5, 1.0, 4.0 and10.0) Ti MA`d for 10 h sintered by SPS at 1400°C .

	Samples Name	Archimedes density (g/cm^3)	Pycnometeric Density (g/cm^3)	Relative Density (%)
1400˚C	W^p-0.5%Ti MA 10h	18.59	18.60	97.94
	W^p-1.0%Ti MA 10h	18.43	18.28	97.80
	W^p-4.0%Ti MA 10h	16.54	16.79	98.41
	W^p-10.0%Ti MA 10h	14.17	14.27	98.21

Microhardness values of samples which sintered by SPS are offered in Figure 4-57. Like sintering density values, microhardness values of samples are the maximum

when used 4 %wt Ti. Microhardness values were increased till 4 wt%Ti and after that microhardness values were decreased. This value is bigger than samples with same compositions sintered at PL sintering method. Vickers microhardness values sintered by SPS is approximately two times larger than samples sintered by PL sintering. Samples which sintered by SPS are more hard than samples were sintered by PL sintering.

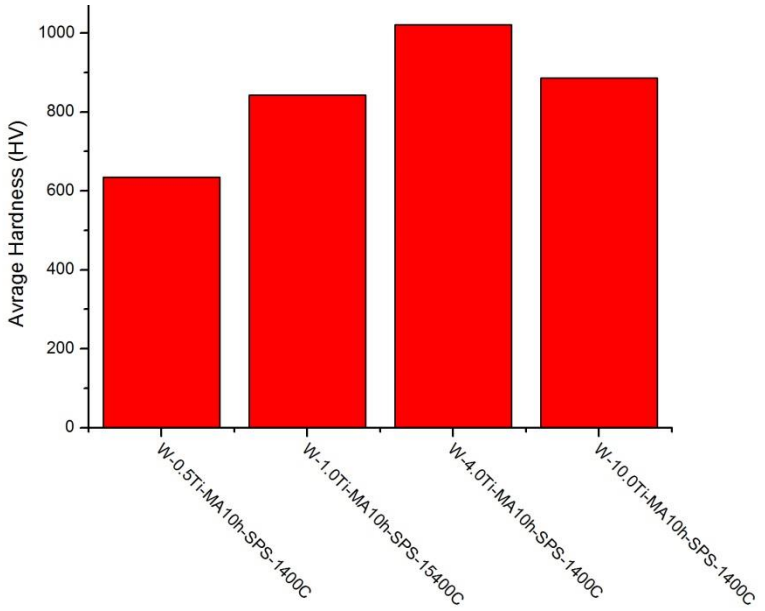

Figure 4.57 : Micro Vickers hardness of W^P – (0.5, 1.0, 4.0 and10.0) Ti MA`d for 10 h sintered by SPS at 1400°C.

- W^P-xTi-2.0LaB_6 x=(0.5, 1.0, 4.0, 10.0) MA`d SPS sintering

Samples with pre-milled W were sintered by SPS at 1400˚C and 1500˚C under vacuumed condition. During sintering, samples were under 50 MPa pressure. Heating rate was 100ºC/min and at 1400ºC samples held for 5 min. this processes were applied to all compositions. According to Figure 4-58, XRD patterns shows that only beta phase of W-xTi are seen. By increasing of Ti amounts, peaks shifted to the left side and lower 2θ values. Like PL sintering there are not any new phases. Samples after sintering by SPS have the same XRD peaks which appeared after PL sintering.

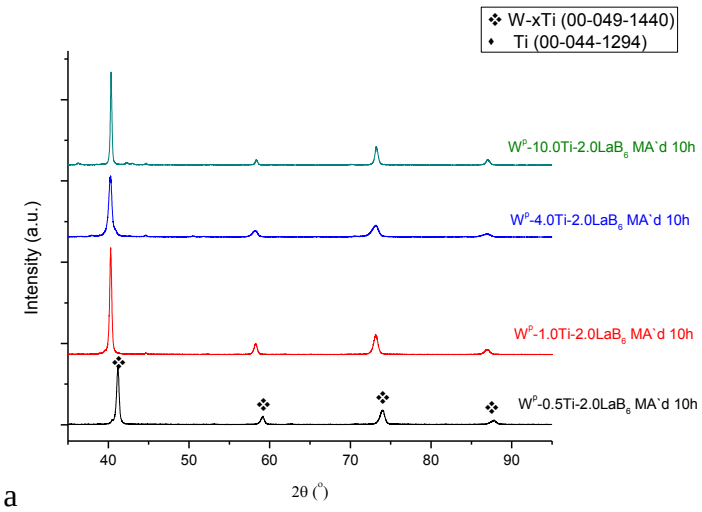

a

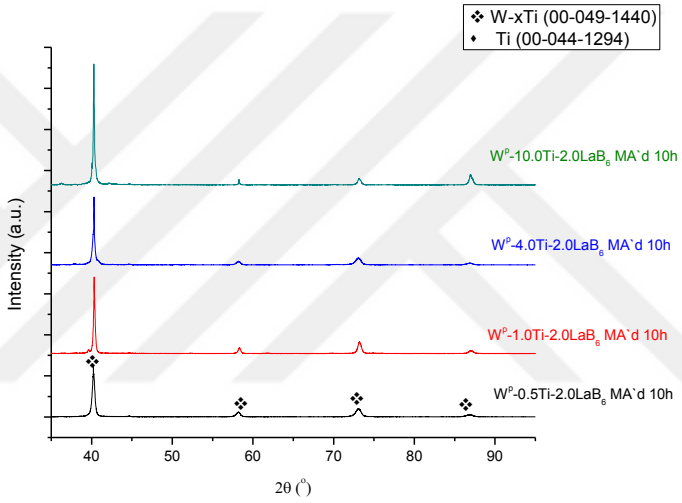

b

Figure 4.58 : XRD pattern of W^P–(0.5, 1.0, 4.0 and10.0) Ti-2.0LaB_6 MA`d for 10 h and sintered by SPS at: a-1400˚C b-1500˚C.

Sintered samples density is offered in Table 4-28. Density increases by Ti addition till 4.0wt%. W^P-4.0Ti-2.0LaB_6 is the densest and their relative densities are 98.08% and 98.38% sintered at 1400˚C and 1500˚C respectively. After 4.0wt% Ti density values were decreased. Like PL sintering, maximum relative density was gotten by 4.0wt% Ti compositions after 10h MA. W^P-4.0Ti-2.0LaB_6 samples MA'd 10 h and sintered in PL sintering method have higher relative density values than W^P-4.0Ti-2.0LaB_6 samples MA'd 10h and sintered in SPS sintering method at both sintering temperatures. Archimedes density of samples is smaller than measured pycnometeric density. He is used in Pycnometeric method. He is smallest noble gas can diffuse in the micro porous. The sintering temperature increment, led to increasing the samples

density except W^P-0.5Ti-2.0LaB_6 MA'd 10h. Samples sintered at 1500˚C are denser than ones sintered at 1400˚C.

Table 4.28 : Sintered density of W^P–(0.5, 1.0, 4.0 and10.0) Ti-2.0LaB_6 MA`d for 10 h sintered by SPS at 1400°C.

	Samples Name	Archimedes density (g/cm^3)	Pycnometeric Density (g/cm^3)	Relative Density (%)
1400˚C	W^P-0.5Ti-2.0LaB6 MA10h	17.36	17.38	96,64
	W^P-1.0Ti-2.0LaB6 MA10h	16.77	16.78	94,73
	W^P-4.0Ti-2.0LaB6 MA10h	15.93	15.93	98,08
	W^P-10.0Ti-2.0LaB6 MA10h	13.66	13.65	97,95
1500˚C	W^P-0.5Ti-2.0LaB6 MA10h	16.76	16.89	93.89
	W^P-1.0Ti-2.0LaB6 MA10h	16.80	16.79	94.78
	W^P-4.0Ti-2.0LaB6 MA10h	15.92	15.98	98.38
	W^P-10.0Ti-2.0LaB6 MA10h	13.71	13.66	98.04

Figure 4-59 shows microhardness of samples. Microhardness of samples sintered by SPS is the maximum when used 4 %wt Ti. This value is two times larger than densities of samples with same compositions sintered at PL sintering.

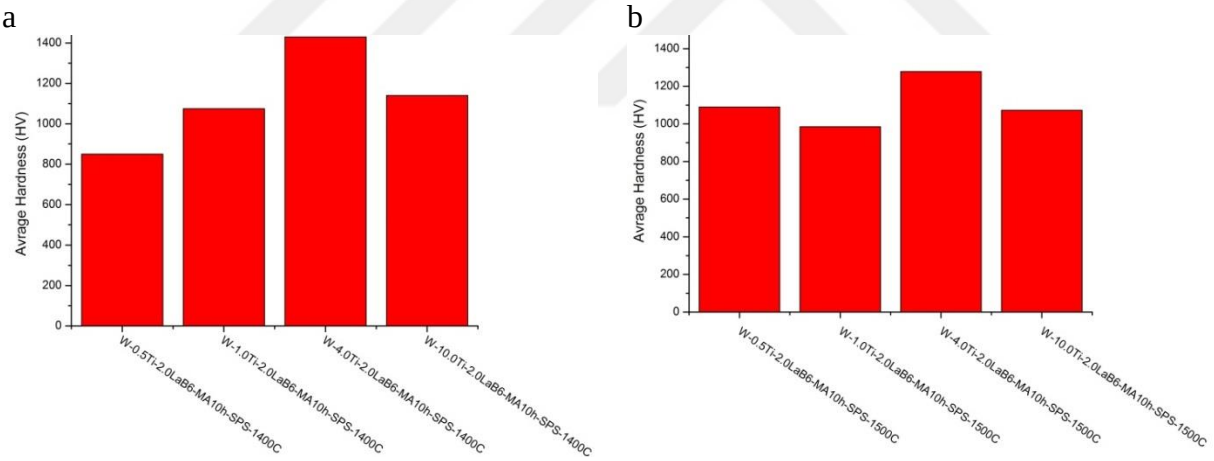

Figure 4.59 : Microhardness of W^P – (0.5, 1.0, 4.0 and10.0) Ti-2LaB_6 MA`d 10 h sintered by SPS at: a-1400°C b-1500ºC.

4.3.3. Friction results

In this section some selected samples were analyzed in Reciprocating Wear Test. In this test 4N was applied as normal force during sliding continuously. Sliding was applied under 10mm/sec rate and Al_2O_3 ball (6mm) were used as sliding abrasive. According to this test, Al_2O_3 ball was moved on the samples to wear it. Ball was moved for 75000 mm distance. This test was carried out at 25˚C and 30% humidity for whole samples. Selected samples are listed in below:

- W^P-xTi x=(0.5, 1.0, 4.0, 10.0) sintered by PLS

1. W^P-0.5%Ti MA`d 10 h sintered at 1400˚C on conventional method
2. W^P-1.0%Ti MA`d 10 h sintered at 1400˚C on conventional method
3. W^P-4.0%Ti MA`d 10 h sintered at 1400˚C on conventional method
4. W^P-10.0%Ti MA`d 10 h sintered at 1400˚C on conventional method

First part of samples 10 h MA`d and conventionally sintered at 1400˚C under controlled atmosphere. In whole of samples W powders were pre-milled for 10 h. As shown in Table 4-29 and Figure 4-60 wear loss volume and track area decreased till 4.0wt% Ti and after that, values were increased. Smallest wear area is belonging to W^P-4.0Ti.

Table 4.29 : Friction resistance values of W^P-x%Ti MA`d 10 h and sintered by PLS at 1400˚C.

Ti amount	Wear Track Area (μm^2)	Wear Loss Volume (μm^3)	Relative Wear Rates
0.5% wt	72,93	$36x10^4$	1,30
1.0%wt	66,99	$33\ x10^4$	1,20
4.0%wt	55,93	$27\ x10^4$	1,00
10.0%wt	64,61	$32\ x10^4$	1,16

As shown in Figure 4-60 the samples with 4.0wt% Ti have more wear resistance than other compositions. These results relation are similar to hardness and density. The maximum values of hardness and density are belonging to W^P-4Ti and the same composition has the lowest wear loss volume and area.

a b

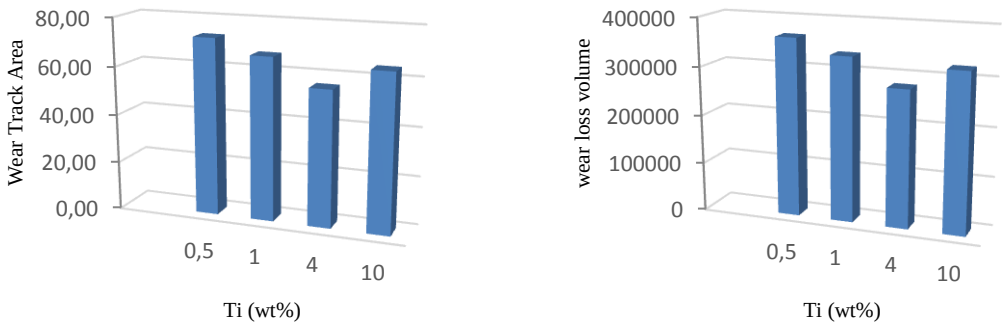

Figure 4.60 : friction test results of W^P-x%Ti MA`d 10 h and sintered by PL sintering at 1400˚C.a-Wear track area b-wear loss volume.

Based on color and morphology of wearied traces which shown in Figure 4-61 two mechanisms can be happened. Firstly, wear being associated with the removal of

sheared layers resulting from plastic deformation and the second mechanism takes place by gradual removal of adhered fragments of material picked up by the contacting surfaces during frictional interaction. So, it can be express that plastic deformation and adhesion are wearing mechanisms which done here. Dark places refer to parts which detached by plastic deformations and during reciprocating wear these parts create traces as parallel lines.

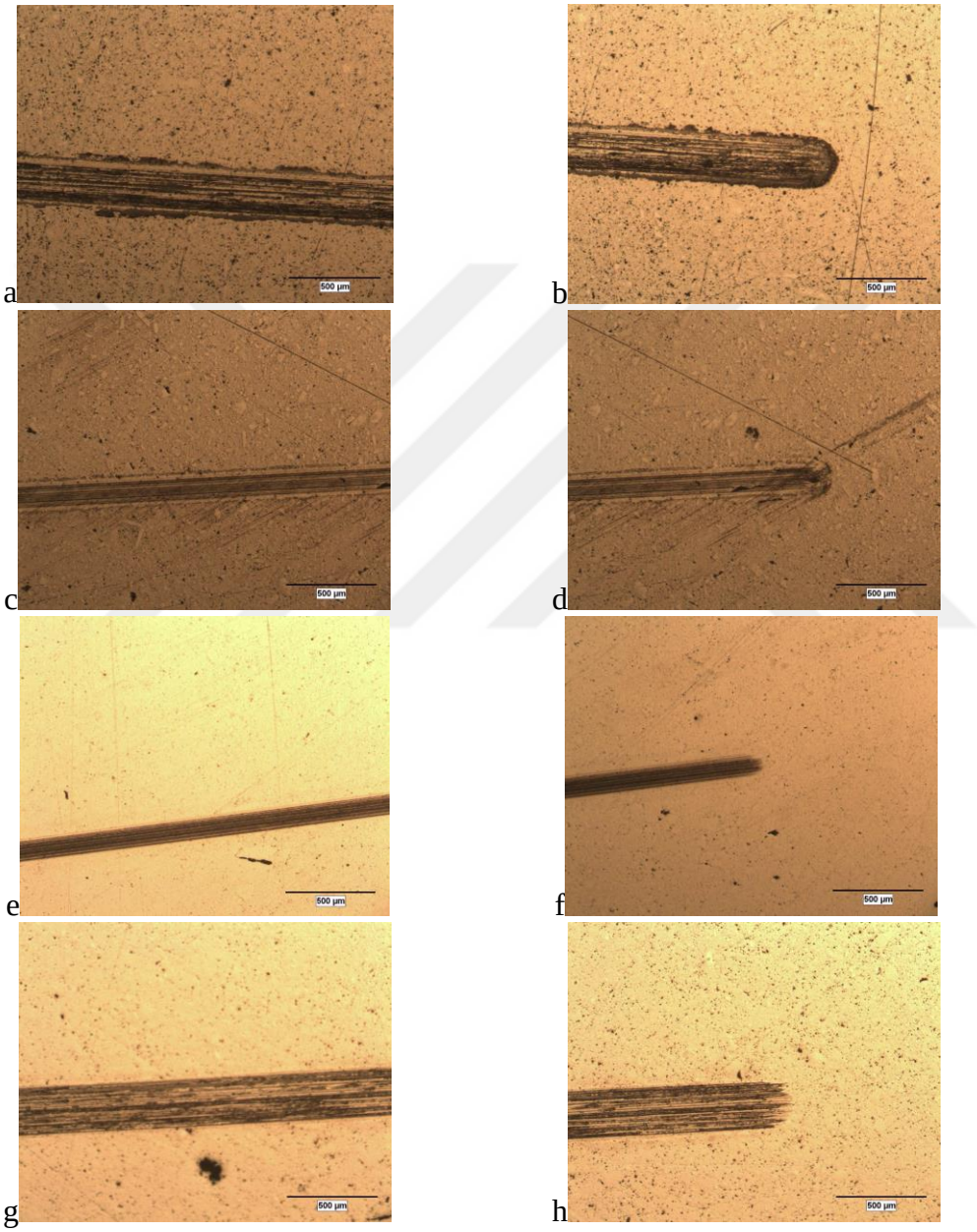

Figure 4.61 : Optical Microscopy of friction test trace of W^{P}-x%Ti MA`d 10 h and sintered at 1400˚C on PL sintering.a-b W-0.5Ti c-d W-1Ti e-f W-4.0Ti g-h W-10.0Ti.

- W^P-xTi x=(0.5, 1.0, 4.0, 10.0) sintered by SPS

5. W^P-0.5%Ti MA`d 10 h sintered at 1400˚C on SPS method
6. W^P-1.0%Ti MA`d 10 h sintered at 1400˚C on SPS method
7. W^P-4.0%Ti MA`d 10 h sintered at 1400˚C on SPS method
8. W^P-10.0%Ti MA`d 10 h sintered at 1400˚C on SPS method

Table 4-30 shows friction test results. Like conventional sintering in SPS sintered samples, composition with 4.0wt% Ti is the most resistive composition. 21 $x10^4$ μm^3 and 27 $x10^4$ are wear loss volume values of W^P-4Ti sintered by SPS and PLS respectively which in both sintering methods composition with 4.0wt% Ti has the least wear loss.

Table 4.30 : Friction resistance values of Wp-x%Ti MA`d 10 h sintered by SPS at 1400˚C.

Ti amount	Wear Track Area (μm^2)	Wear Loss Volume (μm^3)	Relative Wear Rates
0.5% wt	255,375	54 $x10^4$	2.51
1.0%wt	243,852	41 $x10^4$	1.90
4.0%wt	10,9488	21 $x10^4$	1
10.0%wt	86,7306	86 $x10^4$	2.05

As shown in Figure 4-62, the same values are illustrated statistically. As shown in Figure 4-62 the least wear loss volume is belonging to the W-4.0Ti.

a b

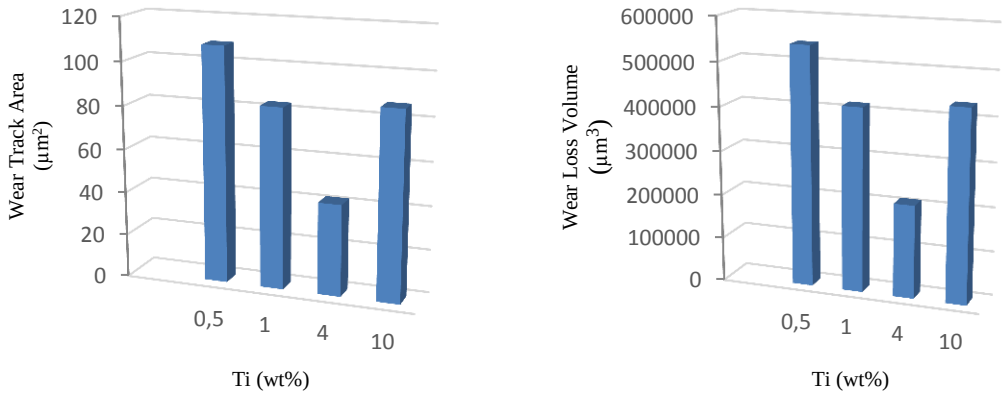

Figure 4.62 : friction test results of W^P-xTi MA`d 10 h and sintered by SPS at 1400˚C a-Wear Track Area b-Wear Loss Volume.

According to the Figure 4-63, wearing mechanism is similar to the samples sintered conventionally. Samples are full of dark places which indicate plastically detached

places. These detached parts cause to parallel wearing traces. In these samples like PL sintering, schematic of wearied traces color and morphology can introduce wear mechanism. This mechanism was started by removing particles from sheared layers that cause plastic deformation the second mechanism takes place by gradual removal of adhered fragments of material picked up by the contacting surfaces during frictional interaction. So it can be express that plastic deformation and adhesion are wearing mechanisms which done here. Dark places refer to parts which detached by plastic deformations and during Reciprocating Wear these parts create traces as parallel lines.

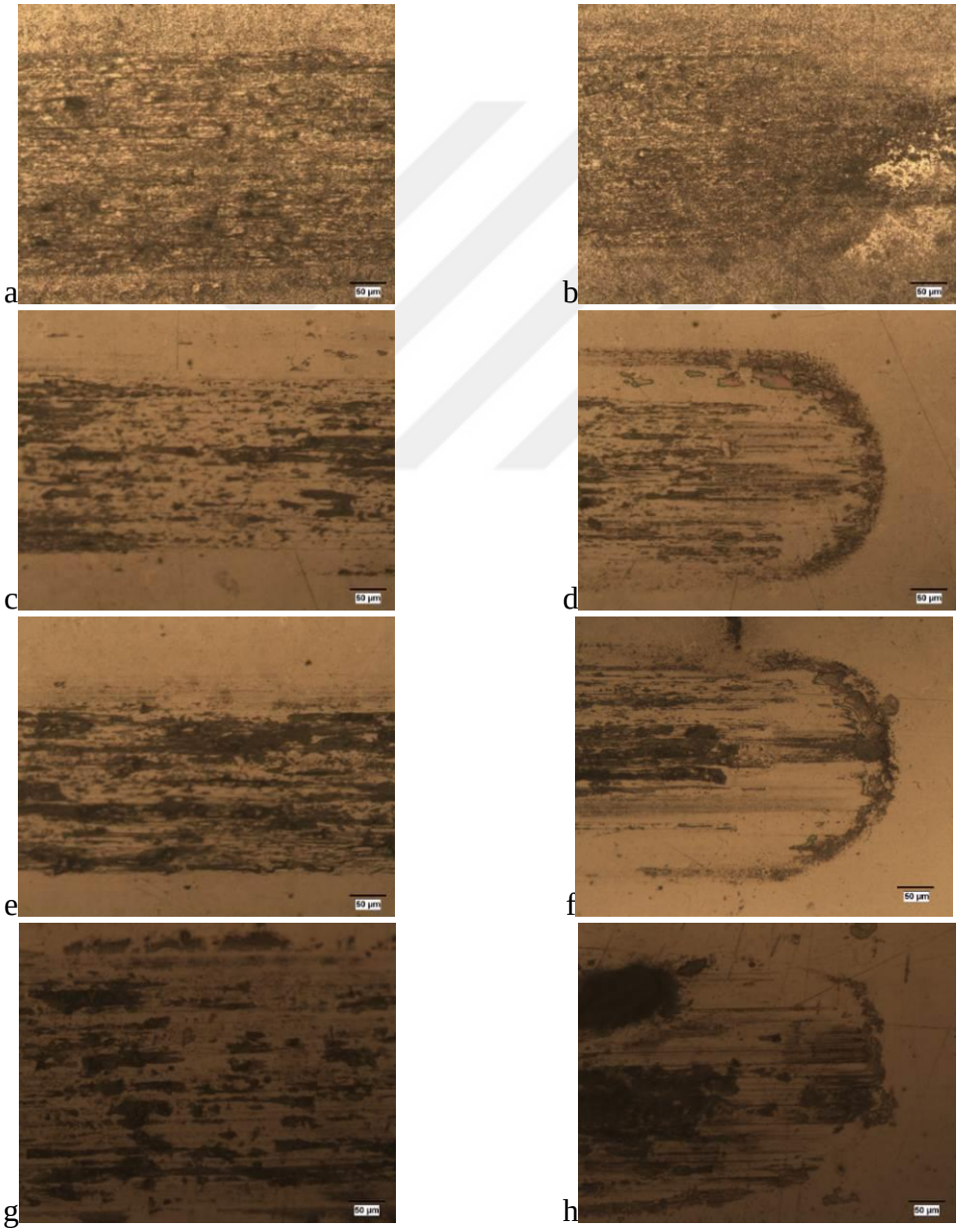

Figure 4.63 : Optical Microscopy of friction test trce of W^{P}-x%Ti MA`d 10 h and sintered by SPS at 1400˚C a-b W-0.5Ti c-d W-1.0Ti e-f W-4.0Ti g-h W-10.0Ti.

SEM micrographs of friction trace are offered in Figure 4-64. According to Figure 4-64, particle removing and plastic deformation are shown. Besides, parallel friction traces are seen. Plastic deformation regions are more in SPS than PLS.

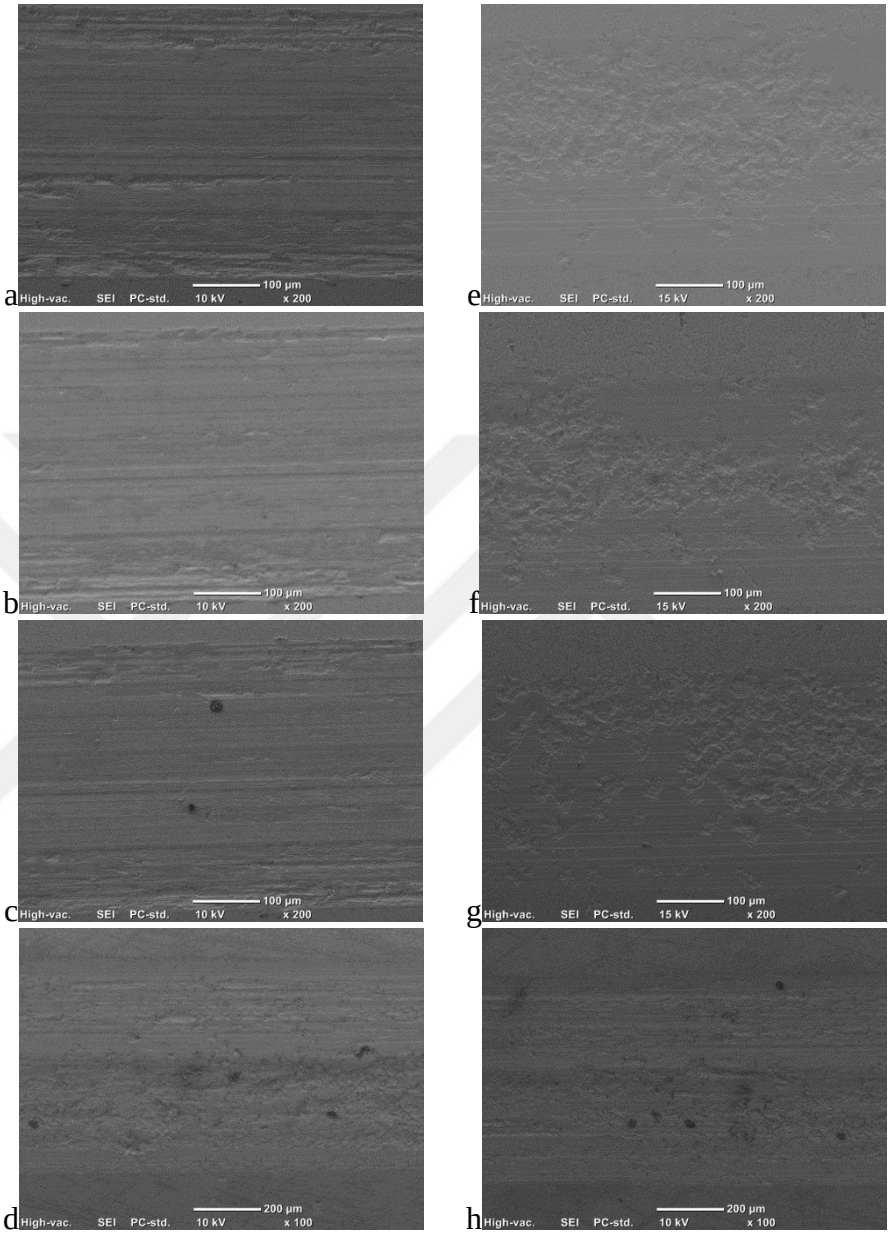

Figure 4.64 : SEM micrographs of friction test trace of W^P-x%Ti MA`d 10 h and sintered by PLS and SPS at 1400˚C 1400˚C PL Sintering: a-W^P-0.5Ti b- W^P-1.0Ti c-W^P-4.0Ti e- W^P-10.0Ti 1400˚C SPS: e-W^P-0.5Ti e- W^P-1.0Ti g- W^P-4.0Ti h-W^P-10.0Ti.

- W^P-xTi-2.0LaB_6 x=(0.5, 1.0, 4.0, 10.0) sintered by PLS

9. W^P-0.5%Ti-2.0LaB_6 MA`d 10 h sintered at 1400˚C on conventional method
10. W^P-1.0%Ti-2.0LaB_6 MA`d 10 h sintered at 1400˚C on conventional method
11. W^P-4.0%Ti-2.0LaB_6 MA`d 10 h sintered at 1400˚C on conventional method

12. W^P-10.0%Ti-2.0LaB_6 MA`d 10 h sintered at 1400˚C on conventional method

These samples reinforced by 2.0wt% LaB_6.so new compositions were predicted to be more resistant under same wearing condition. Friction results of W^P-xTi-2.0LaB_6 are offered in Table 4-31. These values are so less than samples produced without LaB_6. However, like previous ones sample with 4.0 wt% Ti is the most resistance.

Table 4.31 : Friction resistance values of W^P-x%Ti-2.0%LaB_6 MA`d 10 h sintered by PLS at 1400˚C.

Ti amount	Wear Track Area (μm^2)	Wear Loss Volume (μm^3)	Relative Wear Rates
0.5% wt	79,36	$39x10^4$	2,00
1.0%wt	55,12	$27\ x10^4$	1,39
4.0%wt	39,69	$19\ x10^4$	1,00
10.0%wt	55,32	$27\ x10^4$	1,39

Friction resistance values of Table 4-30 are shown in Figures 4-62 schematically. W^P-xTi and W^P-xTi-2.0LaB6 with 4.0wt%Ti in both methods (SPS and PL sintering) are the most resistante compositions. Furthermore, WP-xTi-2.0LaB6 samples are more resistante than W^P-xTi.

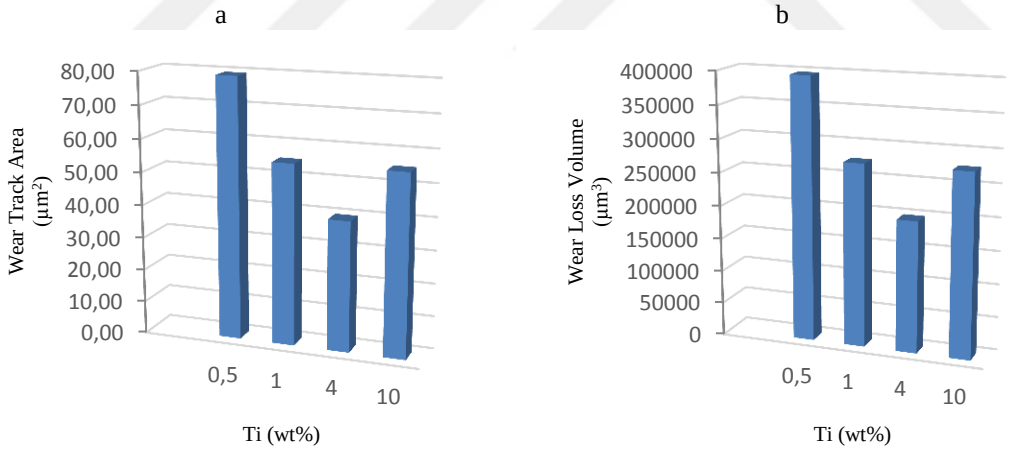

Figure 4.65 : friction test results of W^P-x%Ti-2.0%LaB_6 MA`d 10 h and sintered at 1400˚C on on conventional method. a-Wear Track Area b-Wear Loss Volume.

- W^P-xTi-2.0LaB_6 x=(0.5, 1.0, 4.0, 10.0) sintered by SPS

13. W^P-0.5%Ti-2.0LaB_6 MA`d 10 h sintered at 1400˚C on SPS method
14. W^P-1.0%Ti-2.0LaB_6 MA`d 10 h sintered at 1400˚C on SPS method
15. W^P-4.0%Ti-2.0LaB_6 MA`d 10 h sintered at 1400˚C on SPS method
16. W^P-10.0%Ti-2.0LaB_6 MA`d 10 h sintered at 1400˚C on SPS method
17. W^P-0.5%Ti-2.0LaB_6 MA`d 10 h sintered at 1500˚C on SPS method

18. W^P-1.0%Ti-2.0LaB_6 MA`d 10 h sintered at 1500˚C on SPS method
19. W^P-4.0%Ti-2.0LaB_6 MA`d 10 h sintered at 1500˚C on SPS method
20. W^P-10.0%Ti-2.0LaB_6 MA`d 10 h sintered at 1500˚C on SPS method

These 4 compositions were sintered by SPS at 1400˚C and 1500˚C temperatures. Friction values of sintered samples by SPS methods at 1400˚C and 1500˚C are offered in Table 4-32. Similar previous samples, compositions with 4.0wt% Ti are more resistive than other compositions. Samples which sintered at 1400˚C are more resistive than samples sintered at 1500˚C.

Table 4.32 : Friction resistance values of W^P-x%Ti-2.0%LaB_6 MA`d 10 h sintered at 1400˚C and 1500˚C by SPS.

Sintering Temperature	Ti amount	Wear Track Area (μm^2)	Wear Loss Volume (μm^2)	Relative Wear Rates
1400˚C	0.5% wt	106,3	$53x10^4$	4,79
	1.0%wt	60,5	$30x10^4$	2,72
	4.0%wt	22,1	$11x10^4$	1
	10.0%wt	101,4	$50x10^4$	4,57
1500˚C	0.5% wt	162,3	$81x10^4$	7,32
	1.0%wt	138,9	$69x10^4$	6,26
	4.0%wt	50,5	$25x10^4$	2,27
	10.0%wt	113,4	$56x10^4$	5,11

As mentioned in Table 4-32, Figure 4-66 shows friction values schematically. The minimum friction values are belonging to W^P-4.0Ti-2.0LaB_6. Increasing sintering temperature, increase wear losing values.

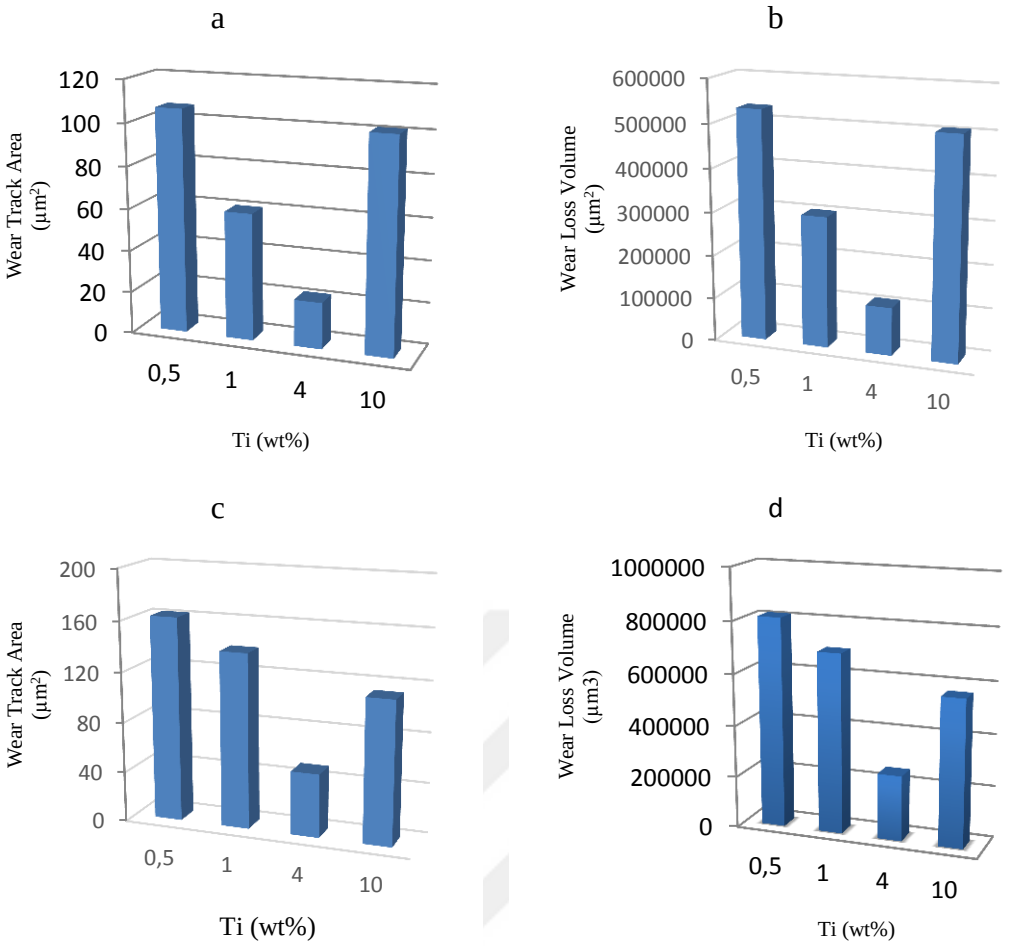

Figure 4.66 : friction test results of W^P-x%Ti-2.0%LaB_6 MA`d 10 h and sintered by SPS method.a-Wear Track Area at 1400˚C b-Wear Loss Volume at 1400˚C c-Wear Track Area at 1500˚C d-Wear Loss Volume at 1500˚C.

Figures 4-67 and 4-68 show friction traces of W^P-xTi-2.0LaB_6 sintered at 1400˚C and 1500˚C by SPS method. Abrasive wear is classified as the removal of material from a surface by hard particles sliding between two surfaces. As shown in optical microscopic Figures, there are parallel lines, which show, there is not any plastic deformation and abrasive mechanism is applied on W^P-xTi-2.0LaB_6 compositions. Abrasive materials slide surface of samples and create parallel lines.

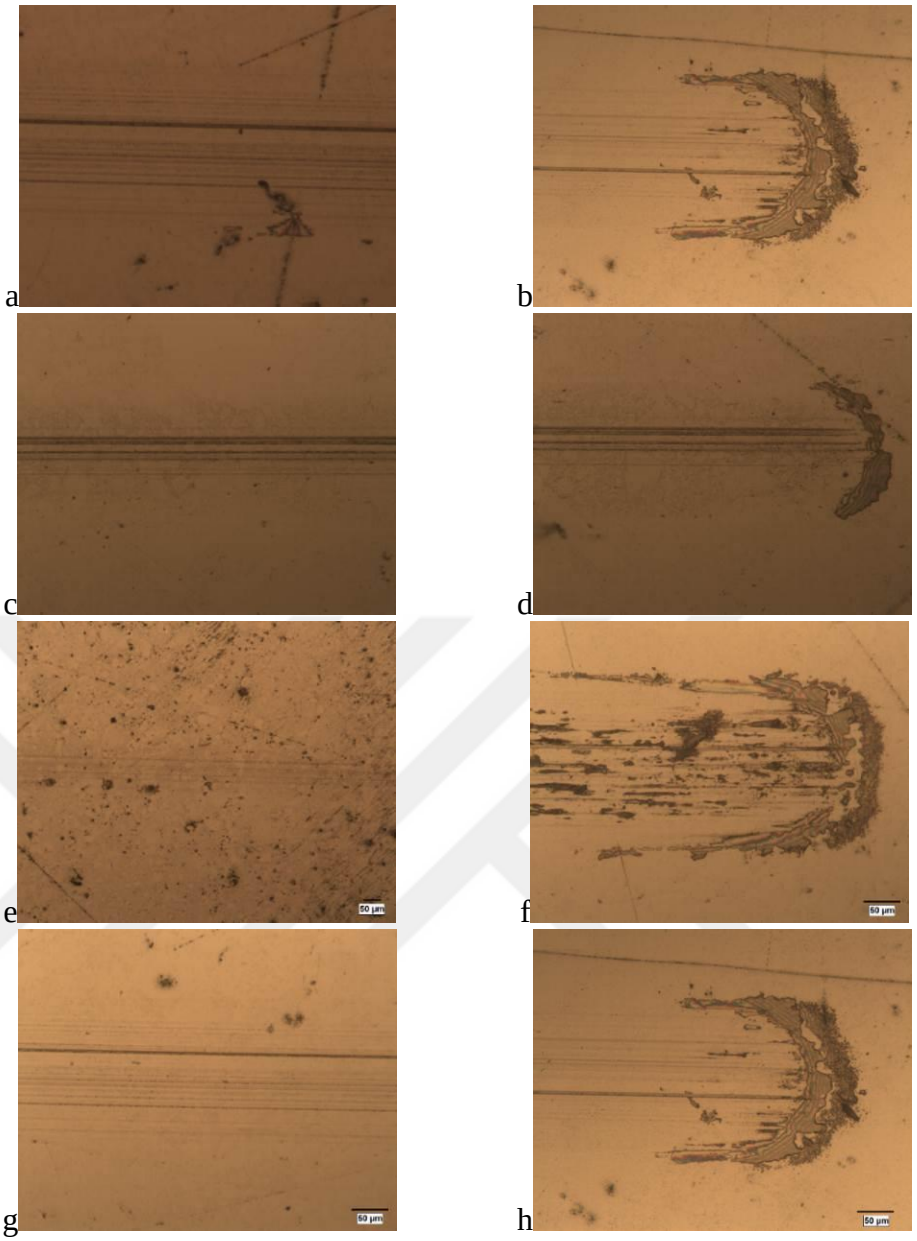

Figure 4.67 : friction test trace of W^{p}-x%Ti-2.0%LaB_6 MA`d 10 h and sintered by SPS at 1400˚C a-b W-0.5Ti c-d W-1.0Ti e-f W-4.0Ti g-h W-10.0Ti.

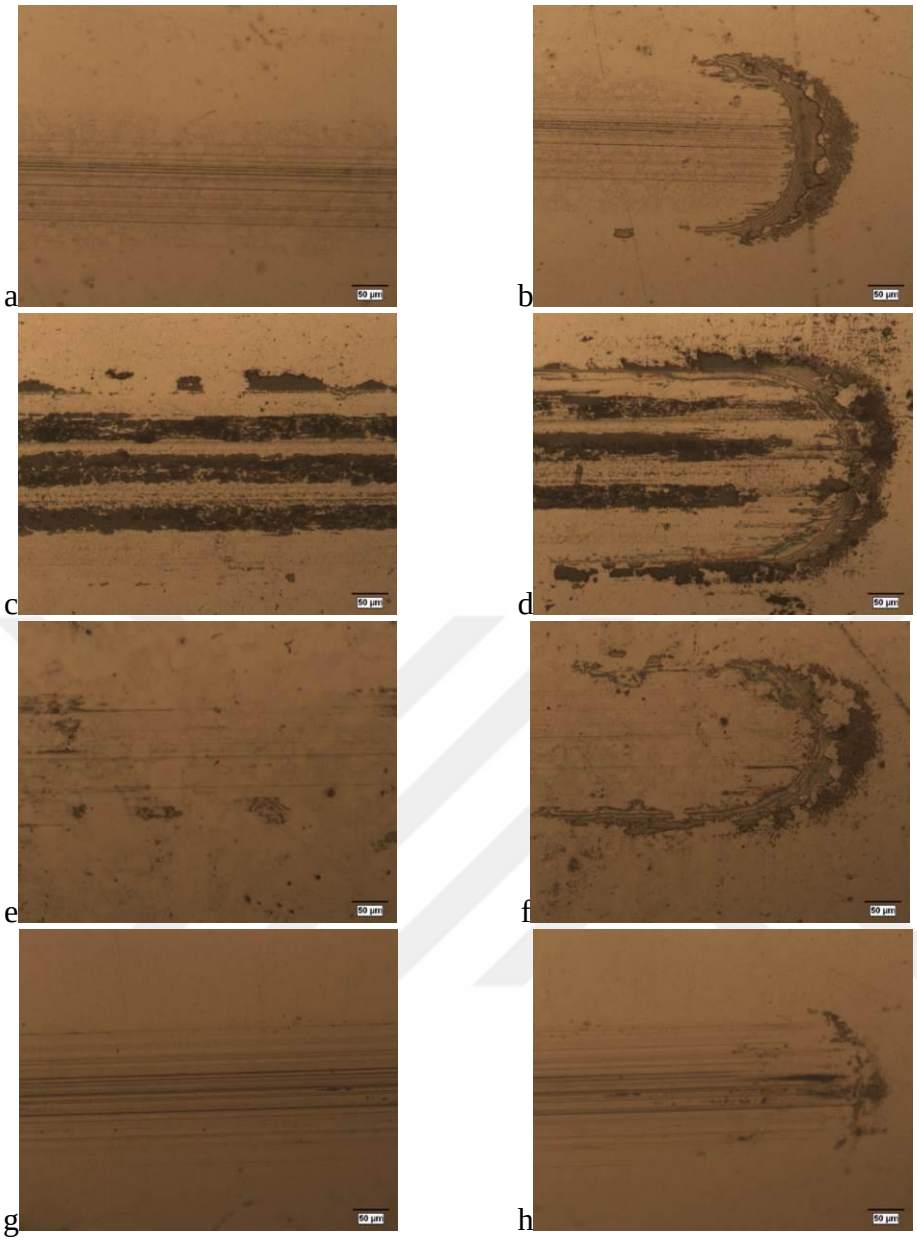

Figure 4.68 : friction test trace of W^{p}-x%Ti-2.0%LaB_6 MA`d 10 h and sintered by SPS at 1500˚C a-b W-0.5Ti c-d W-1.0Ti e-f W-4.0Ti g-h W-10.0Ti.

4.3.4. Microstructure analyzing by SEM micrographs

According to the electron microscopy, grain size and distribution of gain were studied. Before etching grain was not distinguished as seen in Figure 4-69 only two regions were separated.

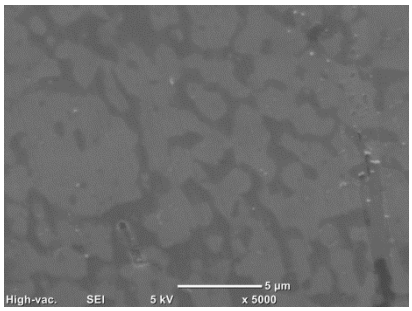

Figure 4.69 : SEM micrograph of W^p-4.0Tiafter sintering at 1400C by PL sintering before etching.

Therefore different types of etchant were tried. Peroxide and Murakami solutions were used during etchant. Peroxide etched unusual and suddenly solves the composite. Its effects on some samples are offered in Figure 4-70.

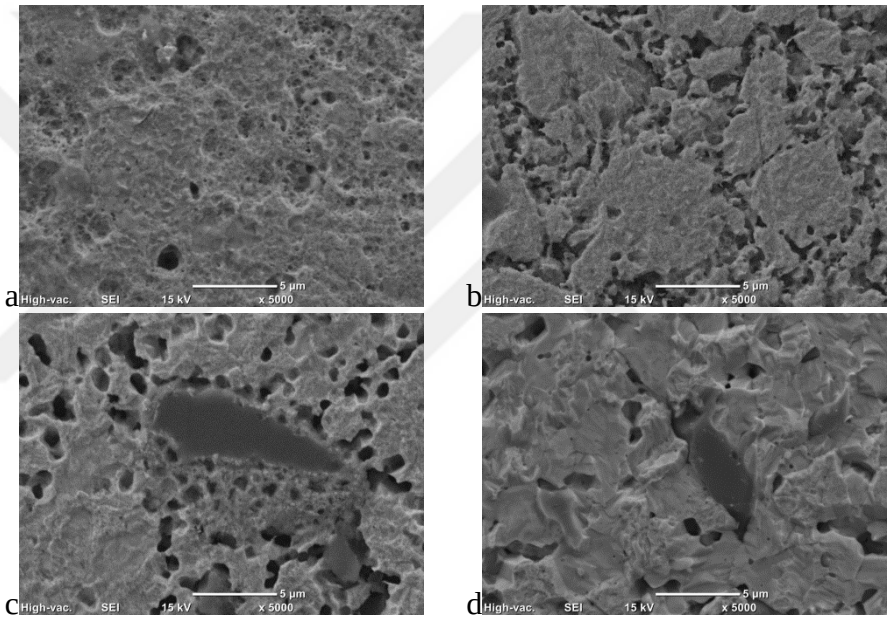

Figure 4.70 : SEM micrograph of W^p-4.0Tiafter sintering at 1400C by PL sintering after etching.

As seen in Figure 4-70 composite were react by peroxide and peroxide diffuse to inside the samples. Holes appear in the grain boundaries and solvent starts to react and diffuse into the graind. Especially small grains are disappeared and remain part will have porous structure. However, Murakami reaction was different. Based on this study Murakami was suitable etchant solution.

Figure 4-71 shows SEM micrograph of samples which sintered by PL Sintering. According to Figure 4-71 it is understood that by increasing of Ti grains get smaller. It can because of Ti solution in W matrix. Meantime, addition of LaB6 decrease grain size too

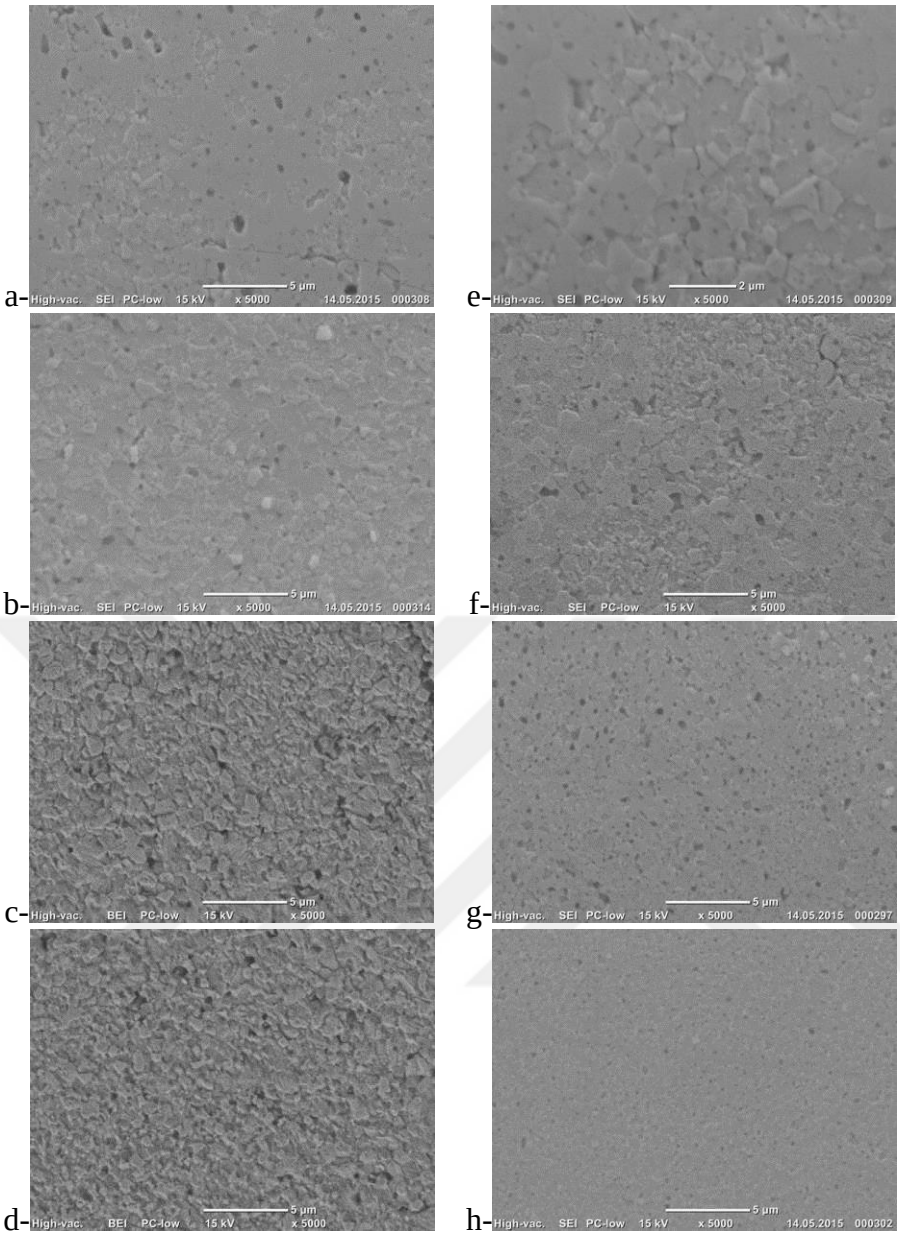

Figure 4.71 : SEM micrograph of W^p-xTi and W^p-xTi-2.0LaB_6 after sintering by PLS at 1400˚C.a-W^p-0.5Ti bW^p-1.0Ti c-W^p-4.0Ti d-W^p-10.0Ti e-W^p-0.5Ti-2.0LaB_6 f-W^p-1.0Ti-2.0LaB_6 g-W^p-4.0Ti-2.0LaB_6 h-W^p-10.0Ti-2.0LaB_6.

Figure 4-72 shows SEM micrograph of samples which sintered by SPS. This Figure shows that by increasing of Ti and LaB_6, grains get smaller. LaB_6 resist in front of grain growth so samples with LaB_6 have small grains that samples without LaB_6. Moreover, increasing sintering temperature can cause to grain growth therefore, grain sizes get larger. Furthermore, comparing Figures 4-71 and 4-72 shows that samples sintered by SPS have smaller grain sizes. SPS method is carried out in short period therefore grain growth is limited.

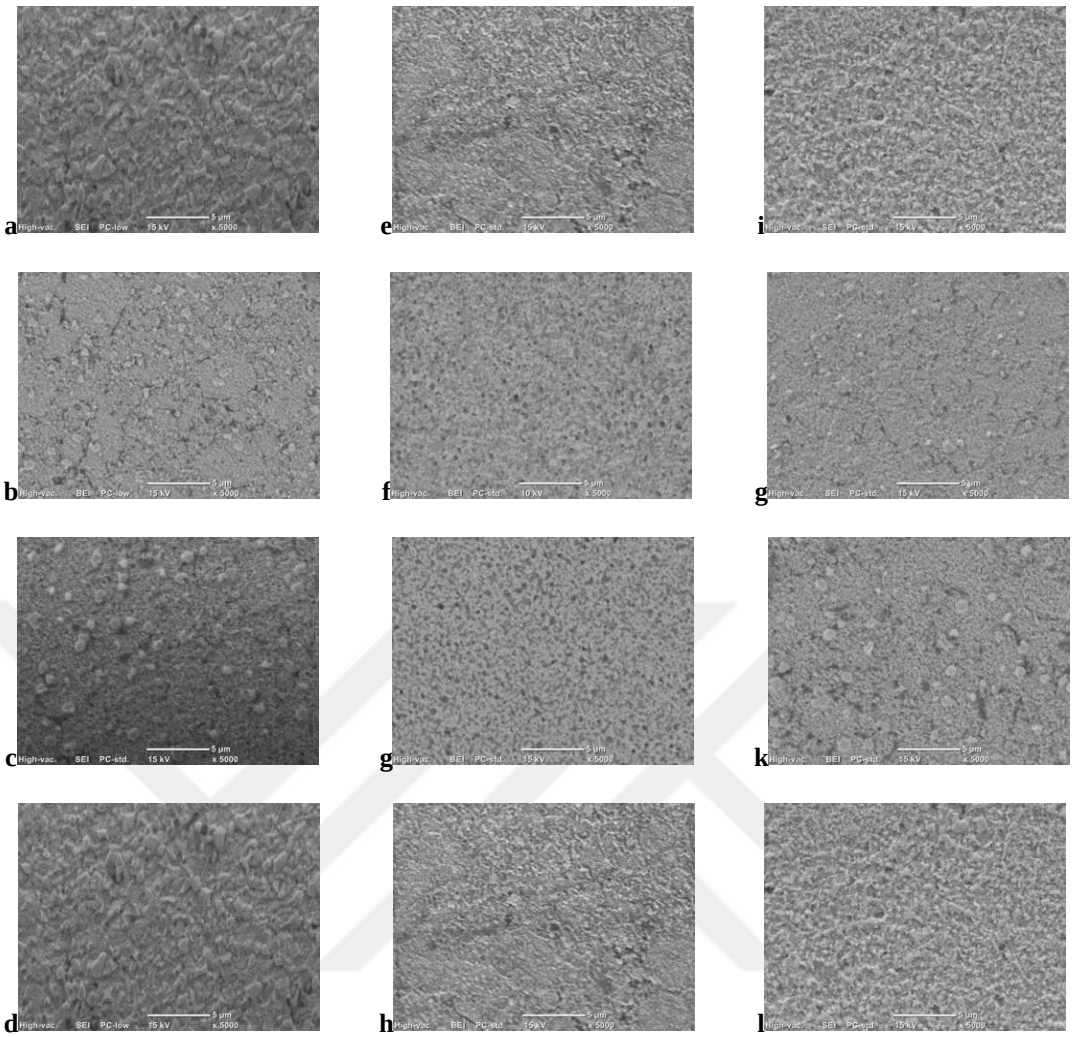

Figure 4.72: SEM micrograph of W^{P}-xTi and W^{P}-xTi-2.0LaB_6 after sintering by SPS at 1400˚C and 1500˚C. 1400˚C: a-W^{P}-0.5Ti b-W^{P}-1.0Ti c-W^{P}-4.0Ti d-W^{P}-10.0Ti 1400˚C: e-W^{P}-0.5Ti-2.0LaB_6 f-W^{P}-1.0Ti-2.0LaB_6 g-W^{P}-4.0Ti-2.0LaB_6 h-W^{P}-10.0Ti-2.0LaB_6 1500˚C: i-W^{P}-0.5Ti-2.0LaB_6 j-W^{P}-1.0Ti-2.0LaB_6 k-W^{P}-4.0Ti-2.0LaB_6 l-W^{P}-10.0Ti-2.0LaB_6.

5. CONCLUSIONS

The results of this study can be discussed in two parts which are the results of powder characterization experiments and the results of characterization experiments of as-consolidated and sintered samples.

In case of powder characterization results, it can be clearly stated that the grain sizes were extremely decreased and the internal strains were increased with increasing amount of mechanical alloying according to SEM and XRD investigations.

On the basis of the results of the powder investigation, the following observations and conclusions can be drawn.

- Peaks belonging to the β(W,Ti) solid solution phase have been identified in all XRD patterns of MA'd W-xTi (x=0.5, 1.0, 4.0 and 10.0 wt% Ti) powder alloys. In addition, Ti phase is present in the W–4 wt% Ti and W-10 wt% Ti powder alloys MA'd for 1 h. With increasing MA durations and Ti contents, the XRD peak intensities of the β(W,Ti) solid solution phase decrease, peak broadening increases and peaks shift to lower 2θ values with increasing FWHM values.
- Williamson-Hall and Lorentzian method (TOPAS 5) were utilized in the analyses of the XRD peaks of the β(W,Ti) solid solution phase. With increasing MA durations and Ti contents, strain values increased and crystallite sizes decreased. A minimum crystallite size of 2.2 nm and a maximum internal strain of 4.57% were calculated for the W-4.0wt% Ti powder alloy MA'd for 20 h.
- Effective lattice parameter values (a_{eff}) of the β(W,Ti) solid solution phase increase linearly with Ti contents and MA durations, as predicted by the TOPAS 5 software. a_{eff} values predicted by TOPAS are very close to those calculated by Vegard's law at low Ti contents (0.5 wt% and 1.0wt% Ti). On the other hand, those for the higher Ti contents (4.0 wt% and 10.0 wt% Ti) show a negative deviation from the Vegard's law. Ti solubility of about 3.1wt% (11.0at%) was calculated for the 10 h MA'd W-10wt% Ti powder alloy which corresponds to a solid solubility extension of about 0.6wt% (≈2at%).

- The powders MA'd produced by dry milling method for both 10 h and 20 h have spherical particle, while wet milling results in layered morphology.
- Particles which MA'd powders in IPA are smaller than the ones milled in Ethanol. On the other hand the MA'd powders in Argon have the smallest particles.
- Comparing wet and dry MA, shows that WC peaks are more intense in wet milling, particularly in IPA.
- There was a rapid reduction in crystallite size of W-0.5wt%Ti powders in between 0 h to 10 h of MA, while after 10 h of MA only a slight further reduction in crystallite size was measured by Lorentzian and Gaussian methods.
- MA media's were highly effective in reducing crystallite size by increasing milling time. The smallest crystallite size belonged to the dried milled powders. Meanwhile, powders MA'd in Ethanol have the biggest crystallite sizes.
- Up to 20h MA, crystallite rate linearly decreased with increase in MA time. The maximum and minimum crystallite rate measured were 65% and 91% , respectively, in Ar and Ethanol medium after 20h MA.
- MA'd W-0.5wt.%Ti powders milled in Ethanol have the highest densities, and the powders MA'd in IPA have lowest.

On the basis of the results of the sintering investigation, the following observations and conclusions can be drawn.

- MA has enormous effect on decreasing of sintering temperature. It cause to decreasing of particle size and internal strain extending that both of them have direct effect on sintering temperature declining. Meantime pre-milling help during sintering. Samples which used Pre-milled W powders were sintered completely.
- After sintering, internal strain reaches to the minimum amount equal zero and it was independent of sintering temperature or MA duration however, crystallite size was increased by increase of sintering temperature and MA time.
- Composites which produced by micron size W, were not sintered completely vice versa, composites that used pre-milled W reached 98% relatively density.
- After sintering, there was not seen any new phases. Only β(W-xTi) phase was detected. Besides, some WC peaks were appeared after long MA time or when LaB6 was used.
- The highest results of density and microhardness belong to W-4.0Ti by 10 h MA and sintering at 1400˚C in both sintering methods (SPS and PLS). Hardness

values were increased by addition of LaB6 but density values were decreased by its addition.

- High amounts of internal lattice strain and lower crystallite size aid sintering at lower temperatures. By comparing whole of compositions and sintering temperatures, it will be clear that 10 h MA had the best microstructural specifications.
- Increasing of sintering temperature was related to decreasing of Vickers microhardness that it can be related grain growth. Crystallite enlargement by increasing of sintering temperature approved grain growth and decreasing of Vickers microhardness .
- Samples sintered by SPS are denser than samples sintered by PLS. the densest samples are W^{P}-4.0Ti which its relative density was 98.4% meantime its hardness value is 1087 VHN. Furthermore, these values for W-4.0Ti-2.0LaB6 were 98.38 and 1432 VHN respectively.
- According to SEM images, it could be clearly seen that the grain size of samples were decreasing with increasing Ti amounts meantime addition of LaB_6 have the same effect.
- In case of consolidated and sintered samples, it was clear that the densities were increased with increasing sintering temperatures because the diffusivity of the atoms, which is the key factor for sintering, was increased with the increasing temperature.
- Density value of the sintered samples containing 4wt% Ti is the highest. This value is the highest in SPS and PLS.
- According to hardness and wear tests results at 1500˚C, samples which sintered by PL sintering are softer than samples sintered by SPS. The hardest sample is W-4.0Ti-2.0LaB_6 which sintered by SPS and its value is 1450 VHN. Based on this study, W-4.0Ti-2.0LaB_6 is the most resistive samples which sintered by SPS. Meantime, samples sintered by SPS are more resistive than samples which sintered by PL sintering.

REFERENCES

Acchar, W., Zollfrank, C. and Greil, P. (2004). Microstructure and Mechanical Properties of WC-Co Reinforced With NbC, *Materials Research, 7***,** 445-450.

Ağaoğulları, D., Balci, Ö., Demirkan, Ö. U., Gökçe, H., Genç, A., Öveçoğlu, M. L., and Duman, İ. (2013). Development of mechanically alloyed and sintered W-1 wt.% Ni matrix composites reinforced with TiB2, In *Solid State Phenomena, 194*, 194-198.

Ağaoğulları, D., Balcı, Ö., Gökçe, H., Öveçoğlu, M. L., and Duman, İ. (2013). Comparative investigations of the activated sintered W–1wt.% Ni composites reinforced with various oxide and boride particles, *International Journal of Refractory Metals and Hard Materials, 41*, 577-584.

Akovali, G., and Uyanik, N. (2001). *Introduction in Handbook of Composite Manifacturing*, Ed. G. Akovali, Rapra Technology Ltd.

Askeland, D. R. (1984). *The Science and Engineering of Materials*, Brooks/Cole Engineering Division, a division of Wadsworth.

Asthana, R., Kumar, A., and Dahotre, N. B. (2006). *Materials science in manufacturing* (pp. 397-484). Amsterdam: Elsevier.

Asthana, R., Kumar, A., and Dahotre, N. B. (2006). *Materials processing and manufacturing science* (pp. 167-245) . Butterworth-Heinemann.

Beere, W. (1976). Stress redistribution during Nabarro-Herring and superplastic creep. *Metal Science, 10*(4), 133-139.

Benjamin, J.S. (1992). Fundamentals of mechanical alloying (pp. 88-90) , *Materials Science Forum*.

Boch, P. and Leriche, A. (2001). Sintering and Microstructure of Ceramics (pp. 1-18), *Ceramic Materials Edited by Philippe Boch and Jean-Claude Niepce*.

Brophy, J.H., Hayden, H.W., Prill, A.L. and Wulff, J. (1963). The Investigation of the Activated Sintering of Tungsten Powder. *Final Report, Prepared under U.S. Navy*, Bureau of Naval Weapons Contract NO w 61-0326-d, Massachusetts Institute of Technology, Cambridge, Massachusetts.

Cahn, R.W. (2001). *The Coming of Materials Science*, Pergamon, Amsterdam.

Callister, W.D-Jr. (2000). *Materials Science and Engineering: an Introduction*, Wiley, New York.

Campbell, F. C. (2006). Metal matrix composites (pp.419-457) , *Manufacturing Technology for Aerospace Structural Materials; Elsevier Science: Oxford, UK.*

Casati, R. and Vedani, M. (2014). Metal matrix composites reinforced by nano-particles—a review. *Metals, 4*(1) 65-83.

Chandrasekaran, D. and Nygårds, M. (2003). A study of the surface deformation behaviour at grain boundaries in an ultra-low-carbon steel. *Acta materialia, 51*(18), pp.5375-5384.

Chawla, N. and Chawla, K.K. (2006). *Metal Matrix Composites*, Springer, New York.

Chawla, N. and Shen, Y.L. (2001). Mechanical behavior of particle reinforced metal matrix composites, *Advanced Engineering Materials, 3:* 357-370.

Chen, Z., Zhou, M. and Zuo, T. (2000). Morphological evolution of second-phase particles during thermomechanical processing of W-La_2O_3 alloy, *Scripta mater., 43:* 291–297.

Chen, Y., Wu, Y.C., Yu, F.W. and Chen, J.L. (2008). Microstructure and mechanical properties of tungsten composites co-strengthened by dispersed TiC and La2O3 particles, *International Journal of Refractory Metals&Hard Materials, 26:* 525-529.

Clyne, T.W. (2001). *An Introductory Overview of MMC Systems, Types, and Developments* Metal Matrix Composites of Comprehensive Composite Materials, Elsevier.

Clyne, T.W. and Withers, P.J. (1993). *Introduction to Metal Matrix Composites*,Cambridge University Press, Cambridge.

Coble, R.L. (1961). Sintering crystalline solids. I. Intermediate and final state diffusion models. *Journal of applied physics*, *32*(5), 787-792.

Caglioti, G., Paoletti, A.T. and Ricci, F.P. (1958). Choice of collimators for a crystal spectrometer for neutron diffraction. *Nuclear Instruments*, ***3***(4), 223-228.

Corti, C.W. (1986). The Role of the Platinium Metals in the Activated Sintering of Refractory Metals. Platinum Metals Rev., *30:* 184-195.

Coskun, S. (2006). Development and Characterization Investigations of Mechanically Alloyed W-SiC and W-SiC-Y_2O_3 Composites. (M.Sc. Thesis), I.T.U., Istanbul.

Coşkun, S. and Öveçoğlu, M.L. (2011). Effects of Y_2O_3 additions on mechanically alloyed and sintered W—4wt.% SiC composites. *International Journal of Refractory Metals and Hard Materials*, *29*(6), 651-655

Courtney, T.H. and Maurice, D. (1996). Process modeling of the mechanics of mechanical alloying. *Scripta Materialia*, *34*(1), 5-11.

Delogu, F., Orrù, R. and Cao, G. (2003). A novel macrokinetic approach for mechanochemical reactions, *Chemical Engineering Science, 58:* 815-821.

Demirkan, Ö.U., Genç, A. and Öveçoğlu, M.L. (2012). Effects of Al_2O_3 addition on the microstructure and properties of Ni activated sintered W matrix composites. *International Journal of Refractory Metals and Hard Materials, 32*, 33-38.

El-Eskandarany, M.S. (2001). *Mechanical Alloying for Fabrication of Advanced Engineering Materials*, Noyes Publications, New York.

El-Eskandarany, M.S., Mahday, A.A., Ahmed,H.A and Amer, A.H. (2000). Synthesis and characterizations of ball-milled nanocrystalline WC and nanocomposite WC–Co powders and subsequent consolidations, *Journal of Alloys and Compounds*, 312: 315–325.

Fang, Z.Z. (2010). *Sintering of advanced materials*, Elsevier.

Fecht, H.J. (2002). Nanostructured materials and composites prepared by solid state processing, *Nanostructured Materials: Processing, Properties and Potential Applications*, Ed. Koch, C.C., Noyes Publications, New York.

Gay, D., Hoa, S.V., Tsai, S.W. (2003). *Composite Materials Design and Applications*, CRC Press LLC, Florida."

Genç, A., Coşkun, S. and Öveçoğlu, M.L. (2010). Decarburization of TiC in Ni activated sintered W–xTiC (x= 0, 5, 10, 15 wt%) composites and the effects of heat treatment on the microstructural and physical properties. *International Journal of Refractory Metals and Hard Materials, 28*(3), 451-458.

Genç, A., Öveçoğlu, M.L., Baydoğan, M. and Turan, S. (2012). Fabrication and characterization of Ni–W solid solution alloys via mechanical alloying and pressureless sintering. *Materials & Design*, 42, 495-504.

Genç, A., Ayas, E., Öveçoğlu, M.L. and Turan, S. (2012). Fabrication of in situ Ni (W)–WC nano composites via mechanical alloying and spark plasma sintering. *Journal of Alloys and Compounds*, 542, 97-104.

Genç, A. and Öveçoğlu, M.L. (2010). Characterization investigations during mechanical alloying and sintering of Ni–W solid solution alloys dispersed with WC and Y_2O_3 particles. *Journal of Alloys and Compounds*, 508(1), 162-171.

German, R.M. (1996). *Sintering Theory and Practice*, John Wiley & Sons, Inc.

German, R.M and Munir, Z.A. (1976). Enhanced Low-Temperature Sintering of Tungsten, *Metallurgical Transactions* A, *7A***,** 1873-1877.

German, R.M and Munir, Z.A. (1982). Activated Sintering of Refractory Metals by Transition Metal Additions. Rev. Powder Metall. Phys. Ceram, *2*, 9-15.

Goff, A. (2003). *Modeling and synthesis of a piezoelectric ceramic-reinforced metal matrix composites.* (MS Thesis), Virginia Polytechnic Institute and State University, Blacksburg, VA.

Groza, J.R. (1999). Nanosintering. *Nanostructured Materials*, ***12***(5), 987-992.

Groza, J.R. and Zavaliangos, A. (2003). Nanostructured bulk solids by field activated sintering. *Rev. Adv. Mater. Sci*, *5*(1), 24-33.

Gupta, V.K. Yoon D-H. (2007). Thin intergranular films and solid-state activated sintering in nickel-doped tungsten, Acta Materialia, *55*, 3131-3142.

Gusev, A.I. and Rempel′, A.A. (2004). *Nanocrystalline materials*, Cambridge Int Science Publishing.

Habashi, F. (1997).Handbook of Extractive Metallurgy, Volume 4.

Hamouda, A.M.S., Sulaiman, S., Vijayaram, T.R., Sayuti, M. and Ahmad, M.H.M. (2007). Processing and characterisation of particulate reinforced aluminium silicon matrix composite. *Journal of achievements in materials and manufacturing engineering*, *25*(2), 11-16.

Hayden, H.W. and Brophy, J.H. (1963). The Activated Sintering of Tungsten with Group VIII Elements, Journal of Electrochemical Society, *110*, 805-810.

Huda, M.D., Hashmi, M.S.J. and El-Baradie, M.A. (1995). MMCs: materials, manufacturing and mechanical properties. *Key Engineering Materials, 104*(107), 37-64.

Hull, D. and Bacon, D.J. (2001). *Introduction to dislocations*, Butterworth-Heinemann.

Hunt, W.H. JR. (2000). *Particulate Reinforced MMCs* Metal Matrix Composites of Comprehensive Composite Materials, Elsevier.

Ibrahim, I.A., Mohamed, F.A. and Lavernia, E.J. (1991). Particulate reinforced metal matrix composites – a review. *Journal of Materials Science*, *26*, 1137-1156.

Kang, S-J.L. (2005). *Sintering Densification, Grain Growth and Microstructure*. Elsevier.

Kasper, E., Schuh, A., Bauer, G., Holländer, B., and Kibbel, H. (1995), Test of Vegard's law in thin epitaxial SiGe layers. *Journal of Crystal Growth*, *157*(1-4), 68–72.

Kern, A.A. and Coelho, A.A. (2006). TOPAS 5 (BRUKER AXS), www.brukeraxs.com

Kim, S.H. and Hahn, H.T. (2006). Size effect in particulate metal matrix composites: an analytical approach. *Advanced Composite Materials*, *15*, 175-191.

Kim, S-W., Lee, S-I., Kim, Y.D. and Moon, I-H. (2003). High temperature compressive deformation and fracture characteristics of the activated sintered W-Ni compacts, *International Journal of Refractory Metals&Hard Materials, 21*, 183-192.

Krivoglaz MA. (2012), *X-ray and neutron diffraction in nonideal crystals*, Springer Science & Business Media.

Krivoglaz, M.A. (1969). Theory of x-ray and thermal-neutron scattering by real crystals, Elsevier.

Kurlov, A.S. and Gusev, A.I. (2013), Nanocrystalline Tungsten Carbide. In Tungsten Carbides *Springer International Publishing*, 109-189.

Landis, C.M. and McMeeking, R.M. (1999). Stress concentrations in composites with interface sliding, matrix stiffness and uneven fiber spacing using shear lag theory. *International journal of solids and structures*, *36*(28), 4333-4361.

Lassner, E. and Schubert, W.D. (1999). *Tungsten: Properties, Chemistry, Technology of the Element, Alloys and Chemical Compounds*, Kluwer Academic, New York.

Lee, K.H., Yoon, J.K., Lee, J.K., Doh, J.M., Hong, K.T. and Yoon, W.Y. (2004). Growth Kinetics of W_5Si_3 Layer in WSi_2/W System, *Surface & Coatings Technology*, *187:* 146– 153.

Li, C. and German, R.M. (1983). The Properties of Tungsten Processed by Chemically Activated Sintering, *Metallurgical Transactions* A, *14A*: 2031-2041.

Lindroos, V.K., Hellman, J.T., Lou, D., Nowak, R., Pagounis, E., Liu, X.W. and Penttiren, I.M. (2004). Designing with metal matrix composites, in *Handbook of Mechanical Alloy Design*, Eds. Totten, G.E., Xie, L. and Funatani, K, M. Dekker, New York.

Lloyd, D.J. (1989). The solidification microstructure of particulate reinforced aluminium/SiC composites. *Composites Science and Technology*, *35*(2), 159-179.

Liu, G.R. (1997). A step-by-step method of rule-of-mixture of fiber-and particle-reinforced composite materials, *Composite structures*, *40*(3), 313-322.

Liu, N., Hu, Z.H., Cui, K. (1997). Valance electron structure and eigen properties of (Ti,W)C ceramic phase, *Journal of Chinese Ceramic Society*, *25*(4), 420-425.

Liu, Y.B., Lim, S.C., Lu, L. and Lai, M.O. (1994). Recent development in the fabrication of metal matrix particulate composites using powder metallurgy techniques. *Journal of Materials Science*, *29*, 1999-2007.

Lubarda, V.A. (2003). On the effective lattice parameter of binary alloys. *Mechanics of Materials*, *35*(1-2), 53–68.

Mabuchi, M., Okamoto, K., Saito, N., Asahina, T. and Igarashi, T. (1997). Deformation behavior and strengthening mechanisms at intermediate temperatures in W-La_2O_3, *Materials Science & Engineering A, 237*, 241-249.

Martin, J.W. (1980). *Micromechanisms in particle-hardened alloys*, CUP Archive.

Massalski, T.B. (1990). *Binary alloy phase diagrams*, 2nd ed., ASM, Metals Park, OH, USA.

Mazumdar, S.K. (2002). *Composite Manifacturing, Materials, Product and Process Engineering*, CRC Press LLC, Florida.

Mitchell, B.S. (2004). *An introduction to materials engineering and science for chemical and materials engineers*, John Wiley & Sons.

Mittemeijer, E.J. (2010). Phase Transformations. In Fundamentals of Materials Science *Springer Berlin Heidelberg*, 371-461.

Munir, Z.A. and German, R.M. (1977). Generalized model for prediction of periodic trends in activation of sintering of refractory-metals. *High Temperature Science, 9*(4), 275-283.

Öveçoğlu, M.L. (1987). *Development of a dispersion-strengthened Al-Fe-Ce alloy by mechanical alloying and related theoretical modeling of dislocations in composite materials,* (Ph.D. Thesis), Stanford University, Los Angeles, CA .

Panichkina, V.V. (1967). Activated sintering of tungsten with small additions of nickel, *Poroshkovaya Metallurgiya in Russian, 2,* 1-5.

Poquette, B. (2005). *Damping Behavior in ferroelectric Reinforced metal matrix composites.* (MS Thesis), Virginia Polytechnic Institute and State University, Blacksburg, VA.

Powder Diffraction Files: Card No. 49-1440, Database Edition, The International Centre for Diffraction Data (ICDD).

Powder Diffraction Files: Card No. 04-0806, Database Edition, The International Centre for Diffraction Data (ICDD).

Powder Diffraction Files: Card No. 51-0939, Database Edition, The International Centre for Diffraction Data (ICDD).

Powder Diffraction Files: Card No. 53-0619, Database Edition, The International Centre for Diffraction Data (ICDD).

Powder Diffraction Files: Card No. 71-6256, Database Edition, The International Centre for Diffraction Data (ICDD).

Powder Diffraction Files: Card No. 72-4509, Database Edition, The International Centre for Diffraction Data (ICDD).

Powder Diffraction Files: Card No. 89-2371, Database Edition, The International Centre for Diffraction Data (ICDD).

Ring, T. A. (1996). *Fundamentals of ceramic powder processing and synthesis*. Academic Press, 781-874.

Ryu, H.J. and Hong, S.H. (2003). Fabrication and properties of mechanically alloyed oxide-dispersed tungsten heavy alloys, *Materials Science and Engineering A, 363:* 179–184.

Ryu, H.J., Hong, S.H. and Baek, W.H. (2000). Microstructure and mechanical properties of mechanically alloyed and solid-state sintered tungsten heavy alloys, *Materials Science and Engineering A, 291***:** 91–96.

Samsonov, G.V. and Yakovlev, V.I. (1967). Activated Sintering of Tungsten with Nickel Additions. Poroshkovaya Metallurgiya in Russian, *8,* 10-16.

Samsonov, G.V. and Yakovlev, V.I. (1969). Activation of the Sintering of Tungsten by the Iron-Group Metals. Poroshkovaya Metallurgiya in Russian, *10,* 32-38.

Scherrer, P. (1918). Estimation of the size and internal structure of colloidal particles by means of röntgen. *Nachr. Ges. Wiss. Göttingen*, *2,* 96-100.

Smallman, R.E. and Bishop, R.J. (1999). Modern physical metallurgy and materials engineering. *Butterworth-Heinemann.*

Schwartz, M.M. (1984). *Composite Materials Handbook*, McGraw-Hill, New York.

Schwartz, M.M. (1997). *Composite Materials-Vol.1*, McGraw-Hill, New York.

Shackelford, J.F. (2001). *Materials Science and Engineering Handbook*, CRC Press LLC.

Song, G.M., Wang, Y.J. and Zhou, Y. (2002). The mechanical and thermophysical properties of ZrC/W composites at elevated temperature, *Materials Science and Engineering A, 334,* 223–232.

Song, G.M., Zhou, Y. and Wang, Y.J. (2003)a. Effect of carbide articles on the ablation properties of tungsten composites, *Materials Characterization, 50,* 293– 303.

Song, G.M., Wang, Y.J. and Zhou, Y. (2003)b. Thermomechanical properties of TiC particle-reinforced tungsten composites for high temperature applications, *International Journal of Refractory Metals & Hard Materials, 21,* 1–12.

Stjernstoft, T. (2004). *Machining of some difficult-to-cut materials with rotary cutting tools,* (PhD Thesis), K.T.H., Stockholm.

Sun, B., Fan, T. and Zhang, D. (2004). Production of morph-genetic TiC/C ceramic, *Materials Letters, 58,* 798-801.

Sun, L.Z., Liu, H.T. and Ju, J.W. (2003). Effect of particle cracking on elastoplastic behaviour of metal matrix composites, *Int. J. Numer. Meth. Eng, 56,* 2183–2198.

Suryanarayana, C. (2001). Mechanical alloying and milling, *Progress in Materials and Science, 46,* 1-184.

Suryanarayana, C., Ivanov, E. and Boldyrev, V.V. (2001). The science and technology of mechanical alloying, *Materials Science and Engineering A, 304,* 151–158.

Suryanarayana C, Norton MG. (2013). X-ray diffraction: a practical approach. *Springer Science & Business Media*.

Suryanarayana C. (2004). Mechanical alloying and milling. *CRC Press*.

Tang, H.G., Ma, X.F., Zhao, W., Yan, X.W., Yan, J.M. and Zhu, C.J. (2004). Crystallization of mechanically alloyed amorphous W–Mg alloy under high pressure, *Solid State Communications, 129,* 147–150.

Tjong, S.C. and Ma, Z.Y. (2000). Microstructural and mechanical characteristics of in situ metal matrix composites, *Materials Science and Engineering, 29,* 49-113.

Toth, I.J. and Lockington, N.A. (1967). The Kinetics of Metallic Activation Sintering of Tungsten. *J. Less-Common Met., **12,*** 353-365.

Url-1: < http://www.crct.polymtl.ca >, date retrieved 30.06.2015.

Upadhyaya, G.S. (2000). *Sintered Metallic and Ceramic Materials: Preparation, Properties, and Applications***,** Wiley, New York.

Upadhyaya, G.S. (2000). Some issues in sintering science and technology. *Materials Chemistry and Physics*, *67*, 1-5.

Vacek, J. (1959). On Influencing the Sintering Behavior of Tungsten. *Planseeberiche fur Pulvermetallurgie, 7*, 6-17.

Vegard, L. (1921). Die konstitution der mischkristalle und die raumfüllung der atome. *Zeitschrift für Physik*, *5*(1), 17-26..

Warren, R. and Andersson, C.H. (1984). Silicon carbide fibres and their potential for use in composite materials. *Part II. Composites*, *15*(2), 101-111.

Warren, B.E., Averbach, B.L. and Roberts, B.W. (1951). Atomic size effect in the X-Ray scattering by alloys. *Journal of Applied Physics*, *22*(12), 1493-1496.

Williamson G.K., Hall W.H. (1953). X-ray line broadening from filed aluminum and wolfram. *Act Metal.*, *1*(1), 22–31.

Yang, S., Sun, Z-M. and Hashimoto, H. (2003). Formation of Ti_3SiC_2 from Ti-Si-TiC powders by pulse discharge sintering (PDS) technique, *Materials Research Innovations*, *7*, 225-230.

Zhang, F.L., Wang, C.Y. and Zhu, M. (2003). Nanostructured WC/Co composite powder prepared by high energy ball milling, *Scripta Materialia*, *49*, 1123–1128.

CURRICULUM VITAE

Name Surname **:** Hadi JAHANGIRI

Place and Date of Birth **:** IRAN- 1980

E-Mail **:** jahangiri_hadi@yahoo.com

EDUCATION **:**

- **B.Sc.** **:** 2003, Tabriz University, Material science Eng. Faculty, Ceramic Eng. Department
- **M.Sc.** **:** 2005, Tehran Azad University, Material science Eng. Faculty, Metallurgical Eng. Department

PROFESSIONAL EXPERIENCE AND REWARDS:

- 2011-2016 ISTANBUL Technical University at the PML Laboratory of the Metallurgical Eng.
- 2016 Completed Doctorate at ISTANBUL Technical University.

PUBLICATIONS, PRESENTATIONS AND PATENTS ON THE THESIS:

- **Jahangiri, H.** and Öveçoğlu, M.L., 2016. "Determination of crystallite size, strain and solubility in mechanically alloyed W-xTi (x= 0.5, 1.0, 4.0 and 10.0 wt%) powder alloys." Materials Letters, 178, pp.193-196.
- **Jahangiri, H**., Sönmez, S. and Öveçoğlu, M.L., 2016. "Influence of Milling Media on the Mechanical Alloyed W-0.5 wt. Ti Powder Alloy."*Indian Journal of Materials Science* 2016.